8-2005

A geodetic investigation of ground deformation at Yucca Mountain, southern Nevada

Emma McCaughey
University of Nevada, Reno

University of Nevada, Reno

A geodetic investigation of ground deformation at Yucca Mountain, southern Nevada

A dissertation submitted in partial fulfillment of the requirements for the degree of Doctor of Philosophy in Geophysics

by

Emma McCaughey

Prof. Geoffrey Blewitt / Dissertation Advisor

August 2005

UNIVERSITY
OF NEVADA
RENO

THE GRADUATE SCHOOL

We recommend that the dissertation
prepared under our supervision by

EMMA MCCAUGHEY

entitled

A geodetic investigation of ground deformation at Yucca Mountain, southern Nevada

be accepted in partial fulfillment of the
requirements for the degree of

DOCTOR OF PHILOSOPHY

[redacted]

Geoffrey Blewitt, Ph.D., Advisor

[redacted]

John Anderson, Ph.D., Committee Member

[redacted]

Jonathan Price, Ph.D., Committee Member

[redacted]

James Taranik, Ph.D., Committee Member

[redacted]

Lee Thomas, Ph.D., Graduate School Representative

[redacted]

Marsha H. Read, Ph. D., Associate Dean, Graduate School

August, 2005

ABSTRACT

The data from 28 continuous BARGEN GPS stations in the Yucca Mountain region were processed for January 2000 to June 2004. The data have been processed independently using both the GIPSY and GAMIT software packages for quality assurance purposes, yielding an RMS of velocity differences between the solutions of 0.06 mm/yr for the east and 0.10 mm/yr for the north. The velocity solution for the local Yucca Mountain network has a relatively smooth signal showing NW-trending right-lateral shear. The magnitude of the velocity contrast across the local network, from east to west, is 0.95 ± 0.04 mm/yr. The GPS results were inverted, using an elastic dislocation model, to estimate fault parameters for the San Andreas (SA), Owens Valley (OV), Panamint Valley-Hunter Mountain (PV-HM) and Death Valley-Furnace Creek (DV-FC) fault systems. Estimated slip rates are 30.4 ± 0.2 mm/yr, 2.6 ± 0.7 mm/yr, 4.5 ± 1.3 mm/yr, and 5.0 ± 0.6 mm/yr, respectively. Estimated locking depths are 12.0 ± 1.0 km, 8.2 ± 7.8 km, 11.5 ± 6.6 km, and 33.0 ± 2.4 km, respectively. The estimated locking depth of ~33 km for the DV-FC fault system is unreasonably deep and caused by the inversion fit to the relatively steep velocity gradient across Yucca Mountain. With a hypothetical local model fault at Yucca Mountain included in the inversion, estimated slip rates are 30.8 ± 0.2 mm/yr, 3.2 ± 0.6 mm/yr, 4.7 ± 1.0 mm/yr, 2.8 ± 0.4 mm/yr, and 0.8 ± 0.2 mm/yr for the SA, OV, PV-HM, DV-FC and local model faults respectively. This results in a total Eastern California Shear Zone (ECSZ) slip rate of 11.5 ± 1.2 mm/yr, which agrees with the GPS estimate of 11.5 ± 0.1 mm/yr. Estimated locking depths are 11.9 ± 1.0 km, 6.6 ± 4.9 km, 7.6 ± 4.6 km, 11.8 ± 3.4 km, and 12.5 ± 3.2 km

for the SA, OV, PV-HM, DV-FC and local model fault systems, respectively. Although the RMS of velocity differences between model and GPS results is not significantly improved by including a local model fault, this puts the DV-FC locking depth at a more physically reasonable level of ~12 km. The addition of a local model fault (which could represent deformation across any number of the mapped faults) is, therefore, one way to explain the GPS results. The models do not account for factors such as varying fault orientation, finite fault length, postseismic deformation, earthquake cycle effects, or oblique slip, and the use of improved fault models is likely to change the estimated fault parameters. However, the inversion results do suggest that it is difficult to explain the GPS results for the local network using only models of the ECSZ faults. Estimated total right-lateral shear strain rate for the local Yucca Mountain network, based on the fault parameters estimated for the ECSZ faults, is 11.3 ± 1.4 ns/yr. This compares with a GPS estimate for all stations in the local network of 18.1 ± 0.7 ns/yr, oriented N16 ± 1^{o}W. The GPS estimate of shear strain rate assumes uniform strain across the network, which is not the case in reality. Estimated model shear strain for stations within the local network at and to the west of Yucca Mountain is 13.6 ± 1.6 ns/yr. This agrees to within one standard deviation with the GPS estimate for the western cluster of stations, which is 15.7 ± 1.1 ns/yr, oriented N20 ± 2^{o}W. The estimate of model shear strain rate for stations in the local network to the east of Yucca Mountain is 8.9 ± 1.1 ns/yr. This is significantly lower than the GPS estimate of 25.1 ± 1.3 ns/yr, oriented N8 ± 2^{o}W. This suggests that it is possible to explain the GPS-measured strain rate for the western cluster of stations using dislocation models of the ECSZ faults (with no local fault necessary), but it is not possible to explain the GPS estimate of strain rate for the eastern cluster

using these models. This highlights the need to investigate further the possibility of left-lateral deformation across the NE-trending Rock Valley fault zone, particularly since the GPS estimate of strain rate is ambiguous, and could represent left-lateral strike-slip faulting on a N82 ± 2^{o}E trending fault system.

Acknowledgments

Geoff Blewitt, my advisor, has been a continual source of both professional and personal support since I started my undergraduate dissertation with him at Newcastle University in 1998. I am thankful to Geoff for giving me the opportunity to come to Nevada in the first place, a decision I have not regretted since my initial, agonizing, flight across the Atlantic. Geoff's careful review of my first dissertation draft greatly improved my writing style and his comments and suggestions over the years have contributed invaluably to the final product. Geoff's wife, Debbie Vigil, has also been a true friend since my arrival in Reno and I am overwhelmingly grateful to them both for making me feel so welcome in their family.

I am grateful to my committee members; John Anderson, Jim Taranik, Jon Price, Lee Thomas, and Steve Wesnousky, for so generously giving their time and energy over the years and for providing useful discussion and constructive criticism of this dissertation. Jon Price kindly replaced Steve Wesnousky as a committee member just before my defense, due to Steve's temporary absence from Reno due to work in South America, and I would like to thank Jon for doing the fastest review of a dissertation ever heard of at UNR. My knowledge of geology can almost entirely be attributed to classes instructed by Steve Wesnousky, and it was Steve who taught me, during my first week in Nevada, that a fault is not just an equation but also a complicated, muddy, reality. Steve's Quaternary mapping classes were not only invaluable to my understanding of

geology, but they also made my first semester at UNR one of the most enjoyable and rewarding. Jim Taranik took pity on me on my first day in Nevada, having found me wandering the corridors of the geology building looking lost, and spent a good deal of time that day explaining the complexities of the university system to me. I was struck by his kindness that day, and have appreciated him since as a helpful and encouraging member of my committee. John Anderson's careful review of my dissertation resulted in a number of changes I am very glad to have made, and I am grateful to him for that. I was also lucky to have Lee Thomas on my committee as the ideal 'graduate school representative'. Lee has been a great friend and source of good cheer and useful advice, and was also the only person to spot the typing mistakes in my list of references! Bill Hammond contributed to this dissertation in the form of useful comments and suggestions, and David Lavallée was an invaluable source of knowledge and advice when I was initially learning to use the GIPSY software.

The GAMIT GPS solution was provided by Jim Davis and Rick Bennett, who also provided useful discussions. The Yucca Mountain GPS network would not exist without the work of Brian Wernicke, and he has inspired a great deal of this research with his ideas and interpretations of the data. Yearly meetings with Brian and the Department of Energy folks in Las Vegas proved to be very useful.

Fellow graduate students Rich Briggs and Andy Rael have been a great source of support and friendship since my early days at UNR, as have been many other friends too numerous to mention here. Rich's patient explanations of geology, given while

wandering around the desert with aerial photographs during Steve's Quaternary mapping class, contributed greatly to my understanding of neotectonics. It is also customary at this point, I believe, to mention Bob the barman, who has been serving beer to the geology graduate students every Thursday evening for at least 5 years, and always with a smile.

Finally, none of this would have been possible without the constant support and encouragement of my husband, Jamie McCaughey, and my family, both British and American. Jamie has dealt with all the ups and downs of my dissertation writing with good humor and patience, been a pillar of strength throughout, and done most of the washing-up for the last month.

Many of the figures in this dissertation were prepared using the Generic Mapping Tools (Wessel and Smith, 1998). Funding for this project was provided by the U.S. Department of Energy *Geodetic Monitoring of the Yucca Mountain Region by Continuous GPS Research Project* (P.I.s Jonathan Price and Geoffrey Blewitt):

This report was prepared by Emma McCaughey pursuant to a Cooperative Agreement fully funded by the United States Department of Energy, and neither the University of Nevada, Reno, nor any of its contractors or subcontractors nor the United States Department of Energy, nor any person acting on behalf of either: Makes any warranty or representation, express or implied, with respect to the accuracy, completeness, or usefulness of the information contained in this report, or that the use of

any information, apparatus, method, or process disclosed in this report may not infringe privately-owned rights; or assumes any liabilities with respect to the use of, or for damages resulting from the use of, any information, apparatus, method or process disclosed in this report. Reference herein to any specific commercial product, process, or service by trade name, trademark, manufacturer, or otherwise, does not necessarily constitute or imply its endorsement, recommendation, or favoring by the United States Department of Energy. The views and opinions of authors expressed herein do not necessarily state or reflect those of the United States Department of Energy.

Table of Contents

List of Figures

List of Tables

Appendix

1. Introduction

1.1 Political background

Yucca Mountain, in southern Nevada (Figure 1), has been selected as the location at which the United States Department of Energy (DoE) is to build a repository to store the approximately 70,000 metric tons of high-level nuclear waste currently being housed at numerous locations across the United States. Yucca Mountain is on the western edge of the Nevada Test Site, which has had a long history of nuclear exposure through underground and atmospheric nuclear tests. Yucca Mountain was selected as the location for a repository partly for political reasons and the low population density of the area, but also because of the arid nature of the region and the low level of the water table; although the repository will be situated approximately 300 m below the surface, it will still be approximately 300 m above the water table. This is important because if water seeps into the storage tunnels it will accelerate the corrosion of the containment canisters. If the canisters break down, this water can then carry radionuclides to the water table and, through both natural and human processes, such as ground water pumping, reach the biosphere (Hanks et al., 1999). This is certainly going to happen at some point, but the big question is how fast. Environmental Protection Agency (EPA) standards originally dictated that for 10,000 years no member of the public should be exposed to >15 millirem of radiation per year as a result of the repository (Macilwain, 2001). On 9 July 2004, however, the Federal Appeals Court ruled that the EPA had ignored National Academy

of Science (NAS) recommendations that the regulatory compliance period extend to at least the time of peak radiation hazard, which is between 300,000 and 1 million years. The cutoff time may therefore be changed to reflect these recommendations.

To complicate the situation, the area has abundant fractures and minor faults, and lies within close proximity to areas of high tectonic activity. The most important variable controlling seepage into the storage containers is likely to be climate change, but some scientists have suggested that earthquake activity along the faults at Yucca Mountain could close or open fractures in the ground and change the level of the water table as a result (Davis and Archembeau, 1997), meaning that these factors, along with many others (such as how the mountain will react to being heated to temperatures around 100^{o}C for thousands of years), need to be well understood. The likelihood of 'unexpected behavior' from volcanism and seismic moment release also, obviously, needs to be well quantified. DoE has therefore funded a multi-billion dollar risk assessment investigation. This investigation has covered many aspects of site characterization, including climatology, hydrology, geology and geophysics. As part of this project, DoE has funded the installation and monitoring of a densely spaced, continuously monitoring GPS network, centered around Yucca Mountain, in order to contribute to characterizations of the local and regional tectonics of the area.

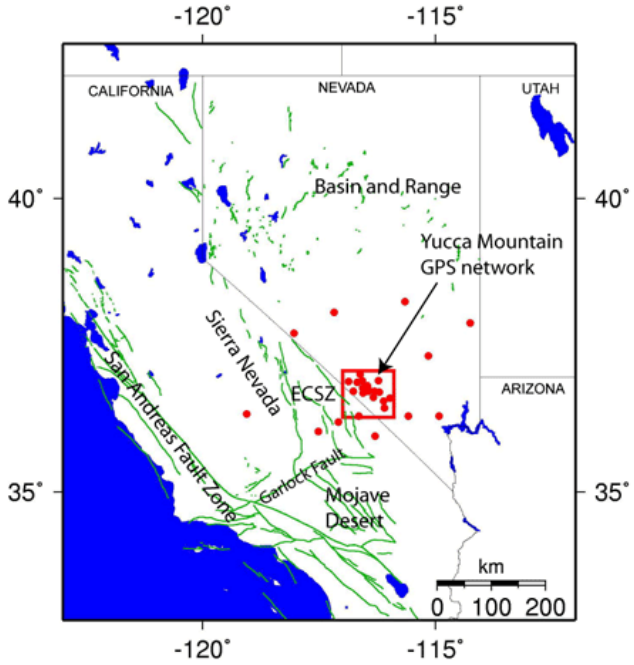

Figure 1. Yucca Mountain location map. Quaternary faults for California and Nevada are shown in green (from Jennings (1975) and Dohrenwend et al. (1996) respectively). BARGEN continuous GPS stations used in this study are shown as red dots.

1.2 Regional tectonic setting

The plate boundary between the Pacific and North American plates is unusually broad and complex. Total relative plate motion is 48.8 ± 1 mm/yr, oriented at N44^{o}W ± 1^{o}, in southern California and 48.2 ± 1.0 mm/yr, oriented at N37^{o}W ± 1^{o}, in northern California (Kreemer et al., 2003). Although, depending on location, 14-39 mm/yr of relative motion is taken up by the San Andreas fault system (USGS Fault Database, 2004; Bennett et al., 2003), the rest is taken up by a zone of deformation that extends at least 1100 km to the Colorado Plateau to the east. The faults in this wide, continental plate boundary have many varied orientations and types of faulting. The plate boundary zone can be divided into a number of distinct tectonic provinces, as shown in Figure 2. Both

Figures 2 and 3 show that Yucca Mountain is located on the boundary of a number of these tectonic provinces. It is located within the Walker Lane and the Basin and Range, and to the east of the Eastern California Shear Zone (ECSZ).

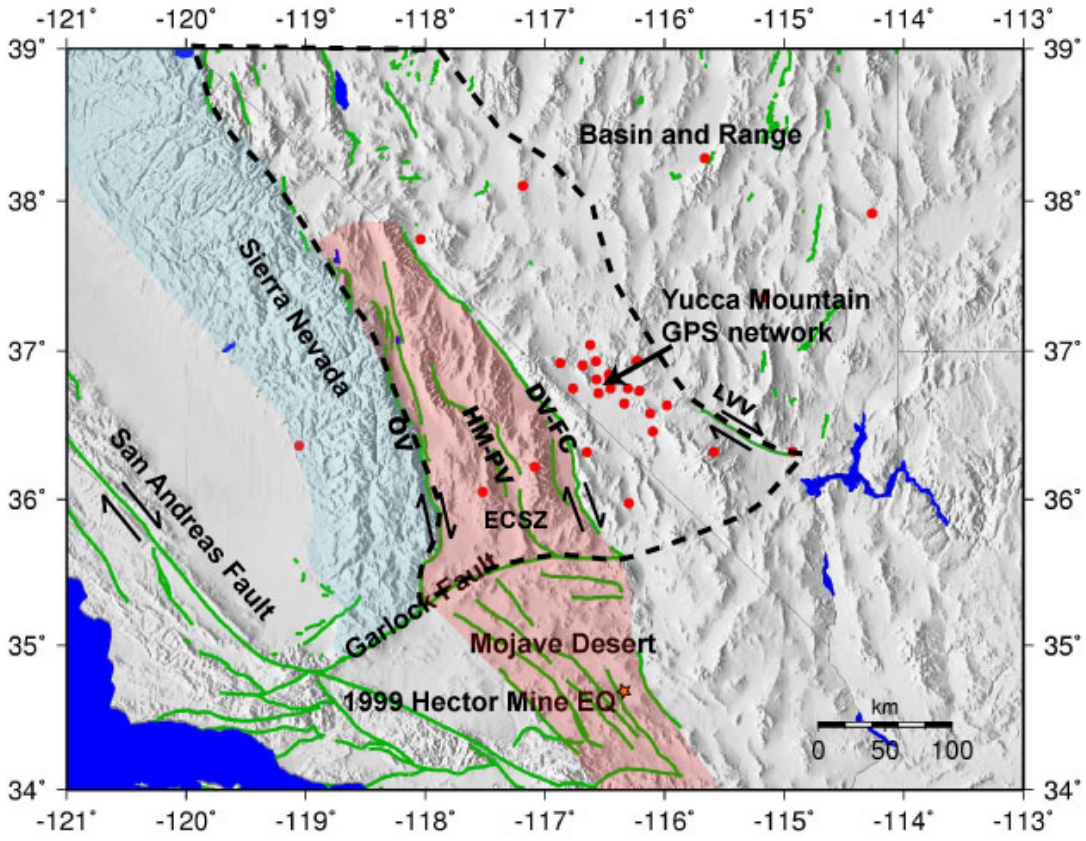

Figure 2. General tectonics of southern Nevada and California. The Walker Lane is outlined by a dotted line (Stewart, 1988). Quaternary fault traces, shown in green, are from Jennings (1975) and Dohrenwend et al. (1996). The ECSZ is highlighted in pink. The Owens Valley (OV), Hunter Mountain-Panamint Valley (HM-PV), Death Valley-Furnace Creek (DV-FC), and Las Vegas Valley shear zone (LVV) are labeled.

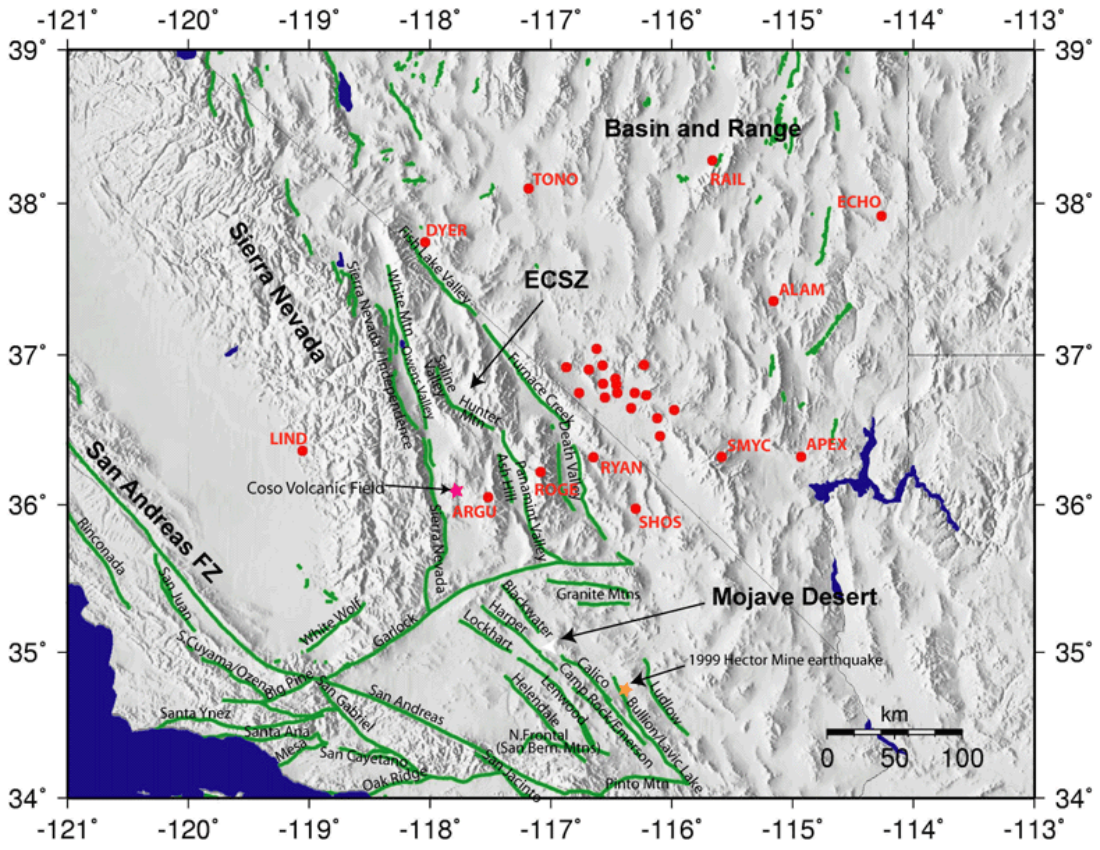

Figure 3. Simplified Quaternary fault map (fault coordinates from Jennings (1975) and Dohrenwend et al. (1996)). BARGEN GPS stations are shown as red dots.

1.2.1 The Walker Lane

The Walker Lane is a topographically and tectonically complex zone of right- and left- lateral faulting and normal faulting (Stewart, 1988) that sits along the western edge of the Basin and Range. It is ~100-300 km wide and ~700 km long, and forms the boundary zone between primarily extensional faulting along NNE-striking faults in the Basin and Range to the east and the Sierra Nevada to the west. The Walker Lane has accommodated a significant portion of Pacific-North American relative plate motion, via right lateral shear and large-scale extension, since the mid- to late-Miocene (Dokka and

Travis, 1990a). The southern end of the Walker Lane is better understood than the northern end.

Stewart (1988) divides the Walker Lane into a number of regions that differ significantly. Some, such as the ECSZ, to the south, and the Pyramid Lake and Walker Lake sections, to the north, demonstrate right-lateral shear on NW-trending faults. In contrast, some regions, such as the Carson Block, Excelsior-Coaldale Block and Spotted Range-Mine Mountain section, contain mostly NE-trending left-lateral faults. The sections defined by Stewart (1988) that concern Yucca Mountain are the Goldfield section, which contains the Yucca Mountain site and is characterized by irregular topography and a lack of major strike slip or Basin and Range style faults, the Spotted Range-Mine Mountain section, to the south of the Goldfield section, which is dominated by NE-striking left-lateral faults, and the Spring Mountain section, to the south of this, which largely displays Basin and Range style faulting.

1.2.2 The Eastern California Shear Zone

The approximately 100 km-wide ECSZ, which partly overlaps the southern Walker Lane, is a zone of concentrated shear strain located approximately 40 km to the west of Yucca Mountain. The term ‘ECSZ’ (Dokka and Travis (1990a)) is used to describe the zone of shear that stretches from the eastern end of the compressive ‘big bend’ in the southern San Andreas fault, through the Mojave Desert and up into the area bounded by the Sierra Nevada to the west and Death Valley - Furnace Creek fault to the

east.

In the Mojave desert the ECSZ comprises a number of sub-parallel, primarily right-lateral strike-slip faults. These are oriented northwest to easily accommodate Pacific-North America relative plate motion with little secular rotation required. Major historical earthquakes occurring in the Mojave desert have been the 28th June 1992 M_w7.3 Landers earthquake and the 1999 M_w7.1 Hector Mine earthquake. The 1992 Landers earthquake ruptured the ~NW-trending Johnson Valley, Landers, Homestead Valley, Emerson and Camp Rock faults, with a total rupture length of ~85 km and an average offset of 3-4 meters. It was followed by a series of aftershocks, the largest of which being the M_s6.4 Big Bear earthquake, which occurred 4 hours later on a left-lateral, conjugate fault approximately 40 km to the west (for example, SCEC Earthquake Database; http://www.data.scec.org, accessed February 2004; Blewitt et al. (1993); Miller (1993)). The Landers earthquake is important to studies at Yucca Mountain as it also served as a precursor to the M_s=5.4 June 1992 Little Skull Mountain earthquake (Section 1.3), which occurred ~22 hours later.

The 1999 Hector Mine earthquake is discussed in more detail in Chapter 2 as it directly affected the Yucca Mountain GPS network. The location of the epicenter is shown in Figure 2. This earthquake ruptured ~41 km of the ~NW-trending Bullion - Lavic Lake faults, with a maximum offset of 5.2 meters. (SCEC Earthquake Database; http://www.data.scec.org (accessed February 2004); Scientists from the USGS et al. (2000)).

It is worth noting that these historical earthquakes have often occurred on previously unmapped faults. The Landers fault, which was ruptured during the 1992 Landers earthquake, was previously unknown, as was the fault which caused the Big Bear aftershock (this fault did not rupture on the surface, so was only identified through examination of its aftershocks). The Lavic Lake fault, which ruptured during the Landers earthquake, had been partially mapped prior to the earthquake but was unnamed and presumed to be inactive during the Holocene. Two possible explanations exist for this; either the fault trace was hidden by high rates of alluvial deposition in the valley, or the fault had not ruptured during the last 10,000 years.

North of the Garlock fault, in the region sometimes referred to as the Inyo-Mono domain, faulting becomes more complex as faults are oriented in a more northerly direction, so relative plate motion must be accommodated by not only right-lateral but also normal faulting. The most important features of the ECSZ north of the Garlock fault are the three, sub-parallel Owens Valley-White Mountain, Panamint Valley-Hunter Mountain-Saline Valley and Death Valley-Furnace Creek-Fish Lake Valley fault zones (discussed in more detail below). These are connected by a number of NW trending normal faults (Reheis and Dixon (1996); Oswald and Wesnousky (2002)). This is the part of the ECSZ concentrated on in this study, since it is located at the latitude of Yucca Mountain.

The approximately 110km long, predominantly right-lateral, Owens Valley fault

lies to the west of the ECSZ, on the eastern flank of the Sierra Nevada. The Owens Valley fault was the location of one of California's largest historical earthquakes, the 1872 Owens Valley earthquake of M_w~7.5, which ruptured 90 to 110 km of the fault, with vertical offsets of ~1 m and right-lateral strike slip offsets averaging 6 m (Beanland and Clark, 1991). The Owens Valley fault is connected at its northern end to the White Mountain fault. To the west of the Owens Valley fault is the Sierra Nevada - Independence fault, a normal fault system with a total length of ~280 km. The Owens Valley and Sierra Nevada - Independence faults together illustrate a system of partitioned slip, with strike slip faulting occurring on the valley-central Owens Valley fault and normal faulting occurring on the range-bounding Sierra Nevada - Independence faults, so as to accommodate relative motion between the Sierra Nevada and Basin and Range at a relative azimuth difference of ~N35^{o}W.

The N60^{o}W trending, ~40 km long Hunter Mountain fault links the N20^{o}W trending, ~95 km long Panamint valley fault, to the south, with the N60^{o}W trending Saline Valley fault, to the north. The Saline Valley fault system comprises a complex scattering of small, mostly < 5 km long, faults. The Hunter Mountain fault is primarily right-lateral strike-slip, while the Panamint Valley and Saline Valley faults also have some element of normal slip (Oswald and Wesnousky, 2002). Slip in Panamint Valley is, again, partitioned, with normal faulting along the range front and right-lateral strike-slip to the west of the range (Zhang et al., 1990).

The Death Valley fault is NNW-striking and 115-200 km long. The fault trace is

complex, with strike-slip faulting along the valley floor and normal faulting along the valley sides. At the northern end of the Death Valley fault, the trend of the fault bends round to the NW and the fault becomes the 180-220 km long, right-lateral Furnace Creek fault. This, in turn, becomes the right-lateral Fish Lake Valley fault at its northern extension. The Fish Lake Valley fault is approximately 80 km long and strikes NW. It is located along the eastern flank of the White Mountains. Dixon et al. (1995), Reheis and Dixon (1996), and Reheis and Sawyer (1997) argue that almost all the slip from the HM-PV and DV-FC fault zones is transferred to the north along the Fish Lake Valley fault, probably along NE trending normal faults such as the Deep Springs or Eureka Valley faults. This would make the Fish Lake Valley fault one of the most important faults in the western Basin and Range.

The Sierra Nevada, to the west of the ECSZ, appears to behave as a relatively rigid block (Dixon et al., 2000). The velocity of this block can be used to constrain total strain over the ECSZ as approximately 11 mm/yr (this value is better constrained with the GPS results from this study in Chapter 6), but it is still uncertain as to how this strain is distributed across the zone. The uncertainty is illustrated by Table 1, which gives a summary of published slip rates for the faults of ECSZ at the latitude of Yucca Mountain. How much slip to allocate to the faults of the ECSZ at the latitude of Yucca Mountain is a question that is vital to understanding the strain rates we observe with the GPS. Of particular interest is whether strain is concentrated along the east or west of the ECSZ, as this directly affects the expected magnitude of strain at Yucca Mountain.

Reference	Source	OV	PV-HM	DV-FC	FLV
Dixon et al. (2003)	geodetic	2.1±0.3	2.4	8.3±1.2	-
Bennett et al. (2003)	geodetic	~3?	~3?	~3?	-
Oswald and Wesnousky (2002)	geologic	-	3.3-4.0	-	-
Miller et al. (2001)	geodetic	7.0	0.0-2.7	3.8 -13.0	-
McClusky et al. (2001)	geodetic	4.6±0.5	2.5±0.8	2.8±0.5	-
Lee et al. (2001)	geologic	1.8-3.6	-	-	-
Gan et al. (2000)	geodetic	6.9±1.6	3.3±1.6	3.2±0.9	-
Dixon et al. (2000)	geodetic	3.0±1.9	-	-	8.4±2.0
Hearn and Humphreys (1998)	geodetic	0.1-1.2	2.5-3.1?	5-6	-
Bennett et al. (1997)	geodetic	0-7	-	3 - 5	-
Reheis and Sawyer (1997)	geologic	-	-	-	~5
Reheis and Dixon (1996)	geologic	3.9±1.1	-	3.3±2.2	6.2±2.3
Savage and Lisowski (1995)	geodetic	~7	-	-	-
Dixon et al. (1995)	geodetic	3.9±1.1	2.6±1	3.3±2.2	6.2±2.3
Beanland and Clark (1991)	geologic	2±1	-	-	-
Dokka and Travis (1990b)	geologic	-	-	6-12	-
Savage et al. (1990)	geodetic	8	-	-	-
Zhang et al. (1990)	geologic	-	2.4±0.8	-	-
Butler et al. (1988)	geologic	-	-	2-3	-
Burchfiel et al. (1987)	geologic	-	2.0-3.2	-	-

Table 1. Published slip rates for the Owens Valley (OV), Panamint Valley – Hunter Mountain (PV-HM), Death Valley – Furnace Creek (DV-FC) and Fish Lake Valley (FLV) faults. Positive slip rate is right lateral. Slip rates are given in mm/yr.

Geologic studies have indicated that strain is either accommodated fairly evenly between the Owens Valley, Panamint Valley - Hunter Mountain and Death Valley - Furnace Creek faults, putting ~2-4 mm/yr of slip on the Owens Valley fault (for example; Beanland and Clark (1991), Lee et al. (2001), Reheis and Dixon (1996)), 2-4 mm/yr on the Hunter Mountain - Panamint Valley fault system (for example; Burchfiel et al.

(1987), Zhang et al. (1990) and Oswald and Wesnousky (2002)), and 2-3 mm/yr on the Death Valley - Furnace Creek fault system (Butler et al. (1988) and Reheis and Dixon (1996)), or they have stated that slip rates towards the east are higher (for example, Dokka and Travis (1990a) put 6-12 mm/yr on the Death Valley - Furnace Creek fault system). Geodetic studies have, on the other hand, put concentrated slip towards the west of the ECSZ, allocating slip rates to the Owens Valley fault that are 2-3 times larger than those estimated through geologic studies and slip rates on the Death Valley - Furnace Creek fault that are lower (for example; Gan et al. (2000), Miller et al. (2001), Bennett et al. (1997)). Several studies put a high slip rate of ~6-8 mm/yr on the Fish Lake Valley fault, suggesting that it takes up much of the slip to the north of the ECSZ (for example; Dixon et al. (1995), Dixon et al. (2000) and Reheis and Dixon (1996)).

A number of explanations for the 'ECSZ controversy' exist. It could partly reflect the difficulty that scientists face in estimating slip rates from geodetic data, particularly when the faults are closely spaced and their strain fields overlap. By necessity the models must simplify reality and ignore many of the complexities of fault systems, so they cannot produce results that fully represent fault activity in the field.

Another explanation for the discrepancies could be the effect of the earthquake cycle. The Owens Valley fault is in an early stage of its earthquake cycle, whereas the Death Valley - Fish Lake Valley fault system is at a late stage. This could result in current geodetically measured rates that are smaller than the average rate over geologic time for faults late in the earthquake cycle, and geodetically measured rates that are

larger for faults early in their earthquake cycle. Bennett et al. (2003) and Dixon et al. (2000) tackle the idea that the geodetic studies are sensitive to the long-term postseismic effects of the M~8 1872 Owens Valley earthquake, and Dixon et al. (2000) use a model to correct their slip rates for the postseismic effects of the 1872 earthquake. This reduces their slip rate for the Owens Valley fault system from 7 ± 2 mm/yr to 3 ± 2 mm/yr, putting a greater proportion of strain on the faults to the east as a result (since total slip must add up to ~11 mm/yr). Gan et al. (2000) also get an estimate 3 times that of geologic rates for the Owens Valley fault, but concede that if this was averaged over the entire earthquake cycle, taking into account that it is still in a postseismic period, the slip rate would be closer to 2 mm/yr.

Alternatively, the explanation could be that slip rates have changed significantly over time. For example, Reheis and Sawyer (1997) conclude that lateral slip rates along the Fish Lake Valley fault have changed dramatically over time, decreasing from 6 mm/yr in the Miocene to 3 mm/yr in the Pliocene, then increasing to around 11 mm/yr in the middle Pleistocene and decreasing to 2-3 mm/yr in the late Pleistocene. They suggest that these changes are related to large volcanic eruptions; for example, the large increase in slip rate during the Pleistocene occurred after the eruption of the Bishop Ash (0.76 Ma) and collapse of the Long Valley Caldera.

Coupled with the idea of changing slip rates is the idea that shear in the ECSZ has shifted from east to west over time, with slip on the Death Valley -Furnace Creek fault system decreasing over the last few million years and slip on the Owens Valley fault

system increasing (e.g. Dixon et al. (1995), Dokka and Travis (1990b)). This assumption is based on the idea that the Owens Valley fault system developed later (~3 Ma) and has less total right lateral offset (10-20km) (Beanland and Clark, 1991) than the Death Valley -Furnace Creek fault zone, which developed around 12-8 Ma. The amount of offset on the DV-FC fault system varies greatly between publications, but ranges between 35 km (Butler et al., 1988) and 80 km (Stewart, 1967). Total offset is most likely between 40-50 km (Reheis and Sawyer, 1997). The Hunter Mountain fault zone is somewhere in-between, with age of inception around 4 Ma and total right lateral displacement approximately 20-30 km (Smith (1979), Zhang et al. (1990)). Upon formation of faults to the west, the slip rates on the DV-FC and/or the PV-HM fault systems had to decrease to accommodate the new faults. Further evidence is the geometry of the Garlock fault. Gan et al. (2003) suggest that the Garlock fault was formed before the initiation of the ECSZ, so has recorded a history of ECSZ shear. Examination of the geometry of the fault with this in mind suggests that, over time, the ECSZ has seen relatively uniform shear across its width at this latitude, but that the shear zone has widened towards the west over time, meaning that the Garlock fault has been displaced more at the eastern edge of the ECSZ than at the west, hence the bend towards the southeast. Using this as a model, Gan et al. (2003) conclude that the eastern side of the ECSZ originated about 5.0 ± 0.4 Ma, but the western side did not start until ~1.6 Myr later.

The Garlock fault itself is a large, left-lateral structure, oriented approximately orthogonal to the ECSZ. It is the subject of another discrepancy, with geologic slip rates high and geodetic results that suggest that the fault is inactive at present (Savage et al.,

2001). Long-term geologic slip rates are approximately 4-9 mm/yr (McGill and Sieh 1993). Examination of Figure 3 shows that fault traces are not continuous across the Garlock fault. Peltzer et al. (2001), however, examined eight years of ERS radar data for an area that trends NE from the Los Angeles basin in the south to the Coso volcanic field. The InSAR data shows a concentrated zone of shear between the southern end of the 1872 OV earthquake rupture and the northern end of the 1992 Landers earthquake rupture, with a slip rate of ~7 mm/yr. This complements GPS results that show a concentration of shear to the west, and Peltzer et al. (2001) also suggest either postseismic effects or a change in slip rate as an explanation for the discrepancy with geologic results. The interesting thing about this is that the zone of shear clearly passes through the Garlock fault, with a NW oriented, right lateral sense of slip across the fault, completely different to the left-lateral signal that would be expected from geologic results. The ECSZ and Garlock fault could together represent a conjugate fault system (similar to the North and East Anatolian faults) that alternates between right-lateral shear across the ECSZ and left-lateral shear across the perpendicular Garlock fault (Peltzer et al., 2001).

Additional to the faults already discussed, the Pahrump-Stateline fault zone extends for ~130 km along the California - Nevada state line. Total offset along the fault is 16-19 km (Stewart, 1988). Whether these faults have been active in Quaternary time is poorly understood, but it is generally accepted that the faults to the west have been more recently active than these (Zhang et al., 1990). Schweickert and Lahren (1997), however, argue for what would effectively be an extension of the ECSZ to the east, describing a

"continuous, through-going, long-lived, NW-striking, dextral strike-slip shear system" extending from the northern end of the Pahrump-Mesquite-Stateline-Ivanpah fault through the Amargosa Desert and up into Crater Flat. The total length of such a fault system would be ~250 km, and such a system could produce earthquakes of up to Mw=7.5. Schweickert and Lahren (1997) base their hypothesis mainly on (1) gravity and seismic reflection data, which indicate a fault underneath Amargosa Valley (the 'Gravity fault'); (2) the fact that a line of springs corresponds with the Gravity fault, and (3) the observation that a projected line from this goes through the basaltic centers of Crater Flat. Schweickert and Lahren (1997) claim that the normal faults of Yucca Mountain are part of a rotation caused by a stepover in their proposed fault system, and that the faults of NW Bare Mountain have undergone right-lateral displacement. The case has been disputed, however, mainly due to the lack of any obvious surface trace, although it is true that the fault could not have ruptured since deposition of alluvium across the Amargosa Desert and Crater Flat. Stamatakos and Ferrill (1998) also argue that Schweickert and Lahren (1997) have misinterpreted the sense of slip on the Bare Mountain faults, interpreting them instead as down-to-the-southeast normal faults that have been rotated so that they appear to have undergone strike-slip faulting. Stamatakos and Ferrill (1998) further argue that the aligned springs and basaltic centers are consistent with a system of WNW-directed extension.

Also to the east of the ECSZ, located to the southeast of Yucca Mountain, is the somewhat poorly understood Las Vegas Valley shear zone, which is considered to be the eastern margin of the Walker Lane. The shear zone is difficult to trace as the faults are

largely buried beneath young volcanics and alluvium. The fault zone has not been active in recent time (Carr (1990); Lagenheim et al. (2001)). The Las Vegas Valley shear zone is right-lateral, and trends approximately NW-SE.

1.2.3 The Basin and Range

Yucca Mountain and the ECSZ are also located in the southern Basin and Range, an approximately 1000 km wide region dominated by Cenozoic extensional faulting along mostly NNE-trending normal faults and ranges. The Basin and Range is a textbook example of a diffuse plate boundary and it accommodates some 25% of total Pacific-North American relative plate motion (Bennett et al., 1999). The ranges are separated by basins filled with thick alluvium. Slip rates in the northern Basin and Range are higher than in the south (Bennett et al., 1999), evidenced by high relief and broad alluvial valleys in the north and lower relief separated by narrower valleys in the south, in the area around Yucca Mountain. Historical seismicity has been concentrated near its western and eastern margins (the Walker Lane and Intermountain seismic zone, respectively), and in the northern Great Basin, in the central Nevada seismic zone (Wallace, 1984). This is in contrast to longer-term geological results, which suggest that deformation has been relatively uniform over the province; hence the uniform spacing between ranges.

The question of what drives Basin and Range deformation has recently been highlighted, particularly in the light of results showing that not just extension, but

also right-lateral shear is an important part of the strain field (Bennett et al. (2003); Hammond and Thatcher (2004)). Extension across the Basin and Range seems to be, in part, a direct manifestation of Pacific - North America relative plate motion. There are several other factors that could drive deformation in the Basin and Range, however, and controversy exists over how important these are. The controversy also reflects an uncertainty over whether the region is, as a whole, uplifting or subsiding. Two of these alternative driving forces are gravitational collapse and magmatic instabilities.

Jones et al. (1996) examine the idea that gradients in gravitational potential energy (GPE) can cause the lithosphere to collapse under its own weight. They use crustal density structures (from seismic profiles) to calculate lithospheric GPE across the western United States. They then compare their estimates of GPE with "modern-day" deformation to conclude that buoyancy forces are, in fact, enough to produce "virtually all active deformation" seen across the region. Jones et al. (1996) estimate near zero values of GPE for the southern Basin and Range, which they associate with the low extensional strain rates interpreted for that region. Jones et al. (1996) suggest that the most likely cause of GPE gradients across the Basin and Range is the buoyancy of the mantle. A thin lithosphere (true for the Basin and Range) is necessary to produce significant differences in strain rate due to gradients in GPE.

Parsons et al. (1994), on the other hand, suggest that the southwest movement of the North American plate over the Yellowstone hot spot (~ 16-17 Ma) may have created a broad swell across the region, centered over northern Nevada, which would have

caused extension across the Basin and Range. A mantle plume will leave a thermal anomaly for a considerable amount of time. This could cause variations in lithospheric mantle thickness or density across the region, which in turn could produce variations in isostatic uplift. This is consistent with the thin crust, high elevation and high heat flow of the Basin and Range.

Hammond and Thatcher (2004) compare dilitational strain rates (calculated using campaign GPS results for the northern Basin and Range) with GPE gradients, to conclude that the two are spatially anti-correlated, with the greatest dilitational strain rates occurring where GPE gradients are lowest. The results of Hammond and Thatcher (2004) would suggest that relative plate motion is more important to explaining Basin and Range extensional deformation. Bennett et al. (2003), however, use a wide range of GPS results to observe two distinct strain fields, one involving northwest directed, right-lateral shear and the other east-west extension. Bennett et al. (2003) conclude that they cannot account for the strain fields using only plate boundary forces, but must also include lithospheric buoyancy forces. The question of how much Basin and Range deformation results from driving forces along the edge of the plate, and how much from forces in the interior is, therefore, yet to be resolved.

1.3 Local tectonic setting

Yucca Mountain itself comprises the remnants of a middle-Miocene (15-7.5 Ma) sheet of ash flow tuffs, faulted and tilted into a Basin and Range style range block. It is

cut by a number of north-south trending, west-dipping normal faults (Figures 4 and 5). Several of these faults show evidence of Quaternary displacement, but geologic slip rates are very low, on the order of 0.01-0.02 mm/yr (Simonds et al. (1995), Whitney and Keefer (2000)). For example, Quaternary slip rates on the Windy Wash, Fatigue Wash and Solitario Canyon faults are given as 0.012 mm/yr, 0.0004 mm/yr and 0.01 mm/yr, respectively, by Whitney and Keefer (2000). The majority of deformation is thought to have occurred in the middle-Miocene. Most of the normal faults have at least several hundred meters of displacement (Carr (1990), Simonds et al. (1995)) and are spaced at 1-3 km apart. The Yucca Mountain faults are thought by some (Scott (1990), Ofoegbu and Ferrill (1998)) to be listric, dipping steeply at the surface and then merging into a low-angle detachment fault, most likely at some depth. To the west of Yucca Mountain is Bare Mountain, which is flanked on the east by the Bare Mountain fault, an east-facing, moderate to steeply dipping range-front fault. Estimated slip rates on the Bare Mountain fault are 0.02 to 0.20 mm/yr (Wernicke et al., 1998).

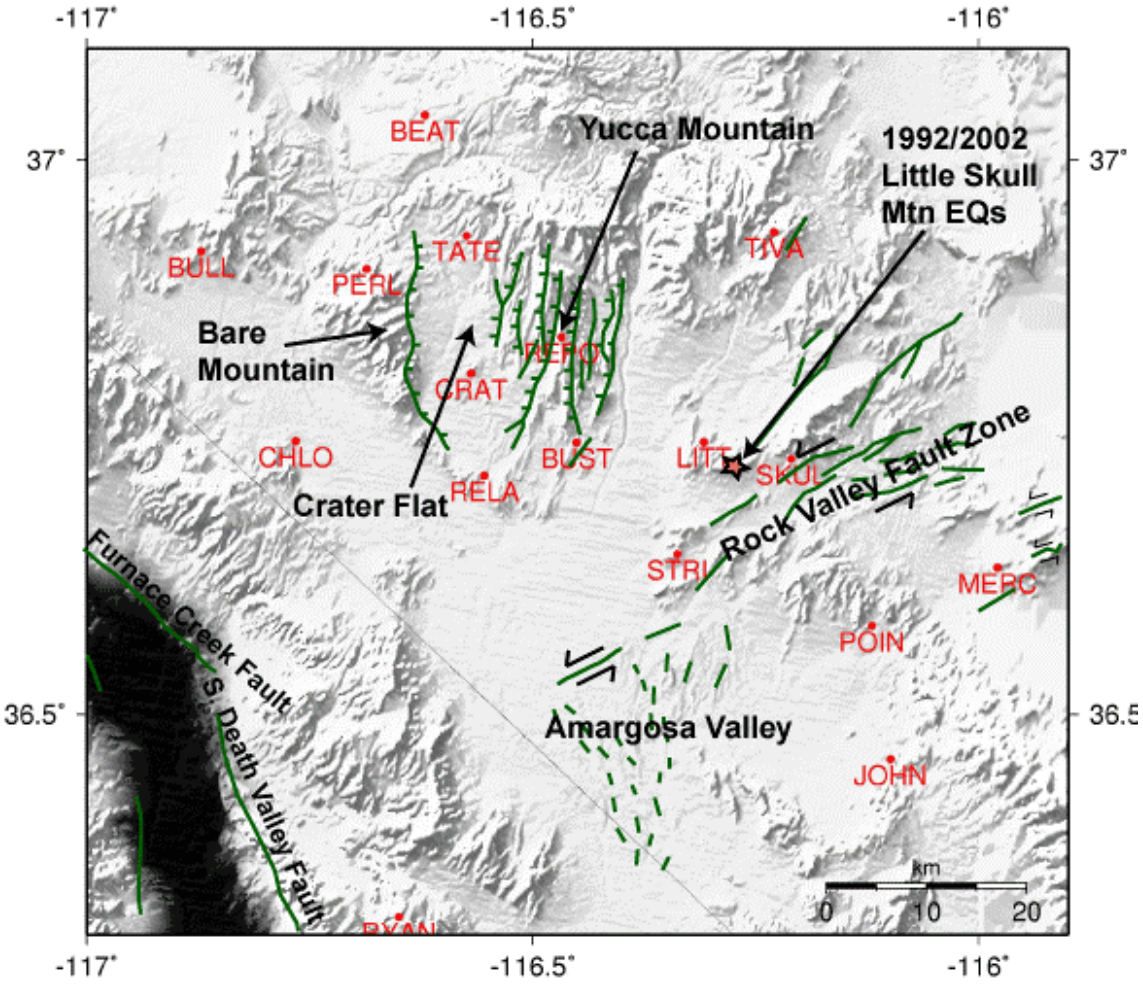

Figure 4. Local tectonic setting. BARGEN GPS stations are labeled in red.

The ENE-trending Rock Valley fault zone (RVFZ), located to the southeast of Yucca Mountain (Figure 4) is an ~5km wide and ~32 km long zone of ENE-striking left-lateral and normal faults (O'Leary, 2000). The fault zone probably originated in Oligocene time (~29 Ma) and is presently active, although estimates of long-term geologic slip rates are low, on the order of 0.002 to 0.02 mm/yr (Anderson, 1998). O'Leary (2000) suggests that it is capable of generating magnitude 7.0+ earthquakes. Quaternary offsets show primarily left-lateral strike-slip displacements. Although the

RVFZ is similar in size and style to other left-lateral fault zones in the Walker Lane, it is not thought to be part of a conjugate system. Its relation to regional structures is poorly known.

The 1992 M_L5.6 and 2002 M_L4.4 Little Skull Mountain earthquakes occurred on faults adjacent to the RVFZ, approximately 20 km to the southeast of Yucca Mountain. The M_L5.6 1992 earthquake occurred on 29th June (it was triggered by the Landers event, 22 hours earlier) and was most likely generated by normal displacement on a N55^o-60^{o}E striking, ~70^o southeast-dipping fault (Smith et al. (2001); Lohman et al. (2002); Meremonte et al. (1995)). The M_L4.4, 14th June 2002 earthquake occurred in the aftershock zone of the 1992 earthquake.

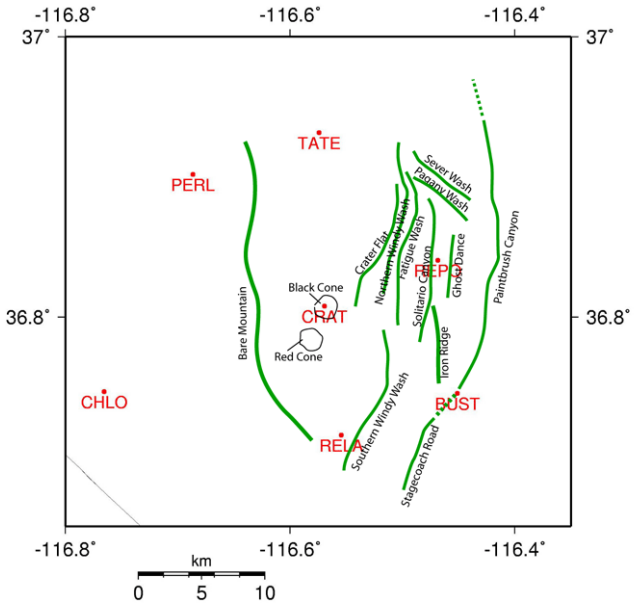

Figure 5. Simplified fault map of Yucca Mountain, adapted from (Simonds et al., 1995). Traces are approximate and shown as green lines. GPS stations are labeled in red.

1.4 Volcanic hazards

The Coso volcanic field is located on the western edge of the ECSZ, between the Sierra Nevada and Panamint Valley faults (Figure 3). The Coso Volcanic field has seen three major episodes of volcanism since ~6 Ma, which has left a landscape of domes, cinder cones and lava flows (Novak and Bacon, 1986). The Coso Volcanic field is currently an active geothermal field with high rates of seismicity. Anomalous velocity at a GPS station close to the Coso geothermal field was noted by Gan et al. (2000). This is important to consider as it is within close proximity to our GPS station ARGU (Figure 2). Wicks et al. (2001) have studied the area using European Remote Sensing satellite (ERS) InSAR data, which shows deformation rates of up to 35 mm/yr in an area ~10 km by 15 km. They propose that the source of this is a leaking deep reservoir of magmatic fluids.

Yucca Mountain is located in the southern part of the southwest Nevada volcanic field. A number of late Pleistocene basaltic centers exist at Crater Flat and at the south end of Yucca Mountain (Figure 6). Volcanic activity in the area could cause localized vertical uplift of the GPS stations. The date of the most recent volcanic activity around Yucca Mountain has been debated, but most recent publications give an age of 81-77 ka; Zreda et al. (1993) measured the accumulation of ^{36}Cl in 11 samples from lava flows at Lathrop Wells to obtain an average age of 81 ± 7.9 ka and Heizler et al. (1999) measured an $^{40}Ar/^{39}Ar$ date of ~77 ka. These dates are now widely accepted. It was previously thought to be more recent; Wells et al. (1990) estimated the age of the most recent eruptions at Lathrop Wells as probably no more than 20 ka and gave ages of the Little,

Red, Black and Northern cones ranging in date from 1.5 to 0.99 Ma. These eruptions, and all eruptions since approximately 6 Ma, have been basaltic. The silicic volcanic activity, which involved the formation of an extensive caldera complex and the eruption of ash-flow sheets that eventually formed Yucca Mountain, started 10 to 11 Ma and ended about 8 Ma (Wells et al., 1990).

Figure 6. LandSat Thematic Mapper image (bands are red=3, green=2, blue=1) showing Quaternary basaltic centers at Crater Flat

As part of the Non-Proliferation Experiment (NPE), the U.S. Department of Energy detonated a 1-kiloton chemical test on the northern part of the Nevada Test Site in September 1993. Using a P-wave refraction profile recorded from this, Smith et al. (2000) modeled the velocity structure of the upper crust around Yucca Mountain and Crater Flat. The results showed a local body of higher velocity material (near 6.8 km/s),

extending to several kilometers depth beneath Yucca Mountain and eastern Crater Flat. There was no indication of anomalously low velocity material, suggesting that it is unlikely that there is molten material at shallow depth at Yucca Mountain. The higher velocity measured suggests that the body could be cooled magmatic material.

1.5 The Yucca Mountain GPS network

The Yucca Mountain GPS network was established in May 1999 as a densification of the Basin and Range Geodetic Network (BARGEN) (http://cfa-www.harvard.edu/space_geodesy/BARGEN (May 2003)). The network is small and dense, which minimizes many of the signals associated with larger, regional-scale GPS networks, and has been carefully designed to produce precise and robust results. The network is quite unique in having identical hardware at each station, consisting of Trimble 4000 SSI receivers and Trimble choke-ring antennas with Dorne Margolin elements. Although the station setup design has several sources of multipath, particularly in the form of chain link fences and solar panels, these are similar at each station (Figure 7). All antennas are mounted with one vertical and three slanted braces extending 5-10 meters into bedrock (Wernicke et al., 2002).

Figure 7. GPS receiver and antenna setup at station BEAT (photograph from BARGEN website)

In order to provide quality assurance for the Yucca Mountain GPS results, the GPS data has been independently processed and interpreted by two groups since network installation. A group at the Harvard Center of Astrophysics (CfA) (James Davis and Richard Bennett) and the California Institute of Technology (Brian Wernicke and Nathan Niemi) has processed the data using the GAMIT (GPS at MIT) software developed by the Massachusetts Institute of Technology, the Scripps Institute of Oceanography and Harvard, while the group at the University of Nevada, Reno (Emma Hill and Geoffrey Blewitt), has processed the data using the NASA Jet Propulsion Laboratory GPS Inferred Positioning SYstem and Orbit Analysis and Simulation II (GIPSY-OASIS II, from hereon referred to as GIPSY) software. These software packages are discussed in more detail in Chapter 2. This has enabled us to analyze the precision of our results through comparison of the two data sets, and has also provided a useful means of examining the effects of using different processing techniques in the GIPSY software. The GAMIT

results have been previously published by Bennett et al. (2003), Davis et al. (2003), Wernicke et al. (2002) and Wernicke et al (2004). A comparison of the two data sets was presented by Hill et al. (2002), and an analysis of vertical precision in Hill and Blewitt (2004a). An interpretation of the GIPSY results was presented by Hill and Blewitt (2004b).

1.6 Previous geodetic surveys of Yucca Mountain

One of the initial motivations for the installation of a continuous GPS network at Yucca Mountain was to assess the results from a campaign GPS survey carried out in the area from 1991 to 1997 (Wernicke et al., 1998). The survey consisted of five stations, located between Bare Mountain and Jackass Flats. This study indicated WNW crustal extension, with the four southeastern sites moving 'significantly' (1.0 ± 0.3 to 1.7 ± 0.3 mm/yr) eastward to southeastward relative to the site located on Bare Mountain (close to the current location of BARGEN site PERL). This reflects a N65^{o}W extensional strain rate of 50 ± 9 ns/yr and is difficult to reconcile with expected strain rates based on local and regional tectonics. It is a rate 3-4 times that of average Basin and Range strain rates. Wernicke et al. (1998) therefore suggested that the Yucca Mountain area is undergoing 'an epoch of anomalously rapid strain accumulation.'

In contrast, Savage et al. (1994) had previously conducted trilateration surveys of Yucca Mountain in the years 1983, 1984 and 1993 and concluded that strain at Yucca Mountain was negligible. In 1993 they complemented the survey with campaign GPS.

After using a dislocation model (Okada, 1985) to estimate the effects of the 1992 Little Skull Mountain earthquake on the network, they estimated a N65^{o}W strain rate of 8 ± 20 ns/yr, a rate they indicated was not significantly different from zero (although with such a large error bar, higher strain rates could not be ruled out). In 1998, in reaction to the Wernicke et al. (1998) paper, they re-surveyed their network with GPS, producing an updated engineering strain rate of 23 ± 10 ns/yr and an extensional strain rate of -20 ± 22 ns/yr (Savage et al., 1999). This corresponds to a N65^{o}W extension rate of -2 ± 12 ns/yr. Only the engineering strain rate is significant at the 95% confidence level. Savage et al. (1999) then estimated strain rates at Yucca Mountain as a result of the Death Valley - Furnace Creek and Hunter Mountain-Panamint Valley fault systems, using a model for infinitely long faults in an elastic half-space and slip rates of 5 ± 1 mm/yr and 2 ± 1 mm/yr respectively. Using this model they estimated a strain rate of 10-14 ns/yr at Yucca Mountain as a result of these faults. They therefore conclude that approximately half of their 23 ± 10 ns/yr engineering strain rate can be attributed to the ECSZ, leaving a remainder of 9-13 ± 10 ns/yr, which, they state, “is not significantly different to zero” (although, again, these error bars cannot rule out strain rates of up to 23 ns/yr).

The large strain rates quoted by the Wernicke et al. (1998) study were controversial, and several published responses criticized the study on a number of levels. Savage (1998) noted that Wernicke et al. (1998) did not account for monument instability, which meant that their errors were underestimated. The survey carried out by Wernicke et al. (1998) used regular survey monuments, which are not designed for stability (notably different to the monuments of the Yucca Mountain continuous stations

now installed) and are of a type known to produce random walk noise. Davis et al. (1998) responded that it is very difficult to evaluate the effect of monument noise. Savage also suggested that they did not account well enough for the effects of the 1992 Little Skull Mountain earthquake.

Lohman et al. (2002) discuss the confusion in interpreting the GPS results of Wernicke et al. (1998) due to uncertainty over which nodal plane had ruptured in the 1992 Little Skull Mountain earthquake; a dislocation model of the SE dipping plane predicts ~7 mm lengthening of the the Wahomie-Mile baseline, whereas the same model on the NW dipping plane gives a baseline lengthening of < 1 mm (Wernicke et al. 1998). The NW dipping plane was favored by Wernicke et al. (1998), although Smith et al. (2001) later confirmed that the SE dipping plane was the most likely. Furthermore, Wernicke et al. (1998) and Savage et al. (1999) also used different locations for the epicenter of the earthquake, which changed the magnitude of the effect on the GPS results. Lohman et al. (2002) were able to invert a combination of seismology and InSAR data to put a better constraint on location of the earthquake than was available from seismology alone. Lohman et al. (2002) used their earthquake model to estimate a Wahomie-Mile baseline lengthening of 4-8 mm, which would decrease the strain rates quoted by Wernicke et al. (1998). Wernicke et al. (2004) confirmed that the 1992 Little Skull Mountain earthquake caused the rapid rates measured in their earlier study.

Another possible explanation given by Wernicke et al. (1998) for their unexpectedly high strain rates was that ‘the anomalous strain could reflect the

development of a second line of north-northeast aligned, low-volume eruptive centers, analogous to the cluster of events near 1.0 Ma on Crater Flat, with the eruption of the Lathrop Wells cone representing the onset of a cluster that would continue over the next few tens of thousands of years." Conner et al. (1998) argued that this cannot be the case; as they disagree with the date given by Wernicke et al. (1998) of 10 ka for the Lathrop Wells basalts, giving instead a date of around 80 ka. Conner et al. (1998) argue that faulting data is inconsistent with the idea that the Lathrop Wells volcano is part of a currently episode of anomalously high strain.

One final note: the results for these studies were obtained by fitting velocity gradients to only six (Wernicke et al., (1998), Figure 2) and three (Savage et al., 1994) or four (Savage et al., (1999), Figure 2) data points. The results in Wernicke et al. (1998) are given relative to station CLAIM, but examination of the time series for CLAIM, particularly in the north component, reveals that the line used to infer zero velocity at CLAIM is not a conclusive fit. The Savage et al. (1999) results show a similar problem. This illustrates the need for a continuous network to solve the discrepancies.

More recently, Wernicke et al, (2004) have submitted an interpretation of the GAMIT solution for the Yucca Mountain BARGEN stations (described in Section 1.5). This study is based on the results of processing 3.75 years of continuous data, and estimates a right-lateral shear strain of 20 ± 2 ns/yr, oriented N20^{o}W, in the vicinity of Yucca Mountain, a much smaller number than the ~50 ns/yr described by Wernicke et al. (1998). Wernicke et al. (2004) do, however, propose that ~1 mm/yr of displacement

must be taken up by local structures at Yucca Mountain, since they find that they cannot explain all the measured strain using models of the Death Valley fault zone.

1.7 Aims of this study

1. One of the primary goals of this project was to confirm or disprove the high strain rates measured by Wernicke et al. (1998).

2. More specifically, we were to provide high precision GPS velocities with proof of quality assurance. This has comprised careful analysis of sources of GPS error, refinement of GIPSY processing techniques to obtain the best results possible and comparison with results independently produced by the Harvard Center for Astrophysics.

3. As described in Section 1.5, the Yucca Mountain GPS network is small, dense, well designed and located in a region that has minimal atmospheric effects. It is also using some of the most advanced hardware and software currently available. This makes it interesting from more than a tectonic point of view. It is an excellent test site for studying the potential success of similar networks in the future, an important topic in the light of the proposed Earthscope Plate Boundary Observatory (PBO) (http://www.earthscope.org/pbo), so this study will allow us to provide recommendations as to how to most precisely process the data from PBO when it becomes available. Part of this has been determining the length of time that the network must be in operation before results become believable; at what point is the precision of the results sufficient

for credible interpretation?

4. Previous geodetic studies of Yucca Mountain (Section 1.6) have illustrated the importance of estimating the effect of earthquakes on GPS results. The Yucca Mountain network has been affected by both the 1999 Hector Mine earthquake and the 2002 Little Skull Mountain earthquake. Results may also be demonstrating the residual postseismic effects of the 1992 Landers, 1972 Owens Valley and 1992 Little Skull Mountain earthquakes. We therefore need to produce reliable methods of dealing with earthquakes that directly affect the network, and need to determine whether historic earthquakes are still affecting results. This ties in with interpreting the results, in that an important element of understanding how geodetic results can be compared with geologic information will come with better understanding of space-time change in slip rate and how they tie into the earthquake cycle. Coupled with the problem of estimating earthquake offsets in the time series is the problem of estimating offsets caused by hardware changes within the network.

5. Having obtained the GPS velocities and strain rates, how do we interpret them? In order to assess how much of the strain we measure at Yucca Mountain might actually be due to local faults, we first need to understand how the Yucca Mountain strain field is affected by regional tectonics. Specifically, to estimate the effect of the ECSZ we first need to contribute to solving the controversy regarding slip rates of individual ECSZ faults (discussed in Section 1.2.2) using our GPS velocities. If the slip rates are higher to the east of the ECSZ, there is a greater chance of them affecting results at Yucca

Mountain. Coupled with this, we must examine the suggestions made by Wernicke et al. (2004) that local faults at Yucca Mountain play a more important role than previously thought, firstly by producing models that more accurately portray ECSZ activity (Wernicke et al. (2004) model only the DV-FC fault system).

2. GPS Processing

2.1 Introduction to this chapter

This chapter is a discussion of the processing methods used to obtain GPS velocity estimates at Yucca Mountain. Part of this study was a 'quality assurance' exercise carried out by comparing results independently obtained from two very difference software packages; GIPSY-OASIS II (from hereon referred to as GIPSY) software, and GAMIT. This chapter also, therefore, examines the differences between the GIPSY and GAMIT software packages, and discusses lessons learned through this comparison about how to improve processing techniques in GIPSY.

In Section 2.2 I give a brief, and simplified, overview of GPS theory. Those familiar with GPS theory can skip this section. The main objective of this section is to give the reader enough understanding of GPS theory and processing that they can understand the difference between the GIPSY and GAMIT software packages, since an understanding of the fundamental differences between the two facilitates the eventual comparison of results. This section should also give the reader a brief introduction into processing techniques such as 'ambiguity resolution', which were an important aspect of this study. Section 2.2 is in large part an overview of information covered in Blewitt (1997), Teunissen and Kleusberg (1998b) and Geoff Blewitt's 2002 American Geophysical Union Bowie Lecture (http://www.agu.org/webcast/Blewitt.html). These

sources give more detailed overviews of GPS theory.

2.2 Overview of GPS theory

The GPS system

The GPS system consists of 24 satellites that carry atomic clocks. These satellites transmit two microwave L-band carrier signals, created by multiplying the frequency of the atomic clock (10.23 MHz) by 154 for the L1 band (which gives a frequency of 1575.42 MHz and a wavelength of ~19.0 cm) and by 120 for the L2 band (which gives a frequency of 1227.60 MHz and a wavelength of ~24.4 cm). The L1 band carries a course acquisition (C/A) code. Both the L1 and L2 carry a precise (P) code. The codes are 'pseudorandom' (looks random, but is absolutely predictable) series of +1 and -1 bits.

Measurements using the pseudorandom code

The GPS system is essentially a timing device. GPS receivers are able to calculate the length of time it takes for the GPS signal to travel from the satellite to the receiver. The method by which a code-based receiver calculates travel time using the pseudorandom code is shown diagrammatically in Figure 8. The receiver uses its own clock to create a replica version of the satellite code, then calculates by how many bits it must shift its own code to match the satellite code. The 'pseudoranage', P_s, to the satellite can then be computed using Equation 1.

$$P_S = \left(T_R - T_S\right)c \qquad [1]$$

where T_R-T_S is the signal travel time from satellite to receiver, and c is the speed of light (in a vacuum). With pseudoranges to at least four satellites, receiver position can then be computed using trilateration.

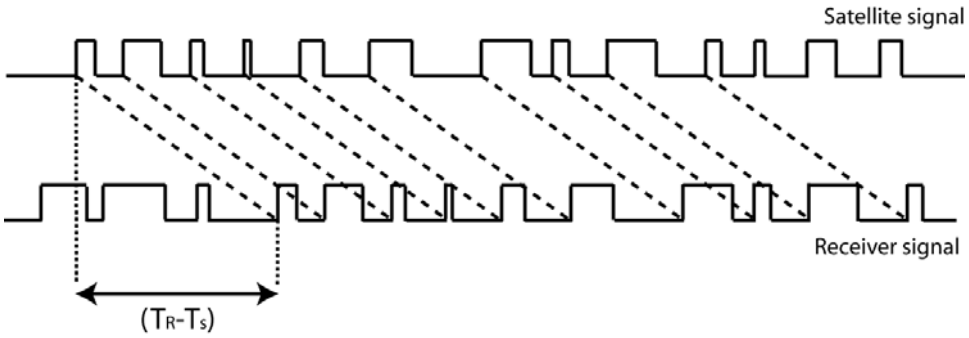

Figure 8. Diagram showing how travel time is calculated using satellite and receiver pseudorandom codes (reproduced from Blewitt (1997)

Of course the situation is more complicated. Firstly, the signal passes through the atmosphere, so it does not travel at the speed of light in a vacuum and, secondly, since the receiver clocks are not high-precision atomic clocks they cannot be relied upon to accurately replicate the satellite signal (hence the need for at least four pseudoranges, to estimate position X, Y, Z and the receiver clock offset). It is also necessary to know the precise position of the satellite to complete the trilateration problem. Furthermore, the precision to which the pseudorange to a satellite can be measured is restricted to a few meters by the fact that each bit of the C/A signal code has a chip length of 293 meters and the chip length of the P code is 29.3 meters. This is why we must resort to the more

complicated technique of ‘carrier phase’ GPS to obtain the sub-mm precision required for measuring interseismic strain accumulation.

Measurements using the carrier phase

Assuming for simplicity that the satellite clock is perfect, the equation for the satellite carrier wave signal can be written as a simple sine function.

$$S(t) = S_o \sin \phi_s(t) \quad [2]$$

where S_o is the amplitude of the signal and ϕ_s is the satellite carrier phase at time t (Figure 9a).

Similarly, the equation for the phase of the receiver clock is

$$R(t) = R_o \sin \phi_R(t) \quad [3]$$

where R_o is the amplitude of the signal and ϕ_R is the receiver oscillator’s phase at time t (Figure 9b).

The two signals are then multiplied together to produce a single, combined signal (Equation 4). Since the satellite clock will arrive with a slightly different frequency to the receiver’s reference signal (due to the Doppler effect), the combined signal will have a high frequency and a low frequency part (Figure 9c).

$$S(t) \times R(t) = \frac{R_o S_o}{2}\left[\cos\left(\phi_R - \phi_s\right) + \cos\left(\phi_R + \phi_S\right)\right] \quad [4]$$

A “baseband” filter is then used to remove the high frequency component of the mixed signal to produce a ‘carrier beat’ signal, which is essentially the difference between the phases of the two signals (Figure 9d). The ‘carrier phase’ is the phase of this beat signal, which represents the difference between the satellite and receiver phases (Equation 5).

$$S(t) \otimes R(t) = \frac{R_o S_o}{2} \cos\left(\phi_R - \phi_S\right) \qquad [5]$$

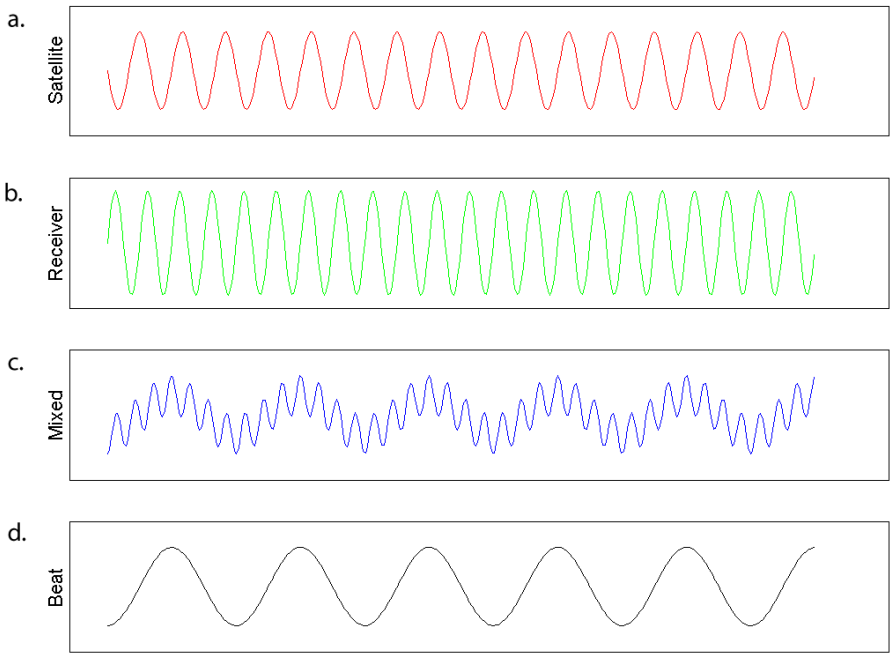

Figure 9. Schematic showing how the satellite and receiver signals can be mixed to produce a carrier beat signal

An observation equation, relative to signal travel time and similar to that obtained through pseudorange measurement, can now be formed, where the phase difference

($\phi = \phi_R - \phi_S$) is expressed as a multiple of f_o, the nominal frequency, and clock time ($T_R - T_S$);

$$\phi = f_o\left(T_R - T_s\right) + 2\pi N \qquad [6]$$

Nominal wavelength is

$$\lambda = \frac{c}{f_o} \qquad [7]$$

Multiplication of Equation 6 by wavelength gives an equation for range;

$$L = c\left(T_R - T_S\right) + N\lambda \qquad [8]$$

where T_R is receiver clock time and T_S is satellite clock time; c is the speed of light in a vacuum; and L is the range to the satellite. With carrier phase GPS, this can be measured to ~0.1 mm. The difference between this and the pseudorange measurement, however, is that now an integer ambiguity, N, remains.

The integer ambiguity comes about because to estimate the phase difference the receiver must take the arc-cosine of the baseband signal;

$$\left(T_R - T_S\right) = \arccos\left(\frac{2S(t) \otimes R(t)}{S_o R_o}\right) \qquad [9]$$

In other words, it is possible to measure the exact phase in the last microwave to arrive at the receiver, but not possible to measure the integer number of waves that came before it. Resolving for the integer number, N, is known as 'ambiguity resolution.' There are various techniques available to carry out ambiguity resolution. These techniques rely

on the idea that although N is unknown, it is also constant, so provided the receiver continuously tracks the satellite, the value of N does not change. An exception to this is when the receiver 'loses lock' on the satellite (for example if the satellite temporarily goes behind a building), which means it stops counting N. This is called a phase break, or cycle slip.

GPS error sources

Numerous factors throughout the GPS system can affect results. Table 2 summarizes the important sources of GPS error, and indicates where in this chapter they are discussed.

Which part of the system is affected?	**How is it affected?**	**Section addressing the problem**	**Comments**
Satellite clock	Clock error	2.4	Downloaded precise satellite clock information from JPL
	General and special relativity		Modeled
Satellite position	Gravity of sun, moon, planets	2.5	Downloaded precise satellite position and velocity information from JPL
	Non-gravitational forces acting on the satellite (e.g. solar radiation pressure)		
Signal propagation velocity not actually speed of light in a vacuum	Ionospheric delay	2.13	Removed using dual frequency combination
	Tropospheric delay	2.13	Modeled as random walk. Desert environment reduces tropospheric effects

Station clock	Clock error	2.4	Estimated as a stochastic parameter
Station position	Monument instability	2.3	Braced monuments set deep into bedrock minimize monument instability noise
	Earth rotation		Downloaded from JPL with the satellite ephemerides.
	Solid earth deformation - daily signals		Modeled
	Solid earth deformation - semi-annual and annual signals	2.15	Long period signals minimized by using baselines to a local station and 4.5 years of data
	Tectonic effects	Chapter 5	Tectonic effects part of the GPS results - tectonic effects analyzed as part of interpretation of results
	Offsets in the time series	2.10 and 2.11	Offsets in the time series included those from the 1999 Hector Mine earthquake and radome changes.

Table 2. Summary of sources of GPS 'error'

2.3 Description of the GPS data

Basin and Range Geodetic Network (BARGEN - described in more detail in Section 1.5 and shown in Figure 3) GPS data were processed in GIPSY for a total of 28 stations. 16 of these stations are local Yucca Mountain network stations (BEAT, BULL, BUST, CHLO, CRAT, JOHN, LITT, MERC, PERL, POIN, RELA, REPO, SKUL, STRI, TATE, TIVA) and 12 are far-field stations in southern California and Nevada (ALAM, APEX, ARGU, DYER, ECHO, LIND, RAIL, ROGE, RYAN, SHOS, SMYC, TONO).

Station locations are shown in Figures 2 and 4 (Chapter 1). A list of station coordinates is given in Appendix A. Further site information is available at the BARGEN website (http://cfa-www.harvard.edu/space_geodesy/BARGEN/).

All stations are outfitted with Trimble 4000 SSI receivers, Trimble choke-ring antennas with Dorne Margolin elements and SCIGN radomes. All antennas are mounted with one vertical and three slanted braces extending 10 meters into bedrock. They are fixed in the bedrock, but not fixed to the less stable upper soil layers in order to reduce the effects of monument instability (Wernicke et al., 2004).

The Yucca Mountain network installation was completed in May 1999. Although some of the far-field stations were installed earlier than this, to ensure consistency we did not process any data prior to May 1999. In the early stages of this project, data was processed from May 1999 onwards, to ensure the longest observation time possible. The 1999 data, however, suffered from a number of offsets in the time series (discussed in more detail in Section 2.10). Solutions using data from 1999 are only, therefore, used in this project to discuss the problems of offsets in the time series. They are also used in the GIPSY-GAMIT comparison, to match the solution available from the group at CfA, which at the time of writing used data from May 1999 to October 2003. The final, 'best' solution in this dissertation, however, uses data from 16th January 2000 (the date after the last known offset) to 31st June 2004, so does not include any known offsets. This is a total of 4.5 years of data. Table 3 summarizes this information.

Focus	Data span	Offsets?
Examination of offsets in the time series	May 1999 to October 2003	yes
GIPSY-GAMIT comparison	May 1999 to October 2003	yes
Final results and interpretation	January 2000 to June 2004	no

Table 3. Summary of observation times used in this project

The BARGEN GPS raw data were downloaded as RINEX files from the UNAVCO ftp site (ftp.data-out.unavco.ucar.edu/pub/rinex/<year>/<doy). The data were processed in 24-hour batches (0.00 to 23.59 GMT), set to sample every 5 minutes. The satellite elevation cut-off angle was set to 15^{o} (i.e. no data from satellites that fell below 15^{o} from the horizon were processed).

2.4 Satellite and receiver clock errors

An understanding of the different methods available to deal with satellite and receiver clock errors is essential to understanding the main difference between the GIPSY and GAMIT software packages. GAMIT and also, for example, the University of Berne's 'Bernese' software and Trimble's GPSurvey, remove clock biases by forming a series of linear equations that can be combined to remove the unwanted parameters. This technique is called 'double differencing.' GIPSY, on the other hand, actually estimates the clock bias as part of the processing routine.

Double differencing (e.g. GAMIT)

'Single differencing' is the first step in double differencing, and it is used to eliminate satellite clock bias. Two observation equations (Equations 10 and 11), in this case for the carrier phase observables, although the equations are similar for pseudorange measurements, are formed with two receivers (A and B) simultaneously viewing the same satellite (j) (Figure 10).

$$L_A^j = \rho_A^j + c\tau_A - c\tau^j + Z_A^j - I_A^j + B_A^j \quad [10]$$

$$L_B^j = \rho_B^j + c\tau_B - c\tau^j + Z_B^j - I_B^j + B_B^j \quad [11]$$

L^j_A and L^j_B are the range to satellite j from receivers A and B, ρ^j_A and ρ^j_B are the ranges to satellite j from receivers A and B, c is the speed of light in a vacuum, τ_A and τ_B are the receiver clock biases, τ^j is the satellite clock bias, Z^j_A and Z^j_B are the tropospheric delay to receivers A and B, I^j_A and I^j_B are the ionospheric delay terms and B^j_A and B^j_A are the integer ambiguity terms (λN^j_A). The convention here is to use the symbol Δ to indicate a difference between two ground-based measurements and the symbol ∇ to indicate a difference between two satellite-based measurements.

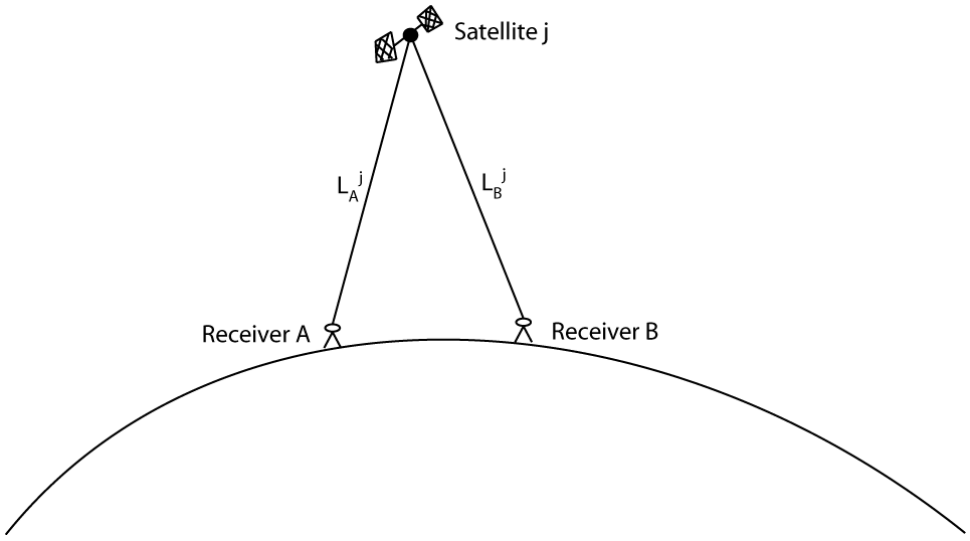

Figure 10. Diagram showing the satellite-receiver geometry required to form a single difference equation

The 'single difference' is the difference between Equations 10 and 11, which removes the satellite clock bias term;

[12]

$$\Delta L_{AB}^j = \left(\rho_A^j - \rho_B^j\right) - \left(c\tau_A - c\tau_B\right) - \left(c\tau^j - c\tau^j\right) + \left(Z_A^j - Z_B^j\right) - \left(I_A^j - I_B^j\right) + \left(B_A^j - B_B^j\right)$$
$$= \Delta\rho_{AB}^j + c\Delta\tau_{AB} + \Delta Z_{AB}^j - \Delta I_{AB}^j + \Delta B_{AB}^j$$

'Double differencing' cancels out both the receiver and satellite clock bias. A 'double difference' is formed when two single differences, observing two different satellites, j and k, are differenced (Figure 11);

$$\Delta L_{AB}^j = \Delta\rho_{AB}^j + c\Delta\tau_{AB} + \Delta Z_{AB}^j - \Delta I_{AB}^j + \Delta B_{AB}^j$$

$$\Delta L_{AB}^k = \Delta\rho_{AB}^k + c\Delta\tau_{AB} + \Delta Z_{AB}^k - \Delta I_{AB}^k + \Delta B_{AB}^k \qquad [13]$$

The double difference is therefore

$$\nabla\Delta L_{AB}^{jk} = (\Delta\rho_{AB}^{j} - \Delta\rho_{AB}^{k}) + (c\Delta\tau_{AB} - c\Delta\tau_{AB}) + (\Delta Z_{AB}^{j} - \Delta Z_{AB}^{k}) - (\Delta I_{AB}^{j} - \Delta I_{AB}^{k}) + (\Delta B_{AB}^{j} - \Delta B_{AB}^{k})$$
$$= \nabla\Delta\rho_{AB}^{jk} + \nabla\Delta Z_{AB}^{jk} - \nabla\Delta I_{AB}^{jk} + \nabla\Delta B_{AB}^{jk}$$

[14]

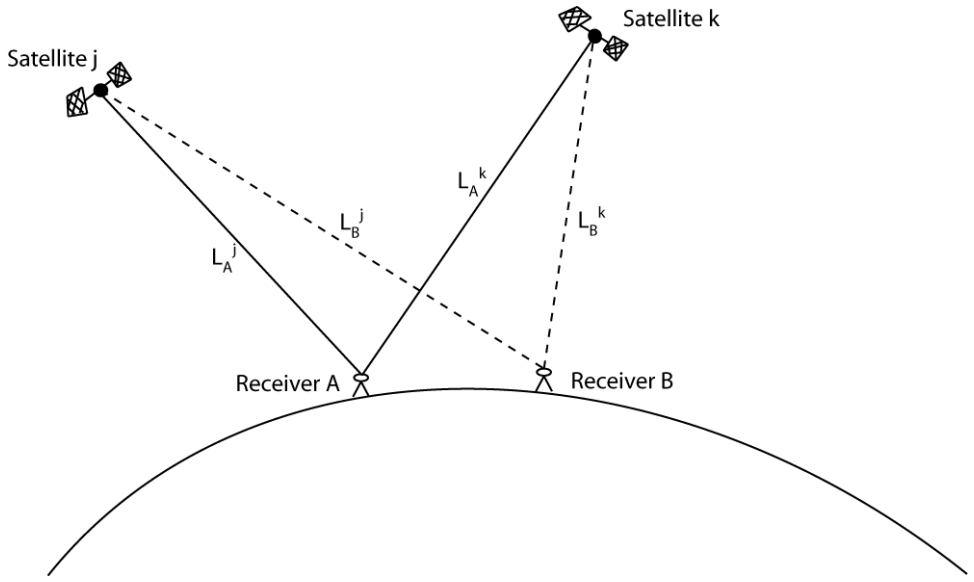

Figure 11. Diagram showing the satellite-receiver geometry required to form a double differencing equation

Estimation of clock bias as a stochastic parameter (e.g. GIPSY)

GIPSY simultaneously estimates all 'unwanted' parameters at the same time as inverting for 'wanted' parameters such as position. It is also possible to input precise values for any parameters that are already well known. In this analysis, receiver clock biases were estimated during processing. Satellite clock biases were fixed to precise

values obtained through the NASA Jet Propulsion Laboratory (JPL). The receiver clock bias was modeled as a stochastic, white noise process (i.e. the bias is uncorrelated from epoch to epoch).

2.5 Satellite orbits and clocks

For the GIPSY analysis I used precise satellite orbit and clock information obtained through JPL (ftp.sideshow.jpl.nasa.gov/pub/gipsy_products/<year>/orbits). These are very similar in precision to the orbits that can be obtained directly through the International GPS Service (IGS), but they are provided in Earth Centered Inertial (ECI) format, meaning that they can be read directly into GIPSY. The ephemerides are calculated using a global network of 365 tracking stations (http://igscb.jpl.nasa.gov/network/list.html, March 2004).

IGS and JPL precise ephemerides are available ~ 2 weeks after an orbit is flown. Prior to the final orbits becoming available, less accurate, provisional (rapid and ultra-rapid) orbits are available. I never used ultra-rapid or rapid orbits for processing during this study, but was careful to wait until final orbits were available. Final orbits are accurate to < 5 cm and satellite clock information to < 0.1 ns (http://igscb.jpl.nasa.gov/components/prods.html). This is in comparison to ~ 200 cm for broadcast orbits and ~ 7 ns for broadcast satellite clocks.

A list of orbit files used in this analysis is provided in Appendix B. Also input to

GIPSY was a planetary ephemeris file obtained from JPL. This file contains the position of planets, and precession and nutation information.

The GAMIT solution used precise orbits and earth orientation parameters from the Scripps Orbit and Permanent Array Center (SOPAC), although these were not tightly constrained. These orbits have a similar accuracy to those obtained through JPL.

2.6 The International Terrestrial Reference Frame

The International Terrestrial Reference Frame (ITRF) is maintained by the International Earth Rotation Service (IERS). It is a physical realization of the International Terrestrial Reference System (ITRS). The ITRF is realized by a combination of many space geodetic measurements; GPS, VLBI, SLR, DORIS and LLR. It is defined to be consistent in time with the NNR-NUVEL1A plate motion model (McCarthy, 1996).

This study used non-fiducial satellite orbits throughout. *Fiducial* orbits are calculated by fixing the coordinates of global tracking stations, which gives results directly relative to the ITRF, but allows inaccuracies in the fixed station positions to distort the network and therefore the orbits. *Non-fiducial* solutions only weakly constrain the tracking station coordinates, and therefore do not suffer from network distortions (Blewitt et al., 1992). This means that station coordinates estimated using non-fiducial orbits make little sense until they have been transformed into the global solution using a

7-parameter Helmert transformation (Blewitt et al., 1992) and transformation parameters made available by the JPL;

$$\begin{pmatrix} x \\ y \\ z \end{pmatrix} = \begin{pmatrix} X \\ Y \\ Z \end{pmatrix} + \begin{pmatrix} t_x \\ t_y \\ t_z \end{pmatrix} + \begin{pmatrix} s & -\theta_z & \theta_y \\ \theta_z & s & -\theta_x \\ -\theta_y & \theta_x & s \end{pmatrix} \begin{pmatrix} X \\ Y \\ Z \end{pmatrix} \quad [15]$$

where X, Y, Z are ITRF coordinates, x,y,z are GPS coordinates, t_x, t_y and t_z are an offset to the origin, s is a scaling factor, θ_x, θ_y and θ_z represent a change in orientation. t_x, t_y, t_z, s, θ_x, θ_y and θ_z are all provided by the JPL.

Using non-fiducial orbits has the benefit that as tracking station positions are refined and updated, particularly because of plate tectonics, the processed results can be easily updated. At the start of this project the current ITRF was ITRF97, but in February 2001 it was updated to ITRF2000. All positions in the GIPSY solution were therefore re-transformed to ITRF2000 to avoid a reference frame offset.

2.7 Precise Point Positioning using the GIPSY processing software

The data were initially processed in GIPSY using the Precise Point Positioning (PPP) technique (Zumberge et al., 1997). In PPP all 'nuisance' parameters are either estimated as part of the inversion routine or fixed to previously determined values. This means that it is unnecessary to process the data as a network solution (as required when double differencing), so positions (and therefore velocities) can be obtained for each

station independent of all other stations in the network (although the positions are tied to the global GPS network as it is the global stations that are used to obtain precise satellite clock and orbit parameters). The PPP approach has the benefit that errors at one station will not propagate through to results for other stations, and time series for the individual stations, relative only to the ITRF, can be examined for problems before a network solution is calculated. It also has the advantage that processing times are significantly reduced compared to processing methods that process all stations in a network simultaneously.

In the PPP routine I used, precise satellite orbits, precise satellite clocks, precise polar motion, earth rotation information, provisional station coordinates and, of course, the raw GPS observations were input. Also input during post-processing were the transformation parameters necessary to transform the 'free network' coordinates to ITRF-2000 (Section 2.5). Parameters that were estimated were given a priori values (defined in the 'wash template'; Appendix C). Parameters that were estimated included precise station coordinates, receiver clocks, tropospheric delay and phase biases.

For information on the algorithms used by GIPSY to estimate unknown parameters, refer to Blewitt (1998), Gregorious (1996) and Teunissen and Kleusberg (1998a). In essence, GIPSY creates a least squares design matrix that combines orbit, earth and observation models. It then linearizes this model with a Taylor expansion and inverts for the unknown parameters. Due to the large size of the design matrix, GIPSY uses the mathematically stable Square Root Information Filter (SRIF) to carry out the

matrix inversion (instead of inverting the matrix as one, it divides it into ‘batches’ and inverts these separately).

GIPSY is a series of binary executables (in ANSI C and Fortran 77/90) that can be run in the order the user chooses using a collection of c-shell and bourne scripts. The scripts can be edited by the user, but not the executables. The processing steps I used to complete the PPP processing are described in Appendix D.

2.8 Ambiguity Resolution

Ambiguity resolution is the determination of the carrier phase ambiguity (defined in Section 2.2). Initially integer ambiguities were left unresolved in GIPSY, at the expense of precision but for the purpose of minimizing the chance of blunders. For example, as baseline length increases, it becomes harder to resolve ambiguities, which can introduce the risk of inconsistency at the far-field stations. Ambiguities were resolved throughout the GAMIT analysis. When results for the two software packages were initially compared, there were significant differences, particularly for the east component (Figures 12 and 13). For data processed between May 1999 and October 2003, with ambiguities resolved in GAMIT but not in GIPSY, the RMS of velocity differences is 0.26 mm/yr in the east component and 0.18 mm/yr in the north.

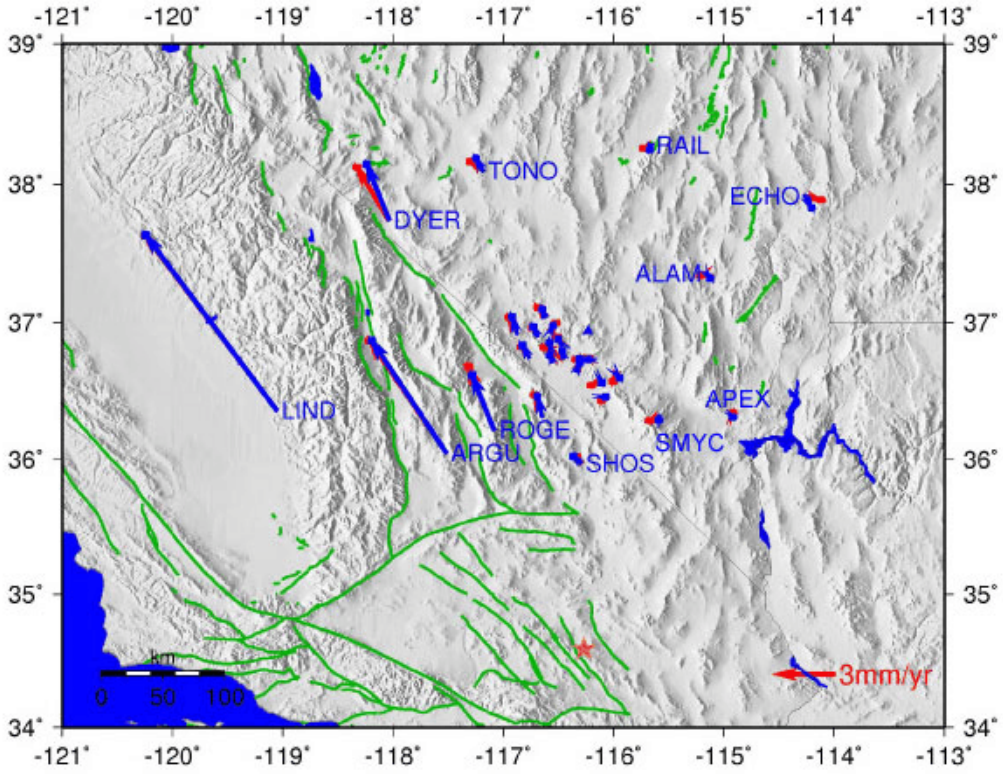

Figure 12. A comparison of GPS horizontal velocity estimates, with and without ambiguity resolution. Shown in red are GIPSY results, with ambiguities unresolved. Shown in blue are GAMIT results, with ambiguities resolved. Error ellipses are 95% confidence. Velocities are plotted relative to station TIVA (blue triangle), in the North America fixed reference frame.

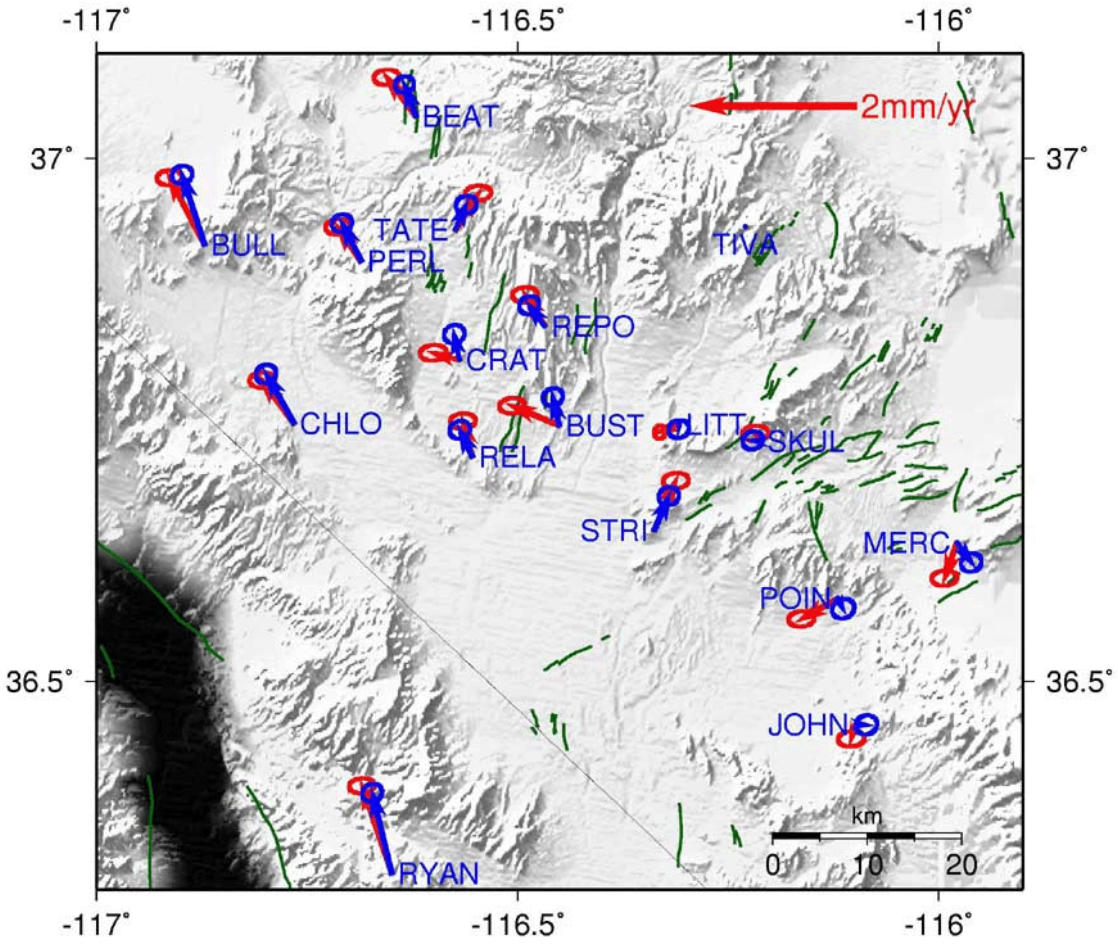

Figure 13. A comparison of GPS horizontal velocity estimates, with and without ambiguity resolution. Shown in red are GIPSY results, with ambiguities unresolved. Shown in blue are GAMIT results, with ambiguities resolved. Error ellipses are 95% confidence. Velocities are plotted relative to station TIVA, in the North America fixed reference frame.

A problem with performing integer ambiguity in GIPSY is that it would take a huge amount of processing time to process an entire network simultaneously on the computing power available at the time (although recent advances in computer technology have made this a less important issue). It was therefore necessary to develop a method of resolving ambiguities on a line-by-line basis. Instead of resolving ambiguities for all 28 stations simultaneously, ambiguities were resolved for each station as a single baseline to

station LITT, which is located in the middle of the network. The processing steps taken to achieve this using the GIPSY software are detailed in Appendix E. As part of the processing software developed, if data for either LITT or the other station for any daily baseline was available, that day was omitted from the processing.

Double differences of the ambiguity parameters are formed in GIPSY to solve for the integer ambiguities, but the technique used in this study still results in a Precise Point Position in the sense that all stations are estimated and satellite clocks remain fixed to JPL values. This approach has the advantage of being able to resolve integer ambiguities while minimizing processing time. It also allows us to maintain some understanding of common mode signals, single station noise, etc. If the entire network was processed simultaneously, it would be impossible to assess which stations are better than others, as problems at one station will be incorporated into the entire network solution.

The resulting improvement in the fit between the GIPSY and GAMIT solutions (after ambiguity resolution in GIPSY) was significant, with the RMS of residual velocity differences reduced to 0.02 mm/yr in the east component and 0.11 mm/yr in the north (Figures 14 and 15). This proves that the chance of blunders from ambiguity resolution is small, and more than compensated for by the improvement in precision of the results.

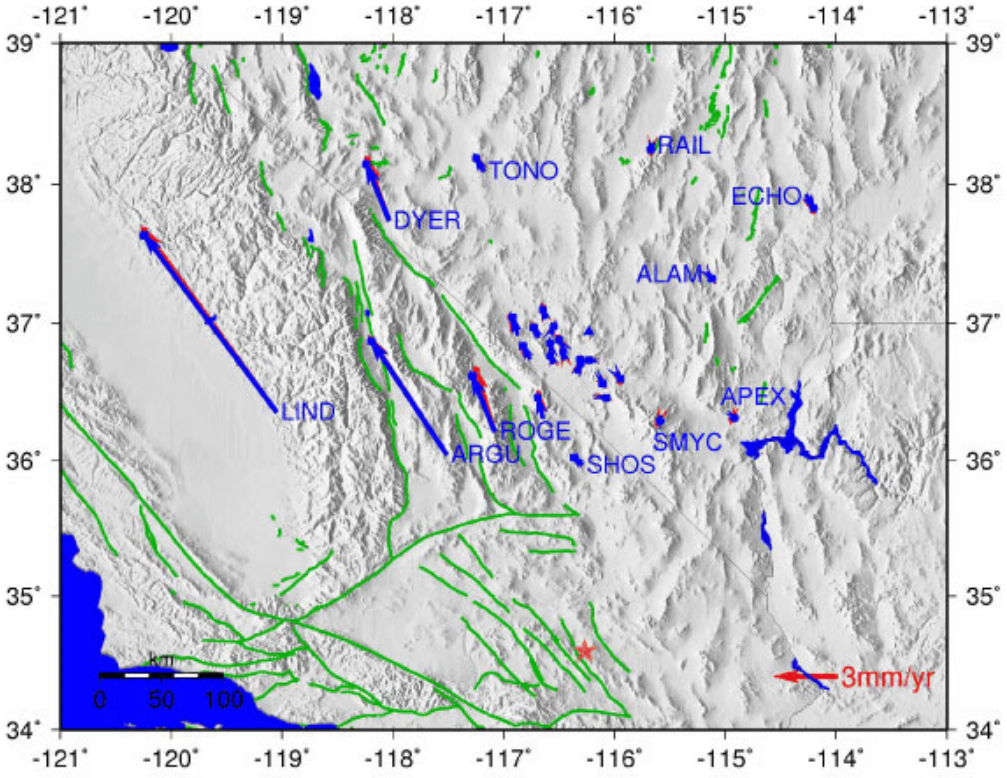

Figure 14. A comparison of GPS horizontal velocity estimates from GIPSY and GAMIT. Shown in red are GIPSY results. Shown in blue are GAMIT results. Ambiguities are resolved for both solutions. Error ellipses are 95% confidence. Velocities are plotted relative to station TIVA (blue triangle).

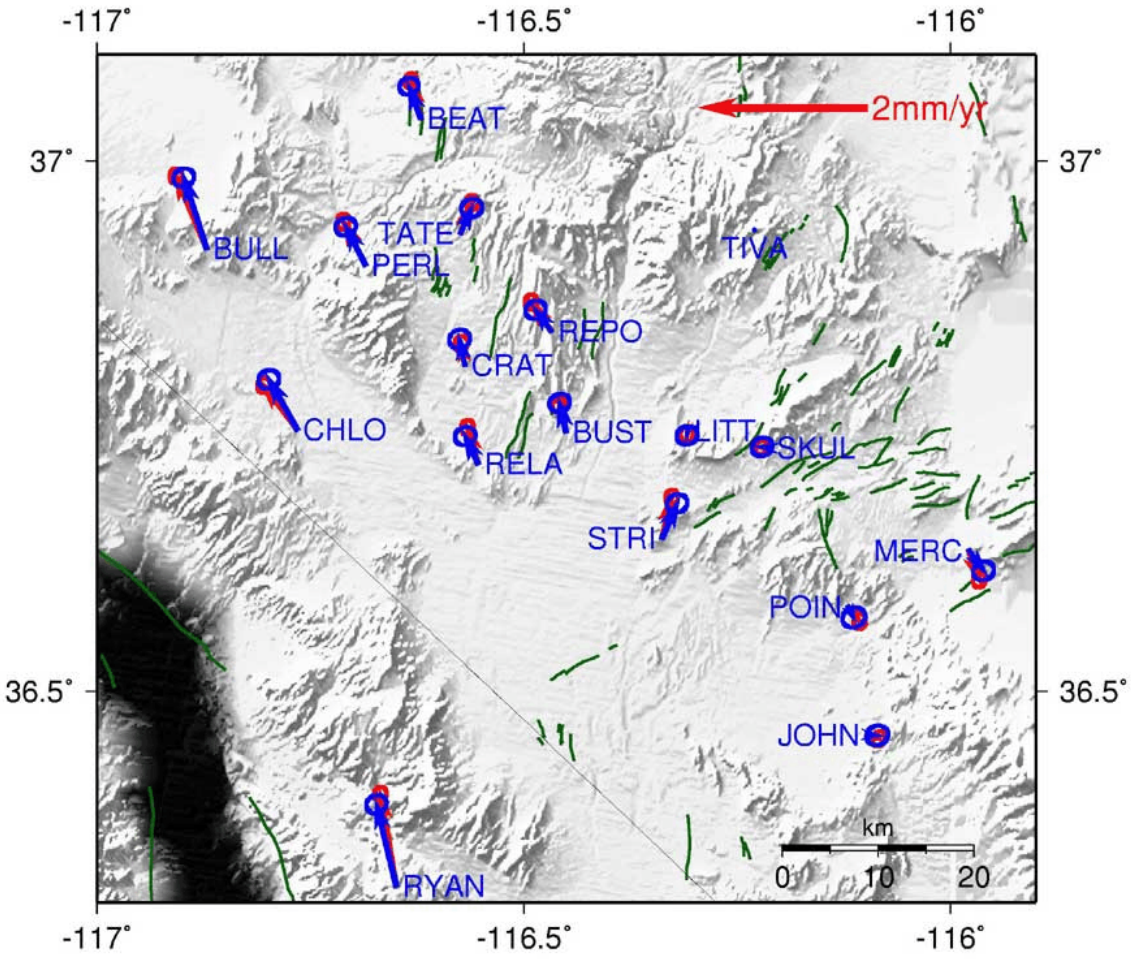

Figure 15. A comparison of GPS horizontal velocity estimates from GIPSY and GAMIT. Shown in red are GIPSY results. Shown in blue are GAMIT results. Ambiguities are resolved for both solutions. Error ellipses are 95% confidence. Velocities are plotted relative to station TIVA.

2.9 Satellite clock problems

Why did ambiguity resolution improve the solution as much as it did (Section 2.8)? Examination of the time series for results without ambiguities resolved reveals unexpected signals in the time series of the PPP results, particularly in the east component and even for baseline time series (Figure 16). The fact that the problems were mainly in the east component is also evident in the velocities (Figures 12 and 13).

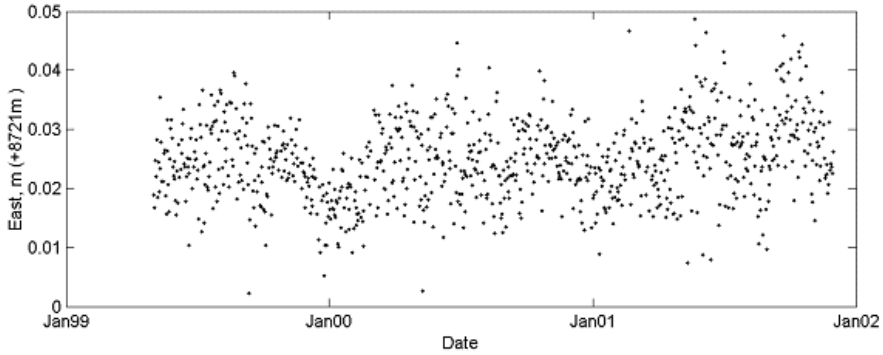

Figure 16. East baseline component for LITT-SKUL. Ambiguities have not been resolved. Receiver clocks were estimated, but satellite clocks were fixed to JPL values. Close examination of the time series reveals an inconsistent signal.

Since systematic problems appeared mainly in the east component, one hypothesis was that the signals were caused by satellite clock problems. To test this hypothesis, I carried out a small study using only stations LITT and SKUL. Using only a short data span, from May 1999 to November 2001, the baseline velocity between LITT and SKUL was estimated to be 1.2 ± 0.1 mm/yr, with SKUL moving in an easterly direction away from LITT. This was contrary to the GAMIT results and unlikely on geological grounds, considering that the stations are within the local Yucca Mountain network and only 9 km apart.

The reference clock was initially set at the average of all the satellite clocks, using the satellite clock parameters provided by JPL. When satellite clocks were estimated as part of the processing, however, rather than fixed to JPL values, the time series had a clear sawtooth pattern (Figure 17).

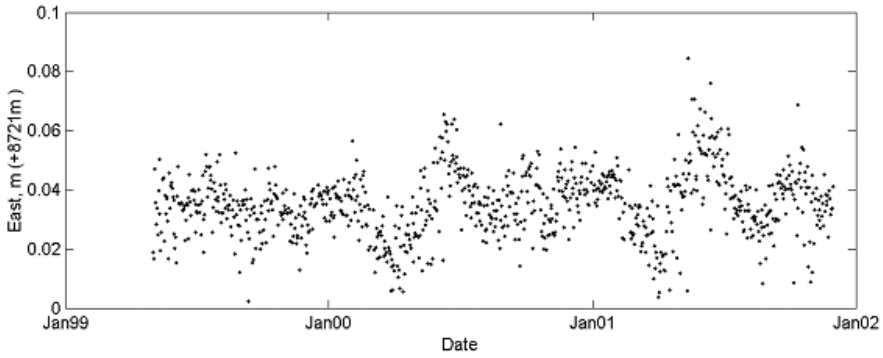

Figure 17. Baseline time series for LITT-SKUL. Ambiguities have not been resolved. Receiver clocks were estimated. The satellite clock for SKUL was fixed to JPL values, but the satellite clock for LITT was estimated.

Figure 17 illustrates that a problem with the satellite clocks was likely to be causing the periodic signal in the time series with clocks fixed (Figure 16). If one station can 'see' a satellite with problems and one cannot see this same satellite, this would bias the time series. If both stations could see the problem satellite, the problem would be obvious for time series plotted directly in ITRF, but would cancel out for baseline time series. Ambiguity resolution solves the problem (Figure 18). This could partly be due to a "book-keeping" effect: double differenced ambiguity parameters can only be formed if BOTH receivers can see the satellite. If one receiver can see a satellite and the other one cannot, the data for that satellite is effectively ignored. When ambiguities were resolved for the LITT-SKUL example, the GIPSY velocity estimate for the May 1999 to November 2001 time period was reduced to 0.02 ± 0.08 mm/yr (with satellite clocks fixed).

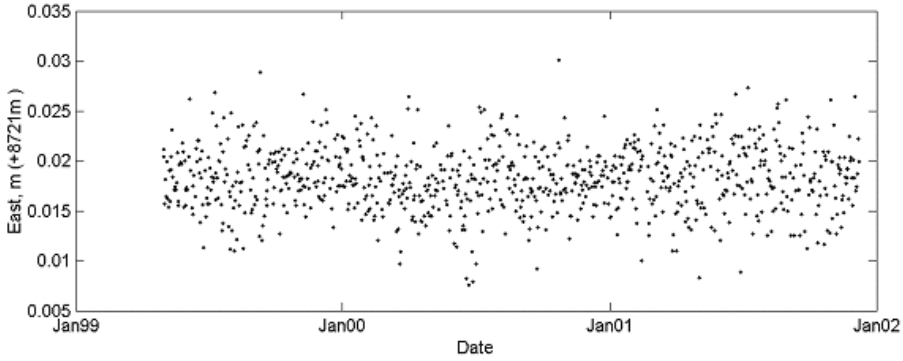

Figure 18. East baseline component for LITT-SKUL. Ambiguities have been resolved. Satellite clocks were fixed to JPL values and receiver clocks were estimated. Note the change in y-axis scale from Figures 16 and 17.

2.10 Offsets in the time series caused by the 1999 Hector Mine earthquake

The M_w7.1 Hector Mine earthquake occurred on 16th October 1999 (see also Section 1.2). The epicenter (shown in Figure 2) was approximately 250 km from Yucca Mountain. The earthquake ruptured the previously unnamed, NW-trending, Lavic Lake and Bullion faults of the Mojave Desert (Scientists from the USGS, 2000).

An offset in the GPS baseline time series on the day of the earthquake is evident for many of the stations (Figures 19-22). In comparison, it is difficult to resolve for an offset in the time series for the 2002 Little Skull Mountain earthquake (described in Section 1.3). Although the final GPS solution discussed in Chapters 3-5 does not include data from 1999 (due to possible problems caused by the offsets), the offsets are discussed here, partly for interest (particularly that GPS stations can be affected by an earthquake at some distance) and partly because the 1999 data are included in the GIPSY-GAMIT

comparison.

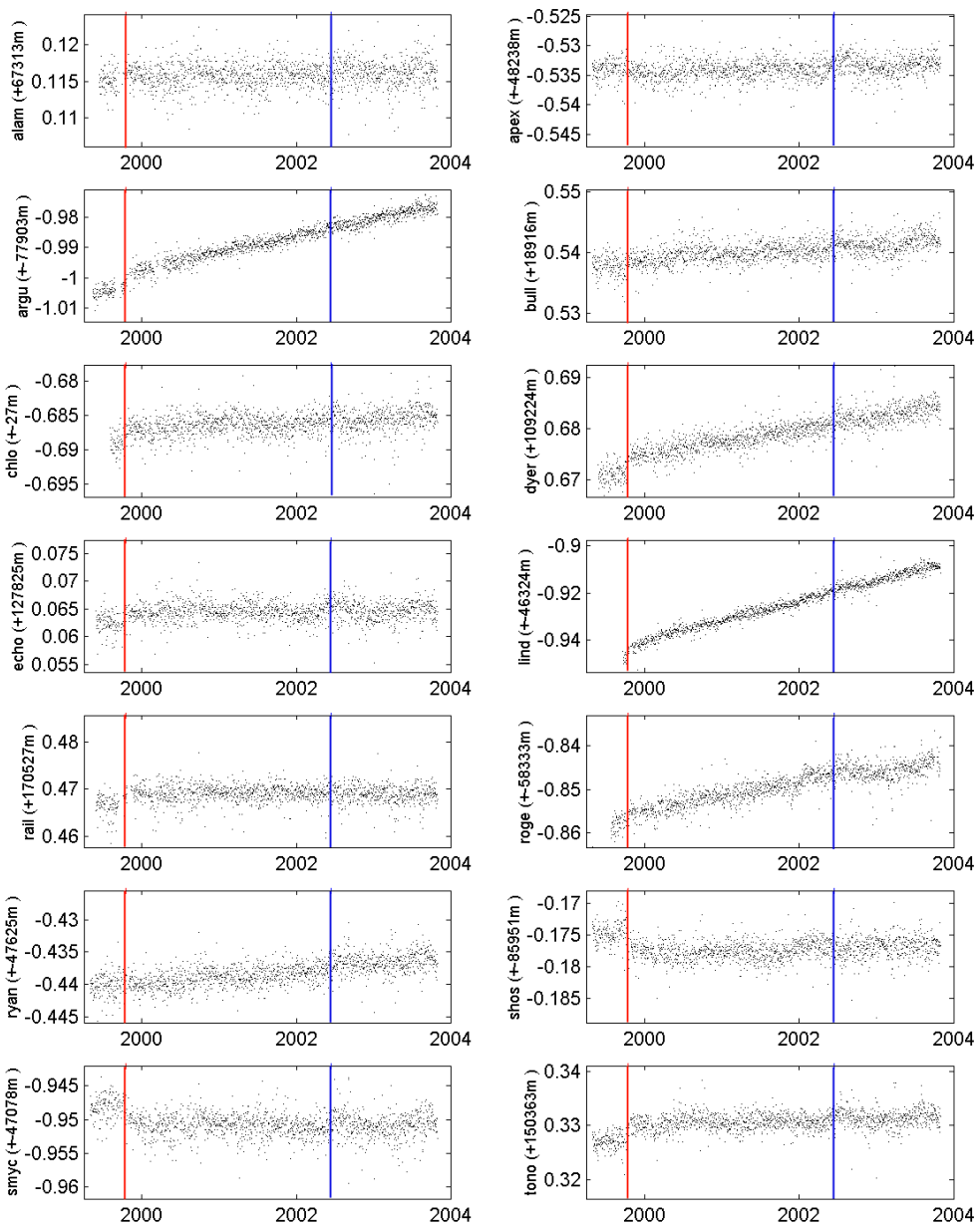

Figure 19. Baseline time series for far-field stations, north component. Red (left) line is 1999 Hector Mine earthquake, blue line is 2002 Little Skull Mountain earthquake. Ambiguities have been resolved.

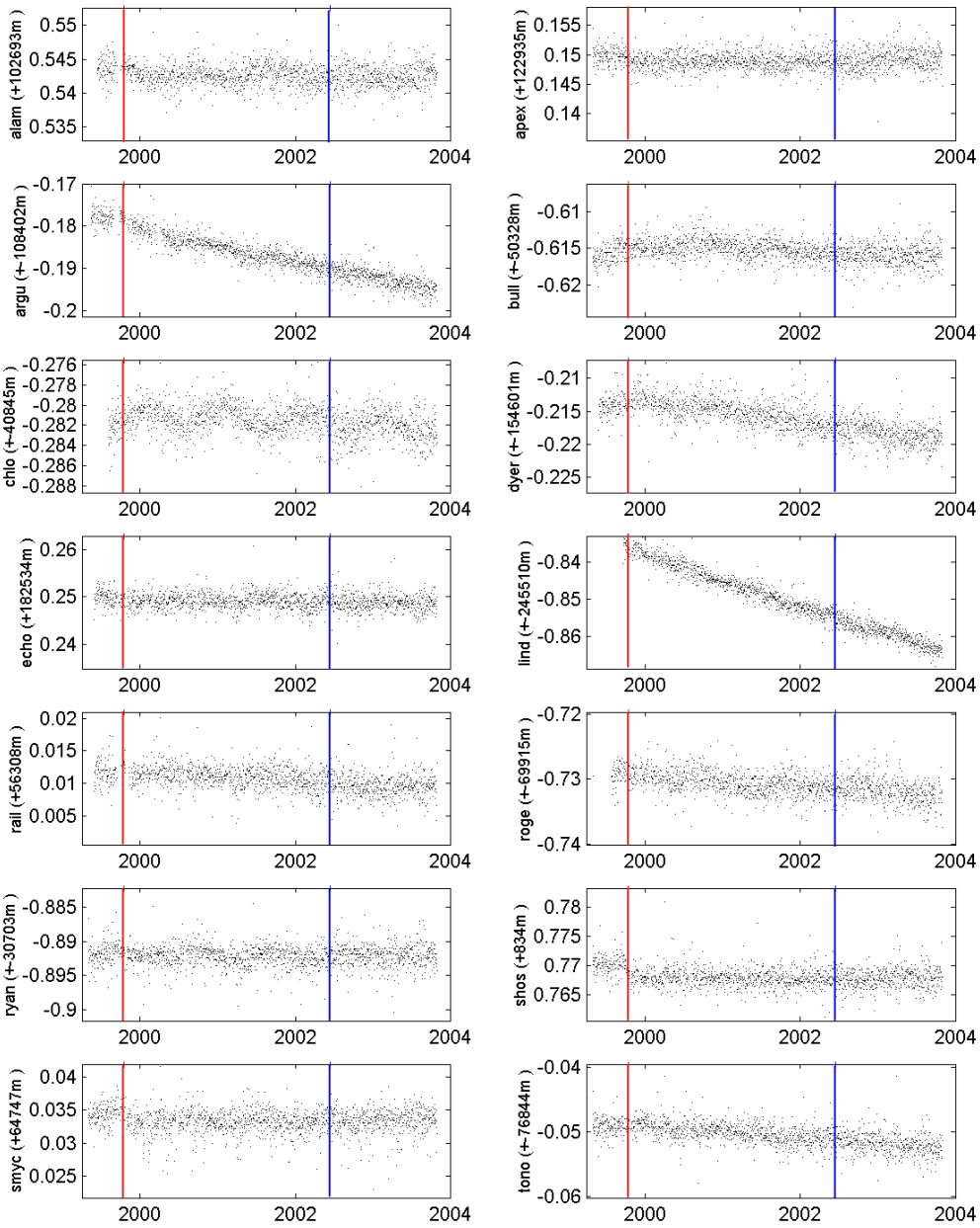

Figure 20. Baseline time series for far-field stations, east component. Red (left) line is 1999 Hector Mine earthquake, blue line is 2002 Little Skull Mountain earthquake. Ambiguities have been resolved.

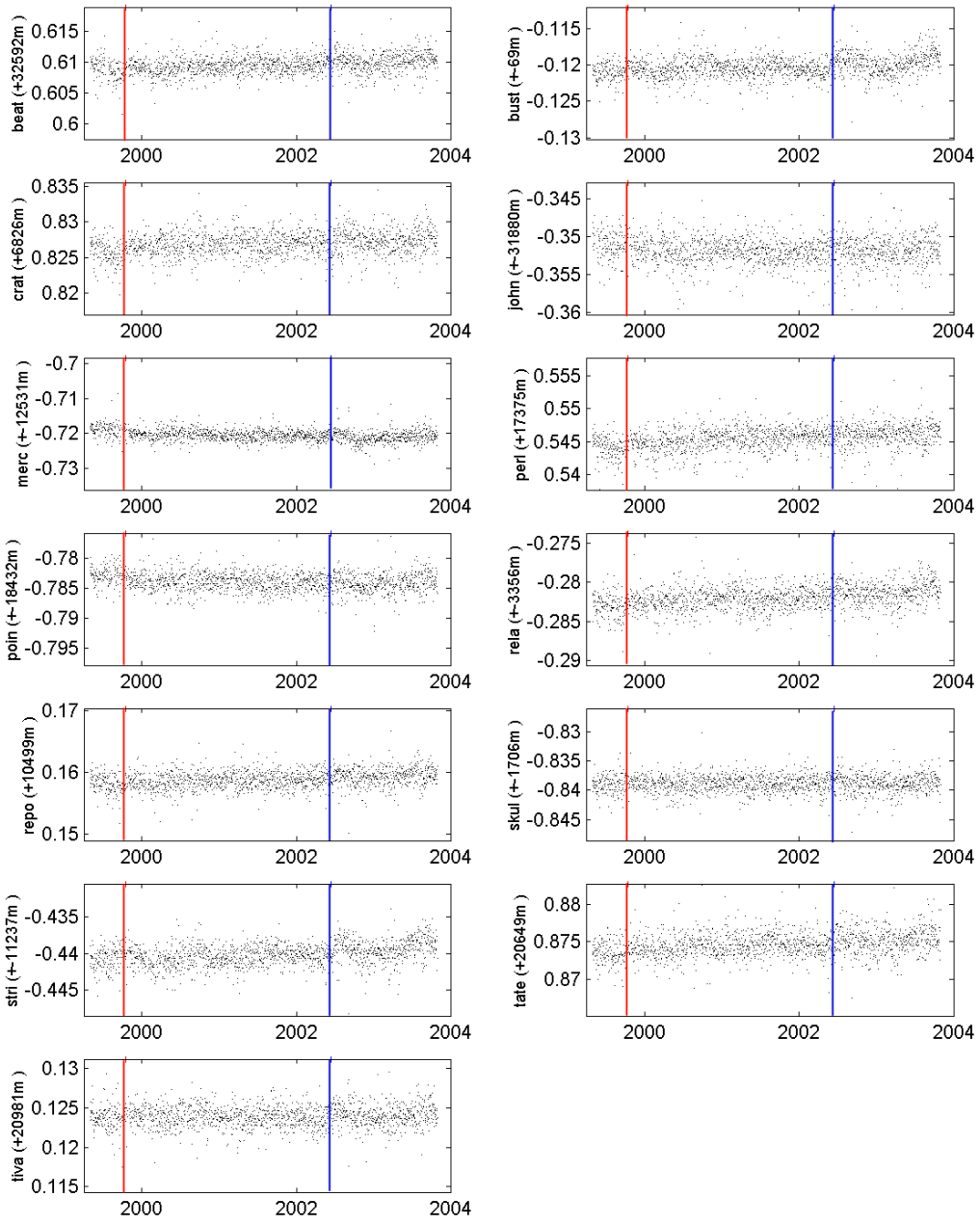

Figure 21. Baseline time series for local stations, north component. Red (left) line is 1999 Hector Mine earthquake, blue line is 2002 Little Skull Mountain earthquake. Ambiguities have been resolved.

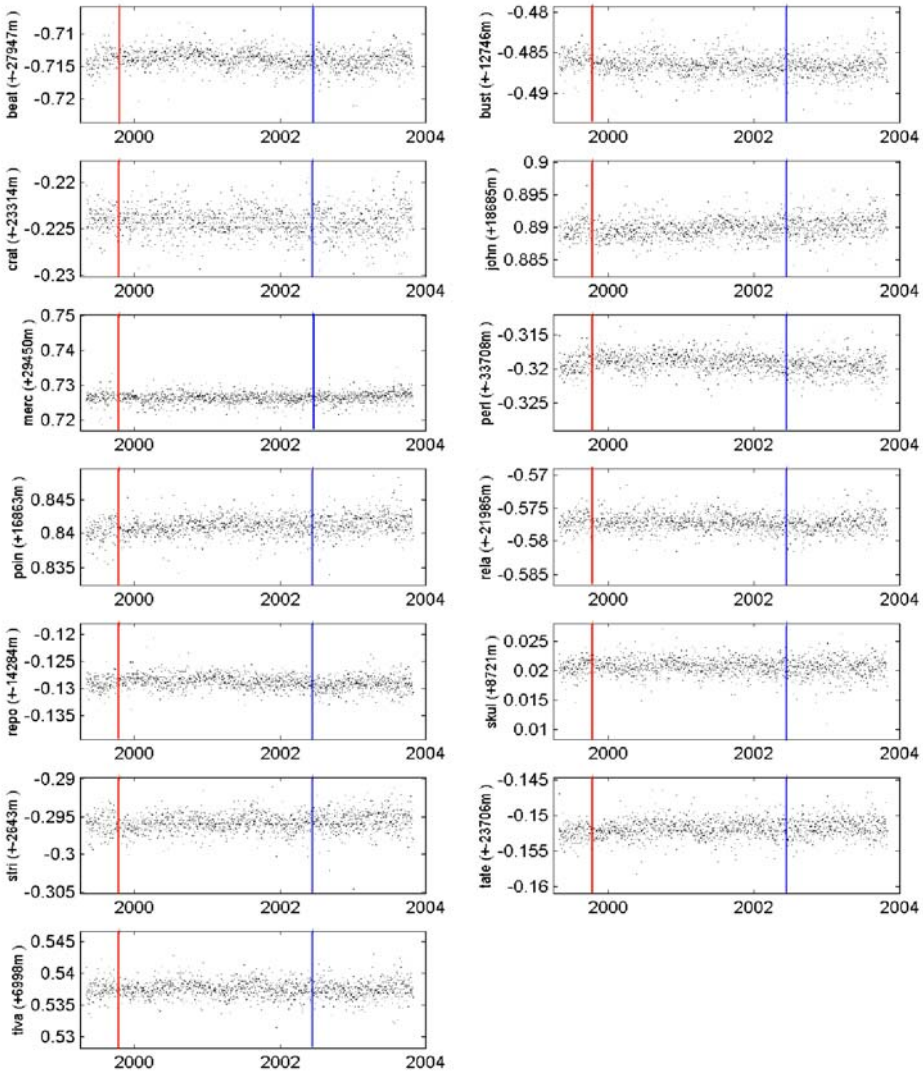

Figure 22. Baseline time series for local stations, east component. Red (left) line is 1999 Hector Mine earthquake, blue line is 2002 Little Skull Mountain earthquake. Ambiguities have been resolved.

The 1999 Hector Mine earthquake offset was estimated during processing as an additional parameter. The linear regression for determining velocity is given as;

$$x_i = x_o + vt_i + \varepsilon(t_i) \quad [16]$$

where x_i is position at time t_i, x_o is position at time t_o, v is velocity and $\varepsilon(t_i)$ is the error term.

This equation is adapted to include an offset (Williams, 2003);

$$x_i = x_o + vt_i + p_i x_{off} + \varepsilon(t_i) \quad [17]$$

where

$p_i = 1$ for $t_i \geq t_{off}$

and $p_i = 0$ for $t_i < t_{off}$

with an offset at time t_{off}, having a magnitude of x_{off}.

The velocities before and after the earthquake were also set to be highly correlated. The GIPSY processing steps used to achieve this, as part of the post-processing routine, are described in Appendix F. Although this procedure successfully removed the effects of the offset, it was unable to resolve the magnitude of the offsets with any significant precision (due to the fact that they are so close to the beginning of the time series).

2.11 Offsets caused by hardware changes in the network

A ‘radome’ is simply a radio-transparent dome attached to the antenna for protection against both the weather and the threat of vandalism (Figure 23). They are important particularly because water damage to the antenna can cause a gradual degradation of results, which can be accidentally interpreted as a signal (SCIGN Radome Project - http://pasadena.wr.usgs.gov/scign/group/dome/). If the radome is changed, it can change the height of the antenna phase center, which will affect the vertical velocity estimates.

Figure 23. REPO station setup. A SCIGN radome is fixed to the antenna.

In late 1999 the BARGEN radomes were changed to specially designed radomes that meet SCIGN specifications. The new radomes are injection molded, rather than thermo-formed, so are stronger and have a more consistent wall thickness. Radome

change dates for the Yucca Mountain network are documented in Appendix G. The first radome changes were on 13th August 1999 and the last were on 15th January 2000. Stations in the local Yucca Mountain network had almost simultaneous radome changes, but stations in the far-field had changes at a later date. This introduced a 'step function' type offset in the baseline time series for the far-field stations (for example, see Figure 24), with one offset as a result of a radome change at the reference station at Yucca Mountain (station LITT) and a second offset caused by the radome change at the far-field station, or vice-versa in a few cases.

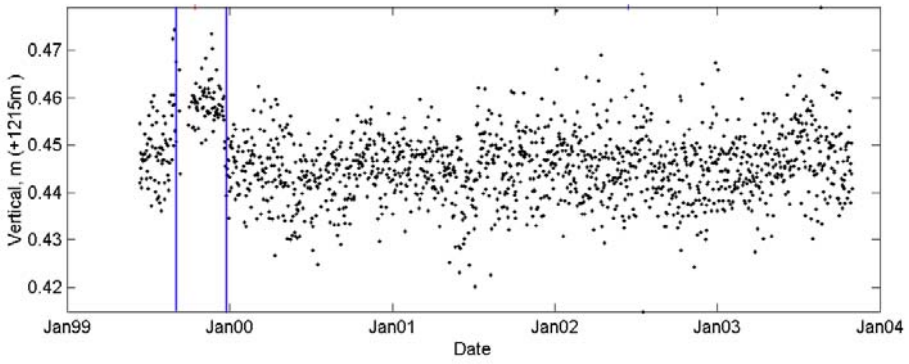

Figure 24. Vertical baseline time series for stations LITT and ALAM. Radome change offsets are indicated by blue lines. The radome at LITT was changed on 19th August 1999 and the radome at ALAM was changed on 21st December 1999.

If radome changes are ignored, the erroneously estimated vertical velocities have a spatial pattern that gives Yucca Mountain the appearance of uplifting relative to stations in the far-field (Figure 25). As with the 1999 Hector Mine earthquake, the effect was most noticeable when the time series was short.

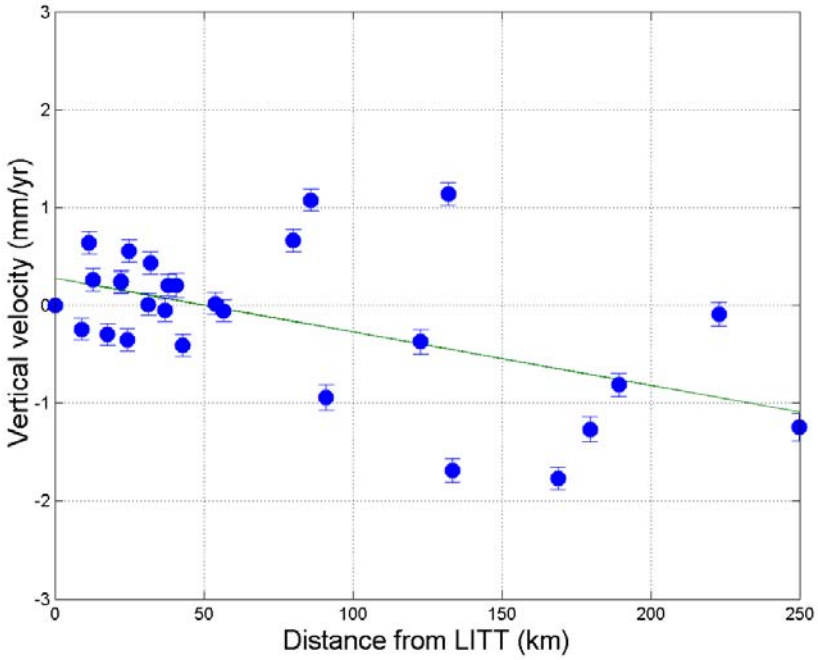

Figure 25. Baseline velocity estimates for the vertical component, relative to station LITT, including the effects of radome changes. Integer ambiguities have been resolved. Data is from May 1999 to October 2003. Error bars are 1σ formal errors.

An effective way of dealing with the effects of these radome changes was to simply remove the data between the two offsets. To ensure consistency I therefore removed all data, for all stations, between the first (13th August 1999) and last (15th January 2000) radome changes prior to velocity estimation. This removed the 'uplift' effect at Yucca Mountain and produced a series of vertical velocities for Yucca Mountain that are tightly clustered around zero (Figure 26). The vertical velocities are discussed in further detail in Chapter 3. Although there is no evidence in the time series for radome offsets in the horizontal component, the data between radome changes was still removed during processing.

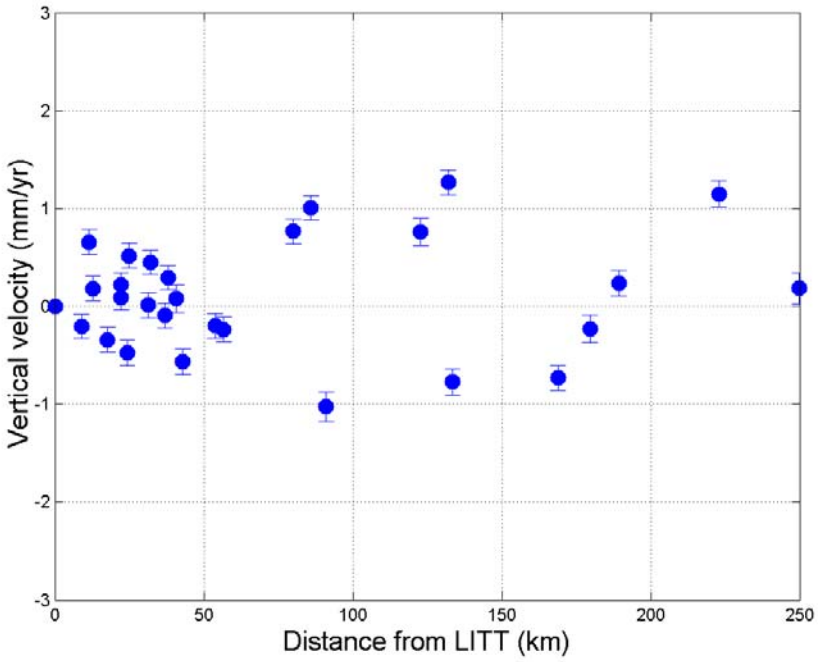

Figure 26. Baseline velocity estimates for the vertical component, relative to station LITT. Integer ambiguities have been resolved. Data is from May 1999 to October 2003, but data from (and including) 13th August 1999 to 15th January 2000 was removed before velocities were calculated. Error bars are 1σ formal errors.

I experimented with estimating the radome offsets using the techniques used for the 1999 Hector Mine earthquake offsets (Section 2.10), but did not favor this approach as it added two additional unknown parameters to the inversion. This approach also tended to over-estimate the magnitude of the offset, resulting in an 'uplift' of the far-field (Figure 27).

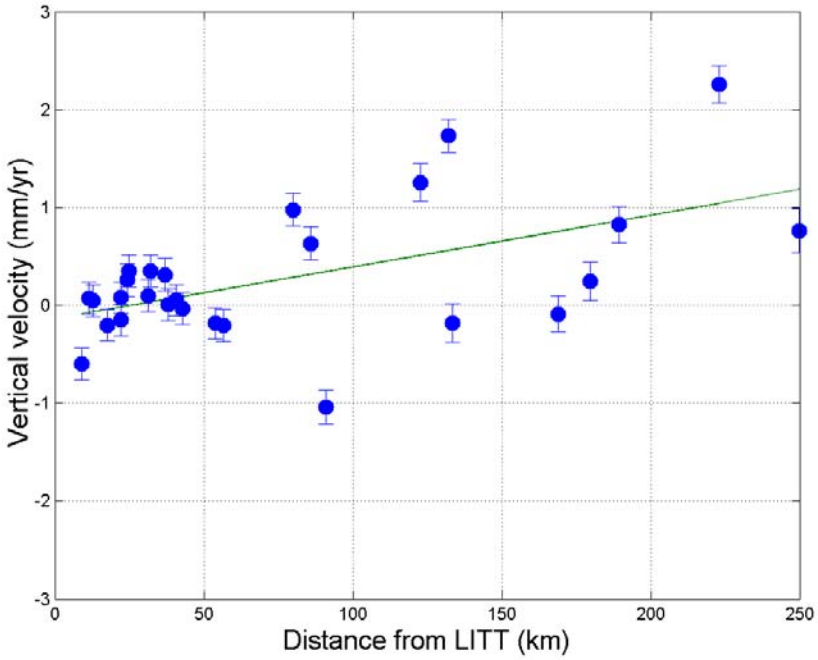

Figure 27. Vertical velocity estimates, relative to LITT, with the radome offset (incorrectly) estimated during the GIPSY inversion procedure.

2.12 Estimation of velocities using only data after the last offset

As increasing volumes of data were collected for the Yucca Mountain GPS network, the period of time before the final offset in the time series became increasingly short compared with the length of time after. This called into question the logic behind using the additional steps described in Sections 2.10 and 2.11 to account for the 1999 offsets. As the data-span reached the 4.5 year mark, a comparison of results obtained using the techniques described in Sections 2.10 and 2.11 with results obtained using only data from after 16th January 2000 revealed almost identical solutions (Figures 28 and 29),

with the RMS of residual velocities differences 0.14 mm/yr for the east component and 0.18 mm/yr for the north (and 0.04 mm/yr for the east and 0.05 mm/yr for the north for only local stations < 55 km from Yucca Mountain). In other words, the benefit of the additional data from 1999 was being lost due to requirements that the effects of the offsets were removed. For this reason, the final solution was processed using data from 16th January 2000 to 30th June 2004, eliminating the need to estimate any offsets. This study does, however, illustrate that should future offsets occur in the time series, we have proven methods of dealing with them. It also suggests that the tectonic velocities have been constant, within error, throughout this time period.

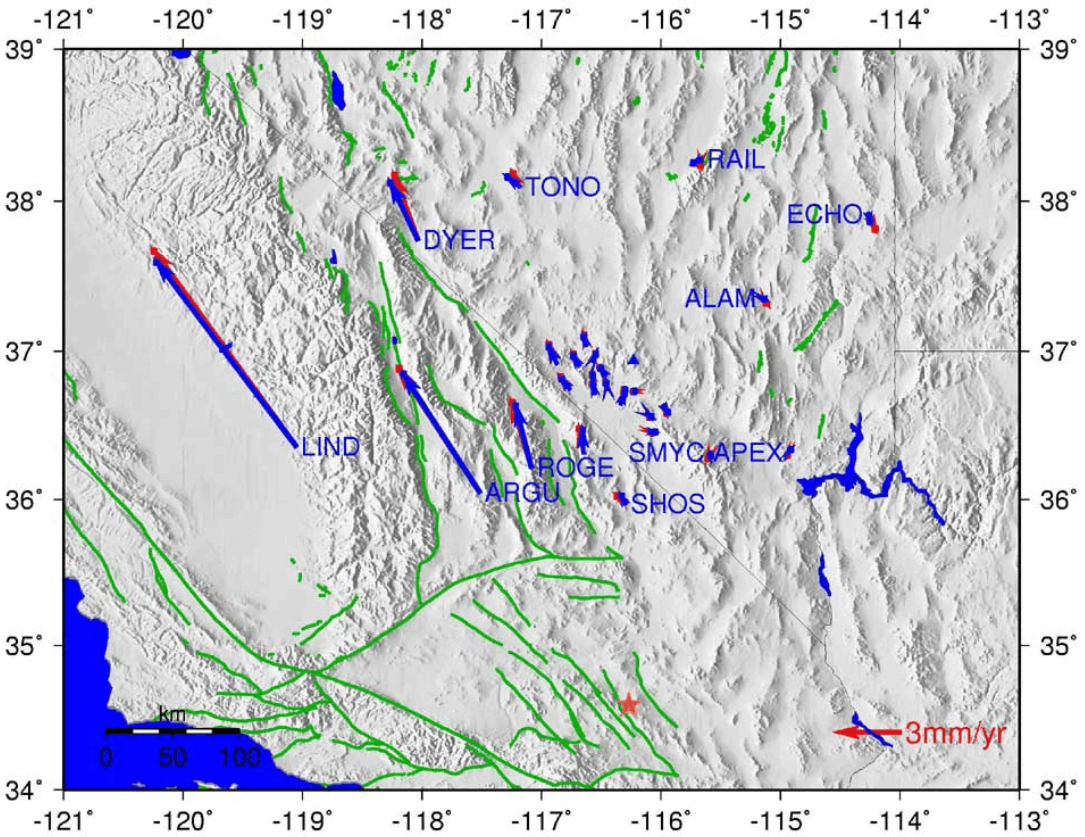

Figure 28. Comparison of results using data from 1st May 1999 to 31st October 2003 (with the effects of the 1999 Hector Mine earthquake and radome offsets removed), shown in red, with results using data from 15th January 2000 to 31st October 2003 (with no offsets estimated), shown in blue. Velocity estimates are plotted relative to station TIVA. Error ellipses are 95% confidence.

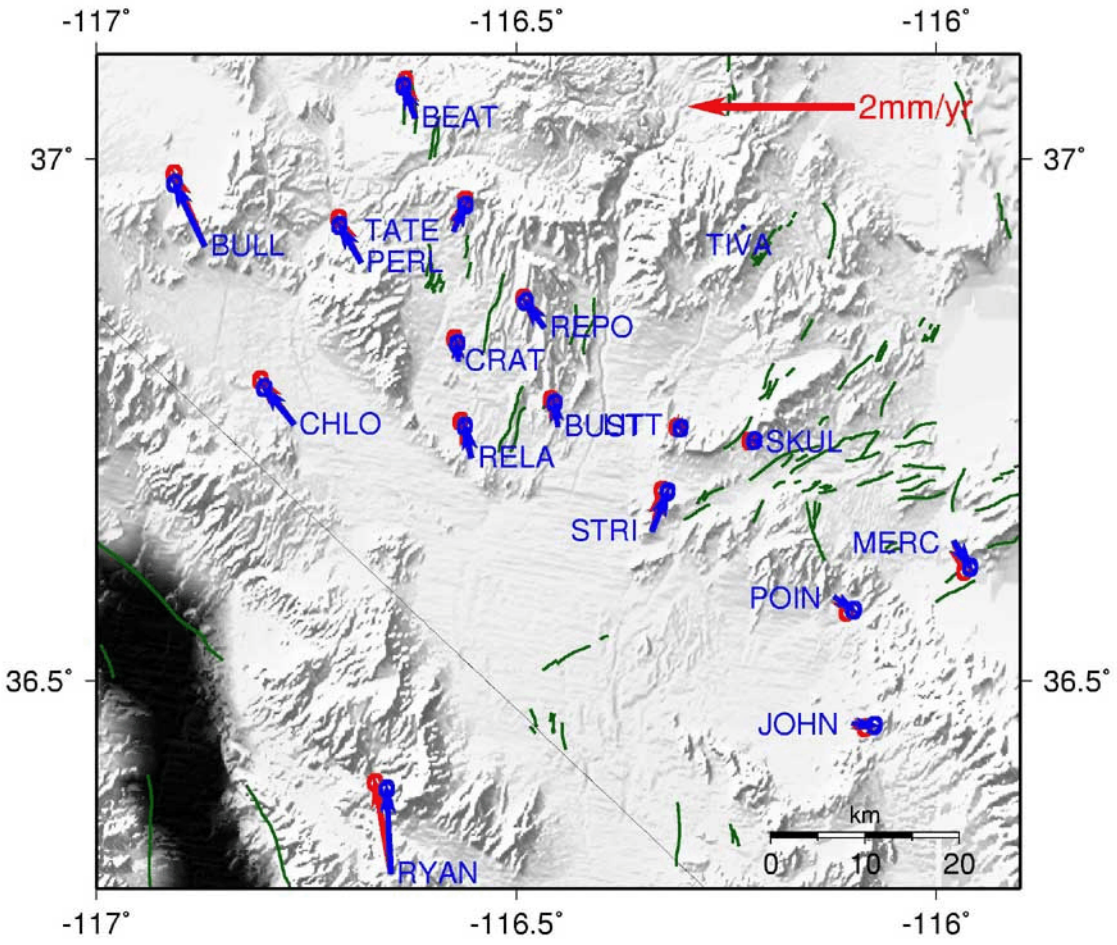

Figure 29. Comparison of results using data from 1st May 1999 to 31st October 2003 (with the effects of the 1999 Hector Mine earthquake and radome offsets removed), shown in red, with results using data from 15th January 2000 to 31st October 2003 (with no offsets estimated), shown in blue. Velocity estimates are plotted relative to station TIVA. Error ellipses are 95% confidence.

2.13 Atmospheric noise and climate

Southern Nevada has a predominantly dry, continental desert climate, with low annual precipitation and high daily temperature range. Precipitation is mainly in the form of large, but infrequent, storms. Pacific storms from the west dominate in the winter, large low-pressure systems originating to the northeast of Yucca Mountain dominate during the spring months, from April to June, and warm summer monsoons, originating in

the Gulf of Mexico and Gulf of California, dominate during the months of July and August (Houghton et al., 1975). The Pacific storms provide the highest levels of precipitation at Yucca Mountain, followed to a lesser extent by Great Basin and Gulf of Mexico storms (Quittmeyer, 2000), although the latter two are more likely to provide higher levels of precipitation throughout much of northern Nevada. Pacific storms provide heavy precipitation to western California, with diminishing levels of moisture towards the east as the air mass moves into the Sierra rain-shadow. Great Basin 'lows' develop in the interior of the continent, and deposit moisture primarily over eastern Nevada. Summer monsoons bring moist, maritime tropical air to southeastern Nevada and usually occur as thunderstorms, as high surface temperatures promote rapidly rising air. The Yucca Mountain region is therefore spread over a region with varying climatic regimes, so it is pertinent to examine how atmospheric delay is approached with our processing technique, and whether local climatic variations could affect results. More specifically, is SMYC, located on top of Mount Charleston, affected by annual snow coverage? Does LIND, located on the Sierra Nevada, have very different tropospheric delay patterns to the stations located in the desert? Are ECHO, RAIL and ALAM, located towards the central Basin and Range, affected by the springtime 'Great Basin Lows'? Is APEX affected by a higher frequency of summer monsoon storms?

As the GPS signal enters the earth's atmosphere, changes in pressure, temperature and water vapor change the refractive index along the path of propagation. In other words, the signal undergoes bending and retardation and no longer travels at the speed of light in a vacuum, which increases the measured range to the satellite. The two layers of

the atmosphere that cause particular problems are the ionosphere and the troposphere.

Ionospheric delay is almost entirely caused by large numbers of free electrons. If left un-modeled, it can change the apparent range to the satellite by up to 30 m in the zenith direction (the path through the atmospheric to a satellite positioned directly above the receiver). Since the main source of energy for ionization is solar radiation, ionospheric delay is variable over a diurnal and annual timescale. Ionospheric delay is, however, dispersive, meaning that the propagation velocity depends on the frequency of the electromagnetic wave. By design, the GPS signal is produced at two different frequencies (L1, 1575.42 MHz and L2, 1227.60 MHz) so that it is possible to use a linear combination of the observation equations for these two frequencies to virtually eliminate ionospheric delay (Langley, 1998).

The effects of tropospheric delay are much harder to remove. Tropospheric delay is non-dispersive within the GPS spectrum and variable on a temporal and spatial scale, so its potential degradation of GPS accuracy can only be modeled. Tropospheric delay is usually divided into a 'hydrostatic' (or 'dry') and a 'wet' contribution (Bevis et al., 1992). Hydrostatic delay, which gives a zenith delay of approximately 2.3 m at sea level (Johansson, 1996), is caused mainly by dry gases such as N_2 and O_2. Hydrostatic delay can be estimated using surface measurements of air pressure if continuous meteorological data is available. The 'wet' delay has the smallest potential effect, less than 1 cm to 40 cm in the zenith direction (Johansson, 1996), but causes the biggest problem. It is caused by the presence of water vapor and is therefore affected by local meteorological

phenomena. It is extremely variable (horizontally, vertically and over time) and difficult to predict from surface measurements.

Ionospheric delay was not modeled in GIPSY, since it was removed by forming the linear combination of the two GPS carrier frequencies (Langley, 1998). Tropospheric wet zenith delay was modeled as a stochastic parameter and treated as random walk. Tropospheric dry delay was estimated using a nominal pressure (based on the elevation of the GPS station). Any residual error in the estimate of dry delay was absorbed into the estimate for the tropospheric wet delay. Tropospheric zenith delays were modeled, then mapped to the correct directions to the satellites using the Niell tropospheric mapping function (Niell, 1996). The Niell model assumes that the atmosphere has horizontal stratification and azimuthal symmetry. Although this is very simplified, this is the common approach in GPS processing.

As part of the GIPSY processing routine, a value for tropospheric wet (plus any residual dry) zenith delay (TZD) was output for every 5 minutes. The daily average TZD was then plotted as a time series. Tropospheric delay data for all stations display a large peak during the summer months and a smaller peak during the winter months (Figures 30 and 31). There are also daily variations, with highest delay between approximately noon and 3pm (highest temperatures) and lowest TZD between approximately midnight and 3am (lowest temperatures) (Figure 32).

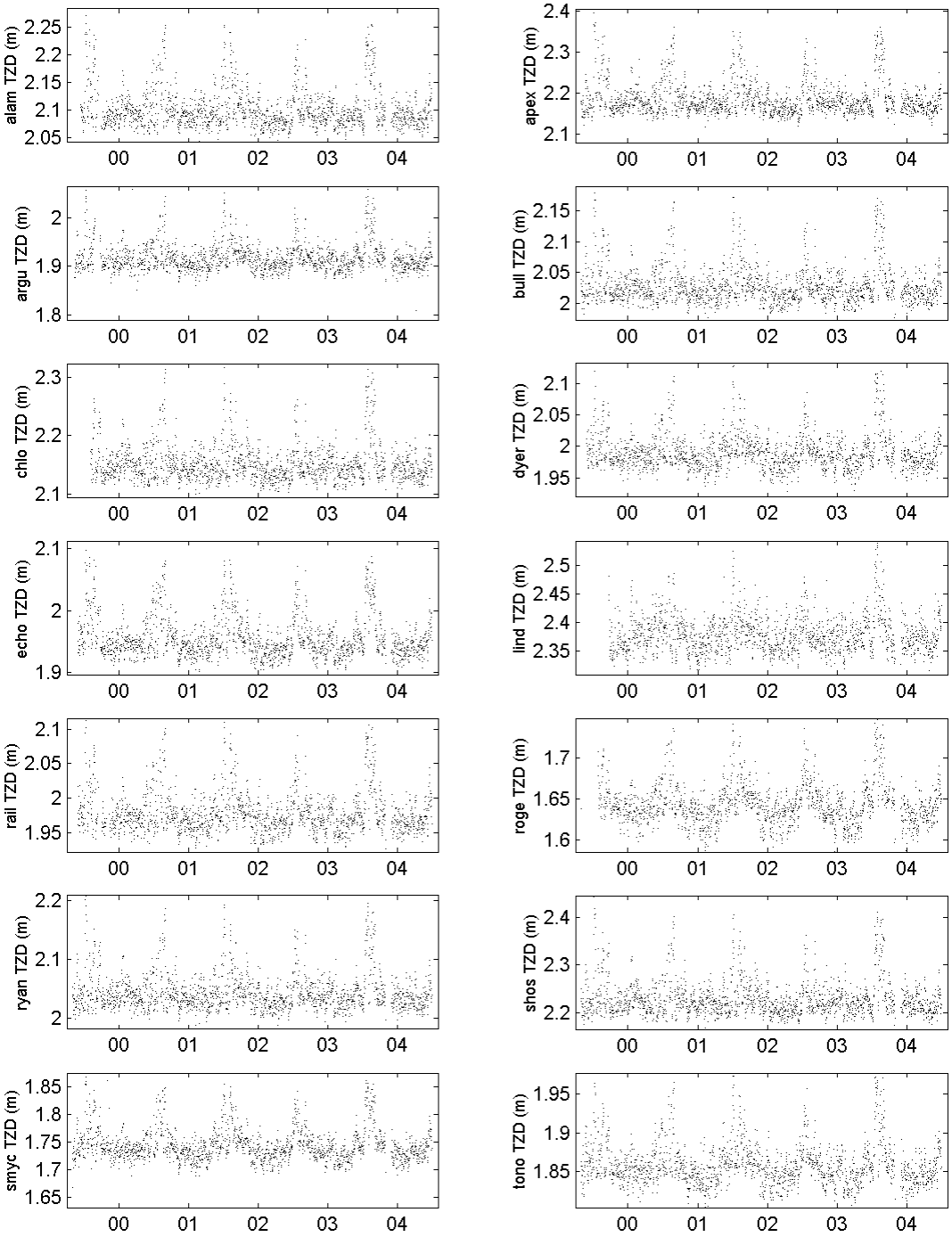

Figure 30. Daily average tropospheric zenith delay for the far-field GPS stations

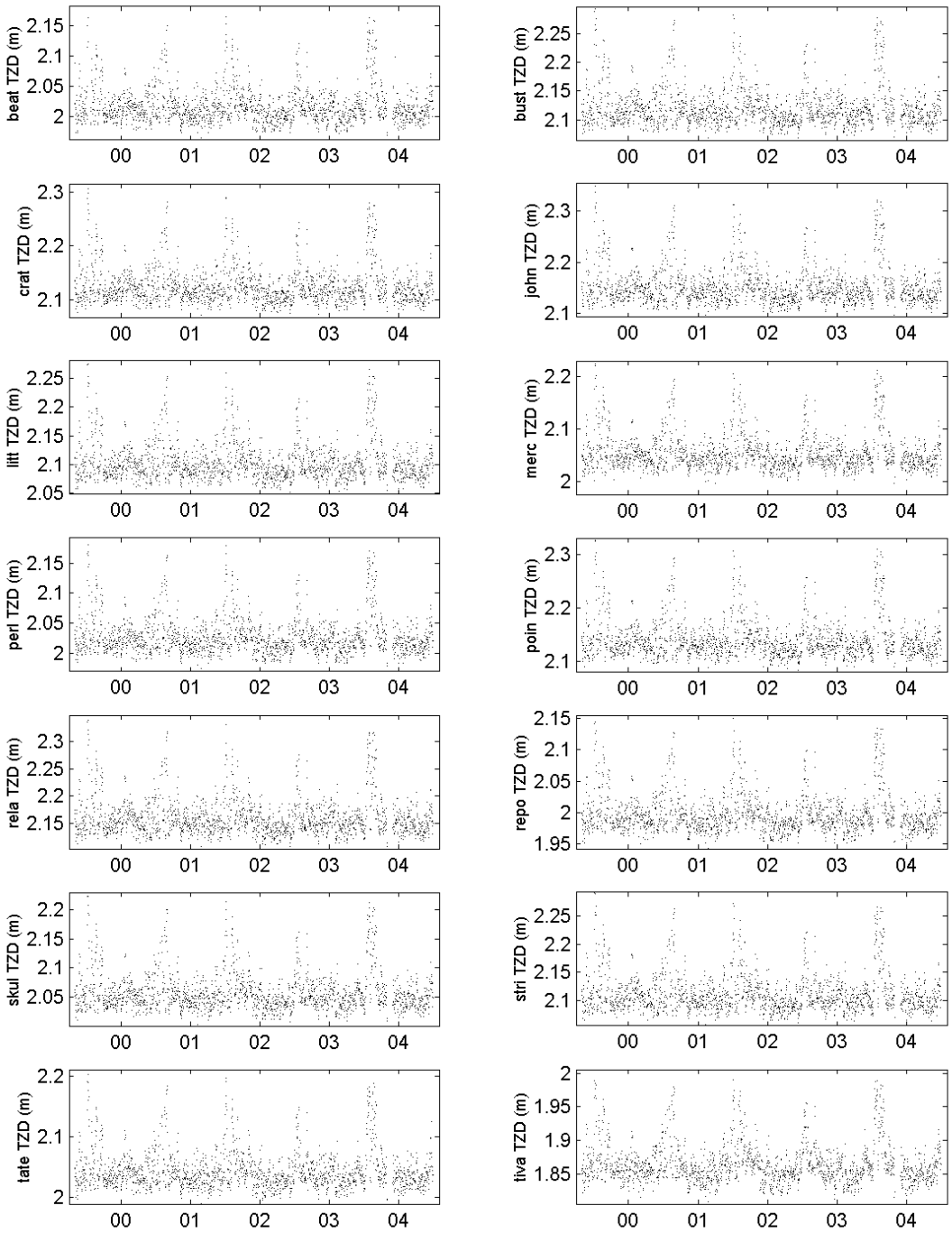

Figure 31. Daily average tropospheric zenith delay for local GPS stations

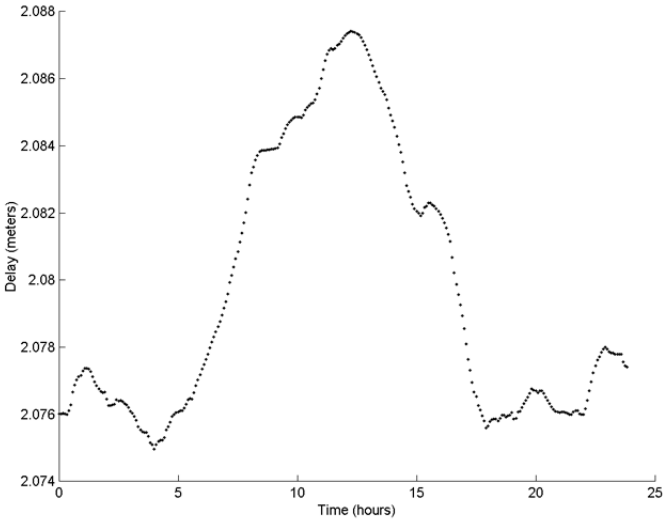

Figure 32. Variations in TZD over 24 hours, at station ALAM

Climate diagrams constructed using NOAA cooperative weather stations (http://lwf.ncdc.noaa.gov/oa/climate/stationlocator.html) show peak levels of precipitation in southern Nevada during the winter months of January and February. Little precipitation is then recorded until the onset of summer monsoons, with relatively higher levels of precipitation during the months surrounding August. All GPS stations show higher levels of TZD in the summer, and a comparison of the TZD time series with the climate diagrams (Figures 33-36) also shows a correlation between peaks in precipitation and peaks in TZD. The higher levels of TZD in the summer months must be attributed to the combination of summer storms, and more importantly, higher temperatures. Summer storms will carry bodies of warm, wet, tropical air, compared with winter storms, where lower temperatures will mean less water vapor can be stored in the air. There is also a smaller peak in TZD during the winter months, when a peak in precipitation indicates the

passing of winter storms, which will also carry relatively higher levels of water vapor.

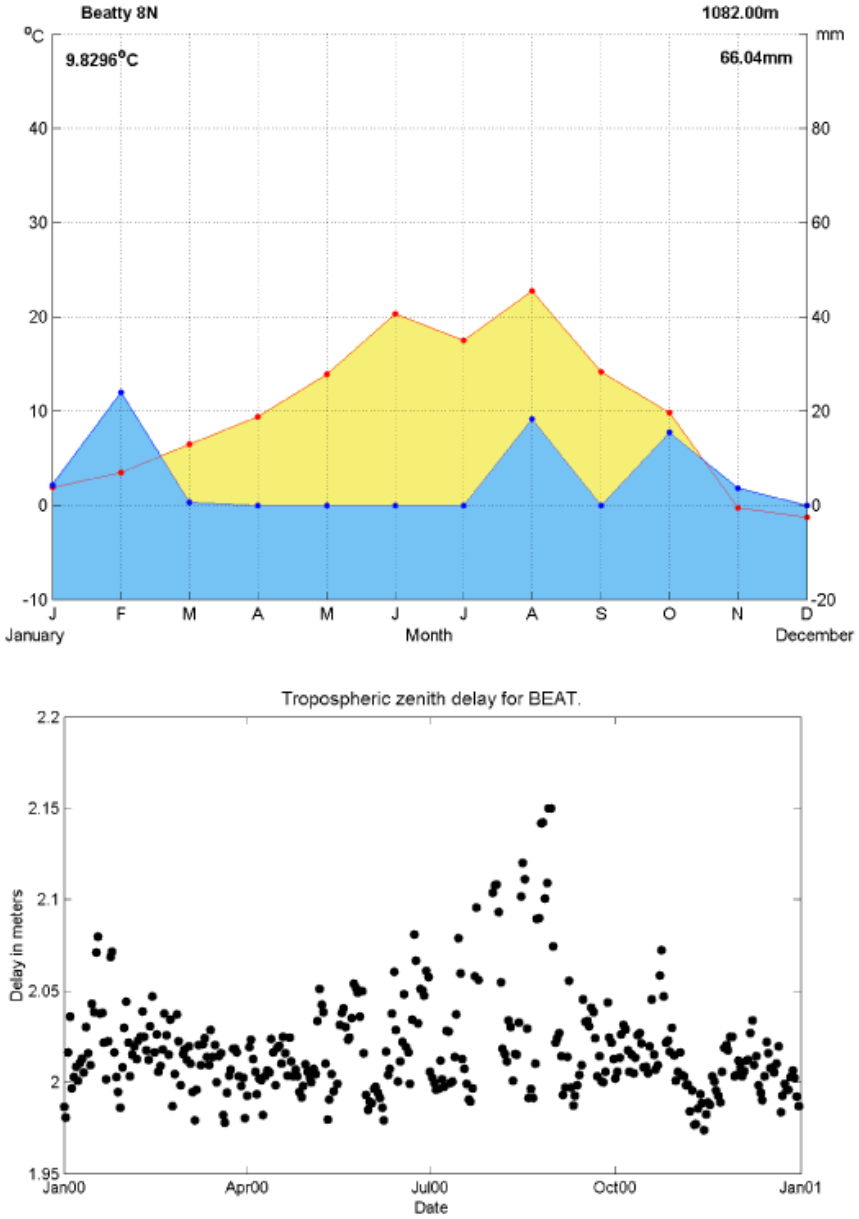

Figure 33. Climate diagram and GPS tropospheric wet zenith delay for Beatty for the year 2000. On all climate diagrams, average annual temperature is given at the top left, average annual precipitation and elevation of the weather station are given at the top right. If the line of precipitation is above the temperature line (blue fill) the month is humid. If the line of temperature is above the line of precipitation (yellow fill) the month is arid and levels of evapotranspiration will be high

.

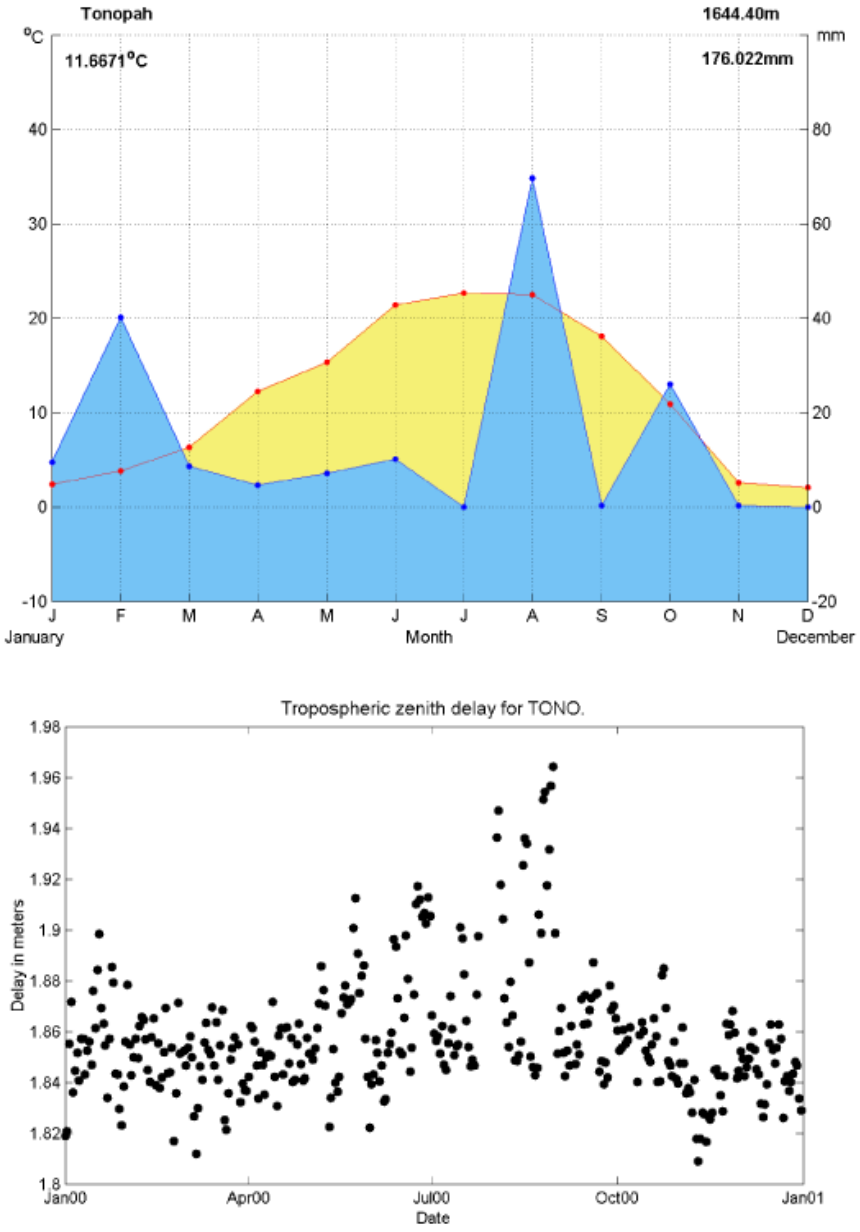

Figure 34. Climate diagram and tropospheric zenith wet delay for Tonopah for the year 2000

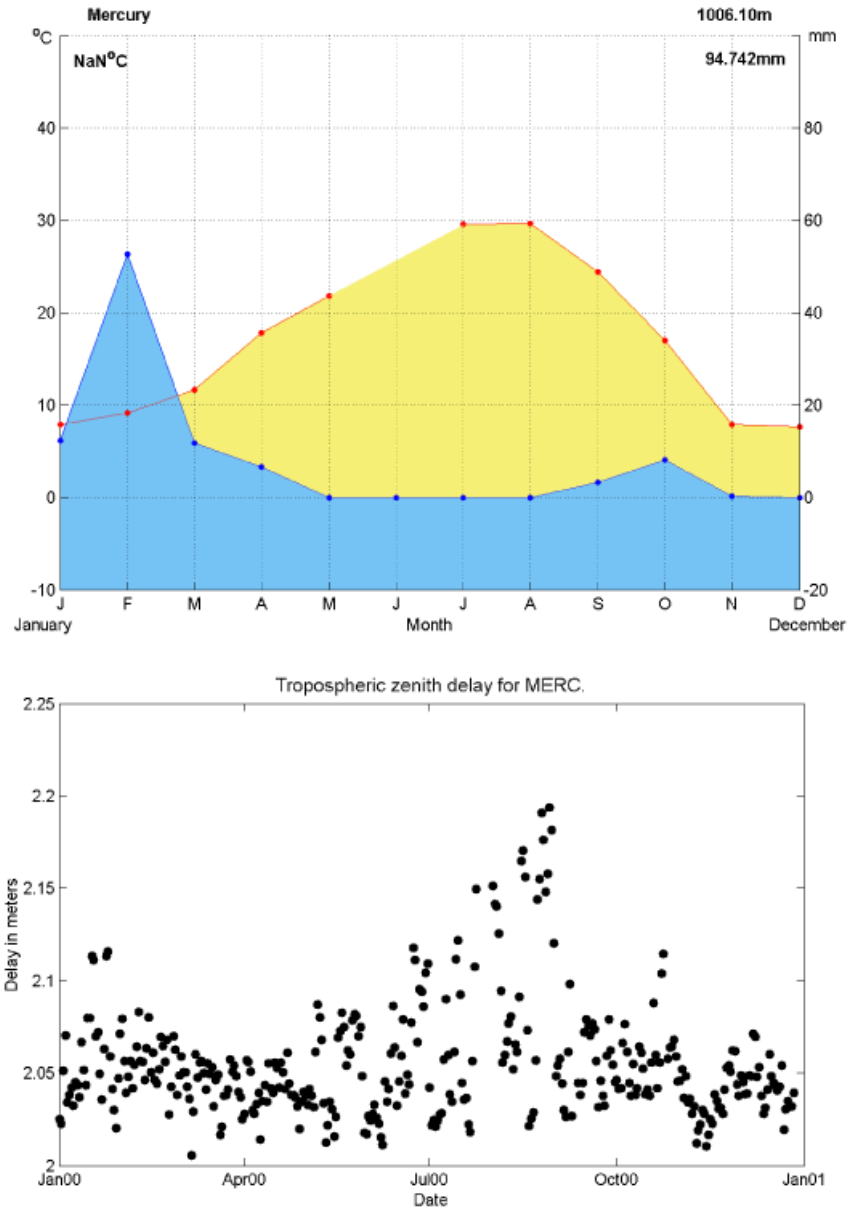

Figure 35. Climate diagram and tropospheric wet zenith delay for Mercury, for the year 2000

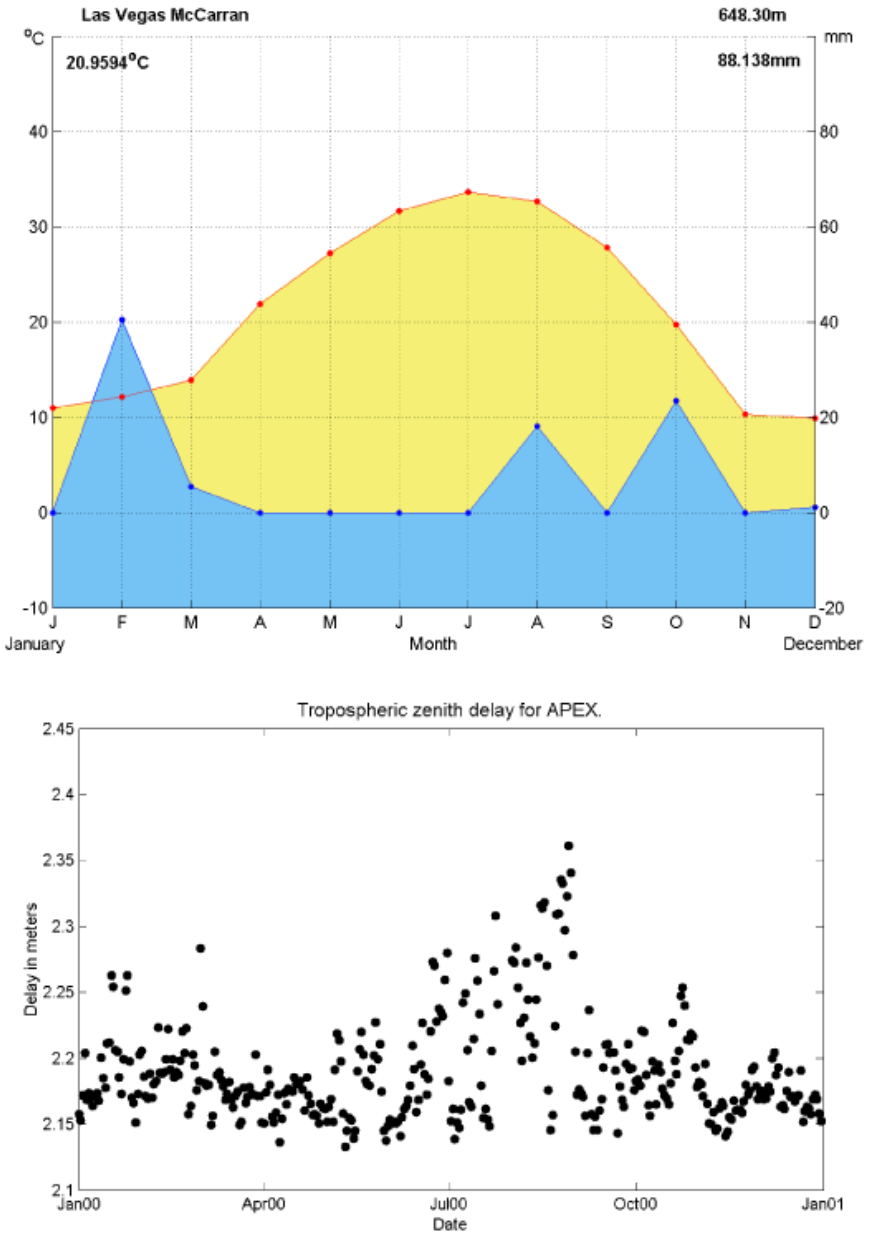

Figure 36. Climate diagram and tropospheric wet zenith delay for Las Vegas, for the year 2000

The effect of elevation dominates tropospheric delay in both summer and winter (Figure 37). The signal traveling from GPS satellites to receivers at higher elevations

travels through less atmosphere than receivers at lower elevations, and levels of water vapor decrease with altitude.

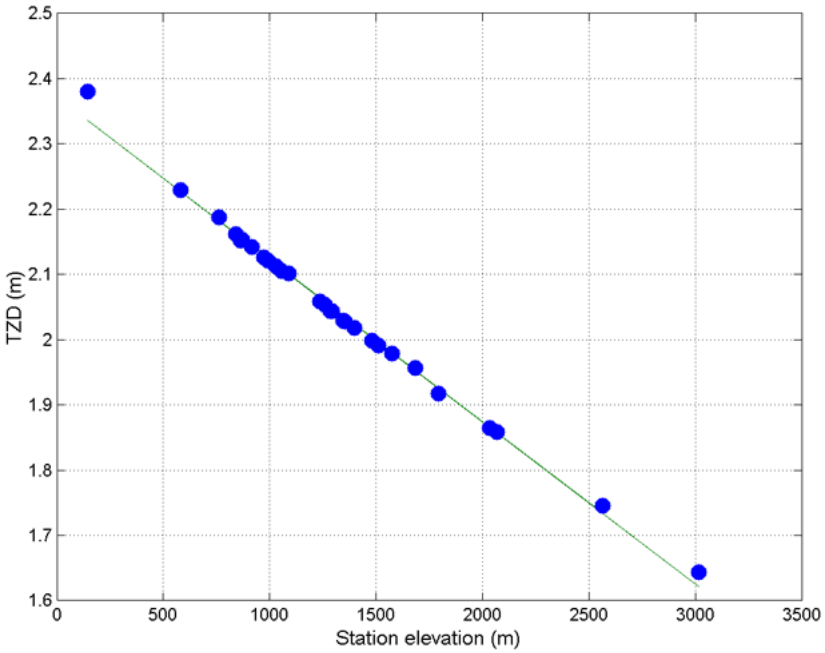

Figure 37. Average tropospheric zenith delay plotted against station elevation

Fitting a linear regression through the data in Figure 37 gives Equation 18.

$$\tau = -0.00002H + 2.4 \quad [18]$$

where τ is tropospheric zenith delay in meters and H is elevation in meters.

2.14 Reference Frame

North American plate rotation was removed as part of the post-processing routine

(Appendix F) by rotating the baseline velocity estimates, to station LITT, by an Euler vector. The Euler vector was the vector provided in Lavallée (2000), but transformed to ITRF-2000 (David Lavallée, personal communication, 2002). This vector has latitude -3.45^{o}, longitude 275.95^{o} and magnitude 0.195^{o}/Myr, and has no net rotation for the North American plate. For comparison, the older NNR-NUVEL-1A solution (DeMets et al., 1994) has latitude -2.438^{o}, longitude 274.105^{o} and magnitude 0.2069^{o}/Myr.

The largest difference between velocity estimates before and after plate rotation was removed is 0.09 ± 0.03 mm/yr in the east component and -0.53 ± 0.04 mm/yr in the north, for the 150 km baseline between LITT and LIND. Figures 38 and 39 show a comparison of results before and after North American plate rotation was removed. The mean difference in magnitude between velocities rotated by the two different Euler poles described above was 0.02 mm/yr. The maximum difference was 0.06 mm/yr.

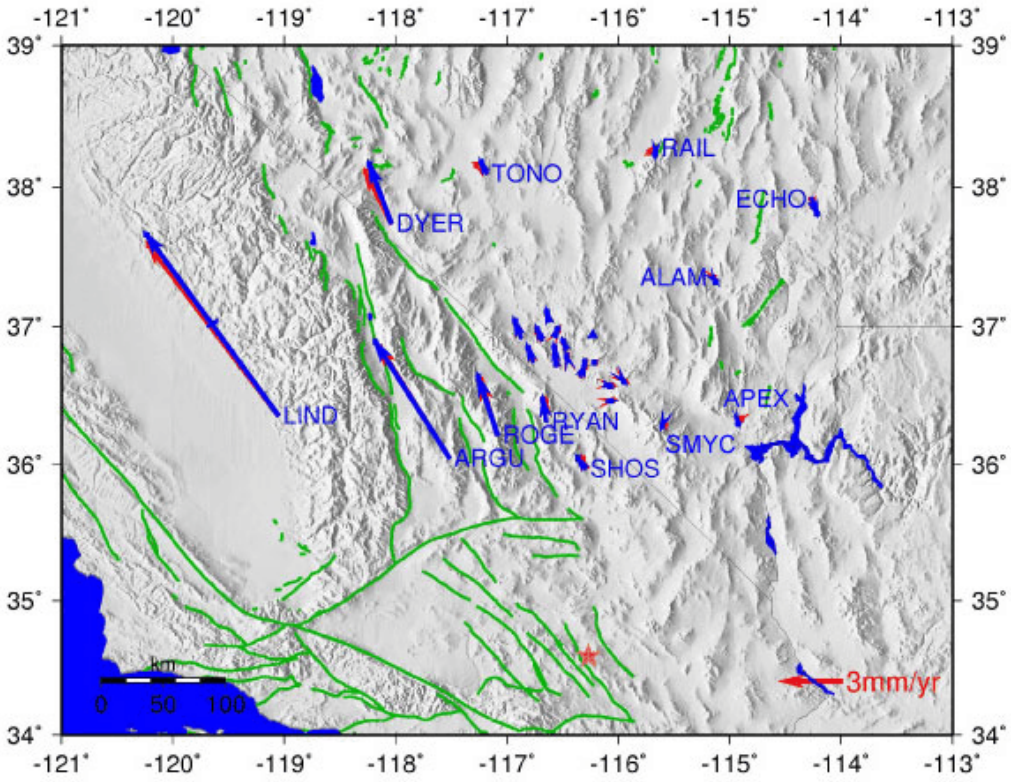

Figure 38. Comparison of results before (RED) and after (BLUE) North American plate rotation was removed. Velocities are plotted relative to station TIVA (blue triangle).

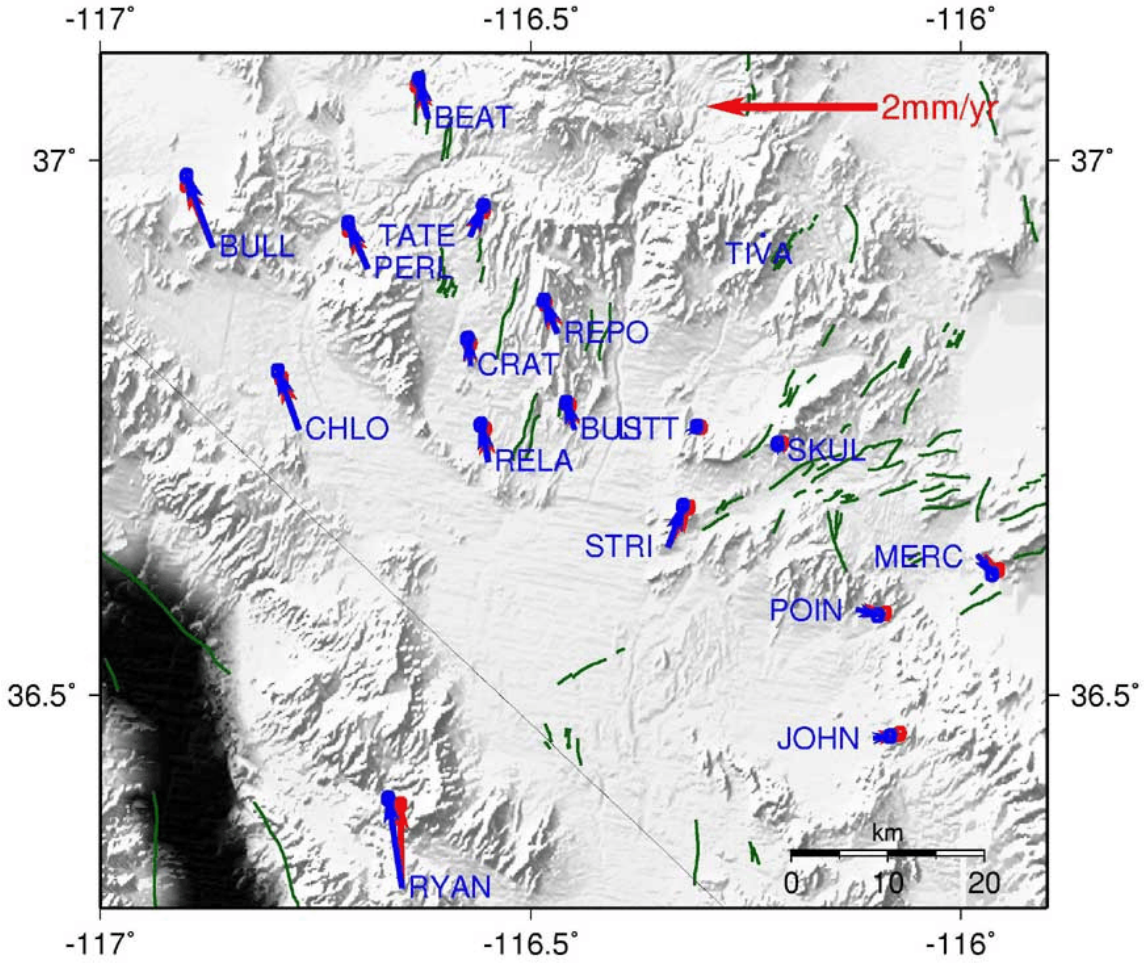

Figure 39. Comparison of results before (RED) and after (BLUE) North American plate rotation was removed. Velocities are plotted relative to station TIVA.

The GAMIT reference frame was defined in a significantly different way to the GIPSY reference frame. Instead of rotating the velocities by an Euler vector, the GAMIT velocities were rotated so as to minimize the velocities at 45 GPS stations located on the 'stable' interior of the North American plate. The disadvantage of this technique is that any non-tectonic effects measured at these stations, such as post-glacial isostatic rebound, will propagate into the results for the Yucca Mountain stations.

After plate rotation was removed, the data were plotted relative to a single station. Ambiguities were resolved to station LITT due to its location in the center of the network. The fact that LITT is in the center of the network, however, makes velocities plotted relative to it difficult to interpret. Velocities were therefore recalculated relative to a station at the edge of the local network, TIVA for the local Yucca Mountain stations and ECHO or APEX for the regional network.

Velocities were also rotated into a Pacific plate frame for interpretation purposes. The NNR-NUVEL-1A Euler vector (DeMets et al., 1994) was used. This vector has latitude -63.045^{o}, longitude 107.325^{o} and magnitude 0.6408^{o}/Myr.

2.15 Periodic signals in the GPS time series

There are many potential causes of periodic signals in GPS, for example; gravity (from the sun, moon and planets), atmospheric pressure loading, ocean tide loading, non-tidal ocean loading, snow and soil moisture mass loading, polar motion, groundwater effects, thermal expansion of bedrock around the antenna, errors in satellite orbits and clocks, errors in atmospheric and water vapor models, phase center variation, antenna noise, multipath and seasonal effects such as snow cover on the antenna (Dong et al., 2002). These signals have the greatest effect on the vertical component (hence the difficulty in obtaining reasonable estimates of vertical velocity and position, compared with the relative ease of obtaining horizontal results). Van Dam et al. (2001) examine the loading effect of continental water storage (in snow-pack, soil and groundwater) on GPS

vertical velocities, resulting in an annual vertical signal with an RMS of up to 8 mm. They note that this can cause a long-period signal, resulting in a linear trend over several years that would be difficult to distinguish from a tectonic signal

Dong et al. (2002) analyzed 171 globally distributed, continuous GPS sites with at least 2.3 years of data. They processed the data in GAMIT. They estimated that most vertical annual signal amplitudes are typically 4-10 mm in a global reference frame, with corresponding formal errors of < 1 mm, and most horizontal annual amplitudes are in the range 1-3 mm, with formal errors of ~ 0.5 mm. They then compared their results with daily solutions from the IGS processing center at JPL (GIPSY in PPP mode). They determined that although GIPSY and GAMIT are able to detect the common seasonal signals, there are significant differences in residual signals.

ITRF-2000 is temporally defined by the velocities of its global tracking stations, so has good long-term stability. On a seasonal timescale, however, un-modeled periodic signals at the tracking stations can contaminate the reference frame. The frame will undergo regional changes as different subsets of the ITRF will suffer different seasonal influences at different times. Also, the entire frame will shift due to seasonal changes in the geocenter (Dong et al., 2002; Blewitt, 2003). Again, this is particularly an issue for vertical GPS results.

An important question to ask when processing continuous GPS data is ‘when is a good time to stop’? As a rule, how many years of data are necessary before the results

represent a reliable reflection of the current tectonic rates rather than the effect of periodic signals? And after that time should the data processing end in a particular month, after an integer or half-integer number of years? These questions apply directly to the Yucca Mountain GPS data.

Blewitt and Lavallée (2002) assess the effects of periodic signals on GPS results. They conclude that a minimum of 2.5 years of data must be processed in order that periodic signals do not significantly bias velocity results. Blewitt and Lavallée (2002) also state that "solutions are minimally biased at data spans of integer-plus-half years", rather than integer numbers of years. They determine that after 3.5 years periodic signals become less important and, after 4.5 years, periodic signals may become insignificant to the results. Section 2.3 described the GPS data used in this project. There are two solutions, one (for the GIPSY-GAMIT comparison) that uses data from May 1999 to October 2003 and one (for the final results) that uses data from January 2000 to June 2004. Both solutions contain 4.5 years of data, the optimal amount suggested by Blewitt and Lavallée (2002). The former solution, however, does not fully meet these requirements since it contains offsets in the time series.

There are several methods of dealing with the effects of periodic signals in GPS. One 'method' is just to ignore them, which is the preferred method in many published results. This is reasonable if, as proven by Blewitt and Lavallée (2002), the data span is greater than 3.5 years (preferably 4.5 years) and is a half-integer number of years. A second method is to produce a solution with a regional reference frame. If the baselines

are short enough, common-mode signals will be similar at each station and will largely cancel out; Figures 40-45 show the PPP time series for the Yucca Mountain network, which all show very similar signals. The idea of 'spatial filtering' is discussed by further by Wdowinski et al. (1997). An extension of this can be achieved by producing time series relative to the average of a number of stations in the local network. A third method is to try to estimate the amplitude of the phase of the periodic signals as part of the processing inversion. This method only works if the data spans more than 2.5 years, due to problems caused by correlated parameters, but beyond 4.5 years there is negligible gain in estimating these parameters (Blewitt and Lavallée, 2002).

For the Yucca Mountain GPS results, the first two methods were used. Data were processed for a total of 4.5 years, and common-mode signals were reduced by producing baseline velocities to a station in the center of the network (Section 2.8). Figures 40-45 show the time series for the PPP results, which include a clear periodic signal. Figures 46-51 show the baseline time series, where periodic signals have been largely eliminated. There is one station that continued to show clear periodic signals in the time series even in the baseline time series and this was station CHLO. This station had the greatest difference in velocity of the local stations (0.16 mm/yr, compared with a mean of 0.07 mm/yr), between results using data from May 1999 to October 2003 (4.5 years, but including offsets) and January 2000 to June 2004 (4.5 years, but with no offsets). The most likely cause of this periodic signal is multipath.

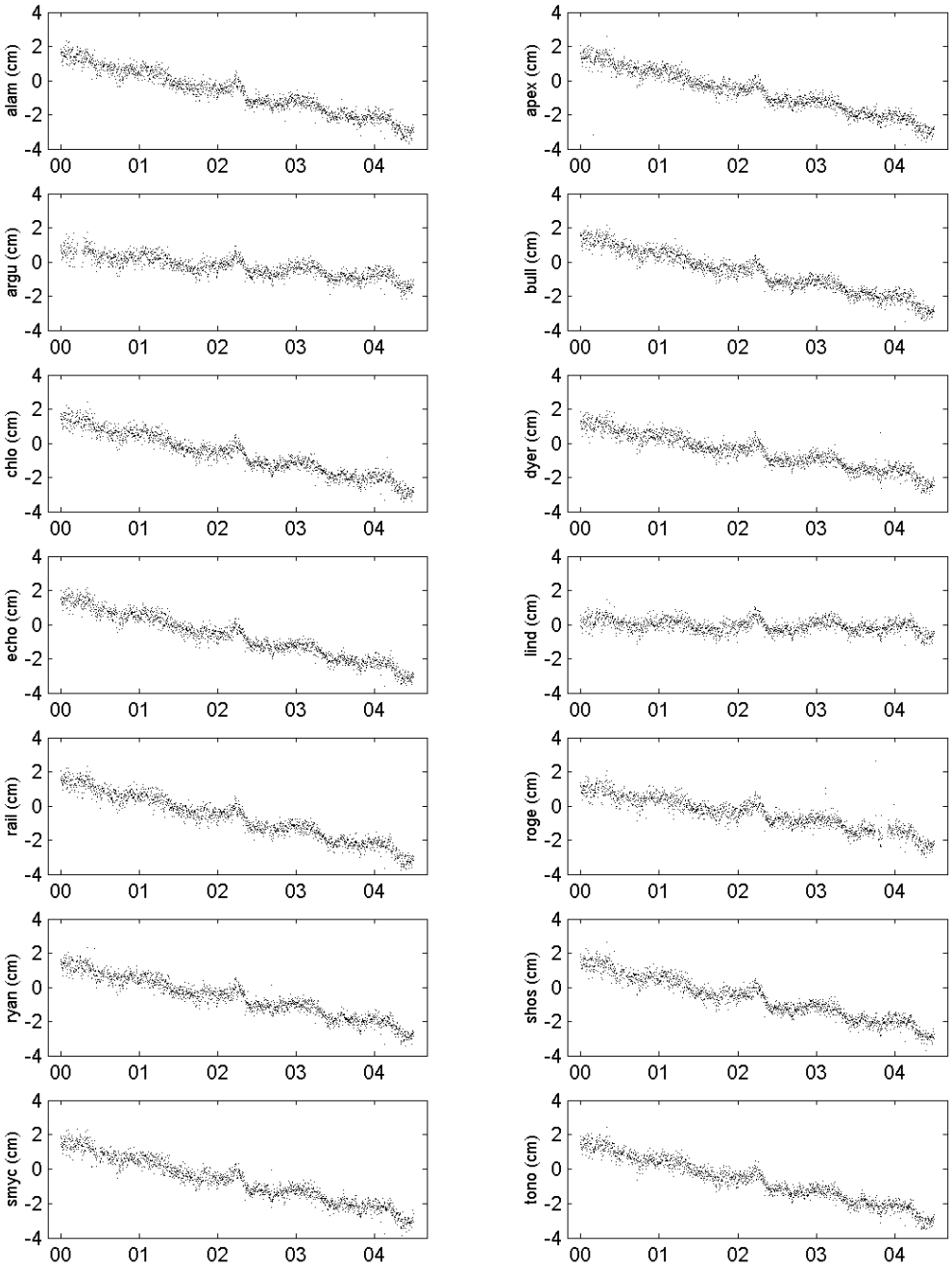

Figure 40. Latitude component of PPP time series for far-field GPS stations, plotted in ITRF2000 relative to the position at the mid-point of the time series.

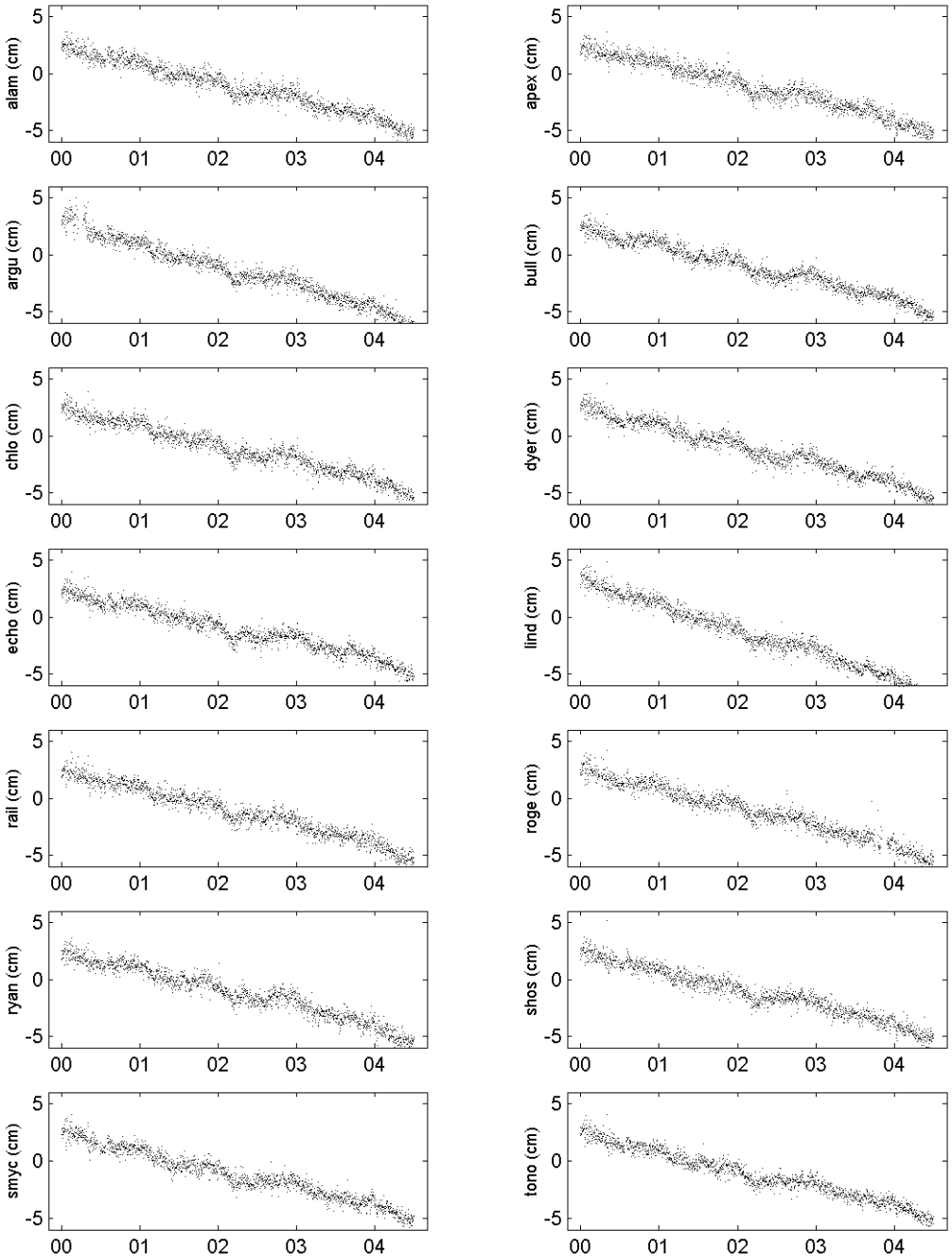

Figure 41. Longitude component of PPP time series for far-field GPS stations, plotted in ITRF2000 relative to the position at the mid-point of the time series.

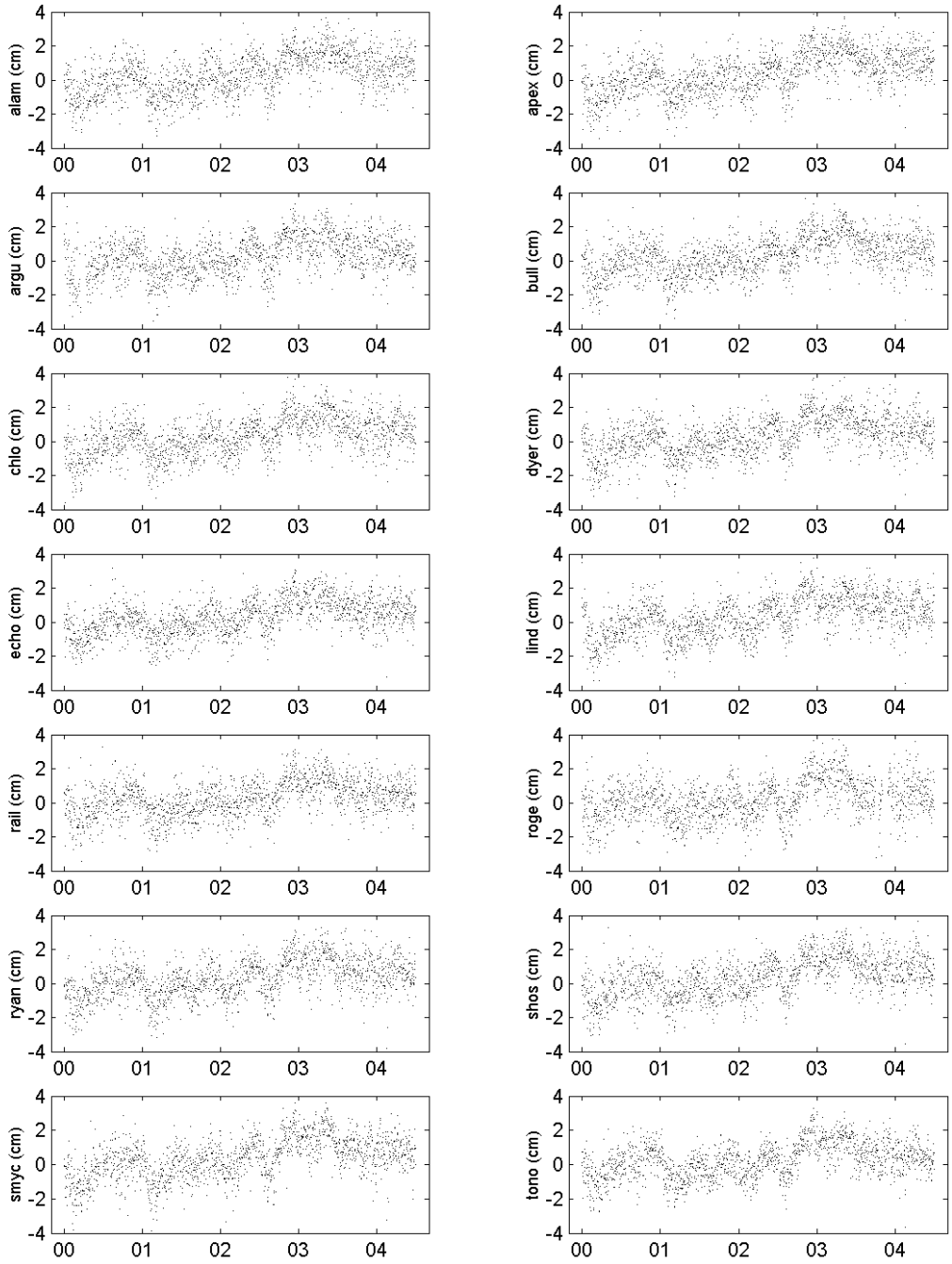

Figure 42. Height component of PPP time series for far-field GPS stations, plotted in ITRF2000 relative to the position at the mid-point of the time series.

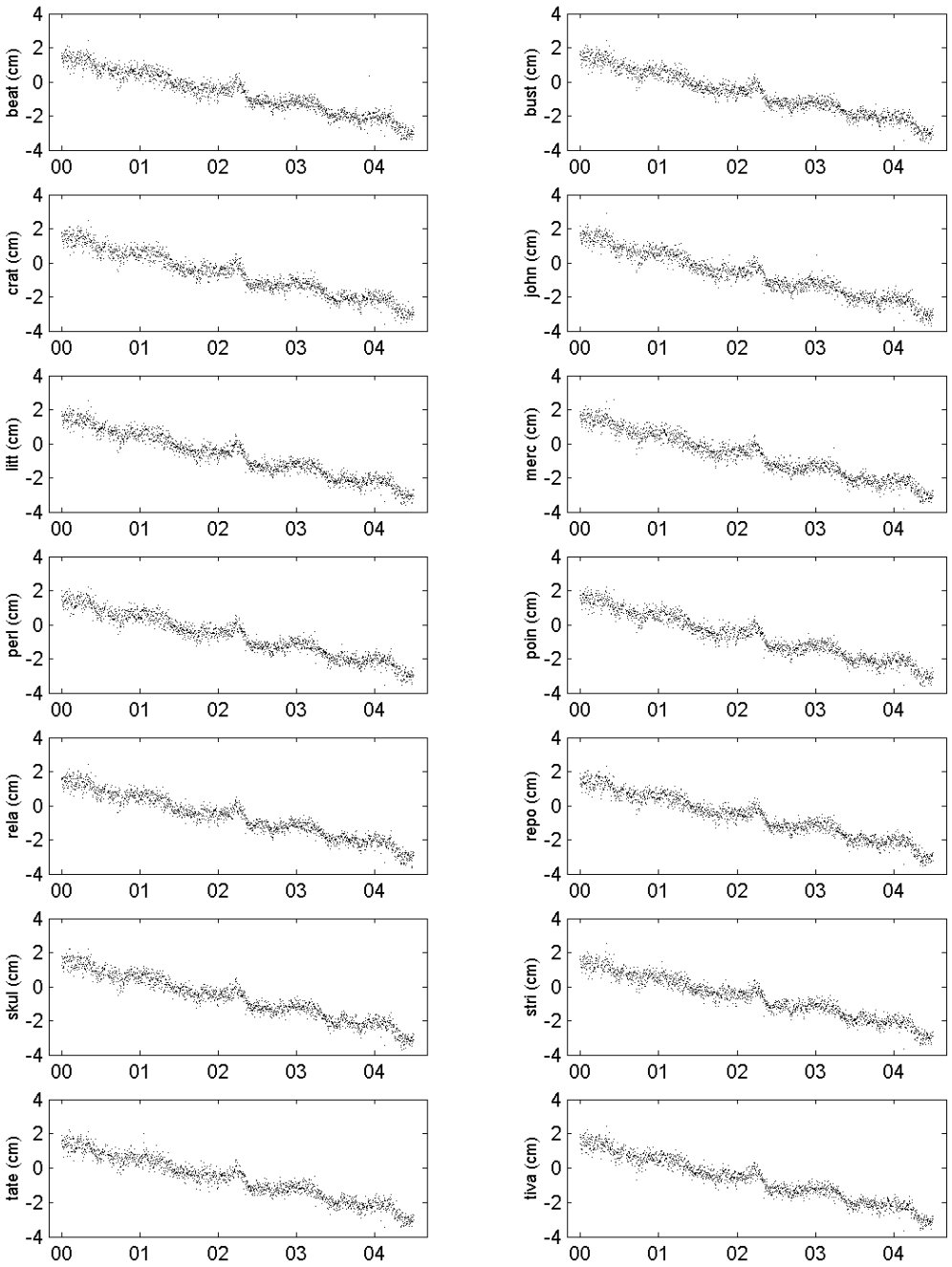

Figure 43. Latitude component of PPP time series for local GPS stations, plotted in ITRF2000 relative to the position at the mid-point of the time series.

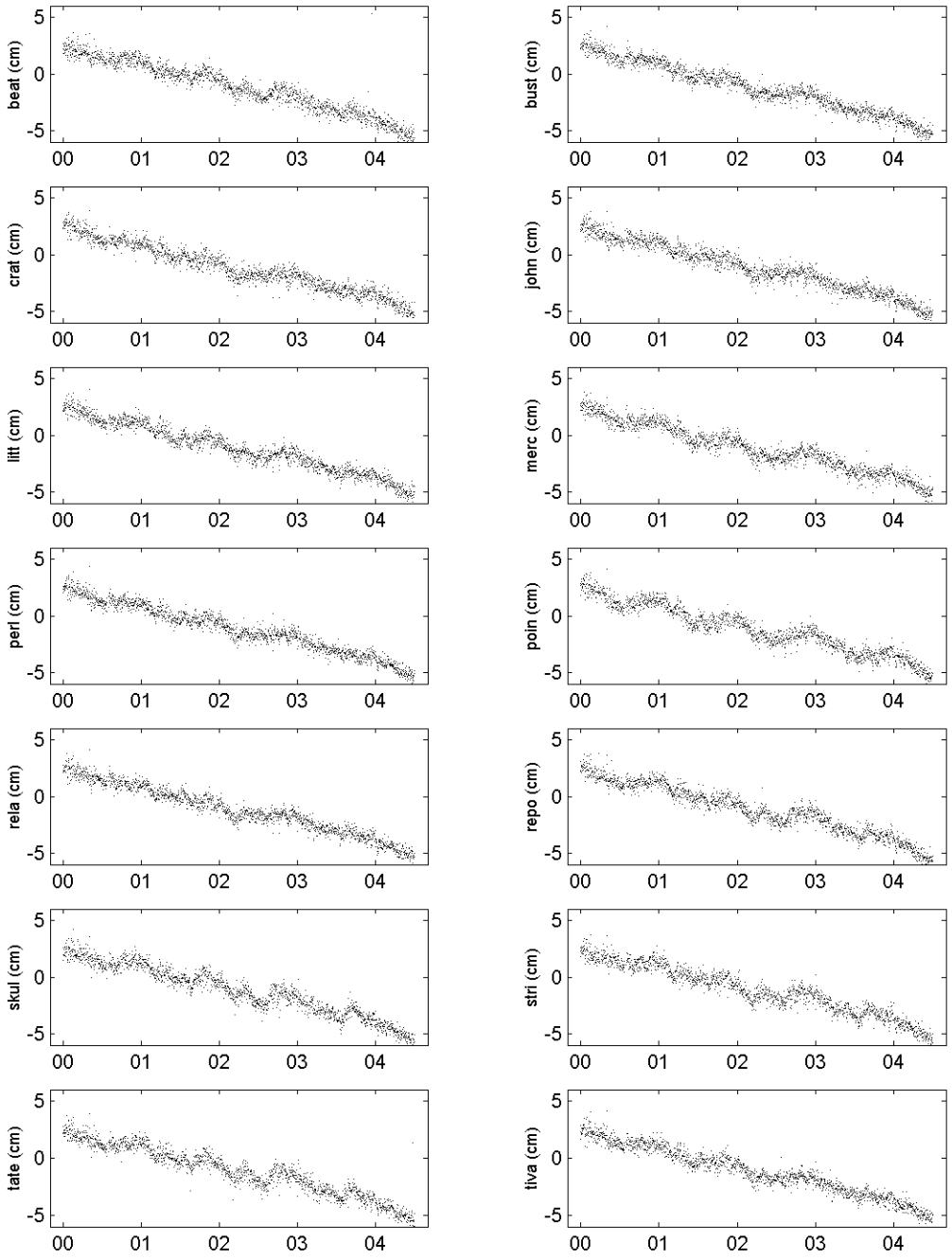

Figure 44. Longitude component of PPP time series for local GPS stations, plotted in ITRF2000 relative to the position at the mid-point of the time series.

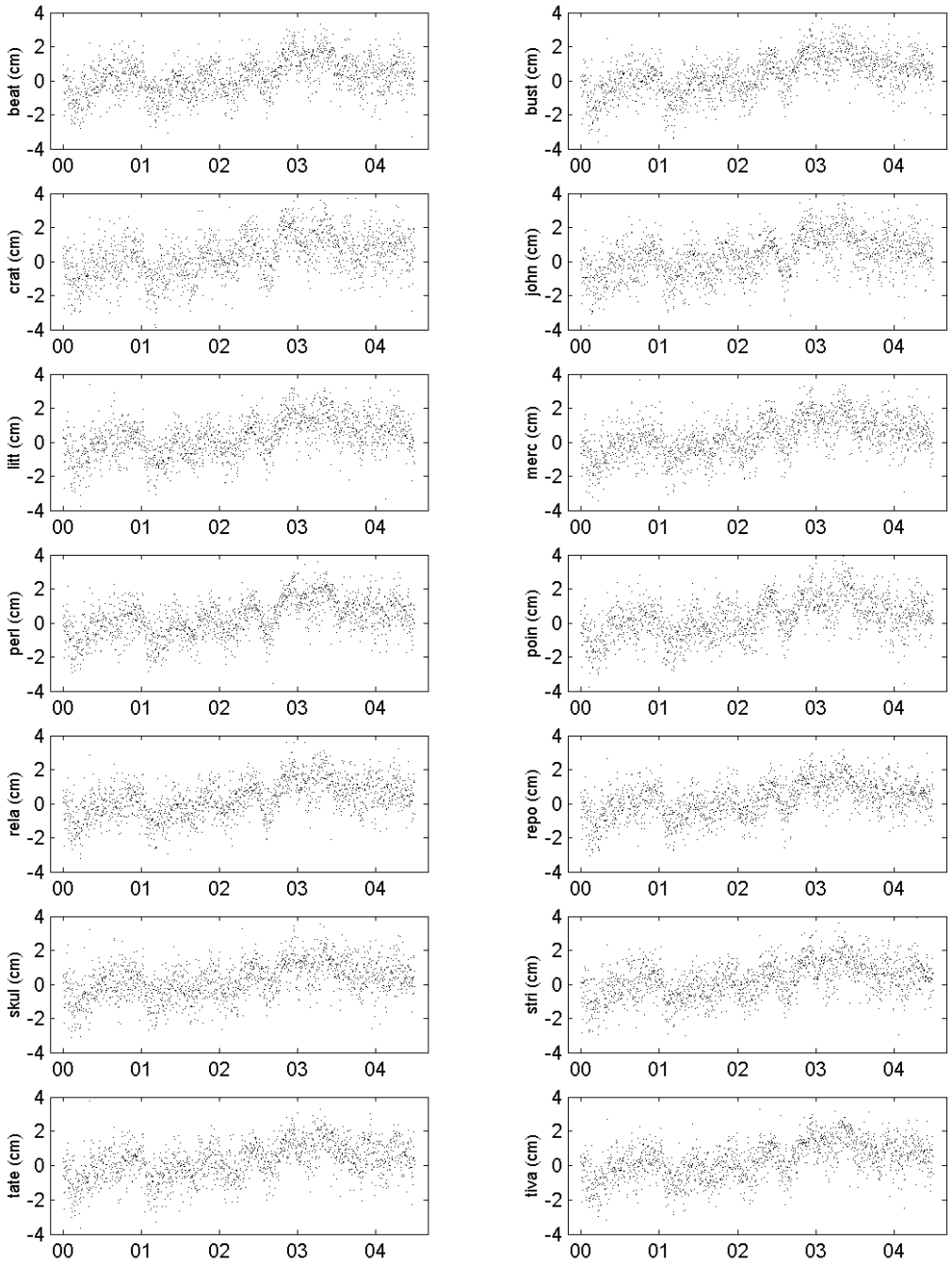

Figure 45. Height component of PPP time series for local GPS stations, plotted in ITRF2000 relative to the position at the mid-point of the time series.

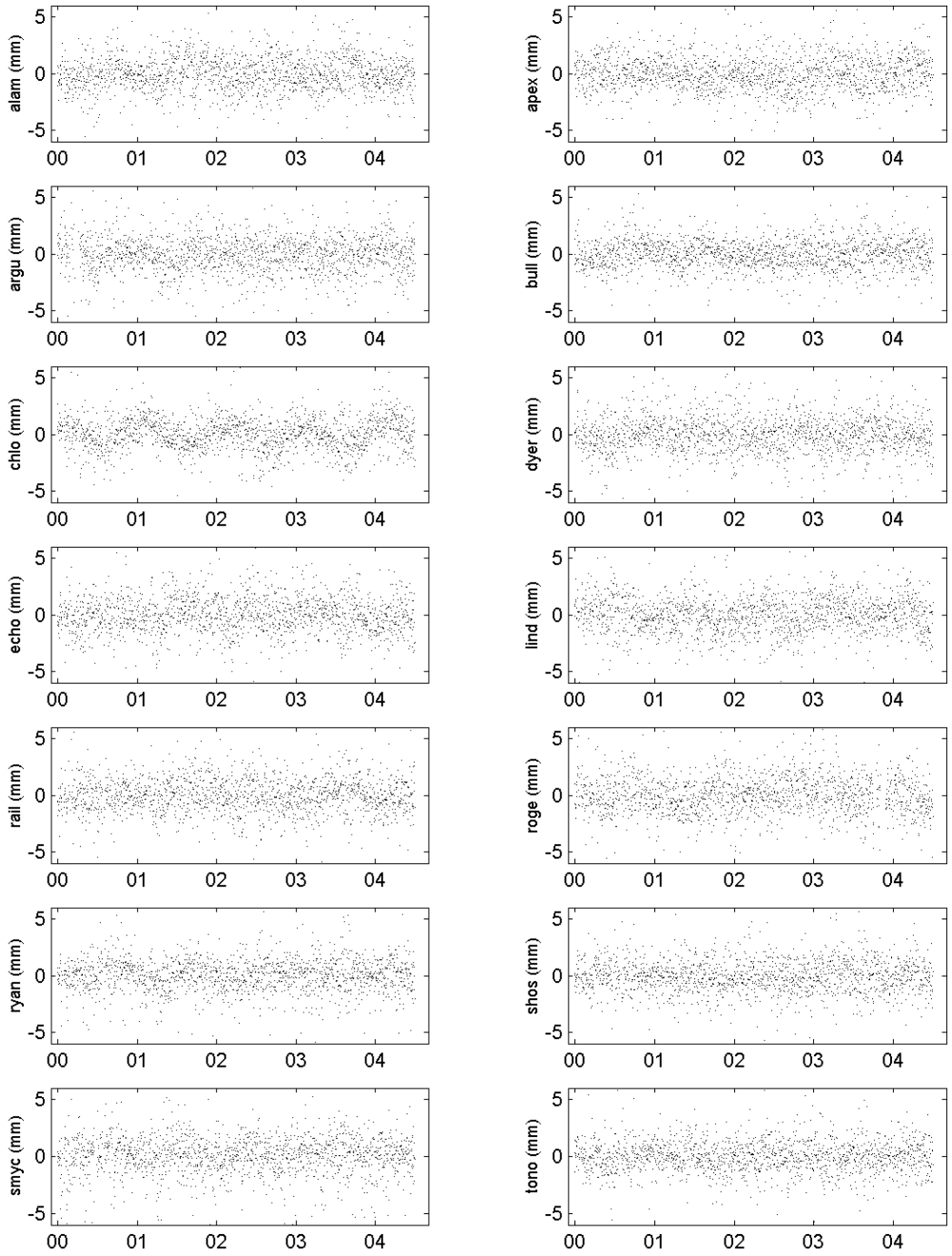

Figure 46. <u>Detrended</u> baseline time series for far-field GPS stations, east component, relative to station LITT.

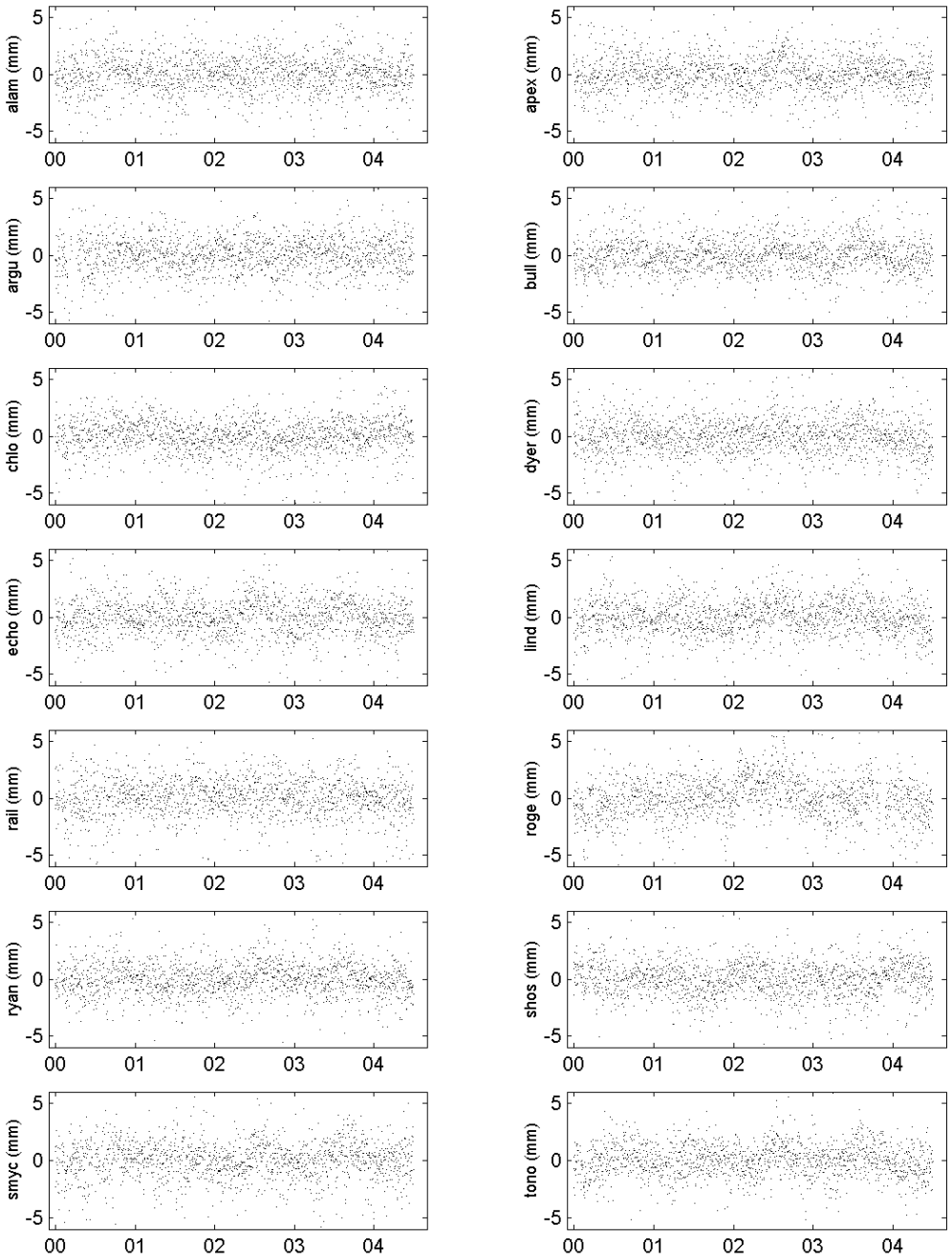

Figure 47. <u>Detrended</u> baseline time series for far-field GPS stations, north component, relative to station LITT.

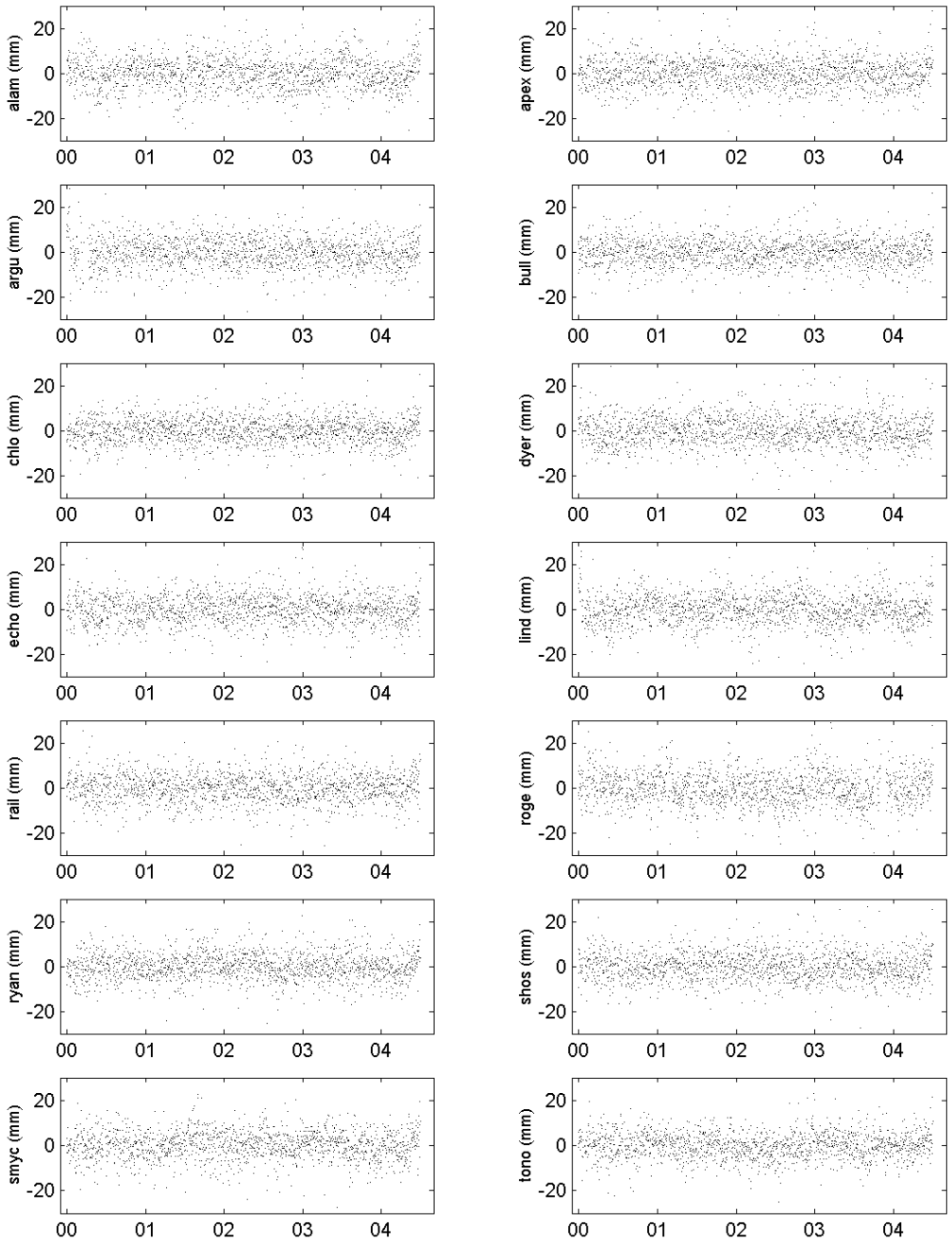

Figure 48. <u>Detrended</u> baseline time series for far-field GPS stations, vertical component, relative to station LITT.

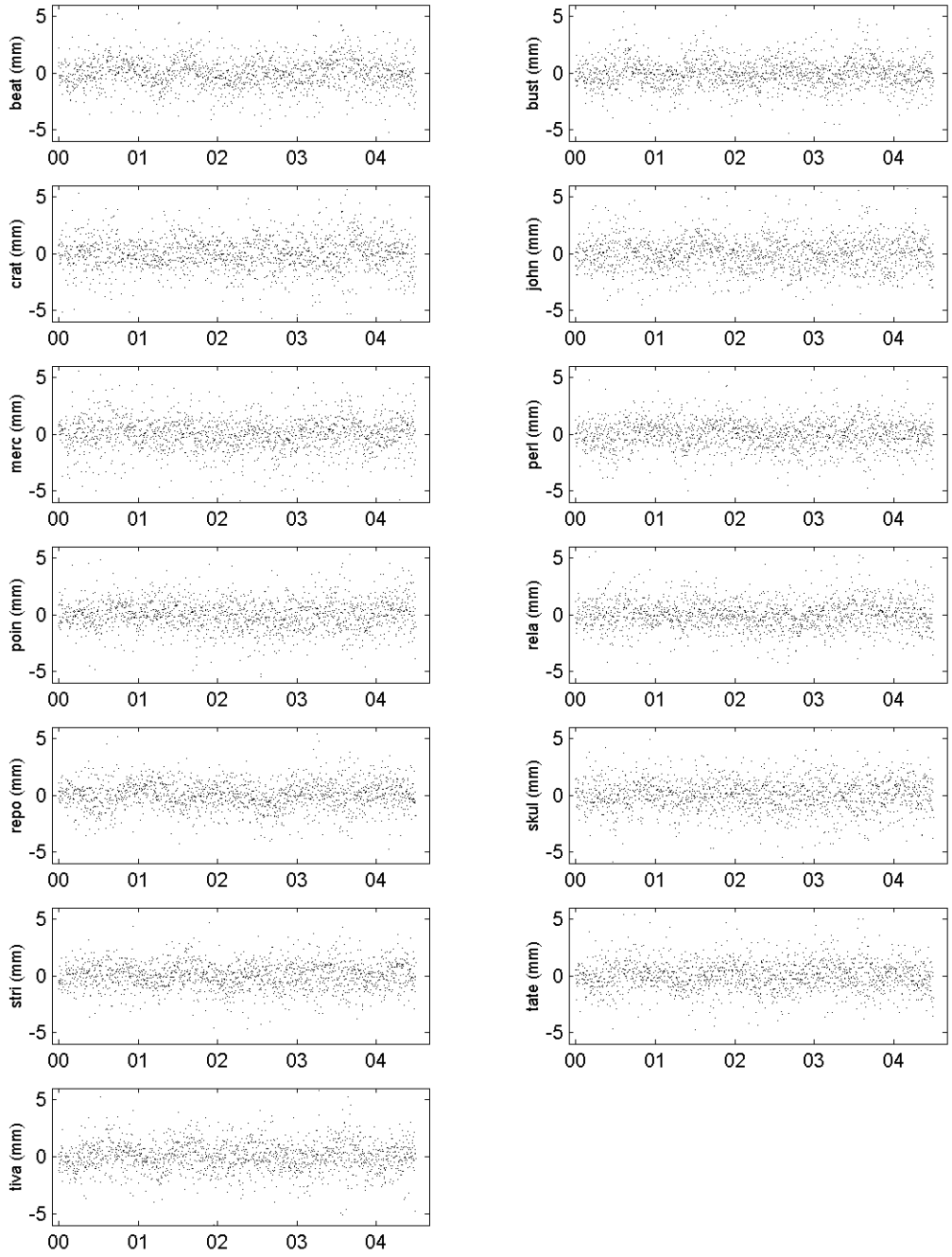

Figure 49. <u>Detrended</u> baseline time series for local GPS stations, east component, relative to station LITT.

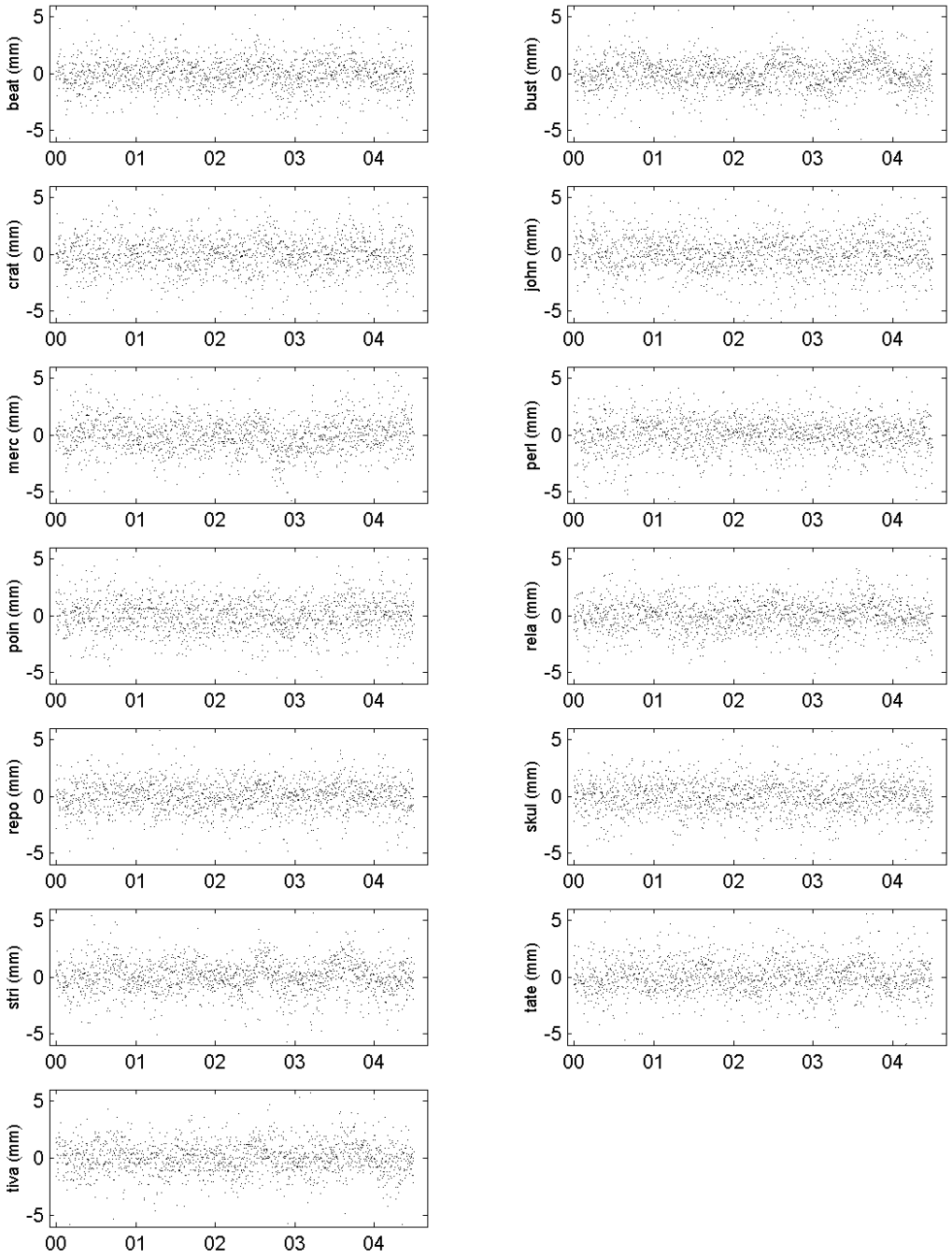

Figure 50. <u>Detrended</u> baseline time series for local GPS stations, north component, relative to station LITT.

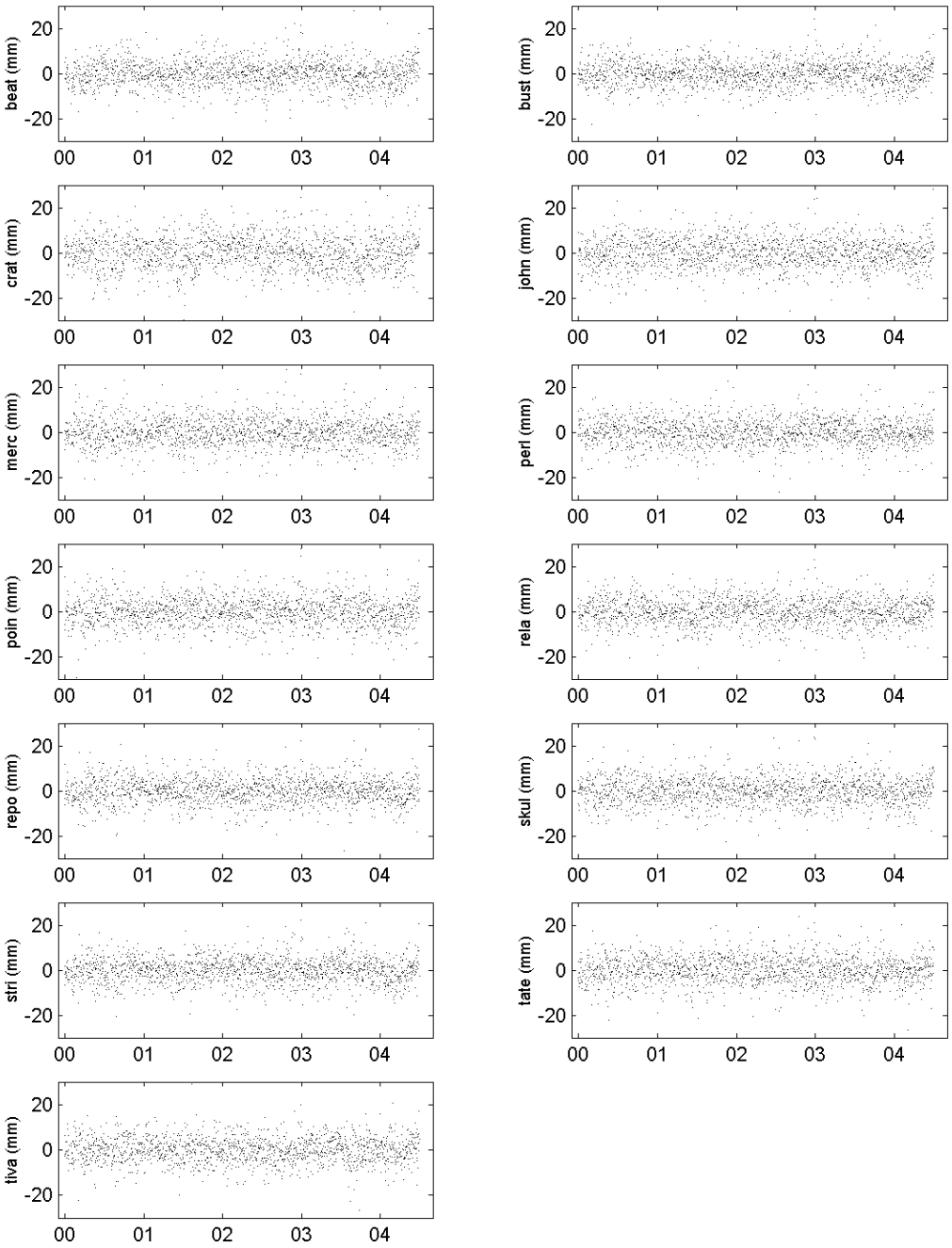

Figure 51. <u>Detrended</u> baseline time series for local GPS stations, vertical component, relative to station LITT.

2.16 Changes in the GPS velocity estimates with increasing volumes of data

In order to assess the direct results of having more data for the Yucca Mountain network, GPS velocities were calculated for batches of data, each with an additional 6 months of data. The results are shown in Figures 52 and 53. In the figure key, Jan00-JunYY represents data processed from 16th January 2000 to 30th June YYYY. Jan00-DecYY is data from 16th January to 31st December YYYY.

These results show the velocities stabilizing after ~2.5 years of data was processed. This agrees with the conclusions of Blewitt and Lavallée (2002), who state that 2.5 years is the minimum recommended data span to avoid an unacceptably large velocity bias caused by annual signals in the time series.

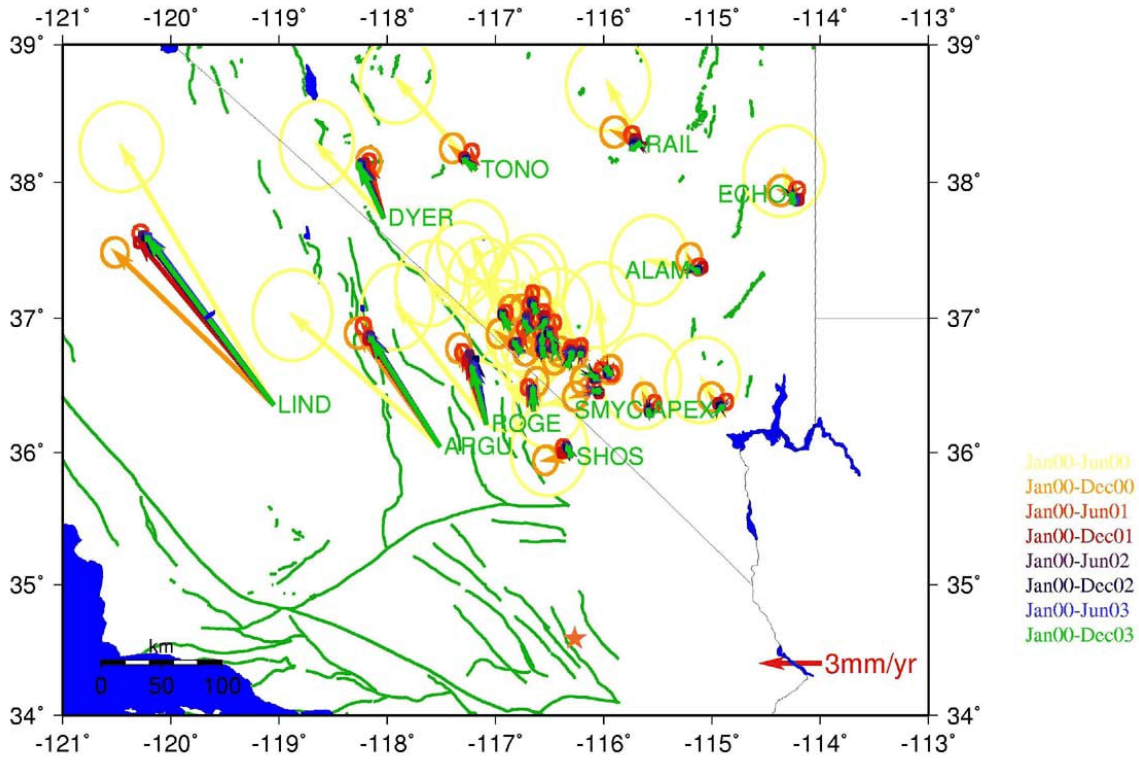

Figure 52. GPS results with increasing volumes of data. Each color increment indicates an addition of 6 months of data. Error ellipses are 95% confidence. Velocities are plotted relative to station TIVA.

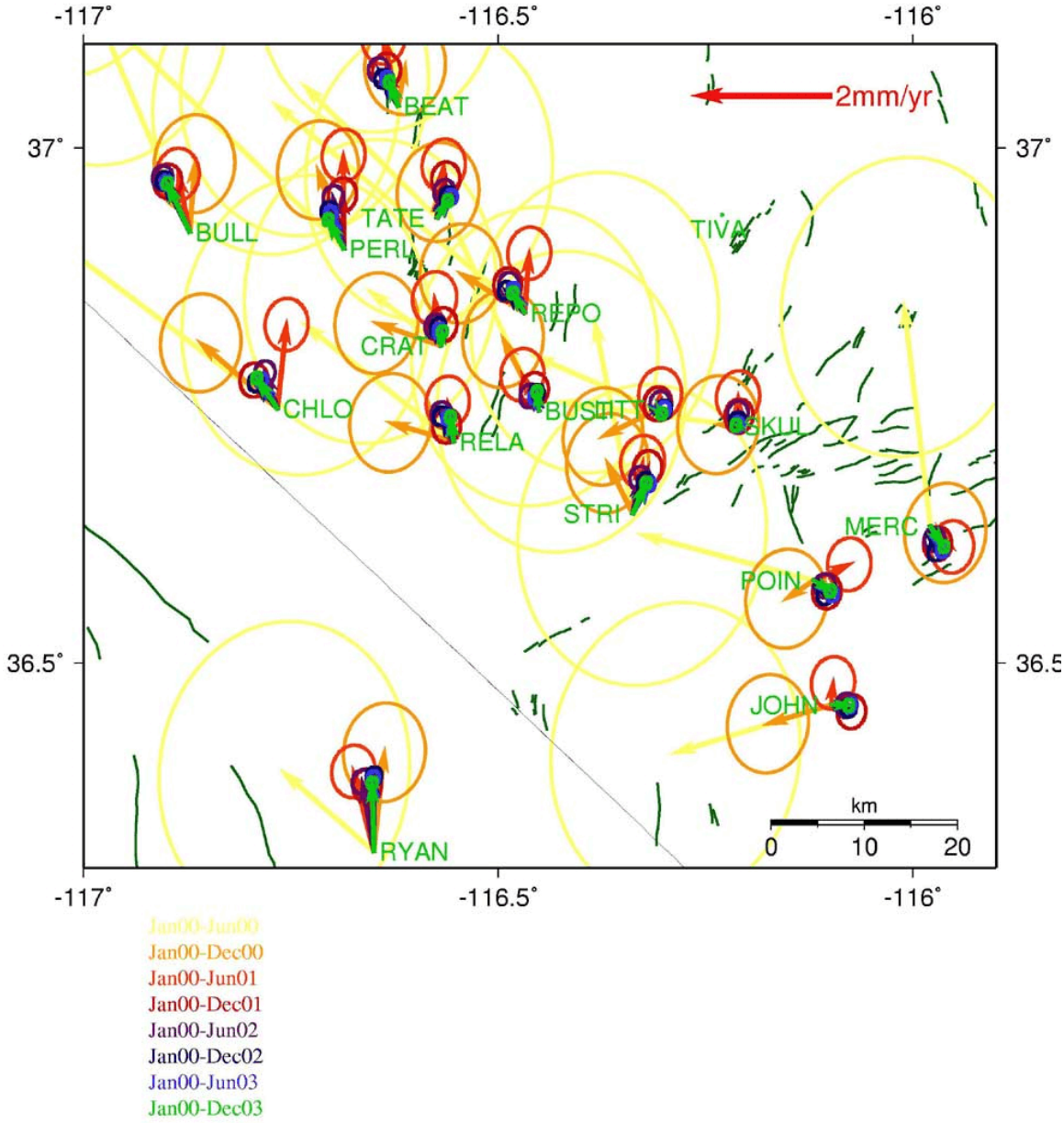

Figure 53. GPS results with increasing volumes of data. Each color increment indicates an addition of 6 months of data. Error ellipses are 95% confidence.

2.17 Discussion of this chapter

This chapter described the processing techniques used to produce the GPS results discussed in the remainder of this dissertation. The GPS data were processed first using the Precise Point Positioning (PPP) method, then PPP time series were analyzed for inconsistencies and outliers. Significant outliers were removed. The data were then processed with ambiguity resolution on a line-by-line basis to a single reference station. Data were processed using precise satellite orbit and clock data from the NASA Jet Propulsion Laboratory. The results were transformed to ITRF-2000 using a Helmert transformation. North American plate rotation was removed using an Euler vector rotation. Tropospheric wet delay was estimated as random walk. Tropospheric dry delay was estimated using a nominal pressure (based on the elevation of the station), with any residual error in the estimate absorbed by estimate of wet delay. The reliability of this processing technique was tested by comparison with GAMIT results from the group at Harvard Center for Astrophysics.

A useful outcome from this project has been the development of processing code that resolves integer ambiguities in GIPSY on a line-by-line basis, which dramatically reduces processing time but results in a similar solution. Although recent increases in computer processing speed have made the consideration of processing time less important, increases in the volume of data (for example with the Plate Boundary Observatory) could again make processing time an important consideration.

The GPS time series show a number of offsets in the time series, all occurring in

1999. The data for 1999 was not included in the final GIPSY solution, but techniques for dealing with these offsets were discussed since the GIPSY-GAMIT comparison does include 1999 data. The offset for the 1999 Hector Mine earthquake was estimated and removed as part of the least squares inversion. Offsets from radome changes in the network were removed simply by removing all data between the first and last radome changes.

When plotted as PPP results in ITRF2000, the time series have clear periodic signals. The signals are generally very similar for all stations, however, so the majority of common mode signals were successfully removed by producing baseline time series to a local station. The effect of periodic signals was also minimized by following the advice of Blewitt and Lavallée (2002) to use a total data span of 4.5 years. Examination of the changes in the velocity results over time has shown the importance of obtaining enough data before attempting to interpret GPS velocities, as the solution has changed significantly over time and did not begin to stabilize until after 2.5 years of data had been processed.

3. GPS Velocity Results

3.1 Introduction to this chapter

This chapter describes the horizontal and vertical GPS velocities. I first discuss the results from the GIPSY - GAMIT software and then discuss the final horizontal velocity solution from GIPSY. Strain rates are discussed in Chapter 4. An interpretation of these results, and a discussion of velocity profiles across the network, is given in Chapter 5.

This chapter also discusses the GIPSY vertical velocity estimates. Possible sources of vertical motion across the network were discussed in Section 1.2 (normal faulting, variations in gravitational potential energy and magmatic instabilities) and Section 1.4 (localized volcanism). Since the vertical GPS results are not reliable, the section on vertical results begins with a discussion of why it is still very difficult to obtain accurate vertical velocities with GPS.

3.2 Results of the GIPSY - GAMIT comparison

The differences between the GIPSY and GAMIT processing software packages were discussed throughout Chapter 2. Figures 54 and 55 show a comparison of GIPSY and GAMIT results after all the procedures described in Chapter 2 had been carried out

(including ambiguity resolution, removal of North American plate rotation and removal of offsets in the time series). The two solutions are very similar, with an RMS of residual velocity differences of 0.06 mm/yr for the east velocity estimates and 0.10 mm/yr for the north (see Appendix H for table showing a comparison of velocity estimates). Considering the number of variables involved, the different algorithms used and the fact that both software packages contains over 1 million lines of code, it is encouraging that the two solutions match so well.

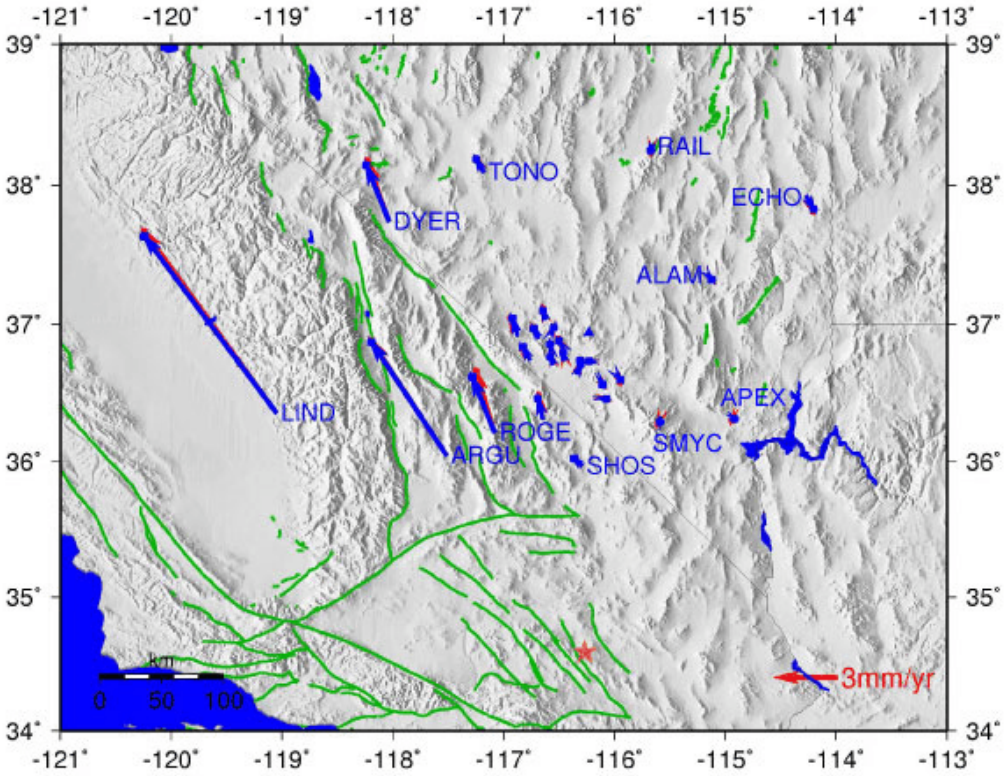

Figure 54. Comparison between GIPSY and GAMIT results (shown in red and blue respectively) for the regional Yucca Mountain network. Data was processed from 1st May 1999 until 31st October 2003. Integer ambiguities have been resolved and the effect of the 1999 Hector Mine earthquake removed. Velocities are shown as baselines relative to TIVA (small blue triangle), with North American plate rotation removed. Error ellipses are 95% confidence

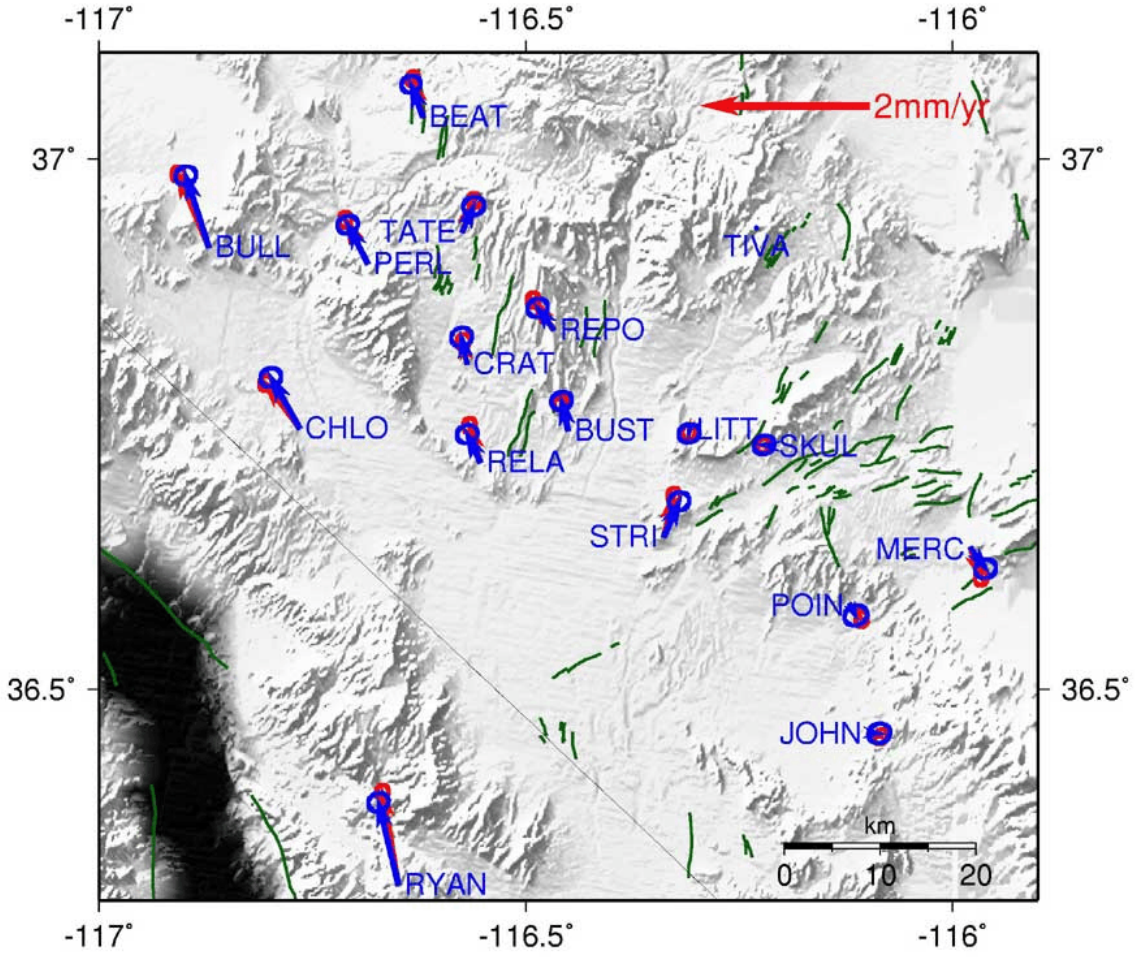

Figure 55. Comparison between GIPSY and GAMIT results (shown in red and blue respectively) for the local network. Data was processed from 1st May 1999 until 31st October 2003. Integer ambiguities have been resolved and the effect of the 1999 Hector Mine earthquake removed. Velocities are shown as baselines relative to TIVA, with North American plate rotation removed. Error ellipses are 95% confidence.

3.3 Horizontal velocity results

The most recent velocity results for the Yucca Mountain network are given in Table 4. These results are for data processed from 16th January 2000 to 30th June 2004 and are plotted as relative velocities to station TIVA. All steps described in Chapter 2

were carried out to obtain these results (including rotation into a North American reference frame), but no offsets were removed (since all known offsets occurred in 1999). These results are illustrated as vectors in Figures 56 - 61. They are plotted relative to TIVA (Figures 56 and 59), ECHO (Figures 57 and 60) and APEX (Figures 58 and 61) for viewing purposes.

Velocity estimates at the local Yucca Mountain stations have a relatively smooth signal across the network, trending northwest and increasing in magnitude from east to west (Figure 59). The magnitude of the velocity contrast across the local network, from TIVA to BULL, is 0.95 ± 0.04 mm/yr. When plotted relative to station ECHO (Figure 60), the orientation of most local velocity vectors range between N17^{o}W and N20^{o}W. The orientations for stations TATE and STRI, however, are N6^{o}W and N4^{o}W respectively. The orientations of velocity vectors for stations POIN, MERC and JOHN are also anomalous compared to the other local stations. Relative to station ECHO, these are N2^{o}W, N10^{o}W and N6^{o}W. One possible explanation for the anomalous behavior of POIN, MERC and JOHN is postseismic deformation from the 1999 Hector Mine earthquake, since these stations were close to the earthquake and had larger offsets than the other local stations (Section 2.10), or postseismic deformation from the 1992/2002 Little Skull Mountain earthquakes. However, there is no clear evidence of postseismic relaxation in their time series (Figures 64 and 65).

The ECSZ stations (LIND, ARGU, ROGE, RYAN and SHOS) have velocities that increase in magnitude from east to west. The magnitude of the velocity contrast

across the ECSZ, from RYAN to LIND, is 10.6 ± 0.04 mm/yr. The orientation of the velocity vectors swings round from north-northwest (e.g. RYAN, at N13^{o}W) to northwest (e.g. LIND, at N35^{o}W) with increasing proximity to the plate boundary.

Station DYER, located just east of the FLV fault system, has a larger velocity estimate than station RYAN, which is located at a similar distance from the DV-FC fault system to the south, hinting at the possible importance of the FLV fault system. Station TONO, located a distance into the Basin and Range, also shows northwest oriented right-lateral shear. Stations RAIL, ECHO and ALAM, further into the central Basin and Range, have very small velocities; the magnitude of the difference in velocity between ALAM and ECHO is 0.53 ± 0.04 mm/yr.

The baseline time series (Figures 62 - 65) show little evidence of periodic signals. Velocity trends are clear, even for the local Yucca Mountain stations.

Station	East vel (mm/yr)	North vel (mm/yr)	East σ (mm/yr)	North σ (mm/yr)
ALAM	0.16	-0.28	0.03	0.03
APEX	0.01	-0.18	0.03	0.03
ARGU	-3.89	6.04	0.03	0.03
BEAT	-0.14	0.46	0.03	0.03
BULL	-0.36	0.87	0.03	0.03
BUST	-0.13	0.30	0.03	0.03
CHLO	-0.29	0.71	0.03	0.03
CRAT	-0.07	0.30	0.03	0.03
DYER	-1.18	3.04	0.03	0.03
ECHO	0.25	-0.81	0.03	0.03
JOHN	0.16	0.00	0.03	0.03
LIND	-6.93	9.44	0.03	0.03
LITT	0.00	0.00	0.00	0.00
MERC	0.14	-0.25	0.03	0.03
PERL	-0.27	0.55	0.03	0.03
POIN	0.23	-0.09	0.03	0.03
RAIL	-0.07	-0.38	0.03	0.03
RELA	-0.12	0.43	0.03	0.03
REPO	-0.20	0.38	0.03	0.03
ROGE	-1.04	2.98	0.03	0.03
RYAN	-0.20	1.10	0.03	0.03
SHOS	-0.40	0.51	0.03	0.03
SKUL	-0.07	0.05	0.03	0.03
SMYC	-0.13	-0.31	0.03	0.03
STRI	0.15	0.48	0.03	0.03
TATE	0.13	0.35	0.03	0.03
TIVA	-0.03	-0.02	0.03	0.03
TONO	-0.30	0.55	0.03	0.03

Table 4. GIPSY horizontal baseline velocities, relative to LITT.

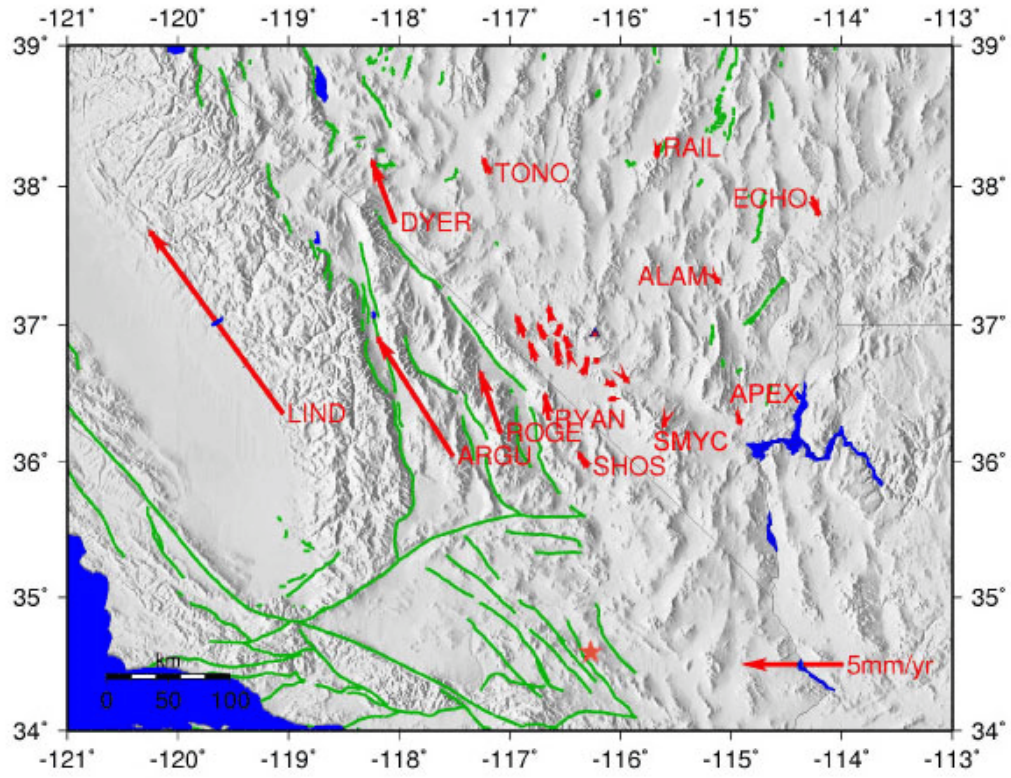

Figure 56. Horizontal baseline velocities for regional Yucca Mountain stations, plotted relative to station TIVA (red triangle). Error ellipses are 95% confidence.

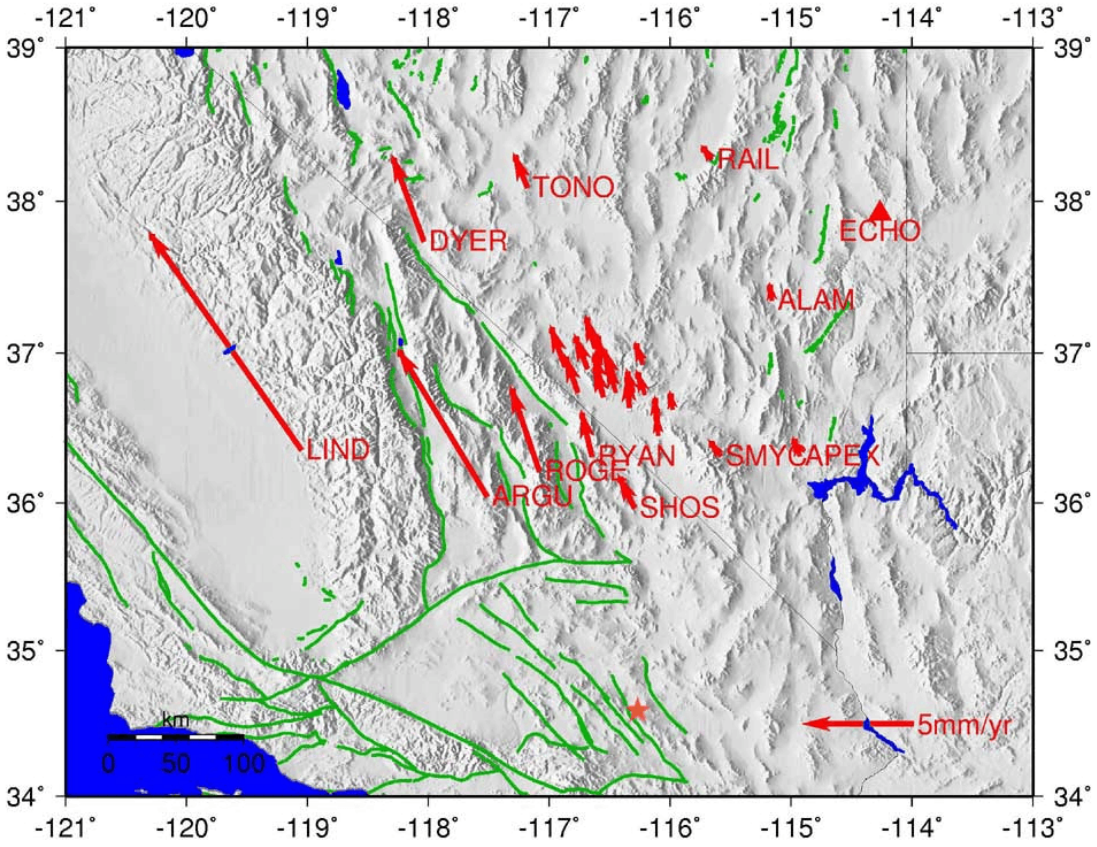

Figure 57. Horizontal baseline velocities for regional Yucca Mountain stations, plotted relative to station ECHO (red triangle). Error ellipses are 95% confidence.

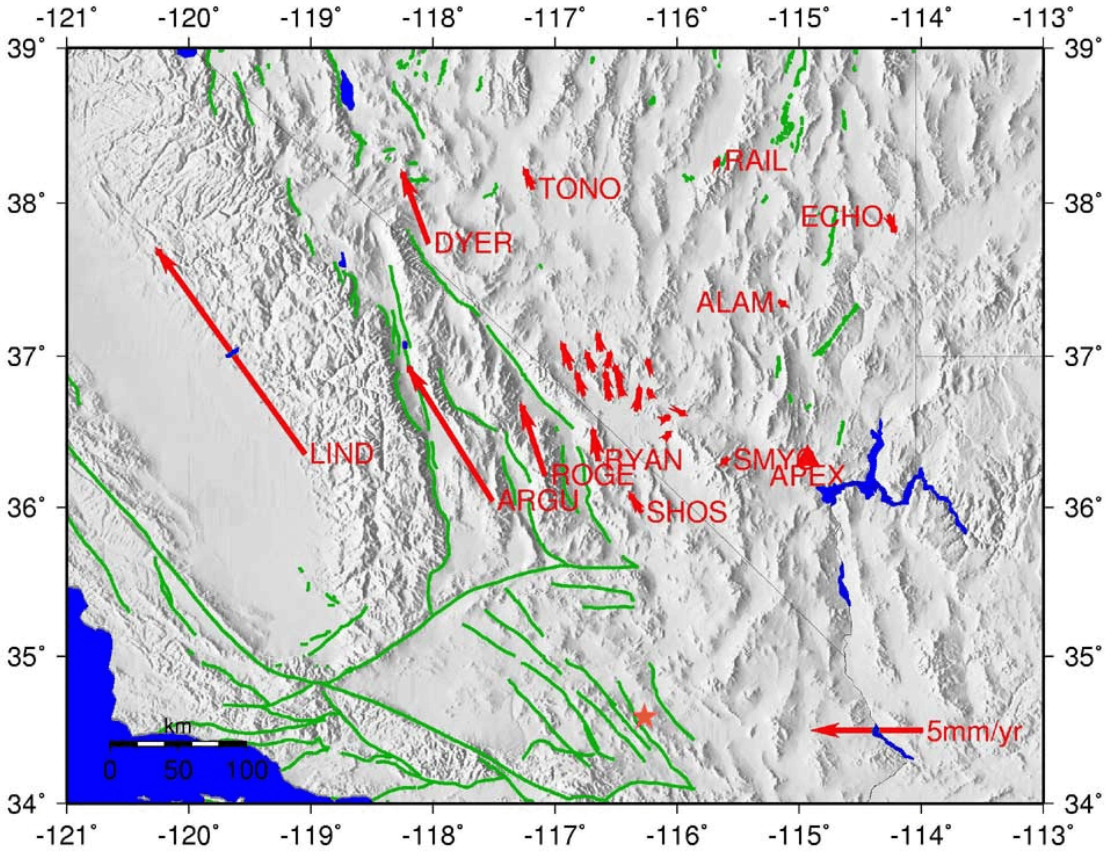

Figure 58. Horizontal baseline velocities for regional Yucca Mountain stations, plotted relative to station APEX (red triangle). Error ellipses are 95% confidence.

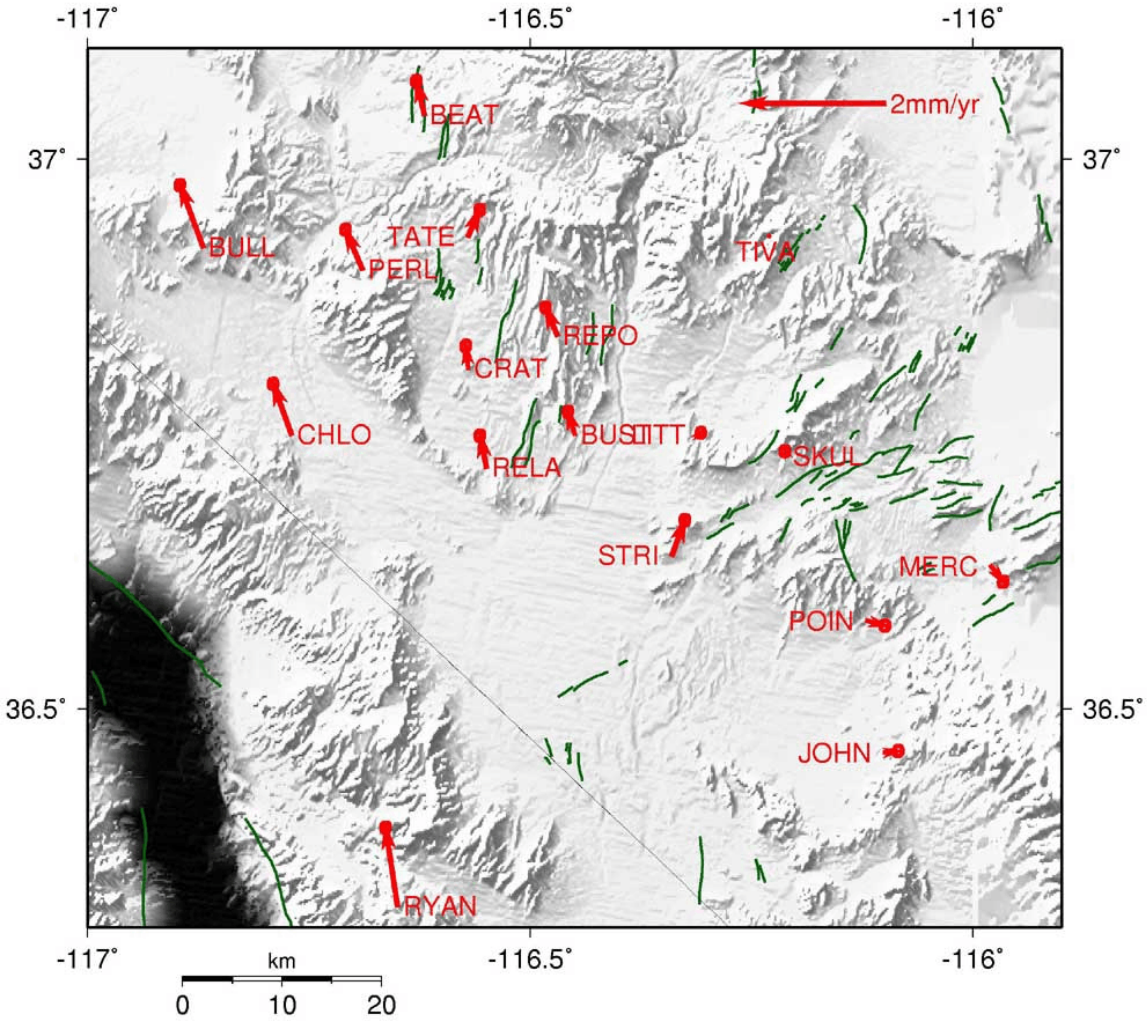

Figure 59. Horizontal baseline velocities for local Yucca Mountain stations, plotted relative to station TIVA. Error ellipses are 95% confidence.

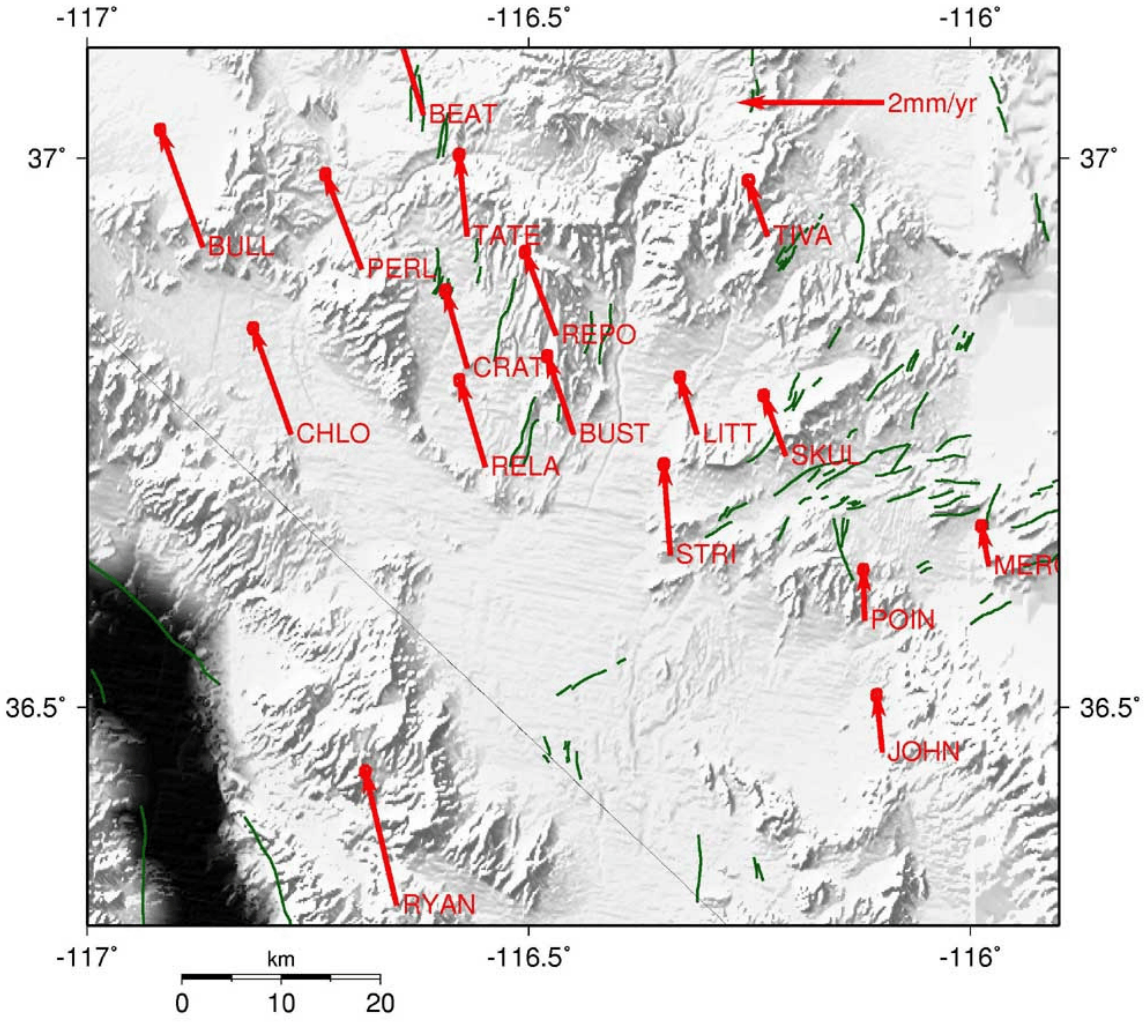

Figure 60. Horizontal baseline velocities for local Yucca Mountain stations, plotted relative to station ECHO (see Figure 57). Error ellipses are 95% confidence.

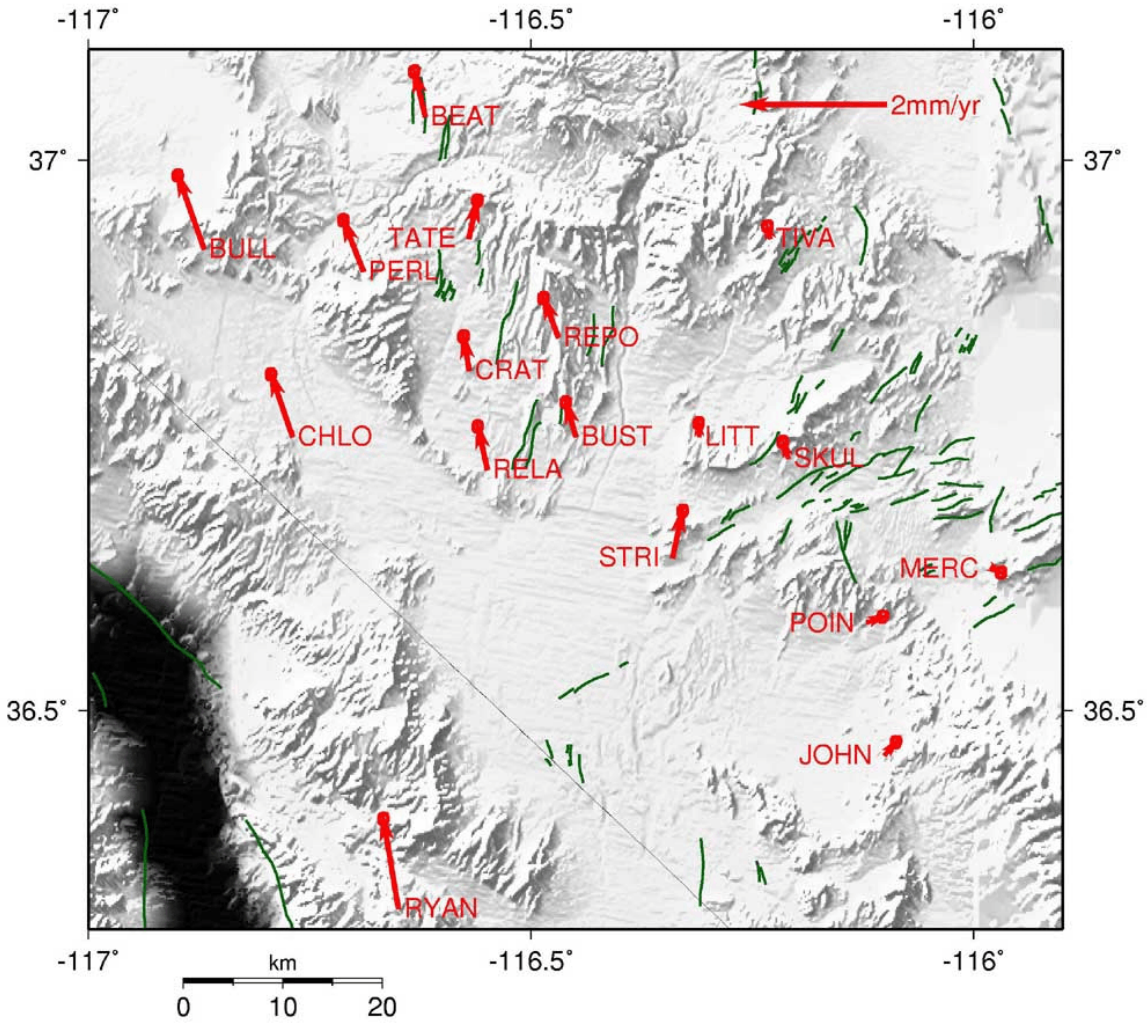

Figure 61. Horizontal baseline velocities for local Yucca Mountain stations, plotted relative to station APEX (see Figure 58). Error ellipses are 95% confidence.

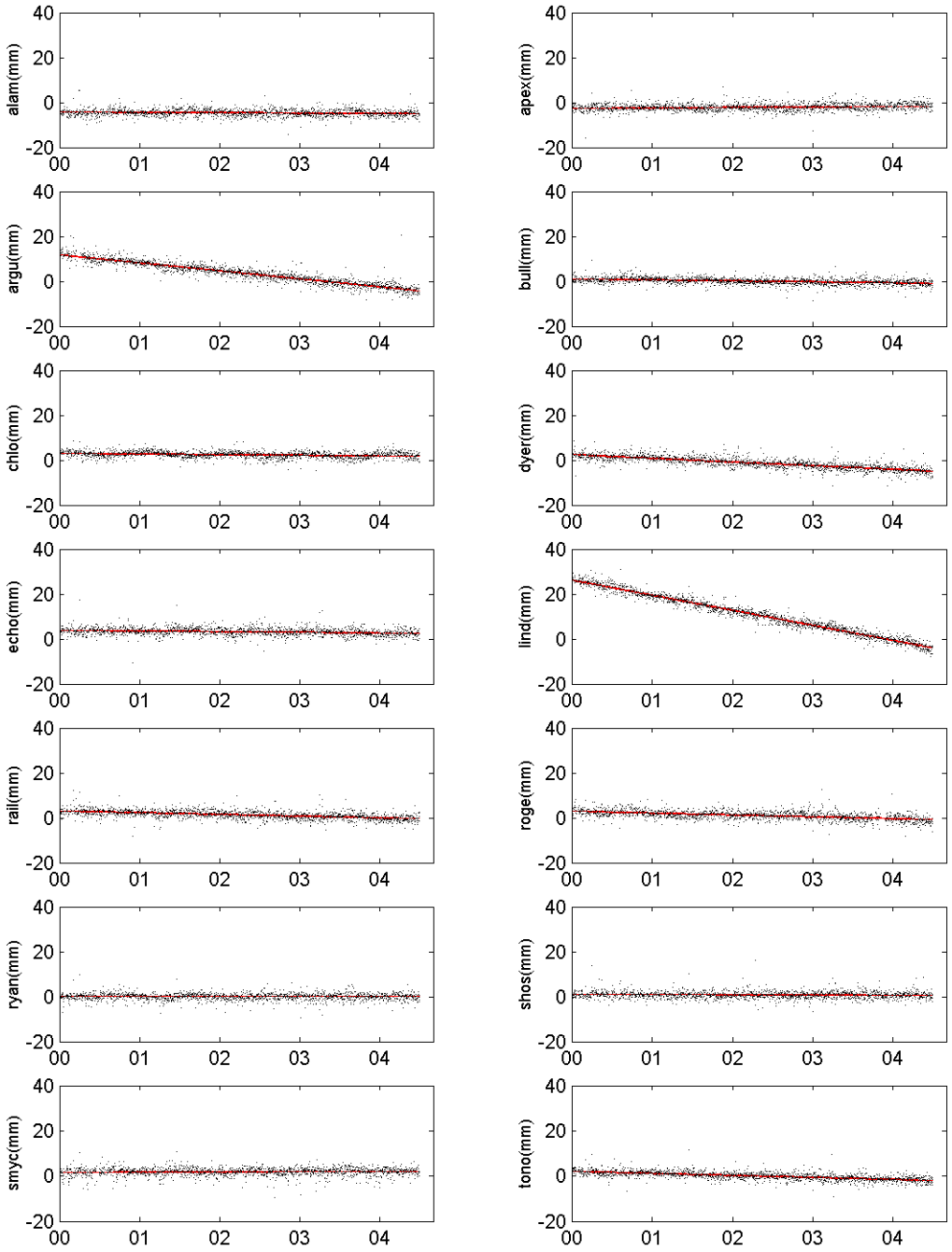

Figure 62. East baseline time series, for far-field stations, relative to LITT, with estimated velocity trend. Velocities are plotted relative to the mid-point of the time series.

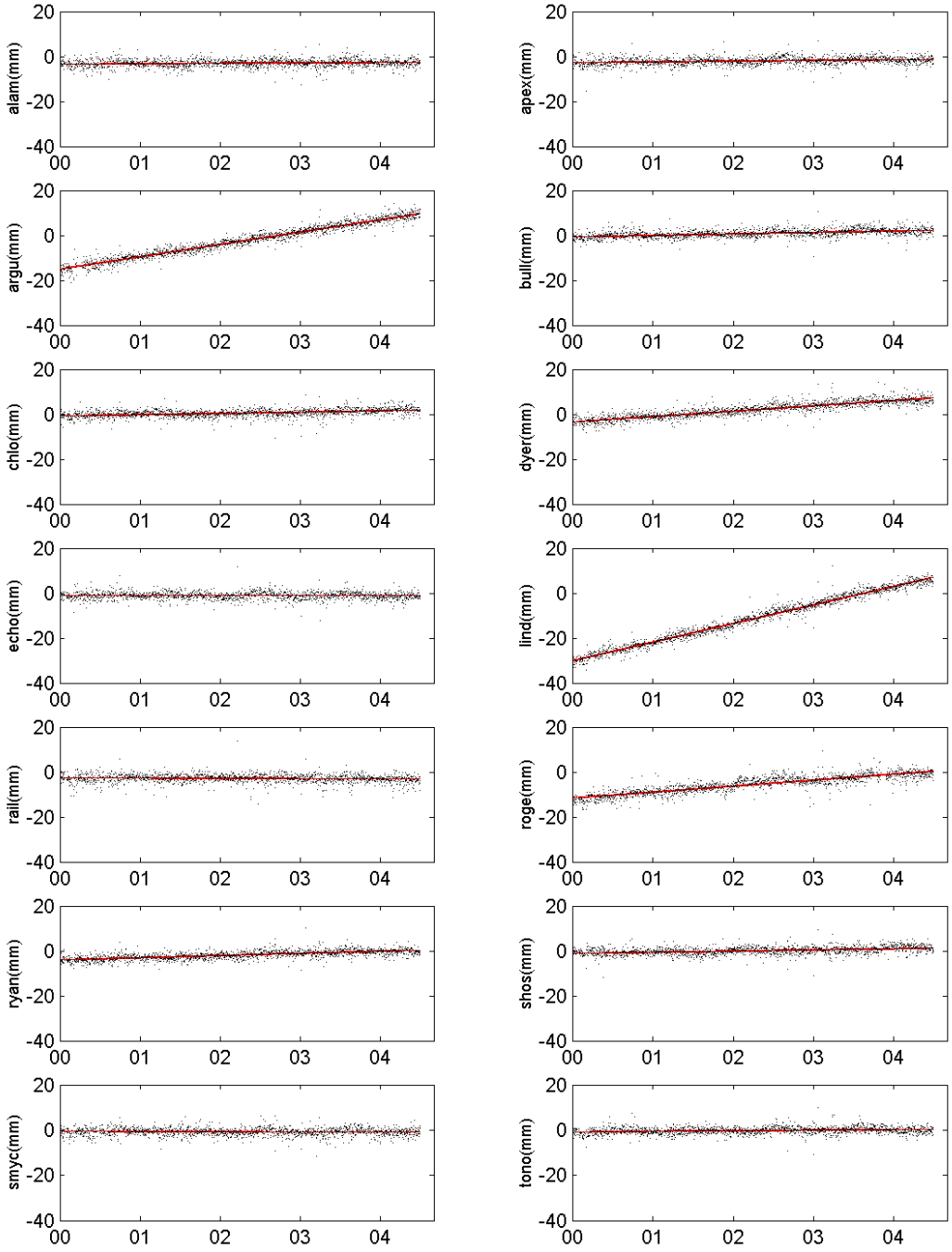

Figure 63. North baseline time series, for far-field stations, relative to LITT, with estimated velocity trend. Velocities are plotted relative to the mid-point of the time series.

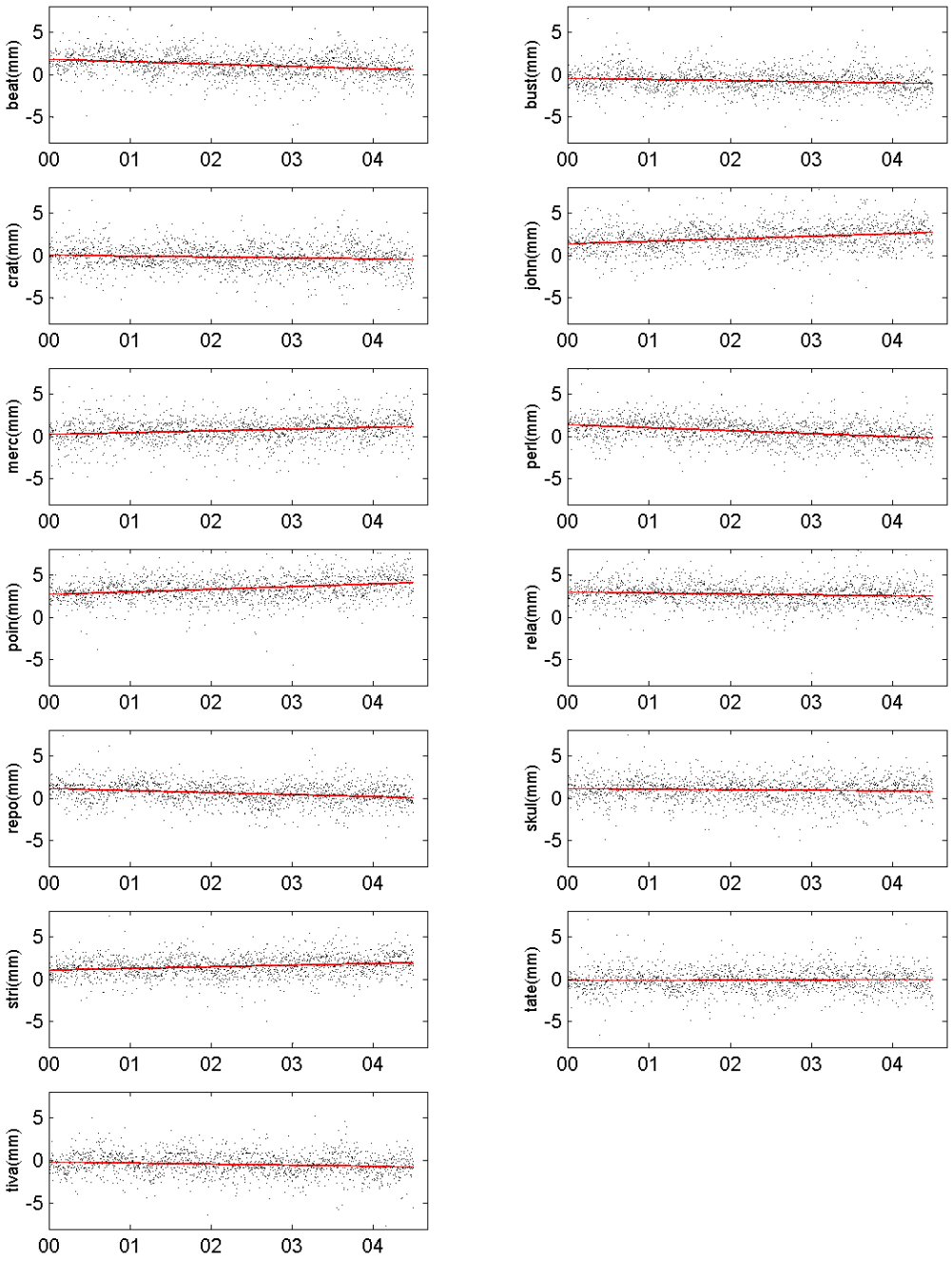

Figure 64. East baseline time series, for local stations, relative to LITT, with estimated velocity trend. Velocities are plotted relative to the mid-point of the time series.

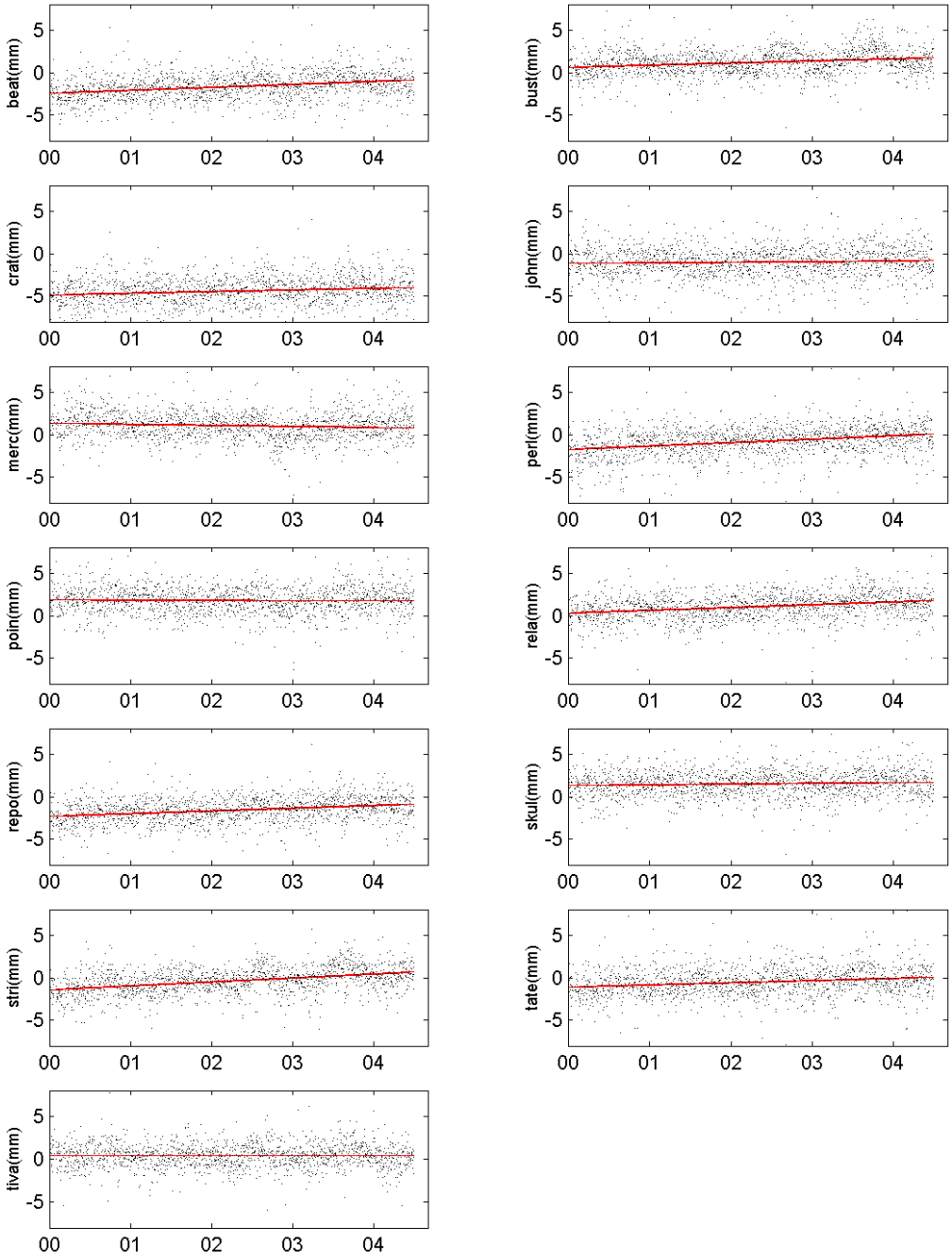

Figure 65. North baseline time series, for local stations, relative to LITT, with estimated velocity trend. Velocities are plotted relative to the mid-point of the time series.

3.4 Problems associated with estimating vertical GPS velocities

Errors in the atmospheric delay models (Section 2.13) are partly cancelled out with horizontal GPS positioning due to the satellite geometry. Put simply, a range measurement to the east that is estimated as too long will partly cancel out an incorrectly long range to the west. Since, however, there are no satellites visible beneath the receiver, this is not the case for vertical positions. Atmospheric delay errors are therefore much more influential in vertical GPS positioning.

Another problem with vertical positioning in GPS is the effect of periodic signals (Section 2.15). Most periodic signals are vertical in nature, so again they will have a greater effect on vertical GPS position than horizontal.

Perhaps the greatest problem in determining vertical velocities with GPS are inconsistencies in reference frame. Blewitt (2003) outlines the problems associated with achieving self-consistency in reference frames. Reference frames are affected by global scale, degree-one deformations and displacements of the geocenter, and it is difficult to remove their effects since the problem is circular.

Finally, Section 2.11 illustrated the results of hardware changes in the network. Particularly, radome substitutions will change the phase center of the GPS antenna, and changes within the Yucca Mountain network resulted in clear offsets in the vertical time series. These results, however, no longer include the effects of radome changes, as data

was not used from the period containing radome offsets.

3.5 Vertical velocity results

Vertical velocity estimates for local Yucca Mountain stations are given in Table 4. They are calculated relative to mean vertical velocity for all stations < 55 km from station LITT. Taking the hypothesis that vertical deformation across the local Yucca Mountain network is likely to be minimal, we see that the GPS results are encouragingly clustered about zero (Figure 66). Vertical velocity estimates for the local Yucca Mountain network range from -0.6 ± 0.1 mm/yr to 0.2 ± 0.1 mm/yr, with an RMS about zero of 0.3 mm/yr.

Far-field stations have a slightly greater spread of vertical velocity estimates than the local stations, ranging from -0.9 ± 0.1 mm/yr to 1.2 ± 0.1 mm/yr, but are still clustered about zero (Figure 66). The RMS of all vertical velocities about zero is 0.5 mm/yr.

Examination of the time series (Figure 67) confirms that vertical velocities for the local Yucca Mountain stations are negligible. Several of the far-field stations, however, show possible trends in their time series (Figure 68). The most visible trend in the time series is for station APEX. The vertical velocity for this station is also higher, showing up in Figure 66 as the only velocity in the network above 1 mm/yr, at 1.2 ± 0.1 mm/yr. It is difficult to tell at this stage, however, whether vertical trends are real velocities or a

reference frame feature, particularly since there is no clear pattern when the vertical results are plotted as vectors (Figures 69-72); this will be an exciting area of research over the coming years. Vectors have been plotted relative to both TIVA (Figures 69 and 70) and ECHO (Figures 71 and 72) for viewing purposes. We do not see a particularly anomalous vertical velocity at station ARGU (-0.8 ± 0.1 mm/yr), despite its close proximity to the Coso volcanic field (Section 1.4).

	Baseline length (km)	Vertical velocity (mm/yr)	Vertical error (mm/yr)
LITT	0.00	-0.21	0.12
SKUL	8.89	-0.57	0.12
STRI	11.54	-0.03	0.12
BUST	12.75	0.17	0.12
REPO	17.73	-0.30	0.12
TIVA	22.14	0.15	0.12
RELA	22.24	-0.17	0.12
CRAT	24.29	-0.09	0.12
POIN	24.98	0.05	0.12
TATE	31.44	-0.21	0.12
MERC	32.01	0.09	0.12
JOHN	36.95	-0.19	0.12
PERL	37.92	0.06	0.12
CHLO	40.85	-0.14	0.12
BEAT	42.94	-0.60	0.12
BULL	53.77	-0.28	0.12
RYAN	56.66	-0.39	0.12
SMYC	80.06	0.46	0.12
SHOS	85.96	0.36	0.12
ROGE	91.06	-0.58	0.12
ALAM	122.79	0.33	0.12
APEX	132.06	1.21	0.12
ARGU	133.51	-0.80	0.12
TONO	168.87	-0.89	0.12
RAIL	179.59	-0.77	0.12
DYER	189.32	-0.16	0.12
ECHO	222.89	0.26	0.12
LIND	249.87	0.29	0.12

Table 5. Vertical velocity estimates, relative to mean vertical velocity of the local Yucca Mountain stations (all stations < 55 km from station LITT). Baselines are to station LITT. Errors are 1σ.

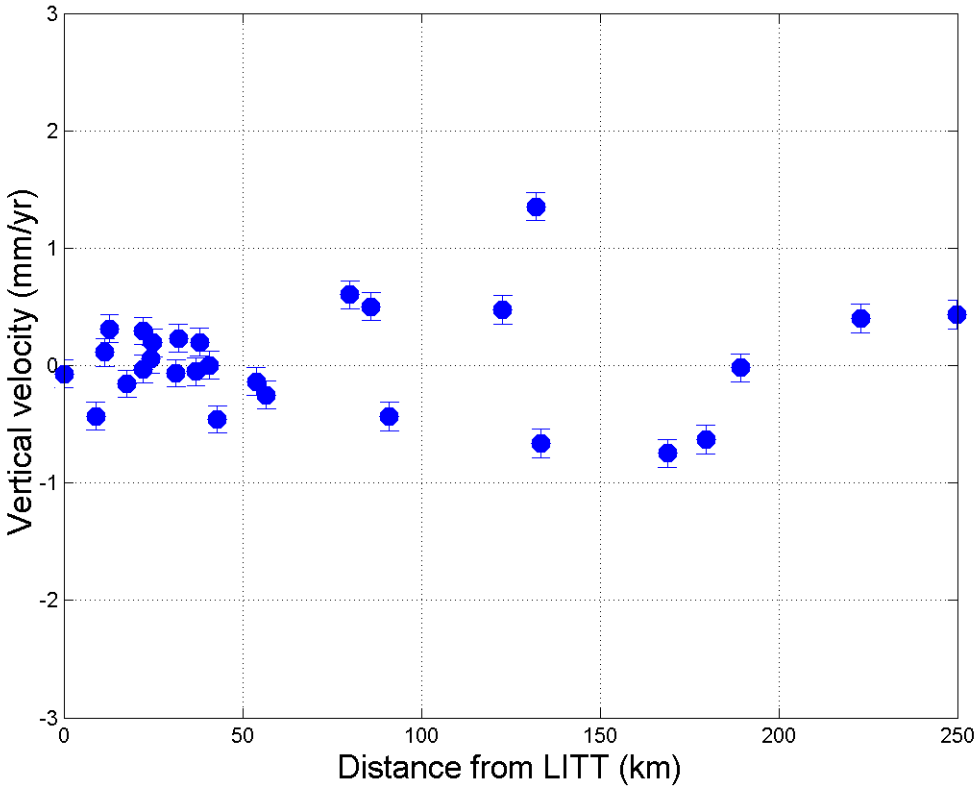

Figure 66. Vertical velocity estimates, relative to the mean velocity of the Yucca Mountain local stations. Error bars are 1σ.

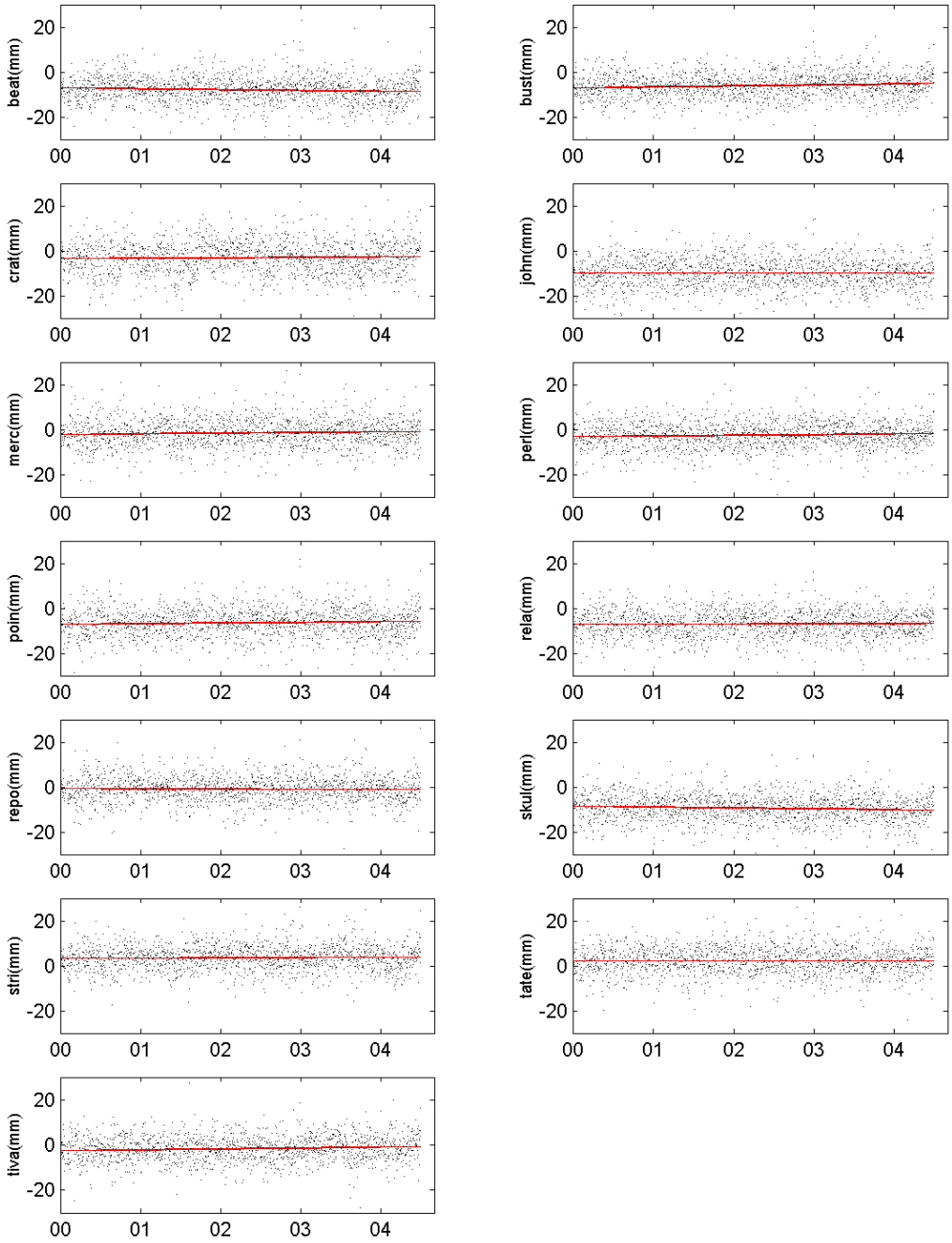

Figure 67. Vertical baseline time series, relative to station LITT, for local Yucca Mountain stations. Positions are plotted relative to the mid-point of the time series.

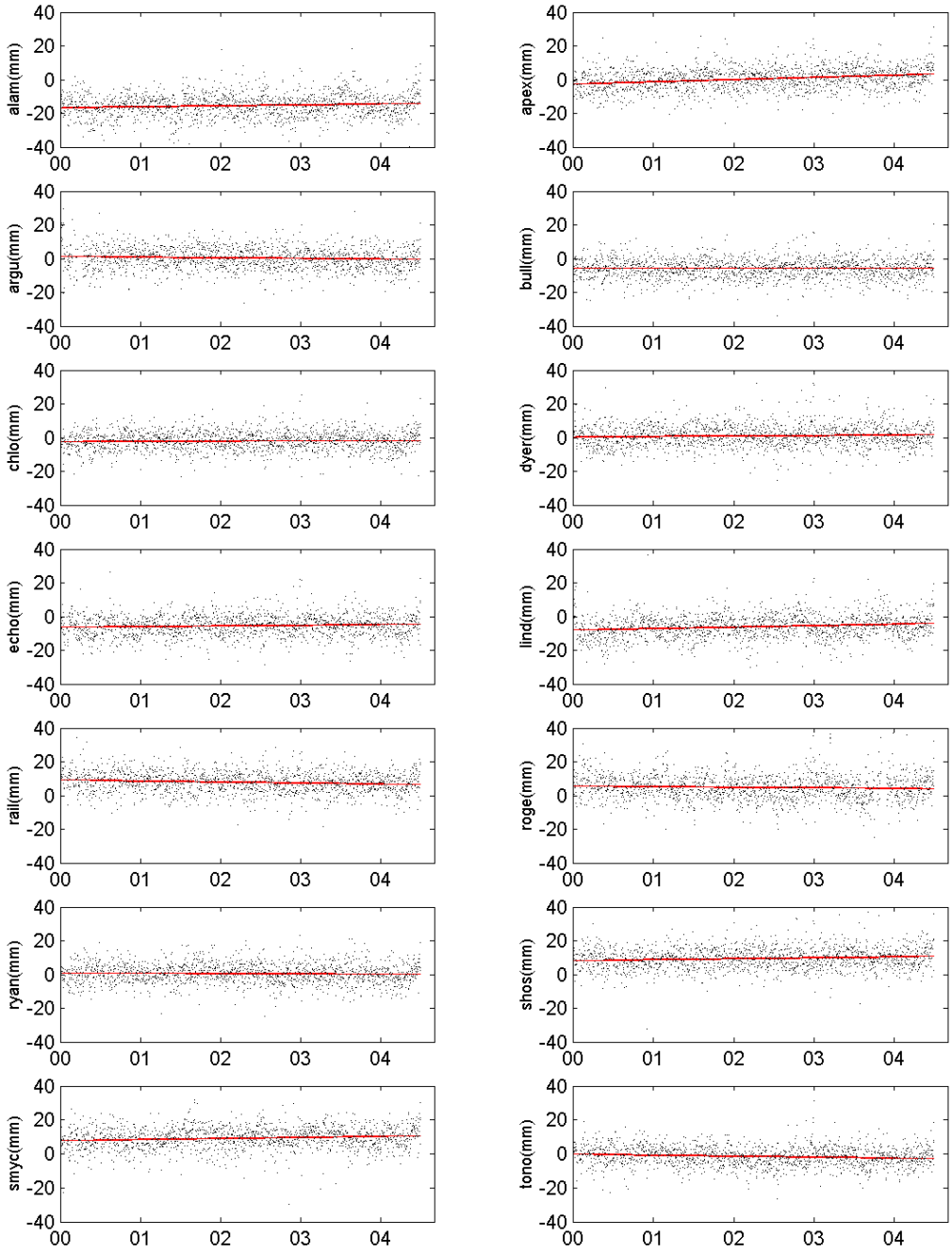

Figure 68. Vertical baseline time series, relative to station LITT, for far-field Yucca Mountain stations. Positions are plotted relative to the mid-point of the time series.

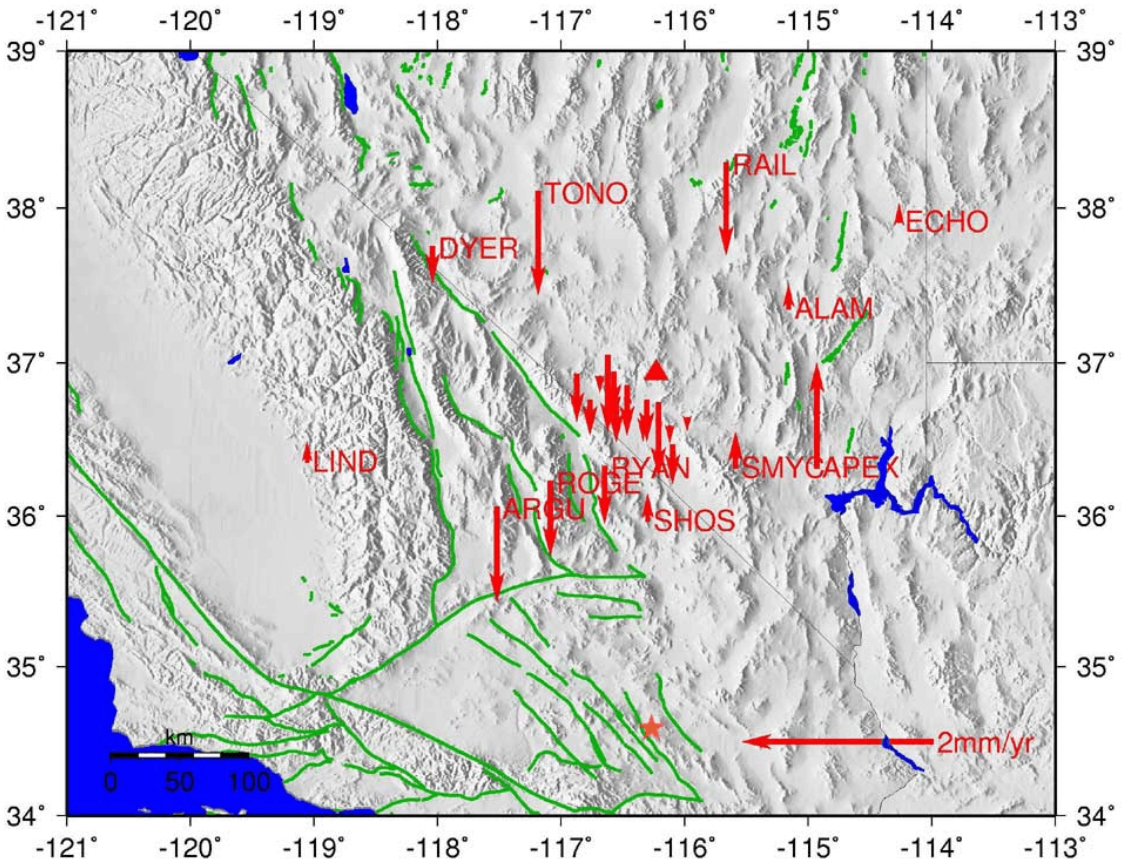

Figure 69. Vertical velocity estimates for the regional network. Velocities were calculated relative to mean vertical velocity for the local Yucca Mountain stations, then these were plotted relative to station TIVA (red triangle). Note the use of a larger scale than for the horizontal velocity plots. Northward pointing arrows indicate uplift relative to the Yucca Mountain stations and southward pointing arrows indicate subsidence relative to the Yucca Mountain stations.

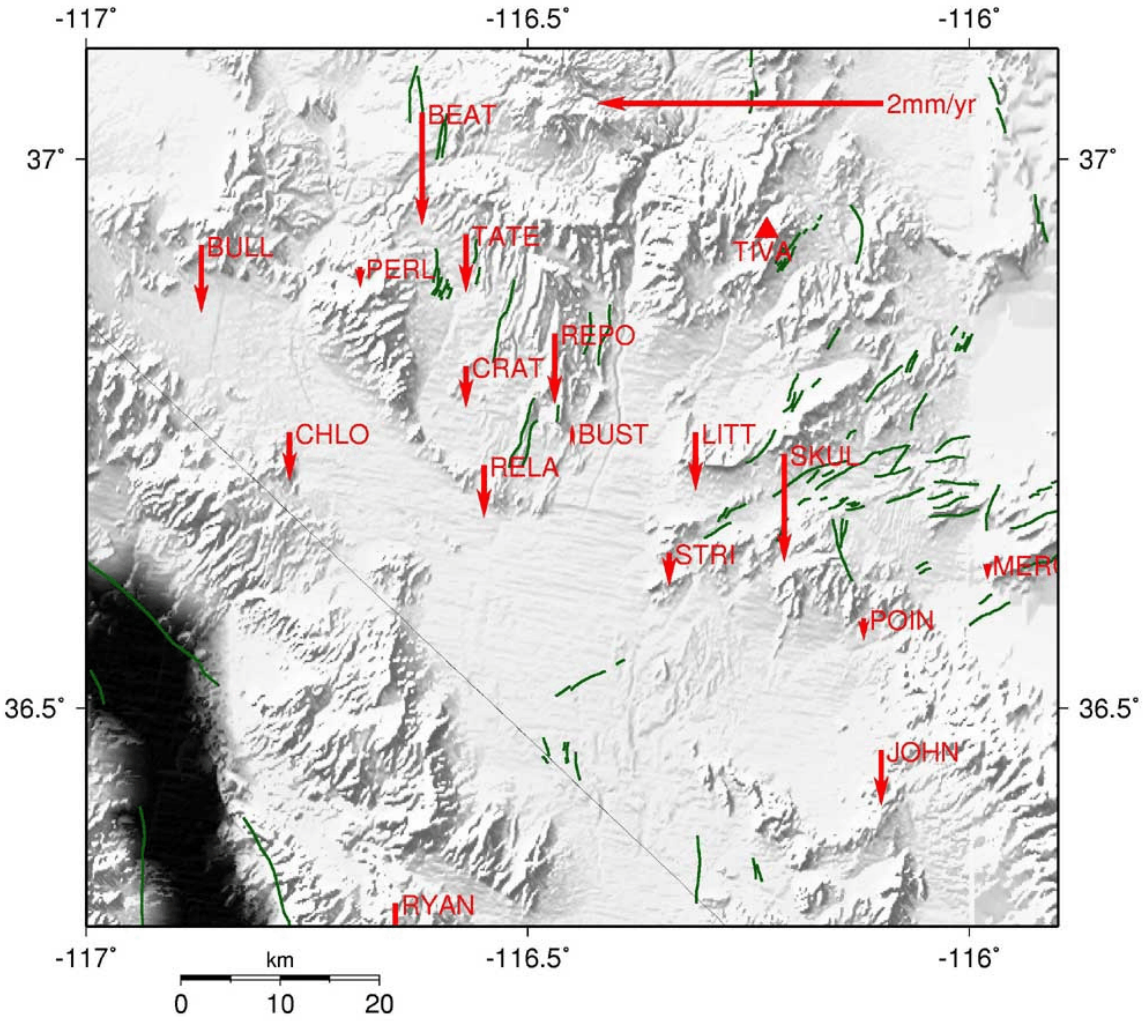

Figure 70. Vertical velocity estimates for the local network. Velocities were calculated relative to mean vertical velocity for the local Yucca Mountain stations, then these were plotted relative to station TIVA (red triangle).

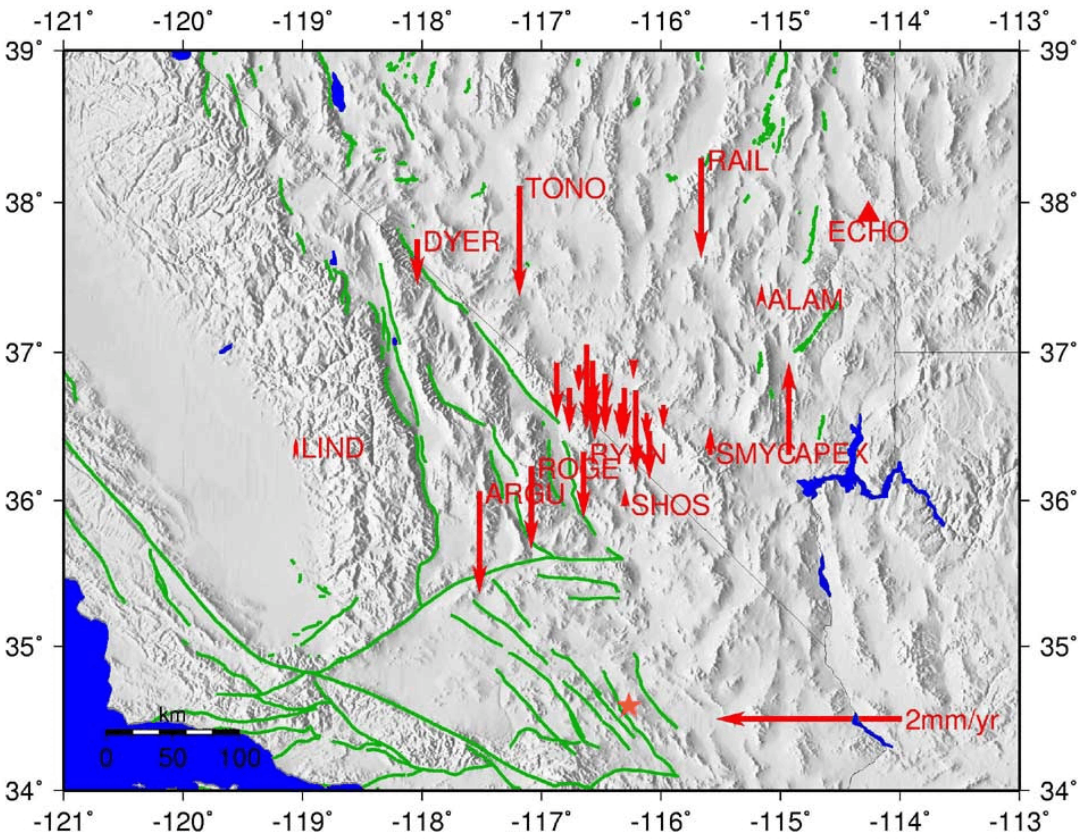

Figure 71. Vertical velocity estimates for the regional network. Velocities were calculated relative to mean vertical velocity for the local Yucca Mountain stations, then these were plotted relative to station ECHO (red triangle).

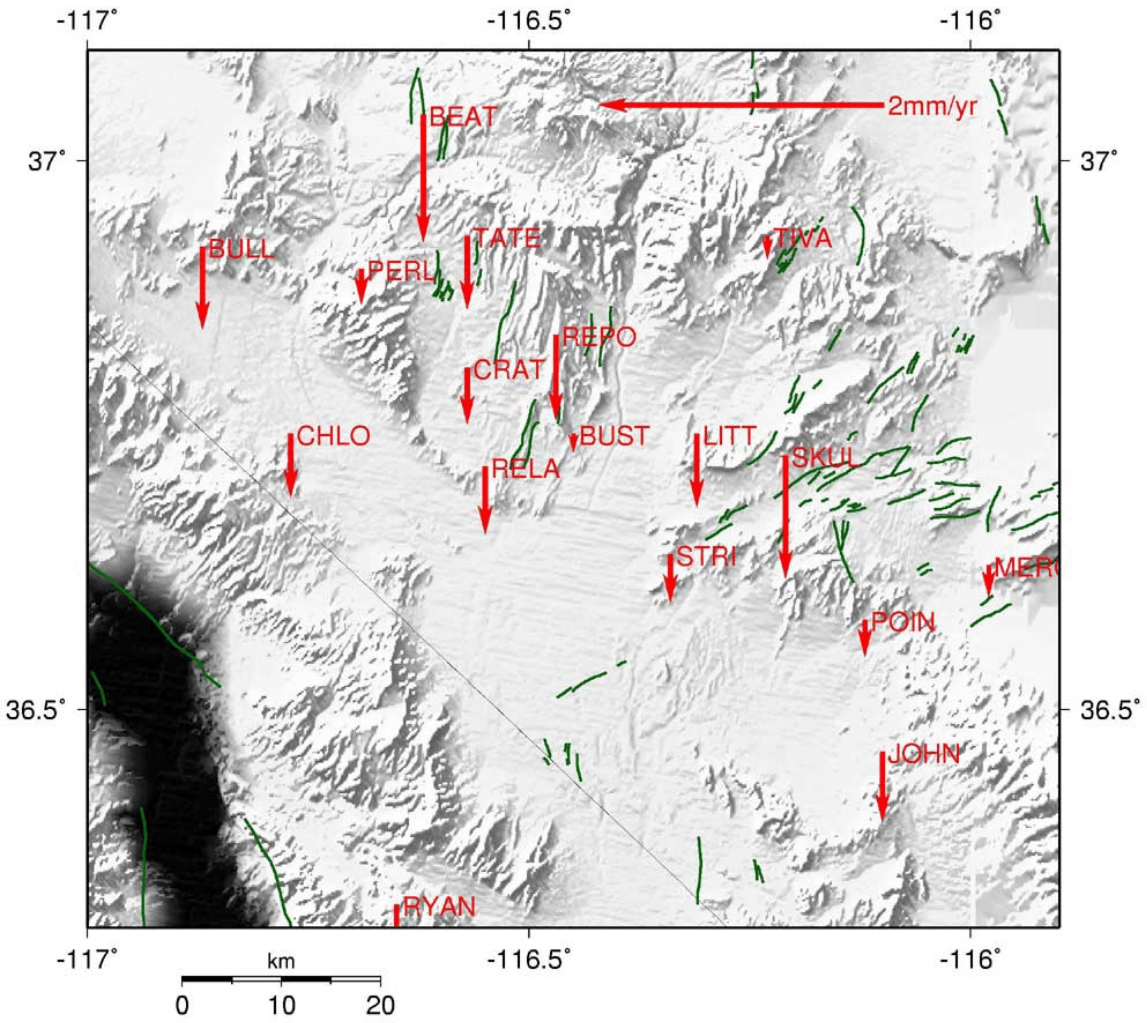

Figure 72. Vertical velocity estimates for the regional network. Velocities were calculated relative to mean vertical velocity for the local Yucca Mountain stations, then these were plotted relative to station ECHO (see Figure 71).

3.6 Error analysis

All velocity estimates in this dissertation are quoted with one standard deviation formal errors. Plots show a 95% confidence error ellipse, which is ~2.45 times the standard deviation. Both error bars and error ellipses are based on the formal errors output by the GIPSY software. Formal errors are calculated by propagating assumed

errors in the original observations through to the estimated station coordinates and velocities (Larson and Agnew, 1991). The assumed value for standard deviation of the pseudorange measurement was 1 m and the value for phase observation was 1 cm. These values are typical for most purposes and have become the convention for most published GIPSY results, but can be changed by the user during processing (Chapter 2). It is therefore easy to change the scale of the resulting formal errors, so even though the formal errors quoted in this dissertation look very small, they are somewhat arbitrary. The formal errors are based on the geometry of the satellites and receivers, and do not take into account any systematic errors in the data. Mean formal errors for the baseline velocity results are 0.026 mm/yr in the east component, 0.030 mm/yr in the north.

Table 5 gives the RMS values for the detrended baseline time series (Chapter 2, Figures 46-51). Mean time series RMS for the east component is 1.5 mm, for the north it is 1.7 mm and for the vertical it is 6.2 mm.

	RMS about mean (mm)		
Station	East	North	Vertical
ALAM	1.62	1.76	6.93
APEX	1.62	1.69	7.09
ARGU	1.73	1.91	6.68
BEAT	1.42	1.50	5.70
BULL	1.40	1.51	5.74
BUST	1.29	1.42	5.34
CHLO	1.42	1.62	5.64
CRAT	1.48	1.63	7.04
DYER	1.68	1.77	6.54
ECHO	1.75	1.77	6.26
JOHN	1.52	1.80	6.36
LIND	1.62	1.68	6.70
MERC	1.51	1.63	6.16
PERL	1.37	1.65	5.74
POIN	1.41	1.59	6.14
RAIL	1.72	2.01	6.35
RELA	1.31	1.42	5.78
REPO	1.34	1.46	5.65
ROGE	1.72	2.07	8.22
RYAN	1.58	1.51	5.96
SHOS	1.69	1.74	6.34
SKUL	1.48	1.53	5.80
SMYC	1.83	1.85	6.43
STRI	1.25	1.46	5.49
TATE	1.36	1.58	5.97
TIVA	1.37	1.40	5.83
TONO	1.50	1.71	5.82

Table 6. Baseline time series RMS values, calculated about the mean of the detrended time series.

3.7 Discussion of this chapter

A comparison of GIPSY and GAMIT results reveals that the two solutions are very similar. The RMS of residual velocity differences is 0.07 mm/yr for the east component and 0.11 mm/yr for the north. To obtain comparable results, the offsets from the 1999 Hector Mine earthquake and offsets from radome changes must be removed. North American plate rotation is also removed from both solutions.

Relative horizontal velocities within the local Yucca Mountain network are small,

on the order of < 1 mm/yr. There is a generally smooth signal across the local network, with total estimates of velocity increasing from east to west and a velocity contrast, from TIVA to BULL, of 0.95 ± 0.04 mm/yr. There is a distinct change in velocity, however, between stations to the east of the network and stations to the west. The change between higher and lower velocities occurs slightly to the east of Yucca Mountain.

Velocities increase rapidly across the ECSZ, with a 10.6 ± 0.04 mm/yr difference between the total velocity estimates of LIND and RYAN. The ECSZ velocity vectors tend increasingly towards the northwest with distance towards the plate boundary. Stations in the central Basin and Range have small relative velocities, with the difference between velocities at stations ALAM and ECHO having a magnitude of 0.53 ± 0.04 mm/yr. Although RAIL, ALAM and ECHO have small relative velocities, station TONO, the most westerly 'Basin and Range station' has a velocity vector that shows NW oriented right lateral shear, showing that the shear zone does extend to the east of the ECSZ to the north of Yucca Mountain.

Considering the difficulty associated with obtaining precise vertical velocities using GPS, the small scatter in vertical velocity estimates gives an indication of the high precision of results from the Yucca Mountain GPS network. The vertical results for the Yucca Mountain local network have an RMS scatter of 0.26 mm/yr about zero, and vertical results for all stations in the network have an RMS scatter of 0.45 mm/yr. It is possible that the regional time series are starting to show small vertical trends, but the velocities have no consistent spatial signal. It is possible that station APEX may be

uplifting relative to the Yucca Mountain stations.

4. Strain Rates

4.1 Introduction to this chapter

The campaign GPS survey carried out by Wernicke et al. (1998) between 1991 and 1997 estimated a N60-65^{o}W extensional strain rate of 50 ± 9 ns/yr (uniform across the 34 km network aperture). This rate was much higher than expected based on the Quaternary history of the area. Wernicke et al. (1998) estimated shear strain at Yucca Mountain due to the DV-FC fault system to be no more than ~ 10 ns/yr, based on a slip rate of 3-5 mm/yr on a fault 35 km from the network, so indicated that this high strain rate at Yucca Mountain could not be due to the ECSZ, but rather that Yucca Mountain was "experiencing an epoch of anomalously rapid strain accumulation."

Savage et al. (1994) estimated the strain rate, using trilateration surveys from 1983 to 1993, to be ε_{11} = 10 ± 20 ns/yr, ε_{12} = -2 ± 8 ns/yr, ε_{22} = -9 ± 21 ns/yr, ε_1 = 10 ± 20 ns/yr N87^{o}W ± 24^{o}, ε_2 = -9 ± 21 ns/yr N03^{o}E ± 21^{o}. The engineering shear rate is γ = 10 ± 16 ns/yr and dilitation Δ = 1 ± 37 ns/yr. They did not correct for the effects of the 1992 Little Skull Mountain earthquake, but eliminated the lines closest to the earthquake before calculating strain rates. These strain rates are not significantly different from zero.

Savage (1998) argued in a reply to Wernicke et al. (1998) that the strain rate measured by Wernicke et al. (1998) was incorrect, partly because the authors had not

included the effects of monument instability in their error budget and partly because they did not include the effects of the 2002 Little Skull Mountain earthquake in their calculations.

In response to the Wernicke et al. (1998) study, Savage et al. (1999) added an additional 5 years to their previous survey. Savage et al. (1999) give the result of combined Geodolite and campaign GPS surveys from 1983 to 1998. In this study they measured strain rates of $\varepsilon_1 = 2 \pm 12$ ns/yr N87^{o}W $\pm 12^o$ and $\varepsilon_2 = -22 \pm 13$ ns/yr N03^{o}E $\pm 12^o$, with $\gamma = 23 \pm 10$ ns/yr and $\Delta = -20 \pm 22$ ns/yr. For comparison with the Wernicke et al. (1998) strain rate, the N65^{o}W extension rate is -2 ± 12 ns/yr. Savage et al. (1999) note that only the engineering shear strain rate is significant at the 95% confidence level. This time, Savage et al. (1999) corrected for the effects of the 2002 Little Skull Mountain earthquake using a dislocation model. They again assumed that strain rate is uniform across the Yucca Mountain network.

Savage et al. (1999) state that "almost half' of the measured strain can be attributed to strain accumulation on the DV-FC and HM-PV fault systems. Their estimate of shear from these faults is based on calculations using the equation to model infinite length faults in an elastic half-space (Okada, 1985; Savage, 1983), with the DV-FC fault system at a distance of 50 km and the HM-PV fault system at a distance of 90 km, and fault slip rates of 5 ± 1 mm/yr for the DV-FC fault system and 2 ± 1 mm/yr for the HM-PV fault system. This gives an expected strain of 10-14 ns/yr, which is half of

the 23 ± 10 ns/yr they measure in total engineering shear, leaving a remainder of 9-13 ± 10 ns/yr, which again is not significantly different from zero.

Using 3 years of BARGEN data, Davis et al. (2003) estimated much smaller principal strain rates at Yucca Mountain. These were 7 ± 1 ns/yr at N64^{o} ± 2^{o}W and -10 ± 1 ns/yr at N26^{o} ± 2^{o}E (extension positive). Once again they assumed strain to be constant across the network. Using 3.75 years of the same data, Wernicke et al. (2004) estimated a strain rate of 20 ± 2 ns/yr, oriented at N20^{o}W (based on a velocity contrast of ~ 1.2 mm/yr across a 60 km aperture).

In this chapter I present strain rates for the Yucca Mountain network, calculated using the horizontal velocities discussed in Chapter 3. I compare these strain rates to those given in previous surveys of Yucca Mountain.

4.2 Solving for Cartesian strain rates using the GPS velocities

The 2D strain rate tensor equation for a single set of observations can be written as shown in Equation 19.

$$\begin{bmatrix} \Delta V_x \\ \Delta V_y \end{bmatrix} = \begin{bmatrix} \dot{\varepsilon}_{xx} & \dot{\varepsilon}_{xy} \\ \dot{\varepsilon}_{yx} & \dot{\varepsilon}_{yy} \end{bmatrix} \begin{bmatrix} \Delta X \\ \Delta Y \end{bmatrix} \qquad [19]$$

where Δ_{vx} and Δ_{vy} are relative velocities between two stations, ε_{xx}, ε_{xy}, ε_{yx} and ε_{yy} are Cartesian strain components and ΔX and ΔY are relative position between the two

stations. This equation assumes that strain is a constant, so ΔX and ΔY must be sufficiently small. These Cartesian strain rate components are defined as shown in Figure 73.

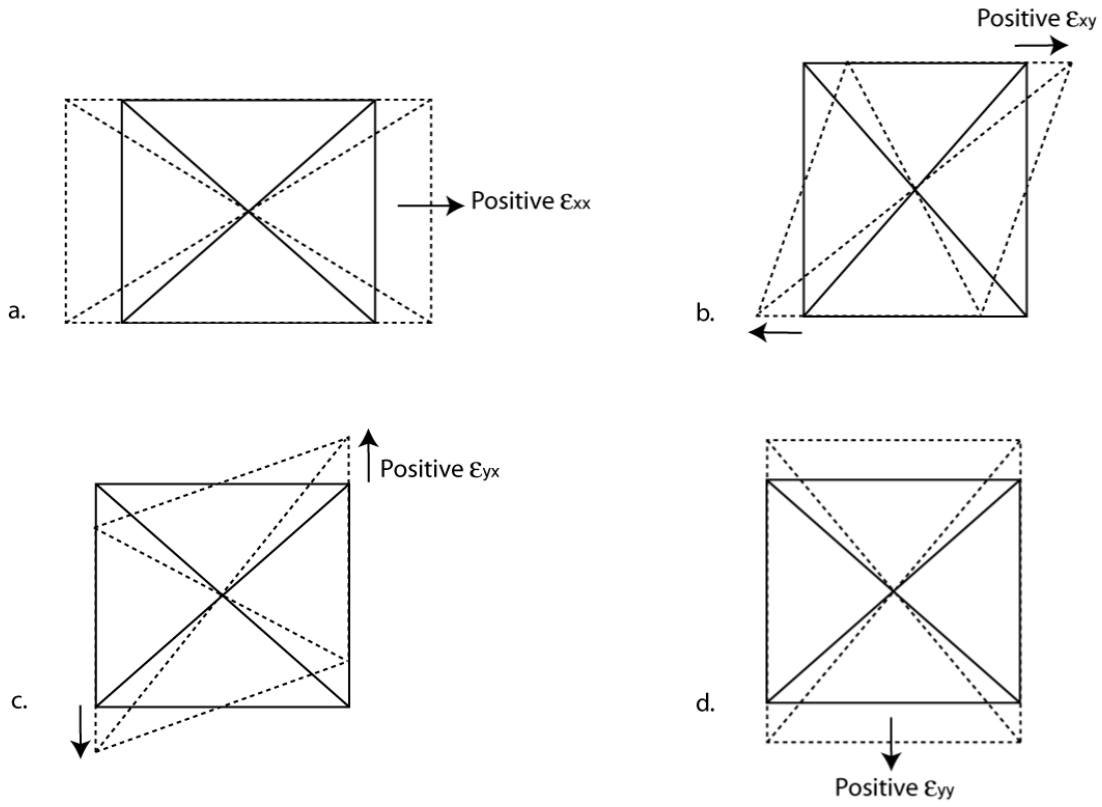

Figure 73. Description of Cartesian strain rates ε_{xx} (a), ε_{xy} (b), ε_{yx} (c) and ε_{yy} (d)

A weighted least squares inversion was used to invert for strain rates, with the horizontal GPS velocity estimates used as the input data matrix. Appendix I gives the full details of the inversion. GPS baseline lengths and velocities were calculated relative to a point at the centroid of the group of stations (i.e. the average position and velocity for the group of stations). For example, when calculating strain for all stations < 55 km

from Yucca Mountain, I took the average position and velocity of all stations < 55km from Yucca Mountain and then calculated relative position and velocity relative to this 'virtual' station. In the case of this group, the 'virtual' station was ~8 km to the southwest of station REPO.

4.3 Calculation of engineering strain rate components

Having obtained the Cartesian strain rate tensor, it is possible to obtain the engineering strain rate components, which give a more easily interpretable set of values for strain rate (e.g. Prescott et al., 1979). The engineering strain rate components are defined as follows.

The dilitation rate, Δ, is calculated using Equation 20. It describes expansion or contraction of the area (Figure 74). Expansion is reckoned positive.

$$\Delta = \varepsilon_{EE} + \varepsilon_{NN} \qquad [20]$$

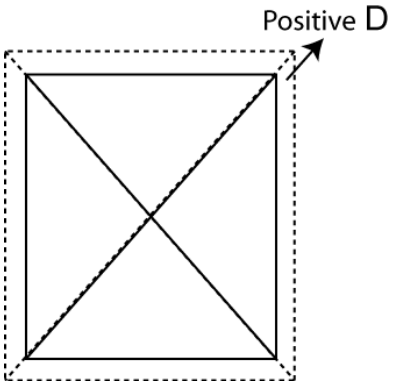

Figure 74. Dilitation, D

Ω is the rotation rate (Figure 75). Counter-clockwise rotation is positive. Ω is calculated using Equation 21.

$$\Omega = \frac{1}{2}\left(\varepsilon_{NE} - \varepsilon_{EN}\right) \qquad [21]$$

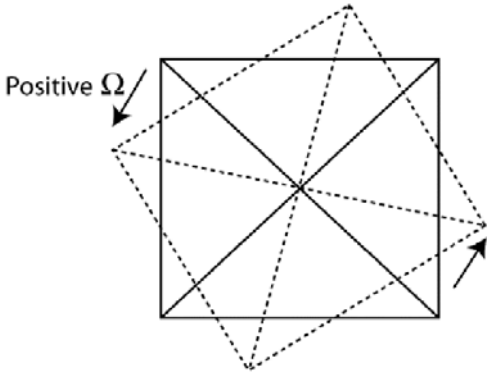

Figure 75. Rotation, Ω

Engineering shear rate 1, γ_1, describes extension and compression along the N-S and E-W axes (Figure 76). The angle between NW and NE lines increases with positive

γ_1, but the angle between N-S and E-W lines stays the same. γ_1 therefore measures right-lateral shear over a N45^{o}W-trending vertical fault, or left-lateral shear across a N45^{o}E-trending vertical fault (Savage, 1983). γ_1 is calculated using Equation 22.

$$\gamma_1 = \varepsilon_{EE} - \varepsilon_{NN} \quad [22]$$

Engineering shear rate 2, γ_2, describes extension and compression along the NW and NE axes (Figure 77). Compression along the NW axis means extension along the NE axis (positive) and extension along the NW axis means compression along the NE axis (negative). Positive γ_2 leads to a decrease in the angle between N-S and E-W lines, but no change in the angle between NW and NE lines. γ_2 therefore measures right-lateral shear across an E-W trending vertical fault, or left-lateral shear across a N-S trending vertical fault (Savage, 1983). γ_2 is calculated using Equation 23.

$$\gamma_2 = \varepsilon_{EN} + \varepsilon_{NE} \quad [23]$$

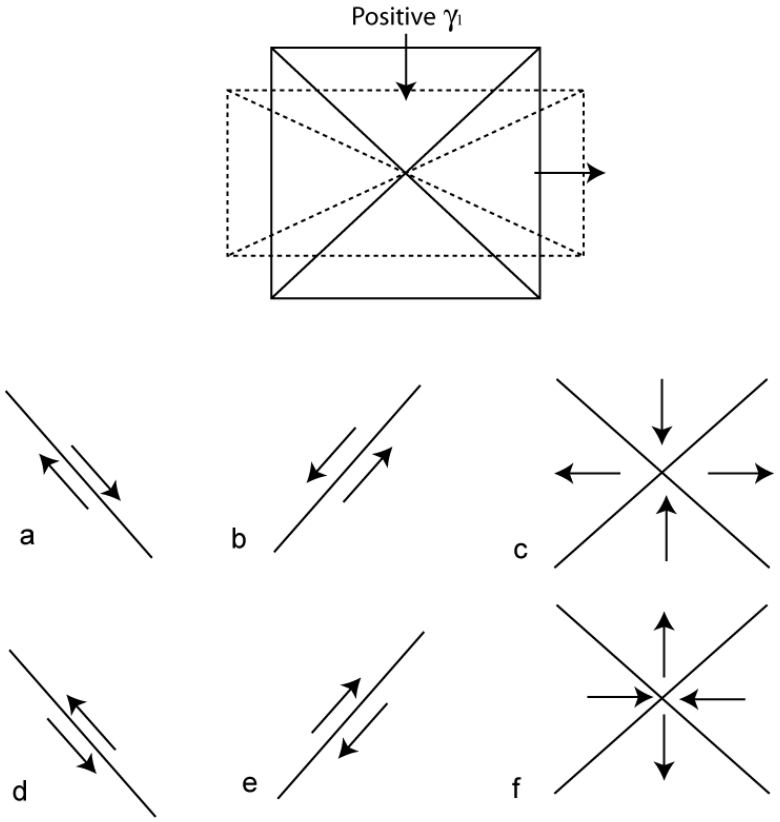

Figure 76. Engineering shear rate 1. (a/b) Positive simple shear, (c) Positive pure shear, (d/e) Negative simple shear, (f) Negative pure shear

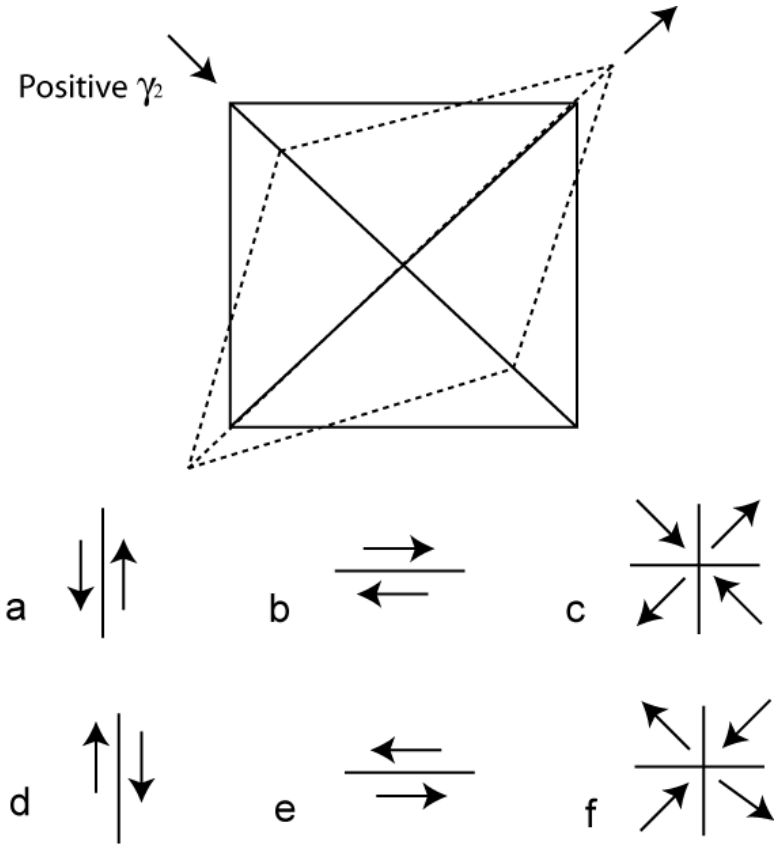

Figure 77. Engineering shear rate 2. (a/b) Positive simple shear, (c) Positive pure shear, (d/e) Negative simple shear, (f) Negative pure shear

Maximum shear strain, $|\gamma|$, was calculated using Equation 24. This is the highest shear strain rate, oriented at 45^{o} to α, the azimuth of the principal strain rate (Equation 25).

$$|\gamma| = \sqrt{\gamma_1^2 + \gamma_2^2} \qquad [24]$$

$$\alpha = \frac{1}{2}\arctan\left(\frac{\gamma_2}{\gamma_1}\right) \qquad [25]$$

The angle of maximum extension, α, is measured positive anticlockwise from the

1-axis (E). The angle of maximum contraction is measured positive anticlockwise from the 2-axis (N). The orientation of maximum shear is half-way between the maximum compression and maximum extension axes (Figure 78). The problem is ambiguous; the axis of maximum shear will be right-lateral in one direction or left-lateral in the direction perpendicular to this.

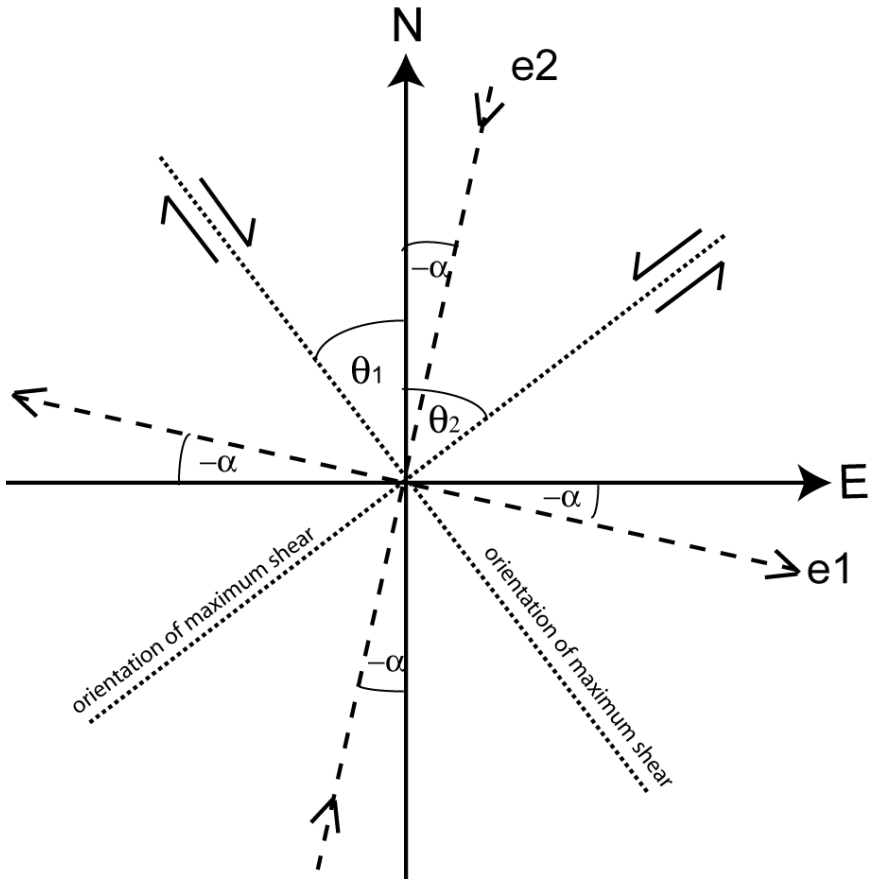

Figure 78. Interpretation of angle α

The least squares calculations output $\sigma\varepsilon_{EE}$, $\sigma\varepsilon_{NN}$, $\sigma\varepsilon_{EN}$ and $\sigma\varepsilon_{NE}$ in the covariance matrix. These errors were propagated through the engineering strain calculations, to

obtain σ_D, σ_Ω, $\sigma_{\gamma 1}$, $\sigma\gamma_2$, $\sigma_{|\gamma|}$ and σ_α, using the general formula for uncorrelated variables, given in Bevington, 1969. The formulae used to propagate the errors are given in Appendix J.

4.4 Comparison of GIPSY and GAMIT strain rates

Table 7 gives a comparison of strain rates estimated using the GIPSY and GAMIT results described in Chapter 3. The strain rates were calculated using the GPS results from all stations in the local Yucca Mountain network, using the procedure described in Sections 4.2 and 4.3. The strain rates all agree to within one standard deviation.

Using the same GAMIT results, from 1999 to 2003, Wernicke et al. (2004) estimated a shear strain magnitude of 20 ± 2 ns/yr. They calculated this rate using a linear regression of all N20^{o}W GPS velocity components for all stations in the local Yucca Mountain network, excluding station MERC. Their estimate agrees, within error, with the GAMIT value shown in Table 7. Our estimated orientation of maximum shear strain is a little more northerly than the estimate of Wernicke et al. (2004), at N16.1±2^{o}W for GIPSY and N16.7±3^{o}W for GAMIT.

	GIPSY	GAMIT
ε_{EE}	6.7 ± 0.4	5.9 ± 0.8
ε_{EN}	0.5 ± 0.6	-0.1 ± 1.1
ε_{NE}	-14.9 ± 0.6	-14.3 ± 0.7
ε_{NN}	-2.3 ± 0.8	-3.6 ± 1.0
Ω	-7.7 ± 0.4	-7.1 ± 0.6
D	4.4 ± 0.9	2.3 ± 1.2
γ_1	9.0 ± 0.9	9.5 ± 1.2
γ_2	-14.3 ± 0.6	-14.4 ± 0.7
$\lvert\gamma\rvert$	16.9 ± 0.7	17.2 ± 0.9
α (degs)	-28.9 ± 2.0	-28.3 ± 2.6

Table 7. Comparison of strain rates for GIPSY and GAMIT, for all stations < 55 km from station LITT. Strain rates are quoted in ns/yr. Errors are 1σ. Strain rates were calculated using relative velocities to a point at the centroid of each group of stations. Extension is reckoned positive. The solution was produced using data from May 1999 to October 2003.

4.5 GIPSY strain rate results

Table 8 gives a summary of strain rates for the local Yucca Mountain network. Group 1 contains all stations < 55 km from station LITT. Group 2 contains all stations < 55 km from LITT except CHLO and BULL, the closest local stations to the DV-FC fault system. Group 3 contains only stations to the west of the local network and Group 4 contains only stations to the east. Groups 5 and 6 are, respectively, stations to the north and to the south of the Rock Valley fault zone. A summary of this information is given in Figure 79. Table 9 gives a summary of strain rates for the far-field GPS stations, divided into an ECSZ group and a Basin and Range group. Tables 10 and 11 show orientations of maximum shear strain for local and regional stations, calculated using the values for α given in Tables 8 and 9.

Group	1	2	3	4	5	6
ε_{EE}	5.8 ± 0.4	4.0 ± 0.5	8.1 ± 0.8	1.1 ± 1.1	-14.2 ± 3.5	-8.1 ± 3.5
ε_{EN}	-1.1 ± 0.5	-2.3 ± 0.6	3.2 ± 0.8	-5.0 ± 0.7	-0.8 ± 1.4	3.6 ± 2.4
ε_{NE}	-14.5 ± 0.5	-14.0 ± 0.6	-15.4 ± 0.9	-19.2 ± 1.3	-16.7 ± 4.1	-8.7 ± 4.2
ε_{NN}	-4.0 ± 0.6	-3.9 ± 0.7	-1.8 ± 1.0	-5.7 ± 0.9	-8.6 ± 1.7	-8.0 ± 2.9
Ω	-6.7 ± 0.3	-5.9 ± 0.4	-9.3 ± 0.6	-7.1 ± 0.7	-7.9 ± 2.2	-6.2 ± 2.4
D	1.8 ± 0.7	0.1 ± 0.9	6.3 ± 1.2	-4.6 ± 1.4	-22.8 ± 3.8	-16.1 ± 4.5
γ_1	9.8 ± 0.7	7.9 ± 0.9	9.9 ± 1.2	6.8 ± 1.4	-5.6 ± 3.8	-0.2 ± 4.5
γ_2	-15.6 ± 0.7	-16.3 ± 0.8	-12.2 ± 1.2	-24.2 ± 1.4	-17.5 ± 4.4	-5.2 ± 4.8
$\lvert\gamma\rvert$	18.4 ± 0.7	18.1 ± 0.9	15.7 ± 1.2	25.1 ± 1.4	18.4 ± 4.3	5.2 ± 4.8
α (degs)	-29.0 ± 1.0	-32.0 ± 1.2	-25.4 ± 1.8	-37.1 ± 1.5	36.0 ± 5.7	44.1 ± 25.1
Stations	LITT	LITT	BUST	JOHN	LITT	POIN
	SKUL	SKUL	REPO	LITT	SKUL	MERC
	STRI	STRI	RELA	MERC	STRI	JOHN
	BUST	BUST	CRAT	POIN	TIVA	
	REPO	REPO	TATE	SKUL		
	TIVA	TIVA	PERL	STRI		
	RELA	RELA	CHLO	TIVA		
	CRAT	CRAT	BEAT			
	POIN	POIN	BULL			
	TATE	TATE				
	MERC	MERC				
	JOHN	JOHN				
	PERL	PERL				
	CHLO	BEAT				
	BEAT					
	BULL					
	All YM	All YM, but no CHLO or BULL	All YM, no Rock Valley stations	All YM, no Rock Valley stations	Rock Valley north	Rock Valley south

Table 8. Strain rates for local Yucca Mountain stations. Strain rates are given in ns/yr. Strain rates were calculated with the 2-axis oriented at N0^{o}E. Extension is reckoned positive. Errors are 1σ. Strain rates were calculated using relative velocities to a point at the centroid of each group of stations.

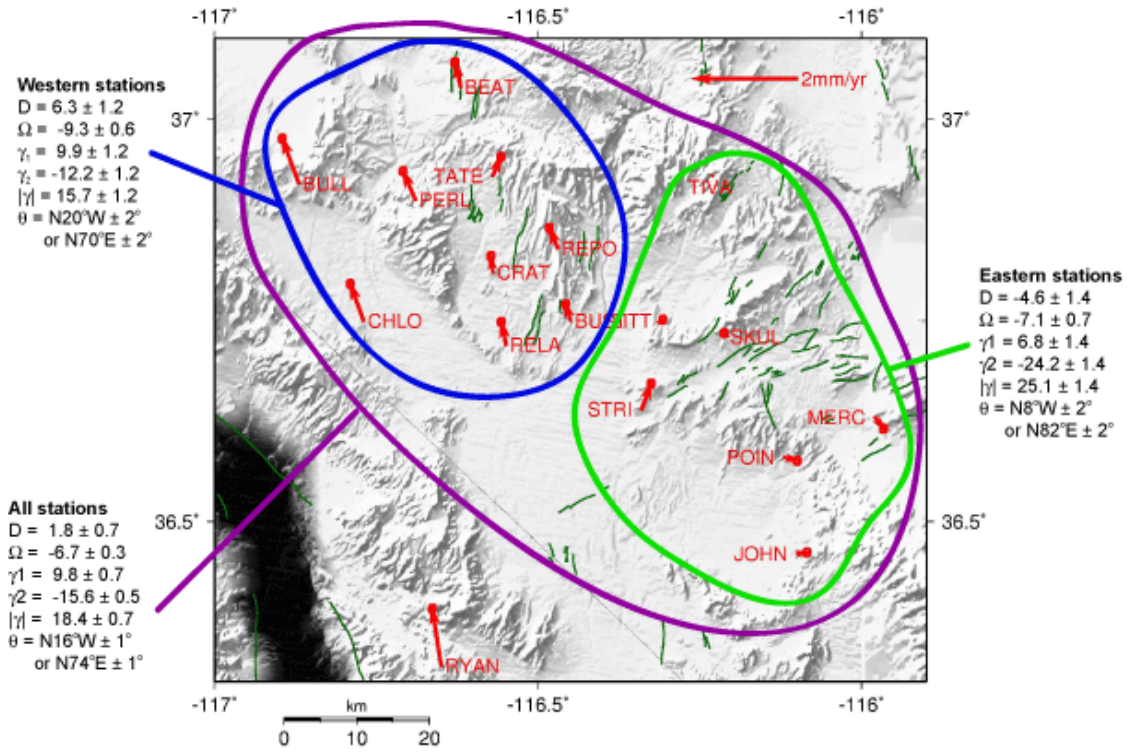

Figure 79. Strain rates calculated using local Yucca Mountain stations. Strain rates are given in ns/yr. Errors are 1σ. Extension is reckoned positive.

Group	B+R	ECSZ
ε_{EE}	2.0 ± 0.2	24.0 ± 0.1
ε_{EN}	-1.3 ± 0.4	3.7 ± 0.7
ε_{NE}	-5.6 ± 0.2	-34.5 ± 0.1
ε_{NN}	-3.0 ± 0.5	-7.2 ± 0.8
Ω	-2.1 ± 0.2	-19.1 ± 0.4
D	-1.0 ± 0.5	16.7 ± 0.8
γ_1	5.0 ± 0.5	31.2 ± 0.8
γ_2	-6.9 ± 0.4	-30.8 ± 0.7
|γ|	8.6 ± 0.5	43.9 ± 0.8
α (degs)	-27.0 ± 1.3	-22.3 ± 0.4
Stations	ALAM	ARGU
	ECHO	LIND
	RAIL	ROGE
	TONO	RYAN
		SHOS
		SMYC

Table 9. Strain rates for the regional network. Strain rates are given in ns/yr. Strain rates were calculated with the 2-axis oriented at N0°E. Extension is reckoned positive. Errors are 1σ. Strain rates were calculated using relative velocities to a point at the centroid of each group of stations.

Group	1	2	3	4
θ_1	N16.0°W	N13.0°W	N19.6°W	N7.9°W
θ_2	N74.0°E	N77.0°E	N70.4°E	N82.1°E
1σ error	1.0	1.2	1.8	1.5
Stations	LITT	LITT	BUST	JOHN
	SKUL	SKUL	REPO	LITT
	STRI	STRI	RELA	MERC
	BUST	BUST	CRAT	POIN
	REPO	REPO	TATE	SKUL
	TIVA	TIVA	PERL	STRI
	RELA	RELA	CHLO	TIVA
	CRAT	CRAT	BEAT	
	POIN	POIN	BULL	
	TATE	TATE		
	MERC	MERC		
	JOHN	JOHN		
	PERL	PERL		
	CHLO	BEAT		
	BEAT			
	BULL			

Table 10. Orientation of maximum shear for local Yucca Mountain stations, calculated using α from Table 8.

Group	B+R	ECSZ
θ_1	N18.0°W	N22.7°W
θ_2	N72.0°E	N67.3°E
1σ error	1.3	0.4
Stations	ALAM	ARGU
	ECHO	LIND
	RAIL	ROGE
	TONO	RYAN
		SHOS
		SMYC

Table 11. Orientation of maximum shear for regional stations, calculated using α from Table 9.

4.6 Discussion of this chapter

The estimate of total right-lateral shear strain for all local Yucca Mountain stations is 18.4 ± 0.7 ns/yr, oriented at N16 ± 1°W. These stations measure a dilitation rate of 1.8 ± 0.7 ns/yr, which is, within error, slightly more than zero. This is considerably lower than the 50 ± 9 ns/yr estimated by Wernicke et al. (1998), but higher than, for example, the 10-14 ns/yr of expected shear strain predicted by Savage et al. (1999).

Strain rate is not constant across the local Yucca Mountain network. Total right-lateral shear strain for the western local stations only is slightly lower than the estimate for all stations, at 15.7 ± 1.2 ns/yr, oriented at N20 ± 2°W. However, the dilitation rate is higher, at 6.3 ± 1.2 ns/yr of extensional strain. Total right-lateral shear strain for the eastern stations only is 25.1 ± 1.4 ns/yr, oriented at N8 ± 2°W. This is higher than expected and higher than the shear strain rate for the western stations; also unexpected since the western stations are closer to the ECSZ. This suggests that there may be a local source of some of the measured strain. It is worth noting that this strain rate is ambiguous, and could represent left-lateral shear strain on a N82 ± 2°E trending fault system, so could represent left-lateral strain accumulation across the RVSZ. Also unexpected is that the dilitation rate for the eastern local stations is -4.6 ± 1.4 ns/yr of contraction.

Total shear strain rate for the ECSZ stations is estimated to be 43.9 ± 0.8 ns/yr,

oriented at N22.7±0.4^{o}W. This orientation agrees with previously published orientations for the ECSZ faults (Gan et al., 2000). The strain rate is a little higher than the rate estimated by Gan et al. (2000), which was 39.2 ± 4.4 ns/yr of right lateral simple shear, but it agrees within error. The rate of extension for the ECSZ stations is not insubstantial, at 16.7 ± 0.8 ns/yr. This reflects the changing orientation of the velocity vectors across the ECSZ, illustrated in Chapter 3 and supports the idea that the Sierra Nevada block is moving away from the Basin and Range in a northwesterly direction (Dixon et al., 2000; Hearn and Humphreys, 1998).

Total shear strain rate for the Basin and Range stations is 8.6 ± 0.5 ns/yr, oriented at N18 ± 1^{o}W. The dilitation rate is almost zero, at -1.0 ± 0.5 ns/yr. This confirms recent suggestions (e.g. Bennett et al., 2003) that right-lateral strike slip is perhaps the most dominant form of deformation in the current tectonic regime of the Basin and Range. The orientation of strike slip shear strain is more northerly than the orientation of strike slip shear for the ECSZ stations, and confirms the idea that the orientation of shear rotates towards the northwest with increasing proximity to the plate boundary.

5. Fault modeling

5.1 Introduction to this chapter

The GPS horizontal velocity results were discussed in Chapter 3 and strain rates in Chapter 4. This chapter is an interpretation and discussion of these results. In this chapter I attempt to understand the GPS velocities and strain rates by using elastic dislocation models to assign slip rates to the nearby fault systems. I constrain the elastic models by fitting modeled velocity profiles to GPS velocity profiles.

The question of whether strain accumulation across the ECSZ can account for measured strain at Yucca Mountain has been discussed by several previous authors (Section 4.1). For example, Savage et al. (1999) use a model of the DV-FC and HM-PV fault systems, located at 50 and 90 km from Yucca Mountain, and with slip rates of 5 ± 1 mm/yr and 2 ± 1 mm/yr respectively. They conclude that it is possible to account for all the strain they measure at Yucca Mountain using these faults; their predicted strain is 10-14 ns/yr, which is half of the 23 ± 10 ns/yr they measure in total shear strain, leaving a remainder of 9-13 ± 10 ns/yr, which is not significantly different from zero. Wernicke et al. (2004), on the other hand, discuss an interpretation of the BARGEN GPS results for Yucca Mountain from the GAMIT processing. Wernicke et al. (2004) measure 20 ± 2 ns/yr of right-lateral shear across the local Yucca Mountain network, oriented at N20^{o}W. They calculate elastic displacement models for the DV-FC fault system, at an orientation

of N20^{o}W, with a locking depth of 15 km, a slip rate of 3-5 mm/yr and a distance from Yucca Mountain of 55 km. They model only the DV-FC fault system, and do not include the effects of faults to the west of this. Wernicke et al. (2004) conclude that they cannot fit the fault model to their GPS velocity estimates using these parameters. Instead, they propose that ~0.9 mm/yr of slip must be accommodated within the local network, with ~2.8 mm/yr on the DV-FC fault system. A similar fault, termed the Amargosa Desert fault, was suggested by Schweickert and Lahren (1997).

In this chapter I examine the validity of these previously published results. I include faults to the west of the DV-FC fault system in the models (the OV, PV-HM and SA fault systems). The GPS and elastic dislocation model are described as rotation rates, in a Pacific plate fixed reference frame, about the North American Euler pole. The GPS rotation rates are then inverted in a simultaneous, constrained, least squares inversion for slip rate, locking depth and fault location. Model velocity profiles are calculated using the estimated slip rates, locking depths and fault locations. I assess the fit of the model profiles to the GPS results by calculating the RMS of the residual differences between model and GPS rotation rates.

5.2 Constraints on total ECSZ deformation

Some discrepancy also exists between published studies on the total slip budget available for the northern ECSZ. For example, Miller et al. (2001) allow 13 mm/yr of motion between the eastern flank of the DV-FC fault system and the western flank of the

Sierra Nevada; Dixon et al. (1995) allow 10.7 ± 1.6 mm/yr; Dixon et al. (2000) give 11 ± 1 mm/yr ('primarily on two faults, the Owens Valley - White Mountain (3 ± 2 mm/yr) and the Fish Lake Valley (8 ± 2 mm/yr) fault zones'); and Bennett et al. (2003) state that the Sierra Nevada - Great Valley microplate translates relative to the Colorado Plateau (a greater aperture than the other studies) at a rate of 11.4 ± 0.3 mm/yr, oriented at N47±1^{o}W. Dixon et al. (1995) give 12.1 ± 1.2 mm/yr of motion for the Sierra Nevada block relative to 'stable' North America, oriented at N38 ± 5^{o}W, while Bennett et al. (2003) state that it is a similar value, ~12.4 mm/yr, but at an orientation of N47 ± 1^{o}W. Table 1 (Chapter 1) summarizes published slip rates for the individual ECSZ faults. Published slip rates for the individual faults were also discussed in detail in Section 1.2.2 (Chapter 1).

The ECSZ has a general strike of ~N23^{o}W, while the local Yucca Mountain faults have a more northerly strike. The estimated orientation of maximum shear from the GPS results is N16 ± 1^{o}W for all local Yucca Mountain stations, N20 ± 3^{o}W for western local stations only and N8 ± 2^{o}W for eastern local stations only (Chapter 4). The general orientation of the Pacific-North America plate boundary at Yucca Mountain (i.e. parallel to a great circle around the pole) is ~N36^{o}W for the NUVEL-1A solution (DeMets et al., 1994) and ~N38^{o}W for the REVEL solution (Sella et al., 2002). The NUVEL-1A North American Euler pole is located at latitude 48.709^{o} and longitude -78.176^{o}. The REVEL Euler pole is at latitude 50.38^{o} and longitude -72.11^{o}.

The GPS velocity estimates were projected to be parallel (from hereon referred to

as 'fault parallel') and perpendicular ('fault perpendicular') to these various orientations, and parallel and perpendicular to the great circles around the NUVEL-1A and REVEL North American Euler poles. They were then converted to velocities relative to station LIND (located on the western side of the Sierra Nevada), in order to put a constraint on the slip budget for the ECSZ.

The solution with the least fault perpendicular displacement was chosen to use as the initial constraint, and data input to the least squares inversion, for the fault models described in the rest of this chapter. This was the solution containing velocities parallel and perpendicular to a great circle around the NUVEL-1A Euler pole, which had an RMS scatter for the fault perpendicular velocities of 0.3 mm/yr. This compares with, for example, an RMS scatter of 2.5 mm/yr for velocities perpendicular to a constant orientation of N23^{o}W. A summary of velocities across the width of the ECSZ, parallel and perpendicular to a great circle about the Euler pole, is given in Table 12 (complete results are given in Appendix K). Incidentally, there does not appear to be any clear signal across the network in the fault-perpendicular velocities.

	Total velocity difference (mm/yr)	'Fault-parallel' velocity difference (mm/yr)	'Fault-normal' velocity difference (mm/yr)
LIND-RYAN	10.4 ± 0.1	10.4 ± 0.1	0.3 ± 0.1
LIND-APEX	11.5 ± 0.1	11.5 ± 0.1	-0.2 ± 0.1
LIND-ALAM	11.9 ± 0.1	11.9 ± 0.1	-0.1 ± 0.1
LIND-ECHO	12.6 ± 0.1	12.6 ± 0.1	0.0 ± 0.1

Table 12. Total slip and total fault-parallel and fault-normal slip across the GPS network, with fault orientation assumed to be parallel to a great circle around the NUVEL-1A North American Euler pole

5.3 Modeling infinite length faults in an elastic half-space

Model velocity profiles were estimated using Equation 26, where u_x is total, fault parallel, strike slip at point x, u_i are long term fault slip rates on faults 1 to N and D_i are locking depths and, in the case of this experiment, x and x_n are the distance of the point and each fault from the Euler pole (Savage, 1983; Okada, 1992).

$$u_x = \frac{u_1}{\pi}\arctan\left(\frac{x - x_1}{D_1}\right) + \frac{u_2}{\pi}\arctan\left(\frac{x - x_2}{D_2}\right)\ldots\frac{u_i}{\pi}\arctan\left(\frac{x - x_i}{D_i}\right) + \frac{\sum_{i=1}^{N} u_i}{2} \qquad [26]$$

This model assumes a number of simple, parallel, locked, strike-slip faults in an elastic half-space. The model has significant deficiencies; in reality the ECSZ faults are not parallel and infinitely long (for example the DV-FC fault system is ~300 km long) and the model does not account for the complicated rheology of the crust. These models

only account for strike-slip deformation, when many of the ECSZ faults are known to also exhibit oblique displacement, nor does it account for varying fault orientations, both along and between the fault systems. Use of these simple models, however, avoids a big problem encountered when attempting to use finite-length fault models (Okada, 1985) for modeling interseismic strain accumulation (compared with the successful application of these models to coseismic displacements). The problem with using finite-length fault models for interseismic strain is that even though these faults have end points, the shear must still, somehow, continue to the north and south, which is difficult to account for, making the infinite fault model somewhat more suitable in satisfying far-field boundary conditions. In fact, there is evidence to suggest that shear may indeed continue across the Garlock fault to the south (Peltzer et al., 2001).

I use Equation 26 to estimate velocity profiles across the network that are the combined effect of the SA, OV, PV-HM and DV-FC fault systems. Fault parallel velocity difference between stations LIND and APEX is 11.5 ± 0.1 mm/yr (Table 12). If this is evenly divided between the three major fault systems of the ECSZ, each fault is allocated a 3.8 mm/yr slip rate. This rate was therefore used as an initial estimate of OV, PV-HM and DV-FC fault system slip rate for the model. An initial estimate of slip rate for the SAFZ was set at 31 mm/yr.

Dixon et al. (1995) state that since Owens Valley has been the location of late Quaternary volcanism, it is likely that the crust there is relatively thin compared to the area to the east. They therefore suggest locking depths of 8, 12 and 16 km for the OV,

PV-HM and DV-FC fault systems respectively. These values were used as initial estimates of locking depth for the inversion.

Figure 80 shows the approximate location and orientation of the model faults, and the GPS stations that were used for the fault modeling calculations. The GPS profile includes stations LIND, ARGU, ROGE, RYAN, SHOS, SMYC and APEX, plus the local Yucca Mountain stations. LIND is located on the western side of the Sierra Nevada block, ARGU between the OV and PV-HM fault systems and ROGE between the PV-HM and DV-FC fault systems. RYAN and SHOS are located on the eastern side of the DV-FC fault system. SMYC is located on Mount Charleston and APEX, the easternmost station in this profile, near Las Vegas. ARGU, ROGE and RYAN are located 10-20 km from the faults, so at a distance of approximately one locking depth from the faults.

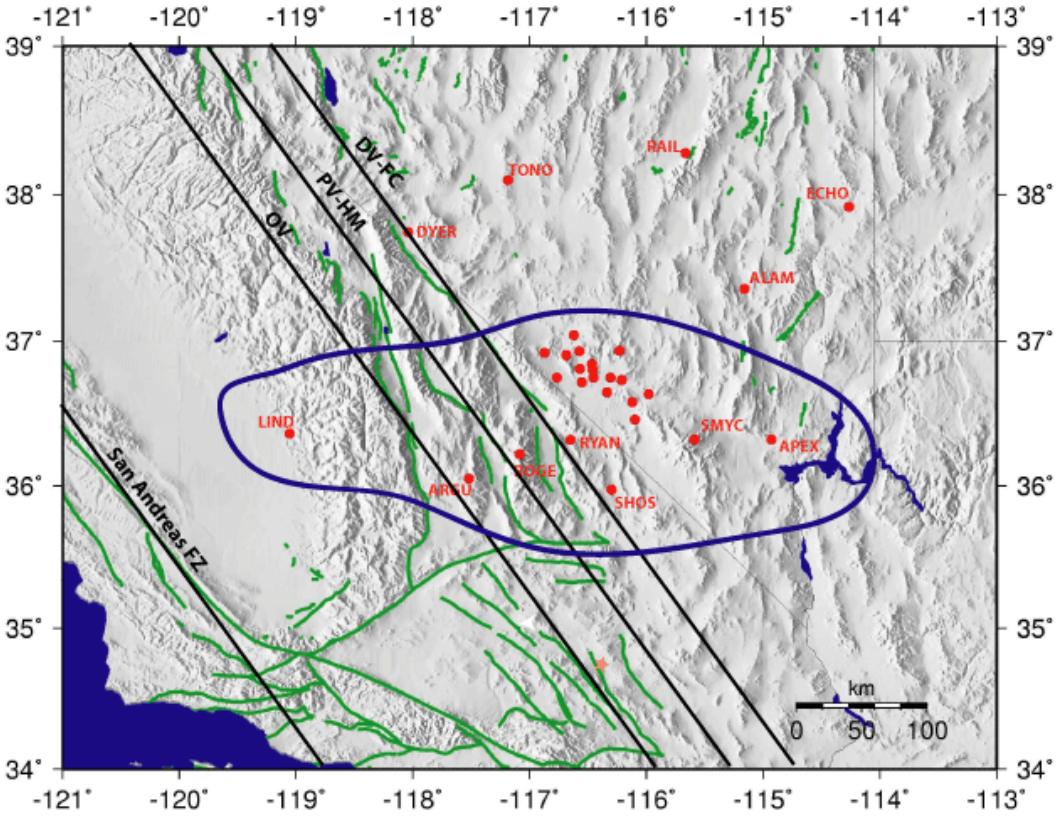

Figure 80. **<u>Approximate</u> locations of model faults (black) and illustration of which stations are included in the GPS velocity profile. BARGEN GPS stations are shown in red and Quaternary faults (from Jennings (1975) and Dohrenwend et al. (1996)) in green.**

5.4 Model velocity profiles in a North America fixed reference frame

Throughout this dissertation, results have been presented in a North America fixed reference frame. Section 2.14 described how velocity estimates were rotated to remove North American plate rotation. There is a problem with using this reference frame for fault modeling, however, because it becomes necessary to add an offset value to the elastic dislocation model. This is necessary due to the fact that the location of 'stable' North America is unknown. In other words, the amount of deformation occurring

to the east of the GPS network (and the actual location of zero model velocity) is unknown, meaning that the model will tend towards zero at the wrong place. This makes it particularly difficult to constrain the effect of the SAFZ on Yucca Mountain and creates an additional unknown parameter that can be adjusted to change the estimated fault slip rates.

Figure 81 illustrates the problem. One profile was calculated using Equation 26 with no changes. The other profile was calculated using Equation 27, so model velocities were offset by the amount required to make model velocity equal to GPS velocity at station LIND. These profiles were produced using the slip rates and locking depths described in Section 5.3.

$$u_x = \frac{u_1}{\pi}\arctan\left(\frac{x - x_1}{D_1}\right) + \ldots + \frac{u_n}{\pi}\arctan\left(\frac{x - x_n}{D_n}\right) + K \qquad [27]$$

where u_x is total, fault parallel, lateral slip at point x (in mm/yr); u_i are fault slip rates on faults 1 to N; Di are fault locking depths; x and x_i are the distances from the point and the fault to the Euler pole and K is the difference between model and GPS velocity at the reference station.

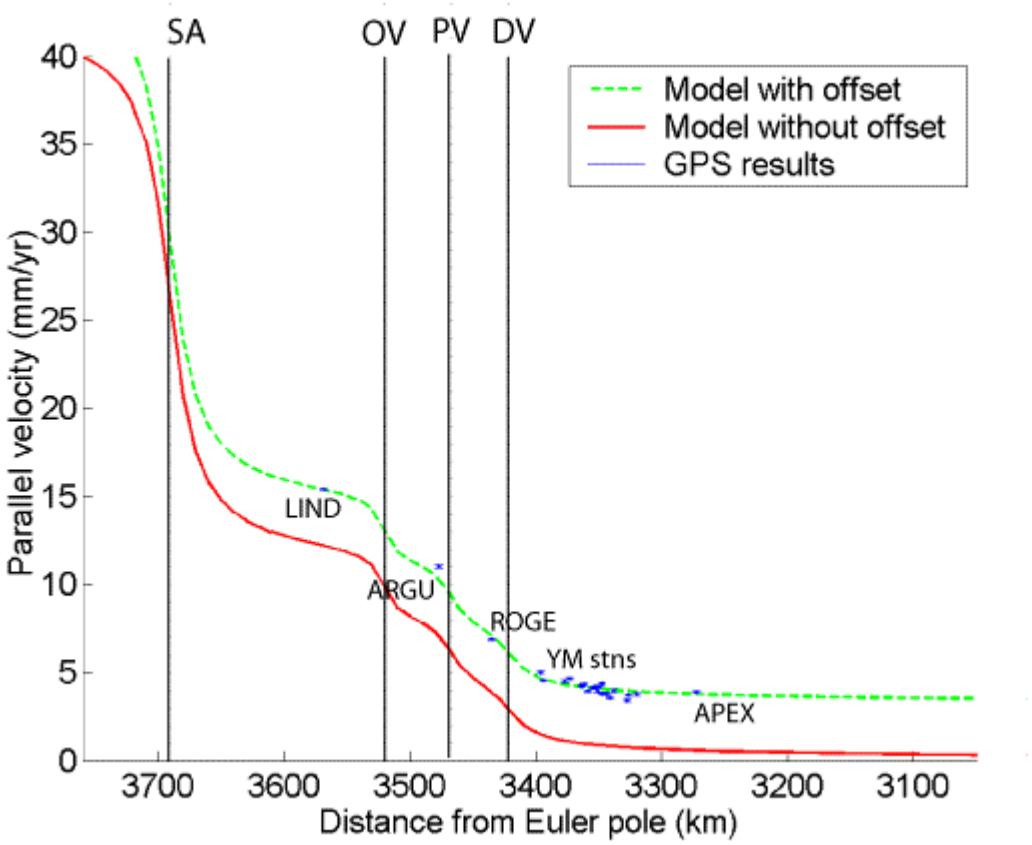

Figure 81. Model velocity profile and GPS results in a North America fixed reference frame, illustrating the necessity of 'shifting' the model profile to fit the GPS results. Model profiles were calculated using slip rates of 31 mm/yr for the SAFZ and 3.8 mm/yr for the OV, PV-HM and DV-FC fault systems respectively. Locking depths for these four faults were set to 16, 8, 12 and 16 km.

A similar technique was used by Wernicke et al. (2004) to model the effect of the DV-FC fault system on the Yucca Mountain strain field in a North America fixed reference frame, although in their case the offset was calculated using stations at the other end of the network, as the difference between model values and the average velocity of stations MERC and ALAM. Wernicke et al. (2004) use this model to argue that it is difficult to fit a profile through the Yucca Mountain GPS results using an elastic strain model of the DV-FC fault system, even with high slip rates on the DV-FC fault system, due to the relatively steep velocity gradient across the local network. They

suggest that an additional fault, to the east of the DV-FC fault system, is required to steepen the profile at Yucca Mountain.

The RMS of residual velocities between the model and GPS results was calculated to assess the fit of each model profile to the data. Table 13 shows the resulting RMS of residual velocities from various slip rates on the SAFZ and evenly distributed slip rate across the ECSZ. Figures 82 and 83 show GPS and model profiles calculated using these numbers. The lowest RMS of residuals (0.28 mm/yr) was obtained using a SAFZ slip rate of 31 mm/yr. However, a change in slip rate on the SAFZ of 6 mm/yr will only adjust the RMS value by ~ 0.05 mm/yr, showing how insensitive this particular model is to SAFZ slip rate.

Slip rates				**RMS of residuals**	
SA	**OV**	**PV**	**DV**	**All stns**	**YM stns**
(mm/yr)	(mm/yr)	(mm/yr)	(mm/yr)	(mm/yr)	(mm/yr)
25	3.8	3.8	3.8	0.33	0.34
31	3.8	3.8	3.8	0.28	0.26
37	3.8	3.8	3.8	0.30	0.27

Table 13. RMS of residual velocities resulting from various different slip rates on the SAFZ.

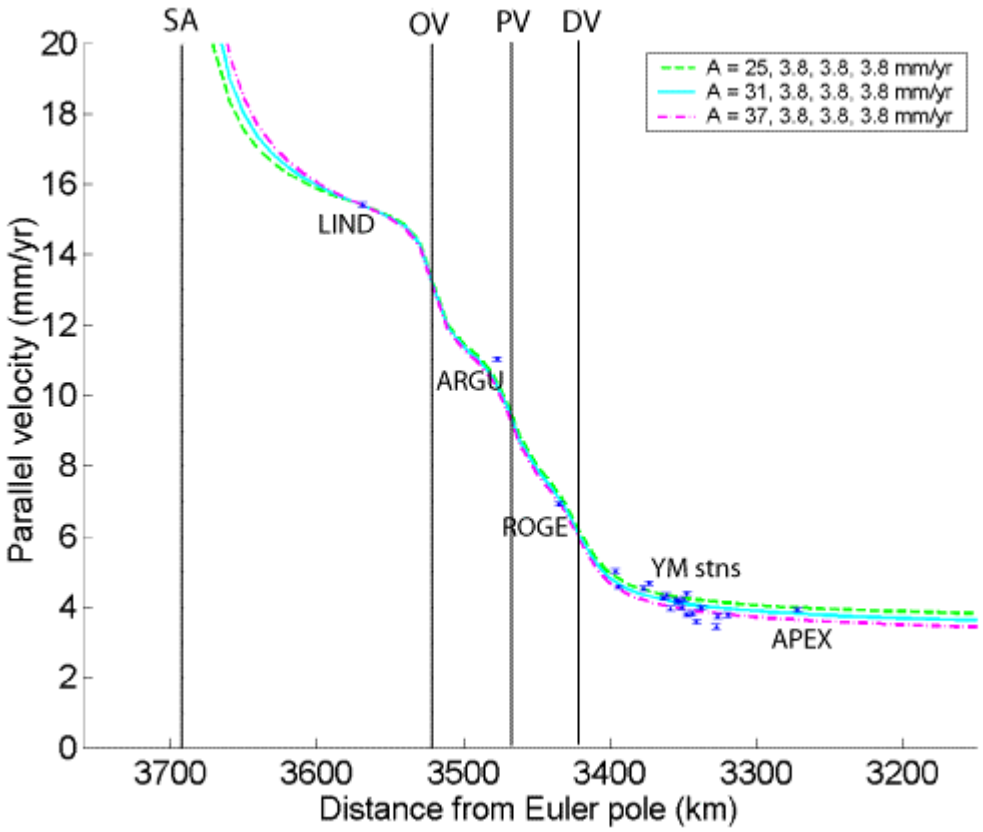

Figure 82. GPS and model velocity profiles, in a North America fixed reference frame. Total ECSZ slip rate was divided evenly between the OV, PV-HM and DV-FC fault systems. SAFZ slip rate was 25, 31 and 37 mm/yr for the three model profiles and slip rate across the ECSZ was divided evenly between the OV, PV-HM and DV-FC fault systems. Locking depths were set to 16, 8, 12 and 16 km for the SA, OV, PV-HM and DV-FC fault systems respectively.

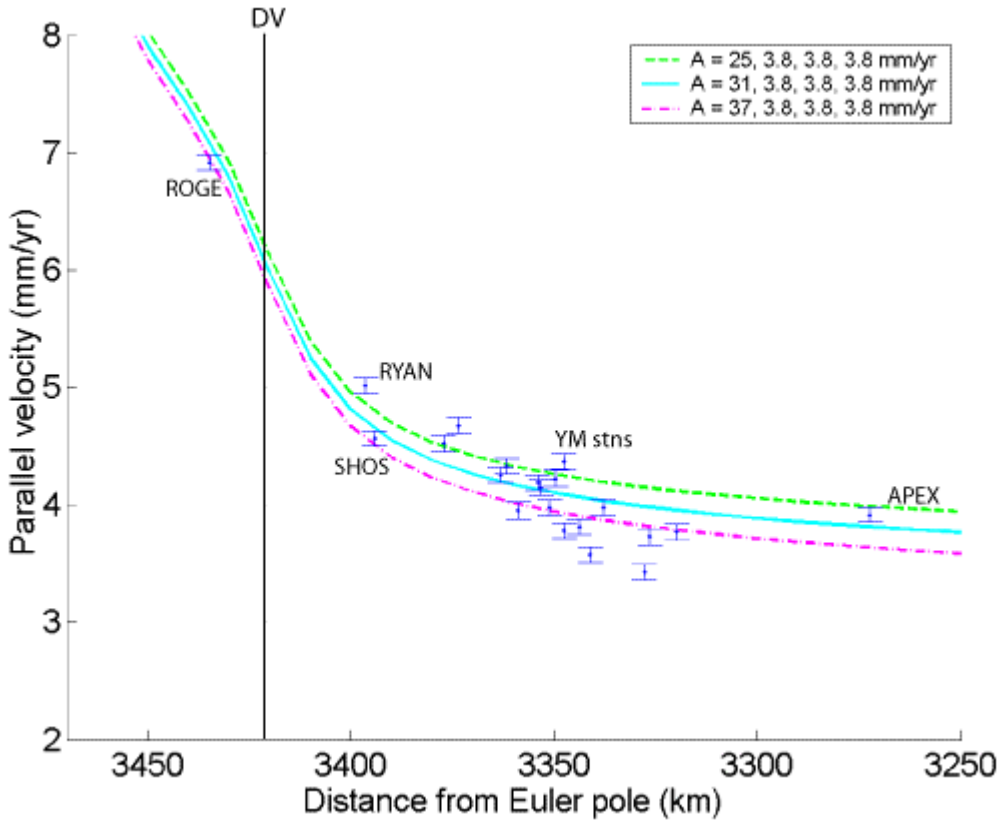

Figure 83. GPS and model velocity profiles, in a North America fixed reference frame. Total ECSZ slip rate was divided evenly between the OV, PV-HM and DV-FC fault systems. SAFZ slip rate was 25, 31 and 37 mm/yr for the three model profiles and slip rate across the ECSZ was divided evenly between the OV, PV-HM and DV-FC fault systems. Locking depths were set to 16, 8, 12 and 16 km for the SA, OV, PV-HM and DV-FC fault systems respectively. The figure shows a close-up of the local Yucca Mountain stations.

Figure 83 shows a drop in velocity for the local Yucca Mountain stations slightly to the east of Yucca Mountain itself (at ~3350 km from the Euler pole). By changing the slip rate on the SAFZ it is possible to produce a model that 'fits' (by eye) the local eastern stations, or the local western stations, but not both. It is this drop in velocity that lead Wernicke et al. (2004) to the conclusion that it was difficult to produce a model profile gradient steep enough to fit the GPS results for the local network, even with very high slip rates on the DV-FC fault system. Wernicke et al. (2004) modeled only the DV-FC

fault system and not the faults to the west. To test this hypothesis, I calculated profiles with a variety of slip rates on the DV-FC fault system, a slip rate of 31 mm/yr for the SAFZ and the remaining ECSZ slip rate (11.5 mm/yr minus the DV-FC slip rate) divided evenly between the OV and PV-HM fault systems.

Table 14 and Figures 84 and 85 show the results of this experiment. These results show that although increasing the slip rate on the DV-FC fault system to 5-7 mm/yr does decrease the RMS for the local Yucca Mountain stations by a very small amount (from 0.26 mm/yr to 0.25 mm/yr) it increases the RMS for all stations in the profile. Furthermore, additional increases to the slip rate of the DV-FC fault system will increase the RMS fit for all stations in the network AND stations in the local Yucca Mountain network, albeit very slightly.

Slip rates				**RMS of residuals**	
SA	**OV**	**PV**	**DV**	**All stns**	**YM stns**
(mm/yr)	(mm/yr)	(mm/yr)	(mm/yr)	(mm/yr)	(mm/yr)
31.00	3.80	3.80	3.80	0.28	0.26
31.00	3.25	3.25	5.00	0.29	0.25
31.00	2.75	2.75	6.00	0.39	0.25
31.00	2.25	2.25	7.00	0.54	0.25
31.00	1.75	1.75	8.00	0.70	0.26

Table 14. RMS of residual velocities resulting from various different slip rates on the DV-FC fault system, for a North America fixed reference frame. Locking depths were set to 16, 8, 12 and 16 km for the SA, OV, PV-HM and DV-FC fault systems respectively.

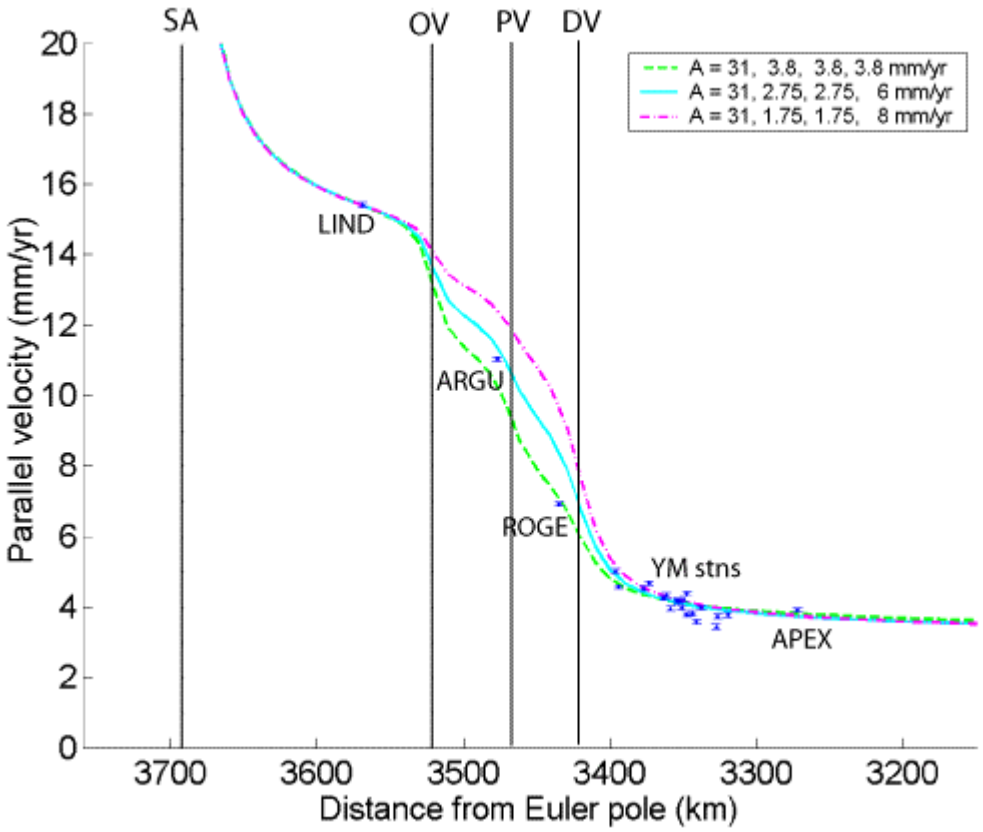

Figure 84. Model and GPS velocity profiles, in a North America fixed reference frame, with various slip rates for the DV-FC fault system.

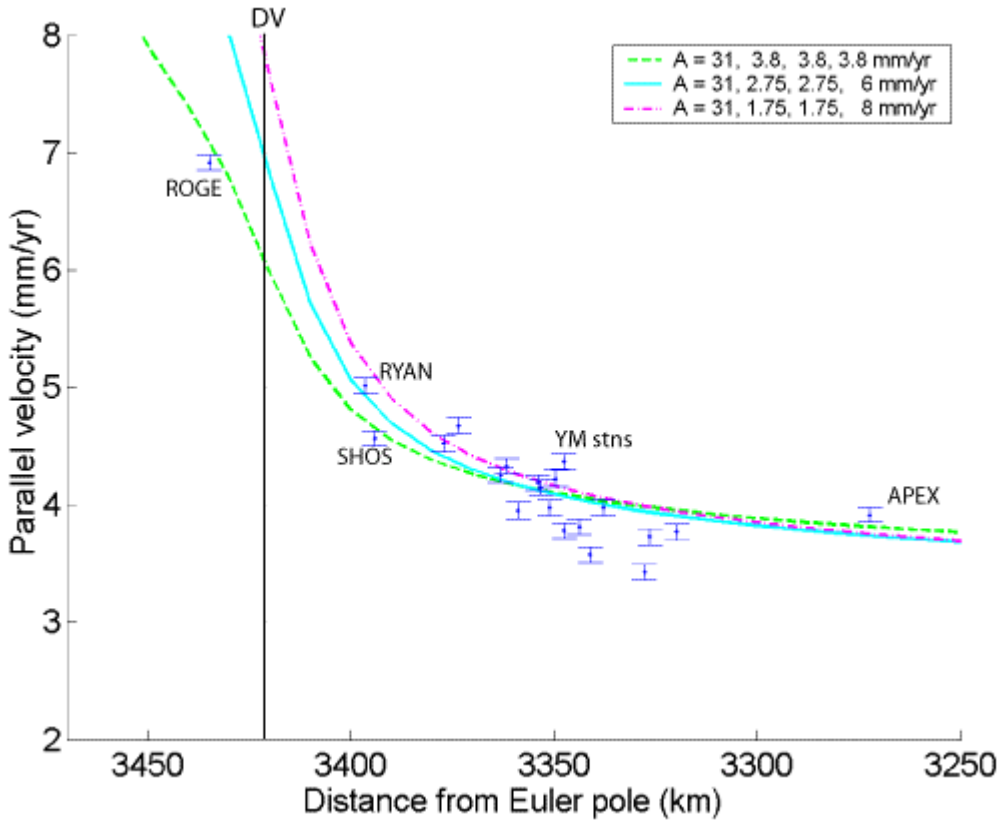

Figure 85. Model and GPS velocity profiles, in a North America fixed reference frame, with various slip rates for the DV-FC fault system. The figure shows a close-up of the local Yucca Mountain stations.

5.5 Model velocity profiles in a Pacific plate fixed reference frame

It is possible to avoid the ambiguity associated with models in a North America fixed reference frame by plotting the GPS and model profiles with respect to a Pacific plate fixed frame instead. The situation is not as simple, however, because in a Pacific fixed frame the velocities will necessarily decrease towards the North American Euler pole with constant rotation of the North American plate. Figures 86 and 87 illustrate this point, as velocities decrease in magnitude towards the east of the network (for example

see station APEX). To fit the model profiles to the GPS data it is necessary to reduce the slip rates of the ECSZ faults to ~ 3 mm/yr, which does not conform to the GPS constraint of 11.5 mm/yr of total ECSZ slip. The rotation effect also has the effect of flattening the velocity profile across Yucca Mountain (Figure 87) so that the relatively steep gradient shown in Figure 85 disappears; it actually becomes easier to fit a model profile through the artificially shallow gradient of GPS velocities.

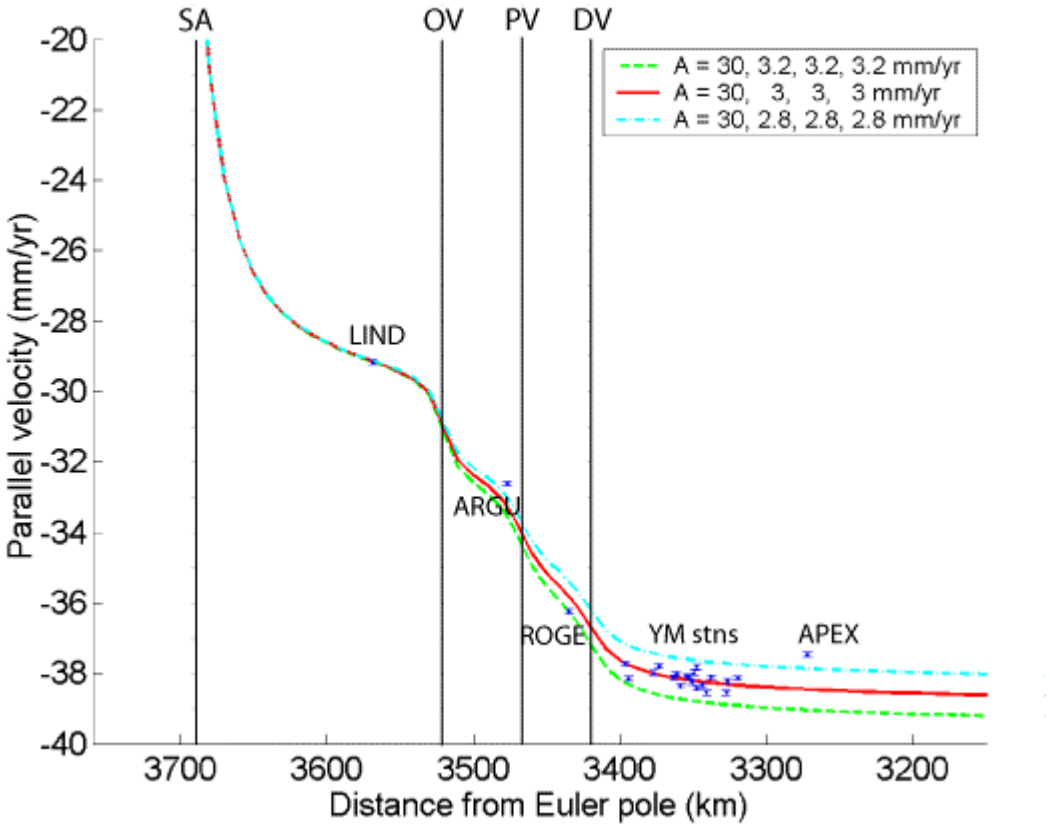

Figure 86. GPS and INCORRECT model velocity profiles, plotted in a Pacific plate fixed reference frame. The reference frame causes GPS velocities to decrease towards the east of the network.

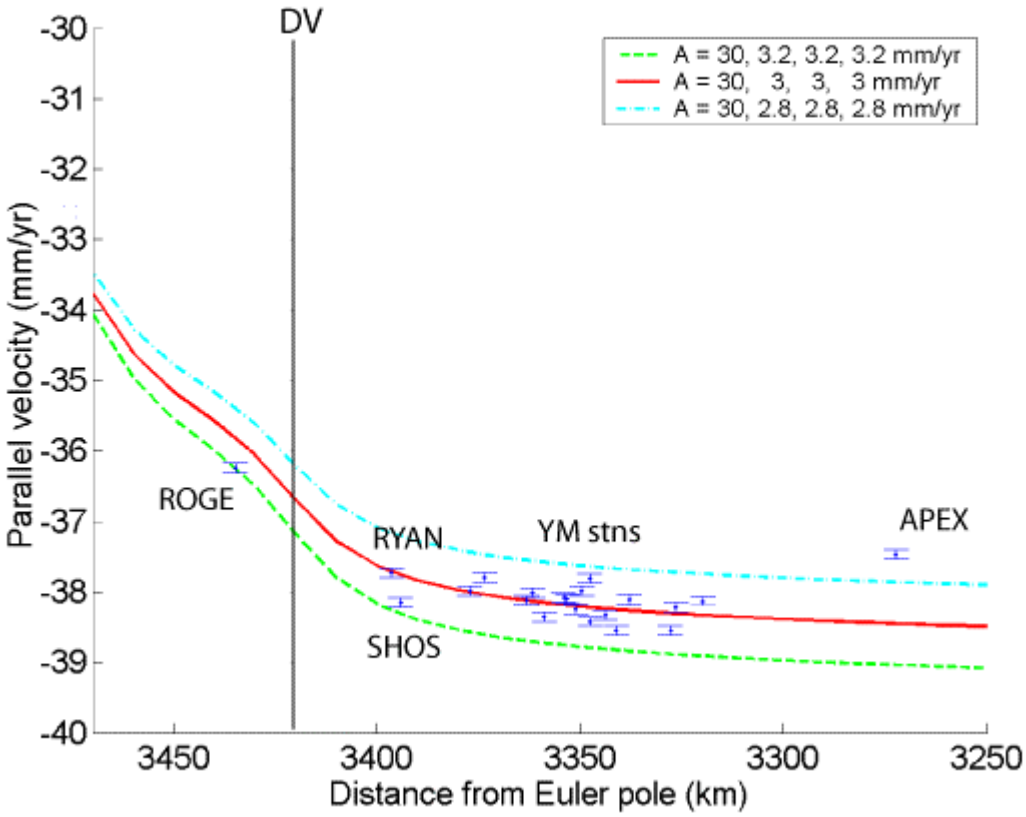

Figure 87. GPS and INCORRECT model velocity profiles, plotted in a Pacific plate fixed reference frame. The reference frame causes GPS velocities to decrease towards the east of the network. The figure shows a close-up of the local Yucca Mountain stations.

The problem illustrated by Figures 86 and 87 can be solved by converting both the elastic displacement model and the GPS results to rotation rates, instead of velocities, about the North American Euler pole (Figures 88 and 89). The full procedure for doing this is given in Appendix L. Because the location of zero model velocity is known for this reference frame, it is possible to utilize the elastic displacement model without requiring an offset value for the profile or needing to fix the model profile to match the GPS results at one end of the network.

Figures 88 and 89 were generated using an even distribution of slip rate across the ECSZ and varied slip rates for the SAFZ. These figures illustrate the increase in sensitivity of this model to SAFZ slip rate, compared to the results obtained in a North American plate fixed reference frame. The RMS of residual velocities for the model and GPS data in a Pacific plate fixed frame, with a SAFZ slip rate of 31 mm/yr, is 0.32 mm/yr for all stations in the profile and 0.29 mm/yr for the local Yucca Mountain stations only (Table 15). A change in SAFZ slip rate of 6 mm/yr will increase the RMS to ~ 5 mm/yr. This compares with a change in RMS for the North American fixed frame, with an adjustment of 6 mm/yr to the SAFZ slip rate, of ~0.05 mm/yr (Table 13).

Slip rates				**RMS of residuals**	
SA	**OV**	**PV**	**DV**	**All stns**	**YM stns**
(mm/yr)	(mm/yr)	(mm/yr)	(mm/yr)	(mm/yr)	(mm/yr)
25	3.8	3.8	3.8	5.24	5.26
31	3.8	3.8	3.8	0.32	0.29
37	3.8	3.8	3.8	5.54	5.48

Table 15. RMS of residual velocities resulting from various different slip rates on the SAFZ, for a Pacific plate fixed reference frame. Locking depths were set to 16, 8, 12 and 16 km for the SA, OV, PV-HM and DV-FC fault systems respectively.

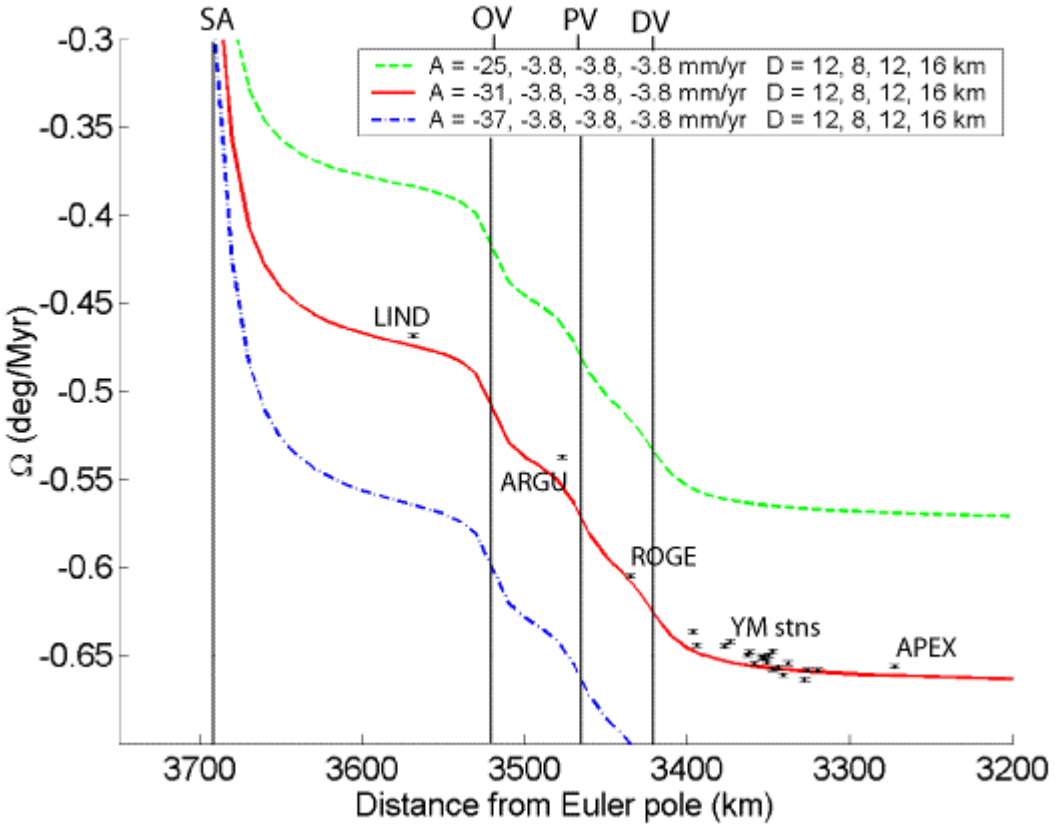

Figure 88. GPS and model profiles, plotted as rotations in a Pacific plate fixed reference frame, with varying slip rate on the SAFZ and an even distribution of slip rate across the ECSZ.

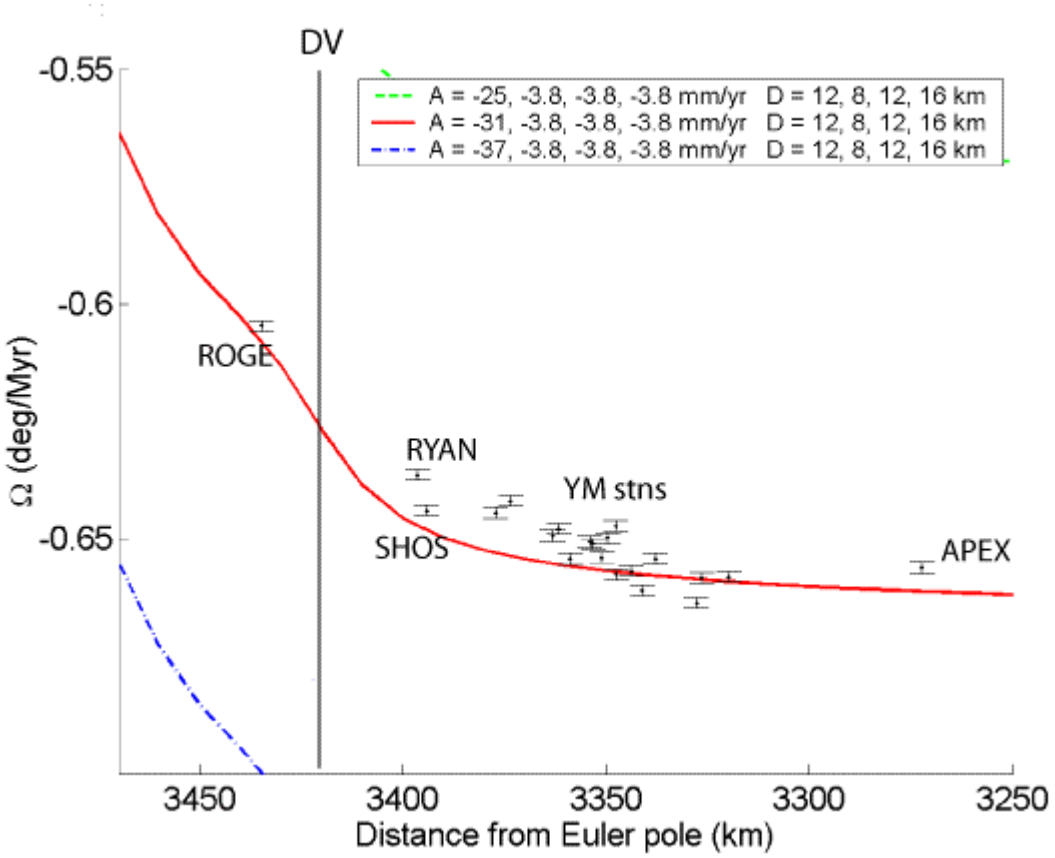

Figure 89. GPS and model profiles, plotted as rotations in a Pacific plate fixed reference frame, with varying slip rate on the SAFZ and an even distribution of slip rate across the ECSZ. The figure shows a close-up of the local Yucca Mountain stations.

5.6 Inversion for ECSZ fault location, slip rate and locking depth

The GPS and elastic displacement models, expressed as rotation rates about the North American Euler pole, were input to a constrained, weighted, least squares inversion for slip rate, locking depth and fault location. The full details of this are given in Appendix M.

The SAFZ fault parameters were tightly constrained for all variations of the inversion procedure; since there were no stations processed in this study that are close to the SAFZ it is impossible to accurately resolve details about this fault system using our GPS results. Instead, a variety of different values were tested for the a priori values for SAFZ slip rate and locking depth. A priori estimates of locking depth for the ECSZ faults were set to 8, 12 and 16 km for the OV, PV-HM and DV-FC fault systems respectively, following Dixon et al. (1995). The GPS measured total slip rate for the ECSZ, 11.5 mm/yr, was divided evenly between the three faults, resulting in a priori slip rate estimates of 3.8 mm/yr per fault. A priori fault locations were estimated by computing the average distance of the fault to the Euler pole, based on a number of sample points selected along the mapped fault (Jennings 1975).

If the ECSZ slip rate and locking depth parameters are tightly constrained, but the distance of each fault from the Euler pole allowed to vary, the estimated fault location for the PV-HM and DV-FC fault systems are closer to Yucca Mountain than the a priori values (Table 16). However, the estimated location of the DV-FC is unreasonably close to Yucca Mountain (Figures 90 and 91) based on geological mapping of the area. This unrealistic fault location is caused by the model trying to fit the relatively steep gradient of GPS velocity across the local Yucca Mountain network.

	SA	OV	PV	DV
A priori D	12.0	8.0	12.0	16.0
A priori S	31.0	3.8	3.8	3.8
A priori X	3691	3520	3467	3421
Estimated D	12.2±1.0	8.5±3.0	12.3±2.8	24.4±2.5
Estimated S	-30.6±0.1	-2.7±0.9	-5.3±0.9	-3.7±0.5
Estimated X	3691.0±2.0	3519.3±10.0	3465.1±8.5	3412.1±3.6
D constraints	1	3	3	3
S constraints	1	2	2	2
X constraints	2	10	10	10

Table 16. Results of inversion with tight constraints on locking depth (D) and slip rate (S), but loose constraints on fault distance from the Euler pole (X). Slip rates are in mm/yr and locking depth and fault location in km.

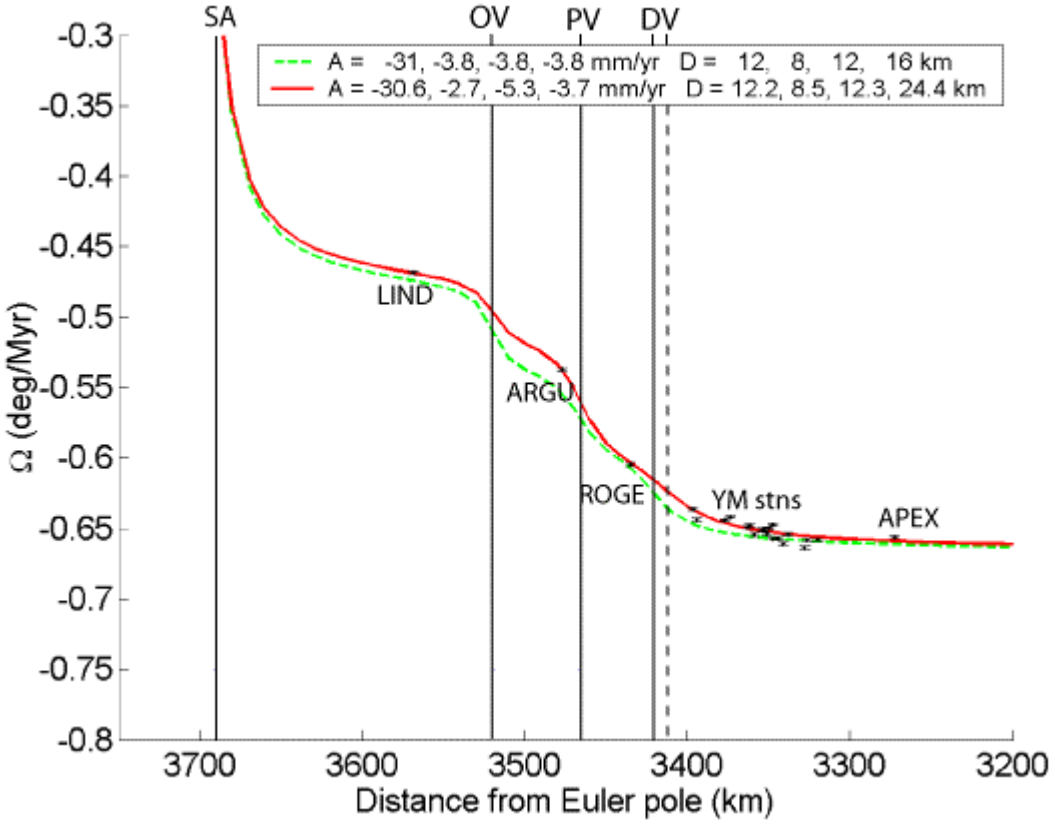

Figure 90. Model profile using estimated slip rate, locking depth and fault location, when slip rate and locking depth are tightly constrained and fault location is loosely constrained. Solid black lines show a priori fault locations (and estimated fault locations if there was no change to the a priori values). Dotted lines show estimated fault locations (no dotted line means estimated location was the same as a priori).

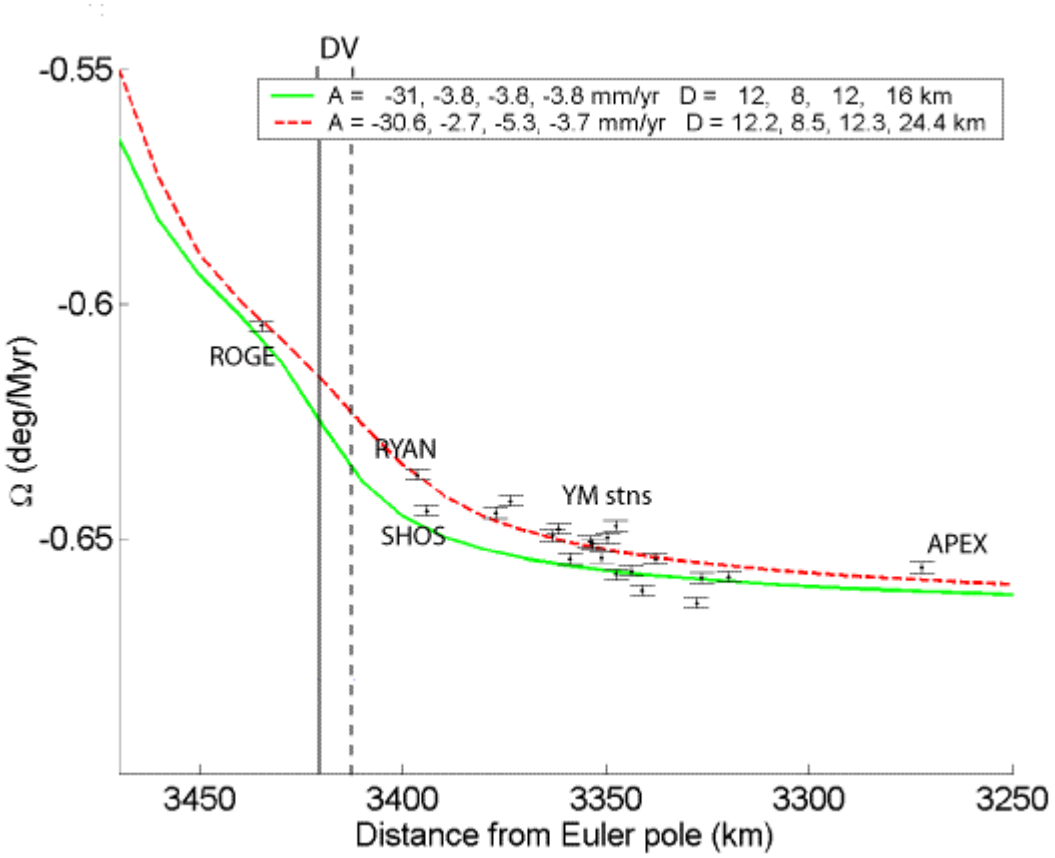

Figure 91. Model profile using estimated slip rate, locking depth and fault location, when slip rate and locking depth are tightly constrained and fault location is loosely constrained. Solid black line shows a priori fault locations. Dotted line shows estimated fault locations (no dotted line means estimated location was the same as a priori). The figure shows a close-up of the local Yucca Mountain stations.

If all ECSZ fault parameters are loosely constrained, however, the DV-FC fault system is estimated to be very similar to the a priori value used (Table 17). If the estimated fault locations are used as a priori values in an inversion in which fault location is tightly constrained, but slip rate and locking depth loosely constrained, the results are almost identical to those where all fault parameters are loosely constrained (Table 18). Similarly, as a check, if the estimated fault locations from the inversion with loose constraints for all parameters are used in an inversion in which only locking depth and

slip rate are estimated (and fault location fixed), the results are identical to those results produced when the fault location is tightly constrained.

Note that the model fault location chosen for the DV-FC fault system is more closely aligned with the NW-trending Furnace Creek strand (also known as the Northern Death Valley fault) than the NNW-trending southern Death Valley fault strand (Figure 80). This results in a model DV-FC fault distance from the repository of 65-70 km. Wernicke et al. (2004) chose to extend the southern, NNW-trending strand of the Death Valley fault to the north for their analysis (Wernicke et al., 2004; Figure 2), which results in a fault distance of ~50 km from the repository.

	SA	OV	PV	DV	
A priori D	12.0	8.0	12.0	16.0	
A priori S	31.0	3.8	3.8	3.8	
A priori X	3691	3520	3467	3421	
Estimated D	12.0±1.0	8.2±7.8	11.5±6.7	32.8±3.6	
Estimated S	-30.4±0.2	-2.6±1.0	-4.5±1.5	-4.9±1.0	
Estimated X	3691.0±2.0	3519.7±10.0	3465.8±9.4	3421.6±6.6	
D constraints	1	8	8	8	
S constraints	1	3	3	3	
X constraints	2	10	10	10	

Table 17. Results of inversion with loose constraints for all parameters (locking depth (D), slip rate (S) and fault distance from the Euler pole (X)). Slip rates are in mm/yr and locking depth and fault location in km.

	SA	OV	PV	DV	
A priori D	12.0	8.0	12.0	16.0	
A priori S	31.0	3.8	3.8	3.8	
A priori X	3691	3520	3466	3422	
Estimated D	12.0±1.0	8.2±7.8	11.5±6.6	33.0±2.4	
Estimated S	-30.4±0.2	-2.6±0.7	-4.5±1.3	-5.0±0.6	
Estimated X	3691.0±1.0	3520.0±1.0	3466.0±1.0	3422.0±1.0	
D constraints	1	8	8	8	
S constraints	1	3	3	3	
X constraints	1	1	1	1	

Table 18. Results of inversion with loose constraints for locking depth (D) and slip rate (S), and tight constraints for fault distance from the Euler pole (X)). A priori fault location was set to the previously estimated values (Table 17). Slip rates are in mm/yr and locking depth and fault location in km.

Regardless of the a priori value used for slip rate on the SAFZ, and despite this parameter being tightly constrained in the least squares inversion, estimated slip rate is ~30.4 mm/yr. A priori locking depth for the SAFZ is less influential. The inversion will not change the a priori locking depth by more than 0.5 km for any input a priori locking depth between 12 and 24 km. Locking depth and slip rate estimates for the ECSZ are quite insensitive to locking depth on the SAFZ, varying by a maximum of ~1 km for locking depth and ~0.2 mm/yr for slip rate. An a priori locking depth of 12 km for the SAFZ produces the lowest RMS of residual velocities between model and GPS results, but the differences in RMS, with varying SAFZ locking depth, are on the 0.0001 mm/yr level (insignificant compared to the errors).

In an inversion where ECSZ slip rates are loosely constrained, but fault location tightly constrained to the values estimated in the previous inversion and SAFZ locking depth and slip rate tightly constrained to 12 km and 31 mm/yr, respectively, the estimated

ECSZ locking depths are 8.2 ± 7.8 km, 11.5 ± 6.6 km, and 33.0 ± 2.4 km for the OV, PV-HM, and DV-FC fault systems respectively (Table 18). Although the locking depths for the OV and PV-HM fault systems are reasonable, the locking depth for the DV-FC fault system is unrealistically deep; approximately 99% of hypocentral depths recorded in the area have been 16 km or shallower (http://quake.geo.berkeley.edu/anss/catalog-search.html). As with the results where the DV-FC fault system was placed unreasonably close to Yucca Mountain, this is caused by the inversion trying to fit the model to the relatively steep GPS velocity profile seen in the local Yucca Mountain network. Estimated slip rates for the OV, PV-HM, and DV-FC fault systems are 2.6 ± 0.7 mm/yr, 4.5 ± 1.3 mm/yr, and 5.0 ± 0.6 mm/yr. Unlike previous geodetic studies, which have estimated either an even distribution of slip rate across the ECSZ (e.g. Bennett et al. 2003), or increased slip rate on the OV fault system (e.g. Gan et al. (2000); Miller et al. (2001)) these results are more in line with many geologic estimates of slip rate (e.g. Beanland and Clark (1994); Dokka and Travis (1990b)), which place a faster slip rate on the PV-HM and DV-FC fault systems than on the OV fault system (see also Table 1). Dixon et al. (2003) also estimate more slip on the DV-FC fault system than the OV fault system, but place less emphasis on the PV-HM fault system. Figures 92 and 93 compare a model profile calculated using the estimated slip rates and locking depth to a model profile calculated using the a priori values. The estimated fault parameters produce an RMS of residual velocities of 0.21 mm/yr for all stations in the profile and 0.22 mm/yr for the local Yucca Mountain stations. This compares with an RMS of residual velocities of 0.32 mm/yr for all stations and 0.29 mm/yr for the local Yucca Mountain stations when the model profile is calculated using the a priori values (evenly distributed slip rate

across the ECSZ).

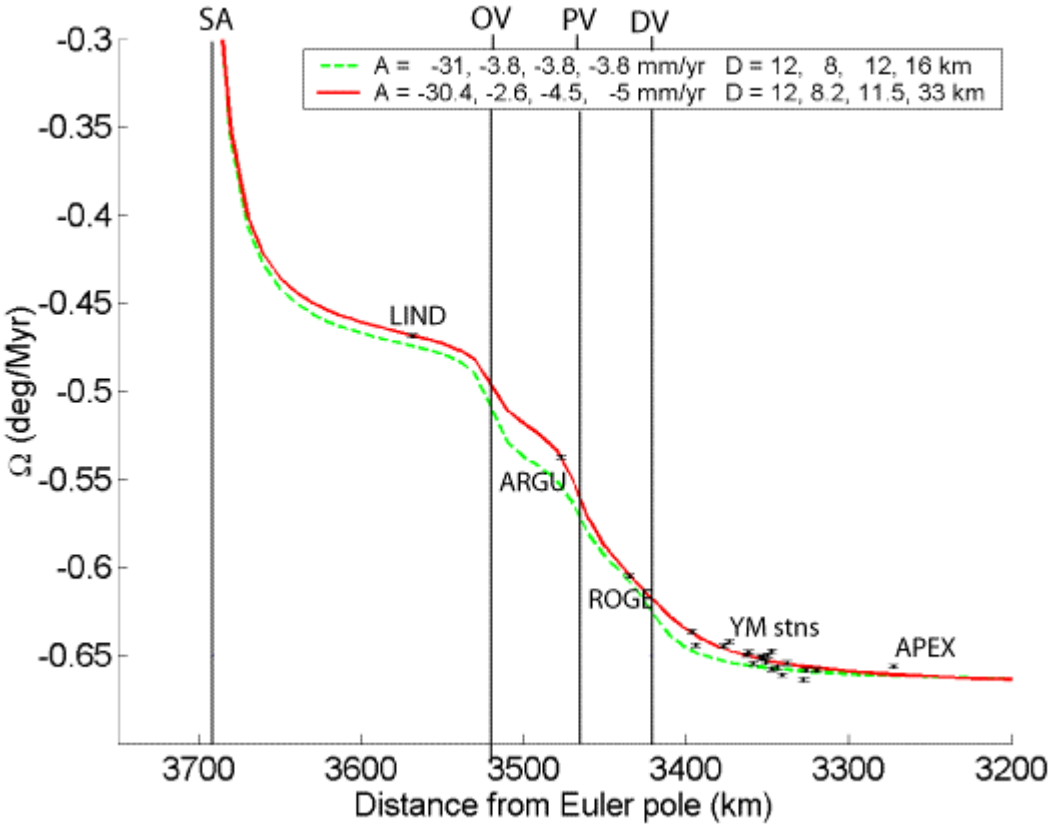

Figure 92. Comparison of model profiles using a priori (green) and estimated (red) slip rates and locking depths, where fault location is tightly constrained and slip rate and locking depth loosely constrained.

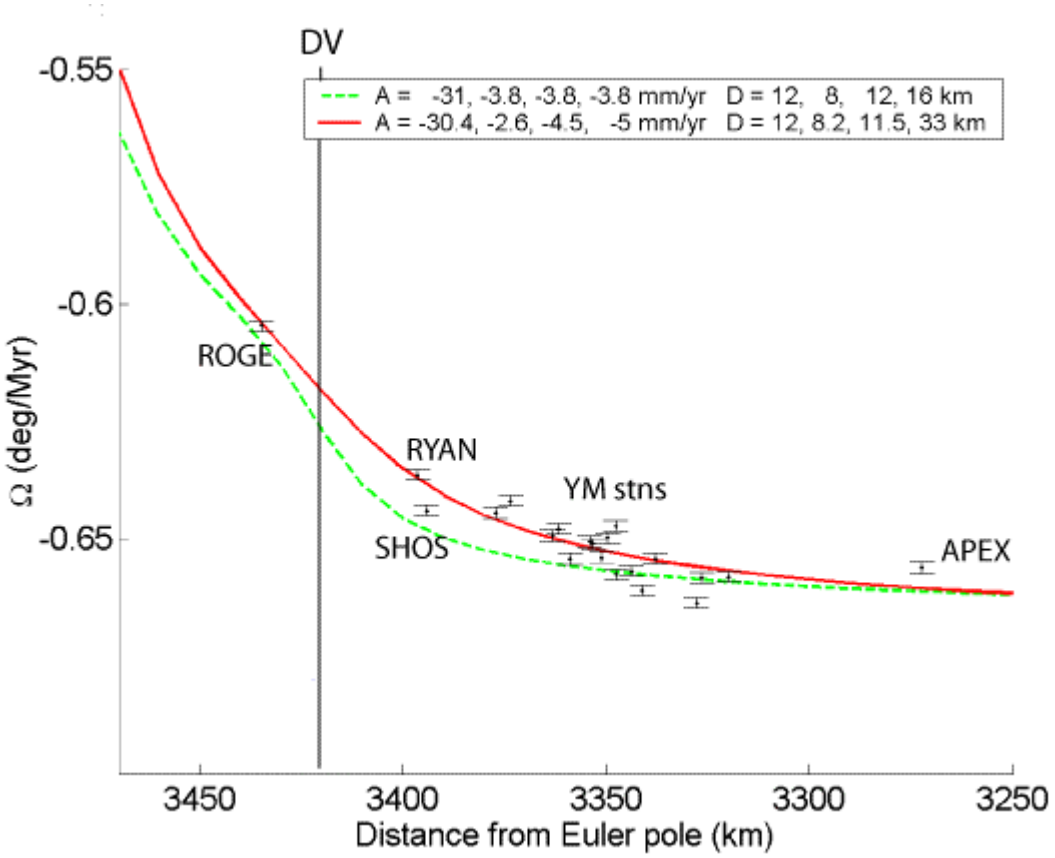

Figure 93. Comparison of model profiles using a priori (green) and estimated (red) slip rates and locking depths. The figure shows a close-up of the local Yucca Mountain stations.

5.7 Inversion for fault parameters with a model fault at Yucca Mountain

The inversion for slip rate was also carried out using an additional model fault located to the east of the DV-FC fault system, as hypothesized by Wernicke et al. (2004). This model fault is termed, in general, the Amargosa Desert (AD) fault after Schweickert and Lahren (1997), although this is purely for reference purposes and does not imply that the model fault is a true representation of the proposed Amargosa Desert fault system. Various different a priori fault locations were tested for the model fault (Figure 94); along the California-Nevada state line (the State Line (SL) fault); along the eastern flank

of Bare Mountain (the Bare Mountain (BM) fault); through Yucca Mountain itself (the Solitario Canyon (SC) fault); approximately 1 km to the east of the repository (the Paintbrush Canyon (PC) fault)) and on the eastern side of Jackass Flats (JF). Again, model fault names are given solely for descriptive purposes, and are based roughly on the closest mapped fault to the location of the model fault. Figure 5 (Chapter 1) shows the locations of actual mapped faults at Yucca Mountain. It is important to note that although the model faults have NW trends (in order to be parallel to the other faults in the model), the mapped faults have more northerly orientations. Furthermore, the mapped faults at Yucca Mountain have fault traces that are approximately 10-25 km long (Simonds et al. (1995)), while the model faults are infinitely long. Many of the mapped faults have primarily normal geologic offsets, while the local model fault is right-lateral strike-slip. It is also highly probable that any local strain accumulation is spread across a number of the mapped faults. However, with the current density of GPS stations it is not possible to invert for fault parameters on multiple local faults. The local model fault used in this study is, therefore, used to represent fault activity on all local faults, and does not necessarily imply that all strain accumulation at Yucca Mountain is occurring at this one location. The aim here is to test for local fault activity at Yucca Mountain in general, and not to provide a detailed picture of individual fault activity. The a priori slip rate for the local model fault was set at 0.5 mm/yr and the a priori locking depth to 16 km.

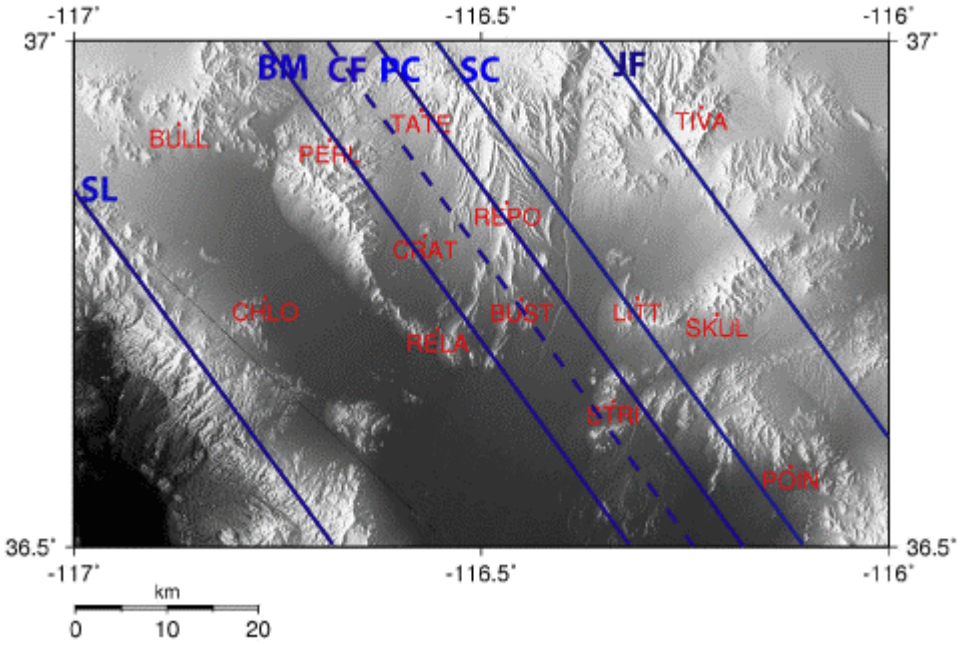

Figure 94. A priori locations for the local model fault

If relatively loose constraints are placed on all fault slip rates and locking depths and tight constraints placed on the location of all faults but the local model fault, the local model fault is estimated to be at the Crater Flat (CF) fault location in Figure 94, regardless of the a priori location used (Tables 19 and 20, Figures 95 and 96). It is not possible to place loose constraints on all parameters because the model becomes unstable and does not converge.

	SA	OV	PV	DV	AD
A priori D	12.0	8.0	12.0	16.0	16.0
A priori S	31.0	3.8	3.8	3.8	0.5
A priori X	3691	3520	3466	3422	3355
Estimated D	11.8±1.0	7.5±3.0	9.9±2.9	13.4±2.6	13.3±2.6
Estimated S	-30.7±0.1	-3.0±0.4	-5.0±0.7	-2.9±0.4	-0.8±0.1
Estimated X	3691.0±1.0	3520.0±1.0	3466.0±1.0	3422.1±1.0	3355.6±2.7
D constraints	1	3	3	3	3
S constraints	1	3	3	3	1
X constraints	1	1	1	1	20

Table 19. Results of inversion with loose constraints for locking depth (D) and slip rate (S), and tight constraints for fault distance from the Euler pole (X) for all faults but the local model fault. A priori fault location was set to previously estimated values (Table 17). Slip rates are in mm/yr and locking depth and fault location in km.

	SL	BM	SC	PC	JF
A priori X	3691	3360	3355	3350	3335
Estimated X	3356.3±2.7	3355.7±2.7	3355.6±2.7	3355.5±2.7	3355.1±2.6

Table 20. A priori and estimated distance of the local model fault from the Euler pole (using constraints given in Table 19)

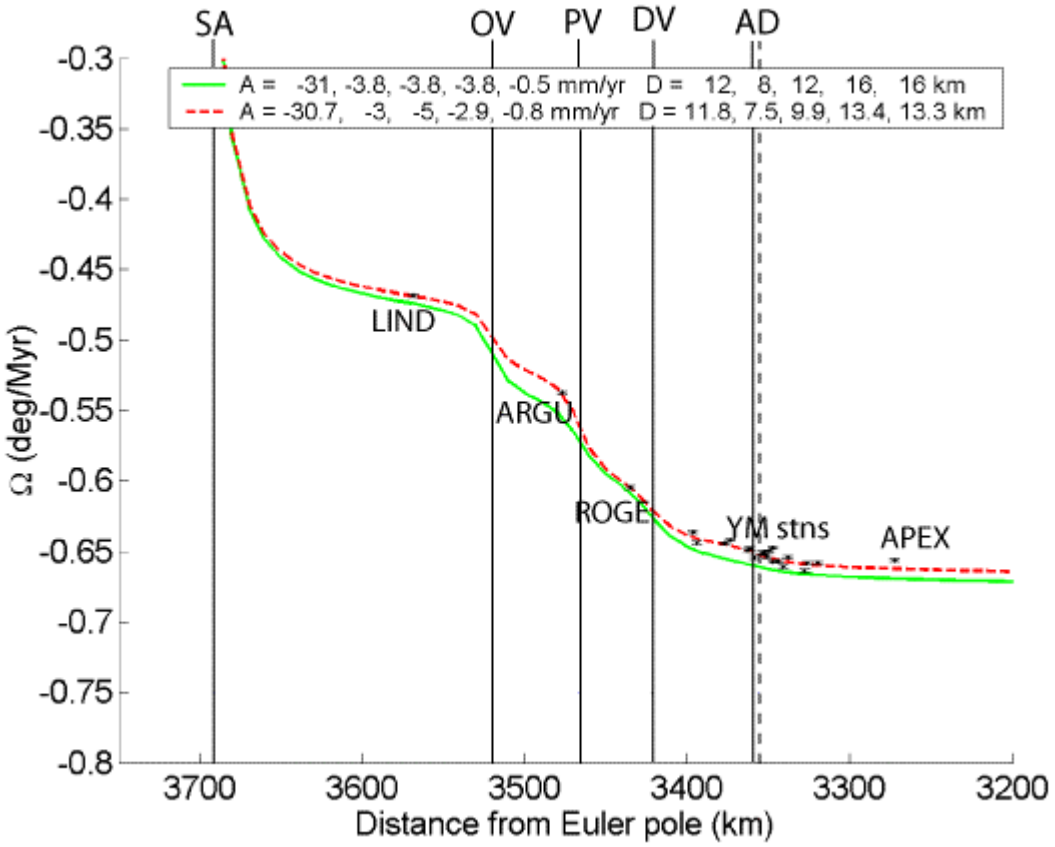

Figure 95. Results of an inversion where all fault parameters except local model fault location were tightly constrained. Solid black lines show a priori fault locations (and estimated fault locations if there was no change to the a priori values). Dotted lines show estimated fault locations. The green profile was calculated using a priori model values. The red profile was calculated using estimated model values.

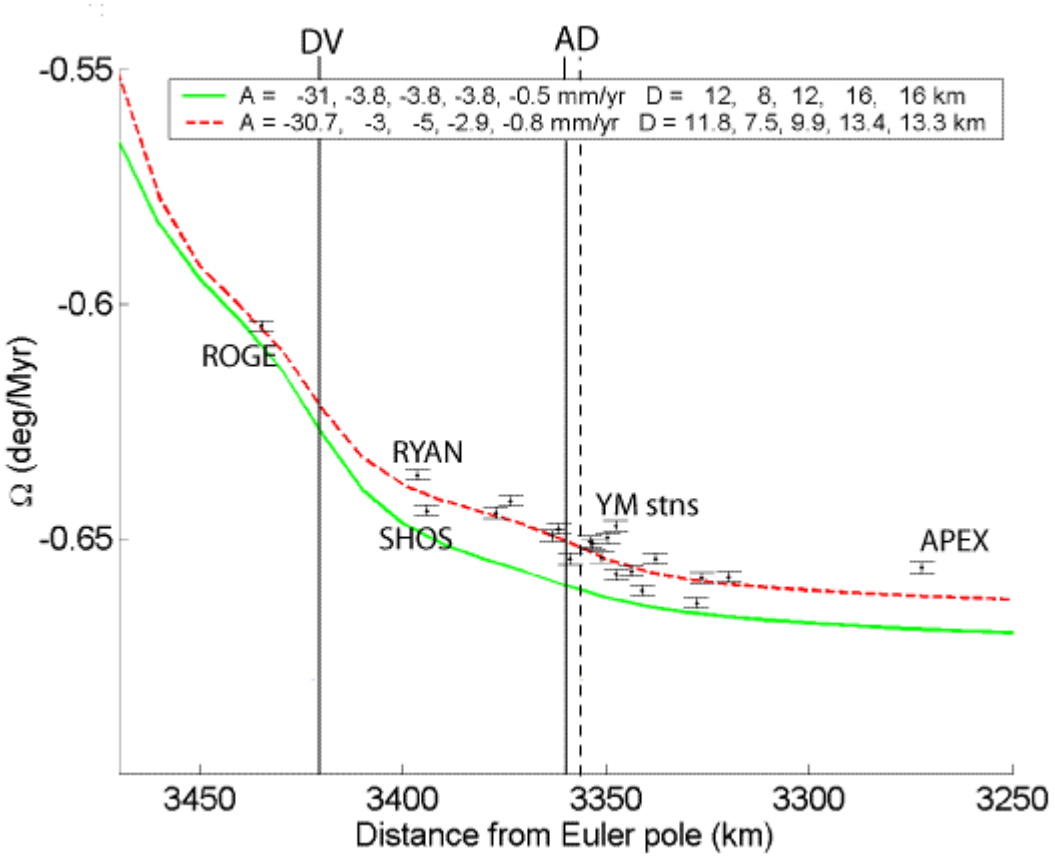

Figure 96. Results of an inversion where all fault parameters except local model fault location were tightly constrained. Solid black lines show a priori fault locations (and estimated fault locations if there was no change to the a priori values). Dotted lines show estimated fault locations. The green profile was calculated using a priori model values. The red profile was calculated using estimated model values. The figure shows a close-up of the local Yucca Mountain stations.

If all a priori fault locations are set to the previously estimated values and this parameter tightly constrained, but slip rates and locking depths loosely constrained, estimated fault locking depths are 11.9 ± 1.0 km, 6.6 ± 4.9 km, 7.6 ± 4.6 km, 11.8 ± 3.4 km and 12.5 ± 3.2 km for the SA, OV, PV-HM-PV, DV-FC and AD model faults respectively (Table 21). Estimated slip rates are 30.8 ± 0.2 mm/yr, 3.2 ± 0.6 mm/yr, 4.7 ± 1.0 mm/yr, 2.8 ± 0.4 mm/yr and 0.8 ± 0.2 mm/yr. This results in an estimated total slip

rate for the ECSZ of 11.5 ± 1.2 mm/yr, which agrees with the GPS estimate of 11.5 ± 0.1 mm/yr (not surprising, since it is the GPS results that are driving the model). A slip rate of 0.8 ± 0.2 mm/yr across structures local to Yucca Mountain would agree with the ~0.9 mm/yr slip rate suggested by Wernicke et al. (2004). Figures 97 and 98 show model profiles using both a priori and estimated fault parameters.

	SA	OV	PV	DV	AD	
A priori D	12.0	8.0	12.0	16.0	16.0	
A priori S	31.0	3.8	3.8	3.8	0.5	
A priori X	3691	3520	3466	3422	3356	
Estimated D	11.9±1.0	6.6±4.9	7.6±4.6	11.8±3.4	12.5±3.2	
Estimated S	-30.8±0.2	-3.2±0.6	-4.7±1.0	-2.8±0.4	-0.8±0.2	
Estimated X	3691.0±1.0	3520.0±1.0	3466.0±1.0	3422.0±1.0	3356.0±0.9	
D constraints	1	5	5	5	5	
S constraints	1	3	3	3	1	
X constraints	1	1	1	1	1	

Table 21. Results of inversion with loose constraints for locking depth (D) and slip rate (S), and tight constraints for fault distance from the Euler pole (X)). A priori fault location was set to the previously estimated values (Table 19). Slip rates are in mm/yr and locking depth and fault location in km.

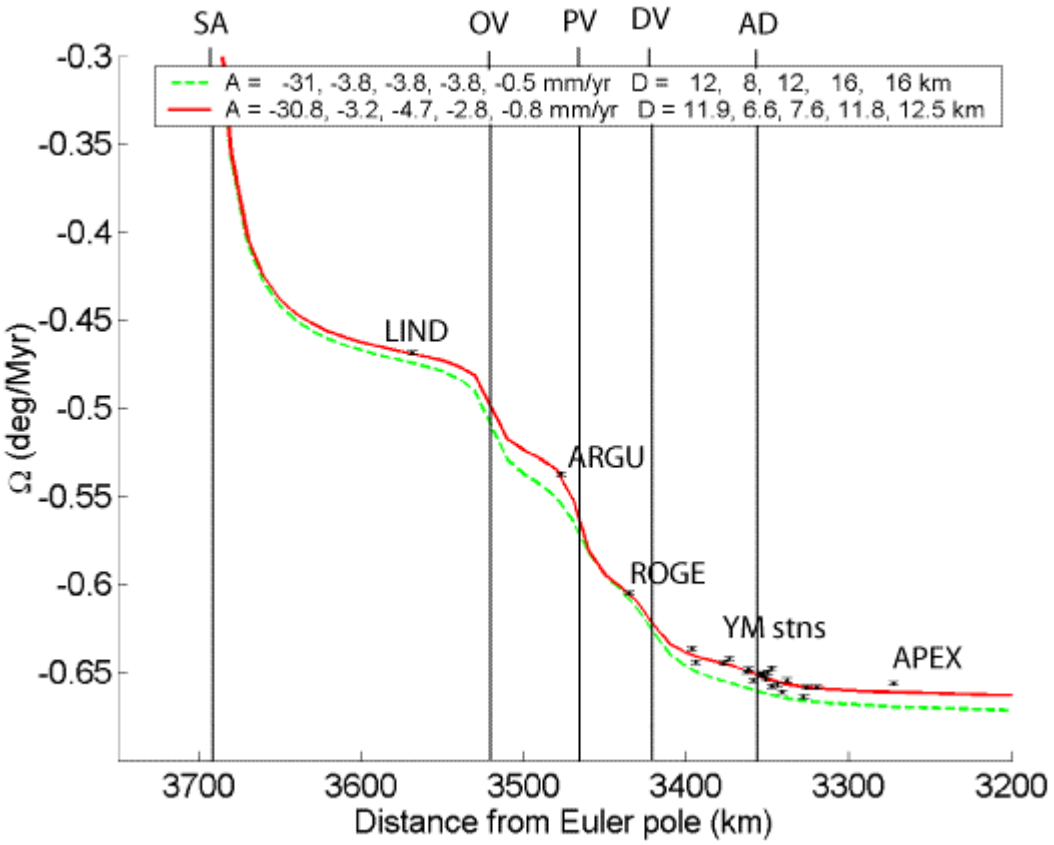

Figure 97. Comparison of model profiles using a priori (green) and estimated (red) slip rates and locking depths, including a model fault at Yucca Mountain, where fault location is tightly constrained and slip rate and locking depth are loosely constrained in the least squares inversion.

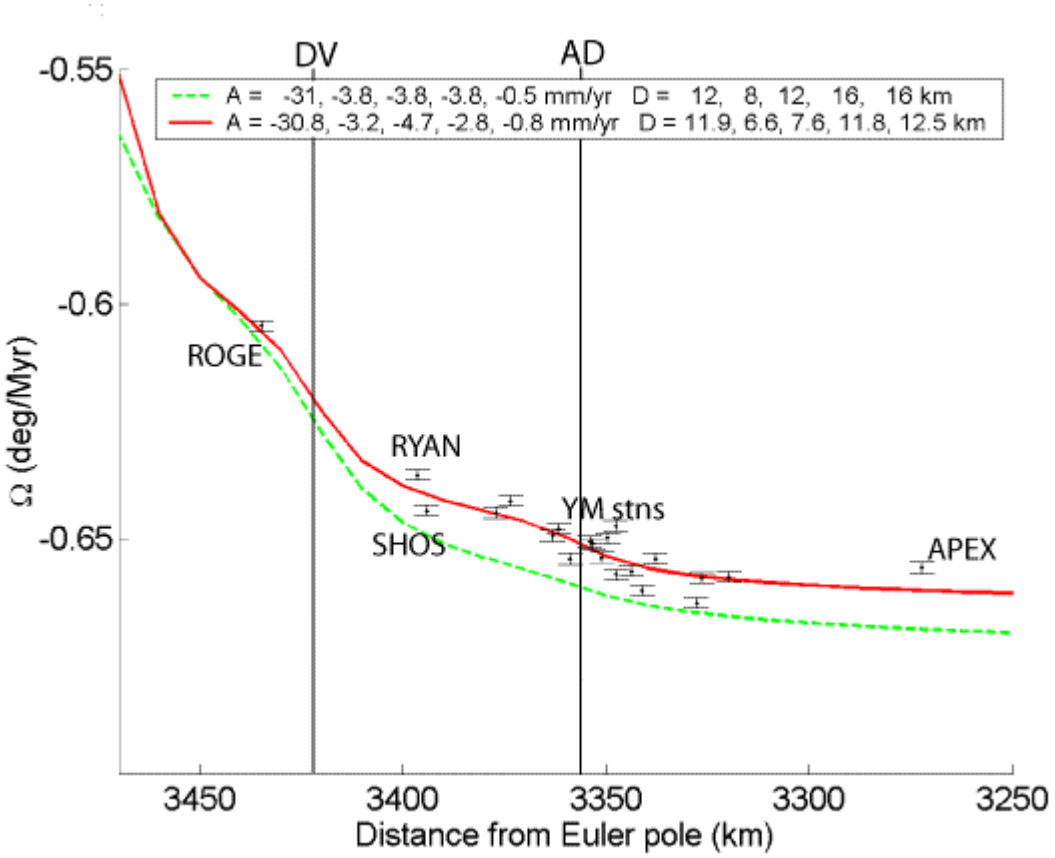

Figure 98. Comparison of model profiles using a priori (green) and estimated (red) slip rates and locking depths, including a model fault at Yucca Mountain, where fault location is tightly constrained and slip rate and locking depth are loosely constrained in the least squares inversion. Figure shows a close-up of the local Yucca Mountain stations.

The RMS of residual velocities for the best fitting solution using only the SA, OV, PV-HM and DV-FC fault systems is 0.21 mm/yr for all stations and 0.22 mm/yr for the local Yucca Mountain stations. The RMS of residual velocities for the solution including an additional model fault at Yucca Mountain is 0.18 mm/yr for all stations and 0.20 mm/yr. This improvement in RMS is barely significant when compared with the estimated errors for the fault parameters. However, the addition of a local model fault does produce a more reasonable estimate of locking depth for the DV-FC fault (11.8 ± 3.4 km) compared with the locking depth estimated when a local model fault is not

included (33.0 ± 2.4 km). Figures 99 and 100 show a comparison of results with and without a model fault at Yucca Mountain.

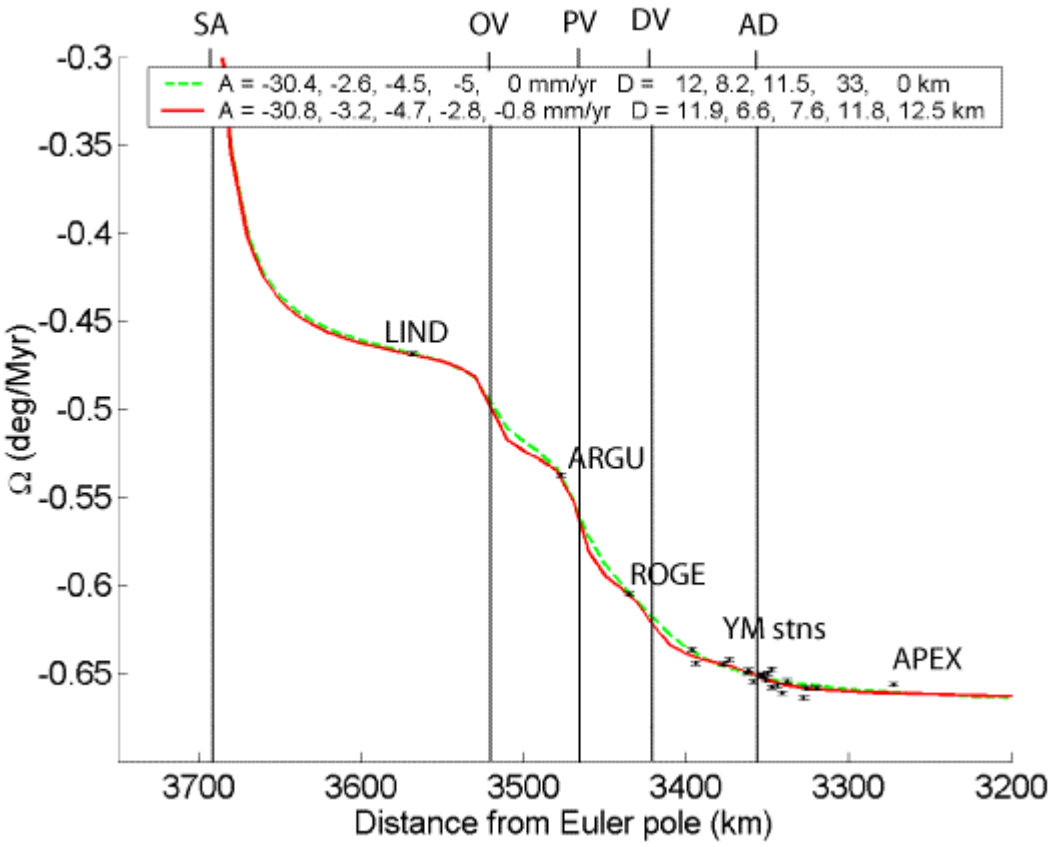

Figure 99. Comparison of model solutions with (red) and without (green) a model fault at Yucca Mountain

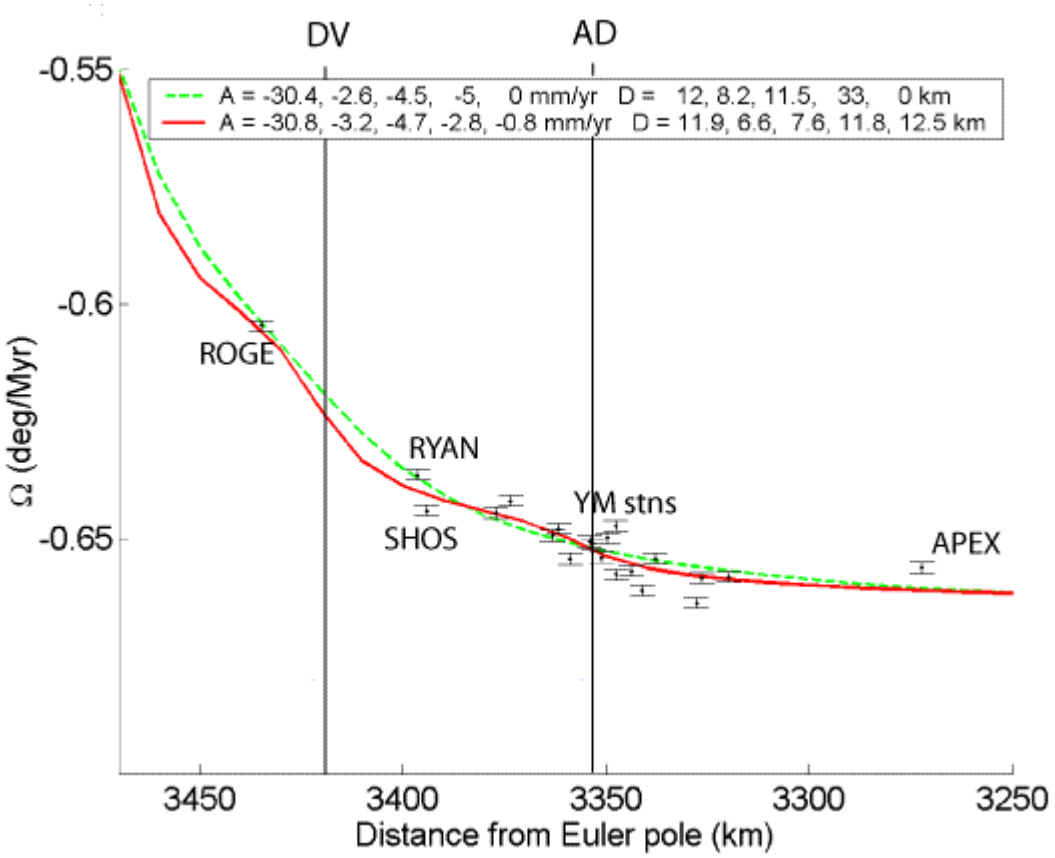

Figure 100. Comparison of model solutions with (red) and without (green) a model fault at Yucca Mountain. Figure shows a close-up of the local Yucca Mountain stations.

5.8 Estimated strain rates based on model results

Expected strain rates at Yucca Mountain, based on the results of the inversions for fault parameters for the ECSZ faults, were calculated using Equation 28 (Savage and Burford, 1973). Appendix N has details on the propagation of errors for modeled strain rate.

$$\dot{\gamma}(x) = \frac{\dot{A}}{\pi}\left(\frac{D}{x^2 + D^2}\right) \qquad [28]$$

where $\gamma(x)$ is total shear strain at distance x from the fault, A is far-field fault slip rate, D is locking depth.

Distance from each fault to the measurement point was obtained by calculating the difference between average distance to the Euler pole for each station cluster and the fault distance to the Euler pole. Strain rates were estimated for all stations < 55 km from Yucca Mountain, the western local Yucca Mountain stations and the eastern local Yucca Mountain stations. These correspond to groups 1, 3 and 4 in Table 8 (Chapter 4). Model strain rates were calculated for the estimated fault parameters for the ECSZ shear zone faults given in Table 18. Model shear strain was not calculated with a local model fault included, since Equation 28 calculates strain at a point. This is an appropriate approximation for faults at a distance from the network, but does not produce a fair comparison with the GPS estimate of strain for faults within the network.

Table 22 compares the estimates of model shear strain with the GPS estimates of total shear strain. The GPS estimate of total shear strain for all stations in the local Yucca Mountain is 18.1 ± 0.7 ns/yr. This is slightly larger (just outside 3σ) than the estimate of shear strain, which is 11.3 ± 1.4 ns/yr. The GPS estimate of total shear for the western local stations is 15.7 ± 1.1 ns/yr. This compares with a model strain estimate of 13.6 ± 1.6 ns/yr, which actually agrees with the GPS estimate within 1σ. The GPS estimate of total shear strain for the eastern local stations is 25.1 ± 1.3 ns/yr. This is

significantly larger than the 8.7 ± 1.1 ns/yr estimated using the model results. As expected the model strain rates decrease with increasing distance from the ECSZ. However, the GPS results do not follow this pattern and are highest for the eastern cluster of stations. These results suggest that it is possible to explain the GPS estimate of shear strain for the western cluster of stations using only the ECSZ faults, but that the eastern cluster of stations is deforming in a pattern that does not conform to simple models of strike-slip deformation across the ECSZ faults.

	All stations	Western stations	Eastern stations
Model	11.3 ± 1.4	13.6 ± 1.6	8.9 ± 1.1
GPS	18.1 ± 0.7	15.7 ± 1.1	25.1 ± 1.3

Table 22. Comparison of model and GPS estimates of total shear strain, for all stations in the local Yucca Mountain network and the western and eastern clusters of stations in the local network.

5.9 Estimation of possible earthquake magnitude and recurrence interval

It is highly probable that if a ~0.8 mm/yr slip rate does exist across the Yucca Mountain area it is, in reality, spread across a number of the mapped faults. The installation of additional GPS receivers and use of more detailed fault models could also change this estimate. However, it is useful to assess what this slip rate could mean in terms of possible earthquakes. The regression of Anderson et al. (1996) was therefore used to predict expected moment magnitude (Equation 29) for a variety of different rupture lengths. This regression is based on a least squares fit through 43 earthquake recordings. Slip rates of 0.8 mm/yr (from Table 21) and 0.9 mm/yr (Wernicke et al. 2004) were used for this hypothesized fault. I also tested slip rates of 0.2 mm/yr and 1.4

mm/yr, 3σ either side of the 0.8 ± 0.2 mm/yr estimate, to assess the sensitivity of the earthquake models to this rate.

$$M_w^e = 5.12 + 1.16 \log L - 0.20 \log S \quad [29]$$

where rupture length L is in units of km and slip rate S is in units of mm/yr.

Geodetic moment rate was calculated (Equation 30) using the same rupture lengths input to Equation 29, with locking depths of 7 km, 12 km (Table 21) and 12 km (Wernicke et al., 2004) and slip rates of 0.5 mm/yr, 0.8 mm/yr (Table 21) and 0.9 mm/yr (Wernicke et al., 2004)

$$\dot{M}_o^g = \mu LDS \quad [30]$$

where rupture length L and locking depth D are input as cm, slip rate S as cm/yr and shear modulus μ fixed at 3x1011 dyne/cm^2.

Expected moment magnitude was converted to expected moment (Equation 31) using the relation of Hanks and Kanamori (1979).

$$\log M_o^e = 1.5 M_w^e + 16.05 \quad [31]$$

Recurrence interval was calculated using Equation 32 (Wesnousky, 1986). This assumes that a single earthquake (along with its associated foreshocks and aftershocks)

will account for all seismic slip on the fault (the maximum magnitude earthquake model).

$$T = M_o^e \Big/ \dot{M}_o^g \qquad [32]$$

Table 23 shows expected moment magnitudes and recurrence intervals for a hypothesized fault with the estimated slip rates and locking depths from both Section 5.7 of this study and the findings of Wernicke et al. (2004) and a variety of rupture lengths. The mapped faults at Yucca Mountain have average lengths of 10-25 km (Simonds et al., 1995) so to obtain a 45 km rupture length it would be necessary to rupture multiple fault segments. Anderson et al. (1996) indicate that a slower slipping fault will produce a larger magnitude earthquake than a faster slipping fault, if rupture length is held fix. This means that the 0.2 mm/yr slip rate will produce slightly larger magnitude earthquakes than the slip rate of 1.4 mm/yr, for example moment magnitudes of 6.8 and 6.6, respectively, for a 20 km rupture length with a 12 km locking depth. However, the faster slip rates dramatically reduce the recurrence time for these model earthquakes, reducing the possibility of a magnitude 6.6-6.8 earthquake from ~11,095 years to ~1031 years.

Slip rate (mm/yr)	Rupture length (km)	Locking depth (km)	Expected M_w	Recurrence interval (yr)
0.2	10	12	6.4	6643
0.2	20	12	6.8	11095
0.2	30	12	7.0	14977
0.2	45	12	7.2	20218
0.8	10	12	6.3	1096
0.8	20	12	6.6	1830
0.8	30	12	6.9	2470
0.8	45	12	7.1	3335
0.9	10	12	6.3	940
0.9	20	12	6.6	1570
0.9	30	12	6.8	2120
0.9	45	12	7.0	2861
1.4	10	12	6.3	618
1.4	20	12	6.6	1031
1.4	30	12	6.8	1392
1.4	45	12	7.0	1880

Table 23. Expected moment magnitudes of recurrence intervals for hypothetical faults with slip rates of 0.5 mm/yr, 0.8 mm/yr, and 0.9 mm/yr and locking depths of 7 km, 12 km and 12 km, for a variety of possible rupture lengths.

5.10 Discussion of this chapter

Modeling the ECSZ faults in a North America fixed reference frame has a number of problems, namely that an offset must be applied to the model results in order that they fit the GPS data. A technique was therefore applied whereby the model was described in a Pacific fixed reference frame, in which GPS results and fault displacements are expressed as rotations about the North American Euler pole. This eliminates the need for

a model offset and allows a better determination of the influence of the SAFZ on Yucca Mountain. The GPS rotation rates were used, in a constrained, weighted, least squares inversion, to estimate the location, slip rate and locking depths of faults that may influence the strain field at Yucca Mountain.

In an inversion for ECSZ fault parameters, estimated fault slip rates were 30.4 ± 0.2 mm/yr, 2.6 ± 0.7 mm/yr, 4.5 ± 1.3 mm/yr and 5.0 ± 0.6 mm/yr for the SA, OV, PV-HM-PV and DV-FC fault systems respectively. These rates follow a similar pattern of increasing slip rate towards the east to that estimated by Dixon et al. (2003), but put a greater emphasis on the PV-HM fault system. Estimated locking depths were 12.0 ± 1.0 km, 8.2 ± 7.8 km, 11.5 ± 6.6 km and 33.0 ± 2.4 km for the SA, OV, PV-HM and DV-FC fault systems respectively. Although these values agree with previous predictions that locking depths could increase from west to east across the ECSZ, due to more recent volcanic activity in the west (for example, Dixon et al. (1995)), this locking depth for the DV-FC fault system is very deep, and unlikely considering the local geologic setting; approximately 99% of earthquakes in the region occur at depths shallower than 16 km (http://quake.geo.berkeley.edu/anss/catalog-search.html). The unusually deep estimate of locking depth for the DV-FC fault system is caused by the inversion trying to fit the model through the relatively steep velocity gradient at Yucca Mountain. If locking depths and slip rates are tightly constrained, but fault location is loosely constrained, there is a similar effect in that to fit the velocity gradient at Yucca Mountain the inversion places the DV-FC fault system unreasonably close to Yucca Mountain compared with geologic maps of the area.

A model using these fault parameters produces an RMS of residual velocity differences with the GPS results of 0.21 mm/yr for all stations in the profile and 0.22 mm/yr for the local Yucca Mountain stations. For comparison, if the slip rate across the ECSZ is divided evenly between the three major fault systems, each fault system is allocated a 3.8 mm/yr slip rate. Using the a priori locking depths of 8, 12 and 16 km for the OV, PV-HM and DV-FC fault systems results in an RMS of residual velocity differences of 0.32 mm/yr for all stations and 0.29 mm/yr for the local Yucca Mountain stations.

If the inversion is adjusted to include a model fault at Yucca Mountain, estimated slip rates are 30.8 ± 0.2 mm/yr, 3.2 ± 0.6 mm/yr, 4.7 ± 1.0 mm/yr and 2.8 ± 0.4 mm/yr for the SA, OV, PV-HM and DV-FC fault systems respectively. The slip rate for the local model fault is estimated to be 0.8 ± 0.2 mm/yr. The slip rate on the DV-FC fault is reduced to account for the slip on the local model fault. This results in a total ECSZ slip rate of 11.5 ± 1.2 mm/yr, which agrees with the GPS constraint on ECSZ slip rate of 11.5 ± 0.1 mm/yr (not surprising since the GPS results are driving the model). Estimated locking depths are 11.9 ± 1.0 km, 6.6 ± 4.9 km, 7.6 ± 4.6 km, 11.8 ± 3.4 km and 12.5 ± 3.2 km for the SA, OV, PV-HM-PV, DV-FC and AD fault systems. This puts the locking depth of the DV-FC fault system at a more reasonable level. The RMS of residual velocity differences with the GPS results is 0.18 mm/yr for all stations in the profile and 0.20 mm/yr for the local Yucca Mountain stations. This is only a marginal improvement on the RMS fit for a model profile with no local fault.

Although, therefore, the addition of a local fault at Yucca Mountain does not significantly reduce the RMS of residual velocity differences between the GPS and model results, it does produce a more reasonable estimate of locking depth and fault location for the DV-FC fault system. These results, therefore, agree with the findings of Wernicke et al. (2004) that one way to explain the data is to add a local fault to the model.

Although the inversion for fault parameters estimates a model fault location through Crater Flat, ~5 km to the west of Yucca Mountain, the results do not imply that all estimated slip within the local network is necessarily being accommodated at this one location. This model fault is used to represent all activity across faults at Yucca Mountain, but in reality it is likely that deformation could be accommodated by a number of faults. The model results do suggest, however, that it is unlikely that significant deformation is being accommodated along the California - Nevada state line (in the approximate location of the Stateline fault); loose constraints on local fault location will place the fault further east, even if the a priori location is along the state line, while tight constraints and an a priori fault location at the state line will result in an unreasonably deep locking depth for the local model fault (28.5 ± 4.0 km). The primary aim of this part of the study was to investigate the existence of deformation at Yucca Mountain that cannot be explained by the ECSZ faults, but not to provide detailed estimates of fault parameters for the local Yucca Mountain faults. It is likely that improvements in the fault models will result in a different estimate of slip rate for faulting at Yucca Mountain,

and may place the likely location of higher slip rate at a different location to Crater Flat or spread it across a number of faults. A higher density of GPS stations within the local Yucca Mountain network will help to improve these results. This is clearly illustrated by the fact that with the current station density, a change in slip rate at one station will significantly change the estimated model slip rate across the Yucca Mountain area. For example, a change in the velocity for station CHLO of ~0.2 mm/yr will change the estimated slip rate on the local model fault by ~0.3 mm/yr. This also illustrates the importance of obtained the most reliable estimates of GPS velocity possible.

Estimated model shear strain for all stations in the local Yucca Mountain network, based on the estimated fault parameters for the SA, OV, PV-HM and DV-FC faults, is 11.3 ± 1.4 ns/yr. This compares with a GPS estimate of total shear strain for all stations in the local network of 18.1 ± 0.7 ns/yr, so only agrees to within 4σ. Estimated model shear for the stations in the western cluster of the local network is 13.6 ± 1.6 ns/yr. This agrees to within 1σ with the GPS estimate of 15.7 ± 1.1 ns/yr. Estimated model shear for the eastern cluster of stations is 8.9 ± 1.1 ns/yr. This is significantly lower than the 25.1 ± 1.3 ns/yr estimated from the GPS results. This is important, because it suggests that although it is possible to explain the GPS results for the western cluster of stations using dislocation models of the ECSZ faults (with no local fault at Yucca Mountain necessary), the eastern local stations do not conform to a model where the majority of strain measured at Yucca Mountain is due to the ECSZ. Although this GPS estimate of high shear strain rate for the eastern cluster could be caused by NW-trending, right-lateral, strike-slip faults across the Yucca Mountain network, an alternative and

perhaps more likely explanation is that the source of the measured strain is left-lateral strike-slip deformation across the NE-trending RVFZ. The GPS estimate of strain rate is ambiguous, and can either indicate right-lateral shear strain on NW-trending faults or left-lateral shear strain on NE-trending faults. This highlights the focus for future studies, in that the next logical step is to model deformation across the RVFZ.

An alternative explanation for the observed velocity profile at Yucca Mountain could be that it is the effect of earthquake cycle on the interseismic deformation field. With increasing time after the last earthquake, the deformation field of a fault will extend outwards (Dixon et al., 2003). This will have an effect on the model profile similar to that of deepening the locking depth. The fact that the DV-FC is late in its earthquake cycle could also, therefore, help to explain the unreasonably deep locking depth estimated in the inversion with no local fault.

Also important for future study is the effect of postseismic deformation on the strain field at Yucca Mountain. Although the time series do not show any obvious evidence of postseismic deformation (that is, there are no significant local changes in velocity of the period of time observed in this study), it is possible that the postseismic deformation fields from the 1992/2002 Little Skull Mountain earthquake, the 1999 Hector Mine earthquake and even the 1872 Owens Valley and 1915-1954 Central Nevada Seismic Zone earthquakes are affecting the GPS results. A longer time series of continuous GPS measurement for the Yucca Mountain network should help to resolve the question of whether the local Yucca Mountain stations are experiencing the effects of the

Little Skull Mountain and other recent earthquakes.

Future modeling of strain in the Yucca Mountain area should include the three-dimensional geometry of mapped faults projected from the surface, hypothetical faults at depth, the interrelations of normal, NW-striking right-lateral and NE-striking left-lateral faults and a representation of the effect of earthquake cycle and postseismic deformation on the models.

6. Conclusions

GPS data were processed from 28 continuous BARGEN stations in southern Nevada and California; 16 of these were stations in the local Yucca Mountain network and 12 were far-field stations in the Eastern California Shear Zone and the Basin and Range. Although data were available from May 1999, data from 1999 were excluded due to a number of offsets in the time series caused by the 1999 Hector Mine earthquake and hardware changes in the network. Data were therefore processed from January 2000 to June 2004. This is a total of 4.5 years of data, which is the amount of data suggested by Blewitt and Lavallée (2002) to minimize the effects of seasonal signals on results.

The GPS data were processed independently by different groups using both the GIPSY and GAMIT (Wernicke et al., 2004; Bennett et al., 2003) software packages, then compared for quality assurance purposes. The RMS of residual velocity differences between the two solutions was 0.06 mm/yr for the east and 0.10 mm/yr for the north. The velocity solution for the local Yucca Mountain network has a relatively smooth signal, showing NW-trending right-lateral strike-slip and increasing in magnitude from east to west. The magnitude of the velocity contrast, from stations TIVA to BULL, is 0.95 ± 0.04 mm/yr. There is a steep change from higher to lower velocities (relative to stable North America) just east of Yucca Mountain, resulting in a relatively steep velocity gradient across the local Yucca Mountain network.

The estimate of total shear strain rate for all stations in the local Yucca Mountain network is 18.4 ± 0.7 ns/yr, oriented at N16±1^{o}W. These stations measure a dilitation rate of 1.8 ± 0.7 ns/yr. Although the rate of extension is considerably lower than the 50 ± 9 ns/yr predicted by Wernicke et al. (1998), the total shear strain rate is higher than, for example, the 10-14 ns/yr of expected shear strain predicted by Savage et al. (1999).

The strain field across Yucca Mountain is not uniform. Total shear strain rate for the western local stations is a little lower than the estimate for all local stations, at 15.7 ± 1.2 ns/yr, oriented at N20 ± 2^{o}W. However, the dilitation rate is higher, at 6.3 ± 1.2 ns/yr. Total shear strain for the eastern local stations is 25.1 ± 1.4 ns/yr, oriented more northerly at N8 ± 2^{o}W. This is higher than expected and higher than the shear strain for the western stations, which is surprising since the western stations are closer to the ECSZ. Also unexpected is that the dilitation rate for the eastern local stations is -4.6 ± 0.4 ns/yr (showing contraction).

The GPS results were used to put a constraint on total ECSZ slip rate. When velocities are calculated parallel ('fault parallel') and perpendicular ('fault perpendicular') to a great circle about the North American Euler pole, the difference in fault parallel velocity between stations LIND (on the Sierra Nevada block) and RYAN (on the eastern flank of the DV-FC fault system) is 10.4 ± 0.1 mm/yr. The fault parallel velocity difference between stations LIND and APEX (located near Las Vegas) is 11.5 ± 0.1 mm/yr and between LIND and ECHO (in the central Basin and Range) is 12.6 ± 0.1 mm/yr.

The shear strain rate for the ECSZ stations is estimated to be 43.9 ± 0.8 ns/yr, oriented at N22.7 ± 0.4^{o}W. However, there is also evidence of extension across the ECSZ, with a dilitation rate estimated to be 16.7 ± 0.8 ns/yr. This is also shown by the fact that the velocity vectors for the ECSZ stations rotate counter-clockwise from NNW, in the east (e.g. station RYAN), to NW, in the west (e.g. station LIND).

Total shear strain rate for the Basin and Range stations is estimated to be 8.6 ± 0.5 ns/yr, oriented at N18 ± 1^{o}W. This is much larger than the dilitation rate, which is -1.0 ± 0.5 ns/yr. This concurs with recent suggestions that right lateral strike slip is perhaps the most dominant form of deformation in the current tectonic regime of the Basin and Range. Although stations RAIL, ECHO, and ALAM have velocities that are so small that there is little evidence of right-lateral shear in the velocity field, station TONO, the most westerly of the Basin and Range stations, has a velocity vector that matches that of the ECSZ velocity vectors.

An elastic dislocation model was used to model the faults of the ECSZ. Since modeling the GPS velocities in a North American fixed reference frame requires the use of an offset parameter (because the location of zero model velocity is uncertain) the results were instead plotted as a profile relative to a Pacific plate fixed reference frame. Velocities relative to the Pacific plate fixed frame will naturally decrease with increasing proximity to the North American Euler pole, so to avoid the problem of having to correct the elastic dislocation model this, the GPS results were first converted to velocities

parallel to a great circle around the Euler pole, then converted to rotation rates around the pole. The elastic displacement model was also adapted to use rotation rates rather than velocities.

The GPS rotation rates were used, in a constrained, weighted least squares inversion, to estimate fault parameters for the major ECSZ faults. The SAFZ was also included in the model, but its fault parameters were tightly constrained, because this study did not include any GPS stations in the near-field of the SAFZ.

In an inversion including the SA, OV, PV-HM and DV-FC fault systems, the estimated slip rates were 30.4 ± 0.2 mm/yr, 2.6 ± 0.7 mm/yr, 4.5 ± 1.3 mm/yr and 5.0 ± 0.6 mm/yr respectively. Estimated locking depths were 12.0 ± 1.0 km, 8.2 ± 7.8 km, 11.5 ± 6.6 km and 33.0 ± 2.4 km respectively. Although these values agree with previous suggestions that locking depth could increase from west to east across the ECSZ, due to the more recent volcanic activity in the west (for example, Dixon et al., 1995) this locking depth for the DV-FC fault system is very deep and therefore unlikely considering the local geology and earthquake history. The unusually deep model locking depth for the DV-FC fault system is caused by the fact that the inversion is trying to fit the model through the relatively steep velocity gradient across the local Yucca Mountain network. If locking depths and slip rates are tightly constrained in the inversion, but fault location loosely constrained, there is a similar effect in that, to fit the velocity gradient at Yucca Mountain, the inversion places the DV-FC fault system unreasonably close to Yucca Mountain compared with geologic maps of the area.

A model using these fault parameters produces an RMS of residual velocity differences between the model and GPS results of 0.21 mm/yr for all stations in the profile and 0.22 mm/yr for the local Yucca Mountain stations only. For comparison, if the slip rate across the ECSZ is divided evenly between the three major fault system (3.8 mm/yr based on the GPS constraint of 11.5 mm/yr of total slip across the ECSZ), and the a priori locking depths of 8, 12 and 16 km for the OV, PV-HM and DV-FC fault systems are used, the RMS of residual velocity differences is 0.32 mm/yr for all stations and 0.29 mm/yr for the local Yucca Mountain stations.

Hypothetically, if a local model fault at Yucca Mountain is included in the inversion for fault parameters, estimated slip rates are 30.8 ± 0.2 mm/yr, 3.2 ± 0.6 mm/yr, 4.7 ± 1.0 mm/yr and 2.8 ± 0.4 mm/yr for the SA, OV, PV-HM and DV-FC fault systems respectively. The slip rate for the model fault at Yucca Mountain is estimated to be 0.8 ± 0.2 mm/yr. This results in a total slip rate of 11.5 ± 1.2 mm/yr for the ECSZ, which agrees with the GPS estimate of 11.5 ± 0.1 mm/yr. Estimated locking depths are 11.9 ± 1.0 km, 6.6 ± 4.9 km, 7.6 ± 4.6 km, 11.8 ± 3.4 km and 12.5 ± 3.2 km for the SA, OV, PV-HM-PV-HM, DV-FC and local model faults respectively. This puts the DV-FC locking depth at a more reasonable level.

The RMS of residual velocity differences between the GPS and model results is 0.18 mm/yr for all stations in the profile and 0.20 mm/yr for the local Yucca Mountain stations. This is only a marginal improvement on the RMS fit for a model profile with no local fault. However, the addition of a local model fault does produce a more reasonable

estimate of locking depth and fault location for the DV-FC fault system. These results, therefore, corroborate the findings of Wernicke et al. (2004), suggesting that one way to explain the velocity gradient at Yucca Mountain is to add an active local fault (or number of faults) to the model, and that it is difficult to explain the data satisfactorily if no local fault activity is assumed.

Although the inversion estimates a location for the local model fault at Crater Flat, the fault geometry for the local model fault is highly simplified and not truly representative of mapped faults in the area. The model fault is oblique to the orientation of mapped faults at Yucca Mountain, and is infinitely long while the mapped faults are approximately 10-25 km long (Simmonds et al., 1995). While there are numerous mapped faults in the area, the current density of the GPS network does not allow us to include multiple faults in the inversion. The aim of using this local model fault is therefore not to produce accurate values for the fault parameters along a local fault at Yucca Mountain, but rather to test for the existence of tectonic activity at Yucca Mountain that cannot be explained using simple dislocation models of the ECSZ faults. In reality, this estimated slip rate may be accommodated by a number of faults in the area, and the use of additional GPS stations and improved fault models may change the estimated total slip rate. What these results do show is that the addition of a local fault at Yucca Mountain to the model seems to explain the GPS data better than a model using only the SAFZ and ECSZ faults, suggesting that it is important to continue working to provide a more detailed picture of deformation within the local Yucca Mountain network.

Predicted total right lateral shear strain rates for all stations in the local Yucca Mountain network, calculated by inputting the estimated fault parameters for the SA, OV, PV-HM and DV-FC fault into an elastic strain model, is 11.3 ± 1.4 ns/yr. This compares with a GPS estimate of total shear strain for all stations in the local network of 18.1 ± 0.7 ns/yr, so only agrees to within 4σ. However, the GPS results show that strain rate is not uniform across the local network. Estimated model shear for the stations in the western cluster of the local network is 13.6 ± 1.6 ns/yr. This agrees, to within 1σ, with the GPS estimate of 15.7 ± 1.1 ns/yr. Estimated model shear for the eastern cluster of stations is 8.9 ± 1.1 ns/yr. This is significantly lower than the 25.1 ± 1.3 ns/yr estimated from the GPS results for the eastern cluster of stations. This result is important, and indicates that although it is possible to explain the GPS results for the western cluster of stations using dislocation models of the ECSZ faults (with no local model fault necessary), the eastern local stations do not conform to a model where the majority of strain measured at Yucca Mountain is caused by the ECSZ. Although this could be caused by NW-trending, right-lateral, strike-slip faults to the east of Yucca Mountain, an alternative and perhaps more likely explanation is that the source of the measured strain is left-lateral strike-slip deformation across the NE-trending RVFZ. Note that the GPS estimate of shear strain is ambiguous, and may represent left-lateral strike-slip on a NE-trending fault system. This highlights the focus for future studies, in that the next logical step is to model deformation across the RVFZ.

An alternative explanation for the observed velocity profile at Yucca Mountain

could be the effect of earthquake cycle on the interseismic deformation field. With increasing time after the last earthquake, the deformation field of a fault will extend outwards (Dixon et al., 2003). It will have an effect on the model profile similar to that of deepening the locking depth. The fact that the DV-FC is late in its earthquake cycle could also, therefore, help to explain the unreasonably deep locking depth estimated in the inversion with no local fault.

One of the important conclusions of this study is that the results seem to indicate some level of deformation occurring across the Yucca Mountain GPS network that cannot easily be explained by modeling of deformation across the ECSZ faults using simple elastic dislocation models. One explanation for this could be that the fault models are simply not representative of faulting in this area and that more complex fault models, taking into account factors such as varying fault orientation, oblique slip, a more realistic rheology, and finite fault lengths, will produce a better fit to the GPS results. Another could be that there is, indeed, some level of right-lateral strike-slip deformation occurring across the local faults at Yucca Mountain that is higher than the geologic rates, in which case the next step is to model multiple faults and attempt to obtain more realistic estimates of slip rate and locking depth for these faults. In order to do this, additional GPS stations are needed within the local network, since the current models are highly sensitive to errors for each individual GPS station and are too sparsely located to produce stable results for multiple local faults in a model inversion. Another possible explanation is that the GPS network is also measuring left-lateral strike-slip deformation occurring across the RVFZ, and perhaps some element of postseismic deformation from any

number of earthquakes that have occurred in both the near- and far-field of Yucca Mountain. Activity across the RVFZ seems a particularly likely explanation, in that the GPS estimate of shear strain rate for the western local stations (stations at and to the west of Yucca Mountain, within the local network) agrees with an estimate of shear strain rate based on the inversion results for the ECSZ faults (not including a local model fault), but this is not possible for the eastern cluster of stations, for which the GPS estimate of shear strain rate is significantly higher than an estimate based on models of the ECSZ faults. In all likelihood a combination of all these factors is contributing to the observed strain field.

References

Anderson, J. G., Wesnousky, S. G., and Stirling, M. W. (1996). "Earthquake size as a function of fault slip rate." Seismological Society of America, 86(3), 683-690.

Anderson, R.E., compiler, 1998, Fault number 1065, Rock Valley fault zone, in Quaternary fault and fold database of the United States, ver 1.0: U.S. Geological Survey Open-File Report 03-417, http://qfaults.cr.usgs.gov.

Beanland, S., and Clark, M. M. (1991). "The Owens Valley Fault Zone, Eastern California, and Surface Faulting Associated with the 1872 Earthquake." U.S. Geological Survey, 1982, 29p.

Bell, J. W., de Polo, C. M., Ramelli, A., Sarna-Wojcicki, A. M., and Meyer, C. E. (1999). "Surface faulting and paleoseismic history of the 1932 Cedar Mountain earthquake area, west-central Nevada, and implications for modern tectonics of the Walker Lane." Geological Society of America Bulletin, 111(6), 791-807.

Bennett, R. A., Wernicke, B. P., Davis, J. L., Elosegui, P., Snow, J. K., Abolins, M. J., House, M. A., Stirewalt, G. L., and Ferrill, D. A. (1997). "Global Positioning Constraints on fault slip rates in the Death Valley region, California and Nevada." Geophysical Research Letters, 24(23), 3073-3076.

Bennett, R. A., Davis, J. L., and Wernicke, B. P. (1999). "Present-day pattern of Cordilleran deformation in the western United States." Geology, 27(4), 371-374.

Bennett, R. A., Wernicke, B. P., Niemi, N. A., Friedrich, A. M., and Davis, J. L. (2003). "Contemporary strain rates in the northern Basin and Range province from GPS data." Tectonics, 22(2), 1008,doi:10.1029/2001TC1355.

Bevington, P. R. (1969). Data Reduction and Error Analysis for the Physical Sciences, McGraw Hill, Inc., USA.

Bevis, M., Businger, S., Herring, T. A., Rocken, C., Anthes, R. A., and Ware, R. (1992). "GPS meteorology: Remote sensing of atmospheric water vapor using the global positioning system." Journal of Geophysical Research, 97(D14), 15787-15801.

Blewitt, G., Heflin, M. B., Webb, F. H., Lindqwister, U., and Malla, R. P. (1992). "Global Coordinates with Centimeter Accuracy in the International Reference Frame using GPS." Geophysical Research Letters, 19(9), 853-856.

Blewitt, G., Heflin, M. B., Hurst, K. J., Jefferson, D. C., Webb, F. H., and Zumberge, J. F. (1993). "Absolute far-field displacements from the 28 June 1992 Landers

earthquake sequence." Nature, 361, 340-342.

Blewitt, G. (1997). "Basics of the GPS technique." Geodetic Applications of GPS, B. Jonsson, ed., Nordic Geodetic Commission, Gavle, Sweden, 9-54.

Blewitt, G. (1998). "GPS Data Processing Methodology." GPS for Geodesy, P. Teunissen and A. Kleusberg, eds., Springer-Verlag, Germany, 231-270.

Blewitt, G., and Lavallee, D. (2002). "Effect of annual signals on geodetic velocity." Journal of Geophysical Research, 107(B7), 10.1029/2001JB000570.

Blewitt, G. (2003). "Self-consistency in reference frames, geocenter definition, and surface loading of the solid Earth." Journal of Geophysical Research, 108(B2), doi:10.1029/2002JB002082.

Burchfiel, B. C., Hodges, K. V., and Royden, L. H. (1987). "Geology of Panamint Valley-Saline Valley pull-apart system, California: Palinspastic evidence for low-angle geometry of a Neogene range bounding fault." Journal of Geophysical Research, 92, 10422-10426.

Butler, P. R., Troxel, B. W., and Verosub, K. L. (1988). "Late Cenozoic history and styles of deformation along the Southern Death Valley Fault Zone, California." Geological Society of America Bulletin, 100, 402-410.

Carr, W. J. (1990). "Styles of extension in the Nevada Test Site region, southern Walker Lane Belt; An integration of volcano-tectonic and detachment fault models." Basin and Range Extensional Tectonics near the latitude of Las Vegas, Nevada, B. P. Wernicke, ed., The Geological Society of America, Boulder, Colorado, 283-303.

Conner, C. B., Stamatakos, J. A., Ferrill, D. A., and Hill, B. E. (1998). "Technical Comments on "Anomalous Strain Accumulation in the Yucca Mountain Area, Nevada" by Wernicke et al." Science, 282, 1007b.

Davies, J., and Archembeau, C. (1997). “Geohydrological models and earthquake effects at Yucca Mountain, Nevada” Environmental Geology, 32 (1), 23-35.

Davis, J. L., Wernicke, B. P., and Bennett, R. A. (1998). "Reply to Comments on Detecting strain in the Yucca Mountain Area, Nevada." Science, 282, 1007b.

Davis, J. L., Bennett, R. A., and Wernicke, B. P. (2003). "Assessment of GPS velocity accuracy for the Basin and Range Geodetic Network (BARGEN)." Geophysical Research Letters, 30(7), doi:10.1029/2003GL016961.

DeMets, C., Gordon, R. G., Argus, D. F., and Stein, S. (1994). "Effect of recent revisions

to the geomagnetic reversal time scale on estimates of current plate motions." Geophysical Research Letters, 21(20), 2191-2194.

Dixon, T. H., Robaudo, S., Lee, J., and Reheis, M. (1995). "Contraints on present-day Basin and Range deformation from space geodesy." Tectonics, 14(4), 755-772.

Dixon, T. H., Miller, M., Farina, F., Wang, H., and Johnson, D. (2000). "Present-day motion of the Sierra Nevada block and some tectonic implications for the Basin and Range province, North American Cordillera." Tectonics, 19(1), 1-24.

Dixon, T. H., Norabuena, E., and Hotaling, L. (2003). "Paleoseismology and Global Positioning System: Earthquake-cycle effects and geodetic versus geologic fault slip rates in the Eastern California Shear Zone." *Geology*, 31(1), 55-58.

Dohrenwend, J., Schell, B. A., Menges, C. M., Moring, B. C., and McKittrick, M. A. (1996). "Reconnaissance photogeologic map of young (Quaternary and late Tertiary) faults in Nevada." An analysis of Nevada's metal-bearing mineral resources, D. A. Singer, ed., Nevada Bureau of Mines and Geology, Reno.

Dokka, R. K., and Travis, C. J. (1990a). "Late Cenozoic strike-slip faulting in the Mojave Desert, California." Tectonics, 9(2), 311-340.

Dokka, R. K., and Travis, C. J. (1990b). "Role of the Eastern California Shear Zone in Accommodating Pacific-North American Plate Motion." Geophysical Research Letters, 17(9), 1323-1326.

Dong, D., Fang, P., Bock, Y., Cheng, M. K., and Miyazaki, S. (2002). "Anatomy of apparent seasonal variations from GPS-derived site position time series." Journal of Geophysical Research, 107(B4), 10.1029/2001JB000573.

Gan, W., Svarc, J. L., Savage, J. C., and Prescott, W. H. (2000). "Strain accumulation across the Eastern California Shear Zone at latitude 36o30'N." Journal of Geophysical Research, 105(B7), 16229-16236.

Gan, W., Zhang, P., Shen, Z.-K., Prescott, W. H., and Svarc, J. L. (2003). "Initiation of deformation of the Eastern California Shear Zone: Constrains from Garlock fault geometry and GPS observations." Geophysical Research Letters, 30(10), 1496,doi:10.1029/2003GL017090.

Gregorious, T. (1996). GIPSY-OASIS II: How it works, Caltech and the University of Newcastle-upon-Tyne.

Hammond, W. C., and Thatcher, W. (2004). "Contemporary tectonic deformation of the Basin and Range province, western United States: 10 years of observation with the Global Positioning System." Journal of Geophysical Research, 109(B08403),

doi:10.1029/2003JB002746.

Hanks, T. C., and Kanamori, H. (1979). "A moment magnitude scale." Journal of Geophysical Research, 84, 2348-2350.

Hanks, T. C., Winograd, I. J., Anderson, R. E., Reilly, T. E., and Weeks, E. P. (1999). "Yucca Mountain as a Radioactive-Waste Repository." Circular 1184, USGS.

Hearn, E. H., and Humphreys, E. D. (1998). "Kinematics of the southern Walker Lane Belt and motion of the Sierra Nevada block, California." Journal of Geophysical Research, 103(B11), 27033-27049.

Heizler, M., Perry, F. V., Crowe, B. M., Peters, L., and Appelt, R. (1999). "The age of Lathrop Wells volcanic center: An 40Ar/39Ar dating investigation." Journal of Geophysical Research, 104, 767-804.

Hill, E., Bennett, R. A., Blewitt, G., Davis, J. L., and Wernicke, B. P. (2002). "Sub-millimeter Signal Detection by GPS: Cross Validation using GIPSY and GAMIT Solutions for the Yucca Mountain Network." EOS Trans. AGU, 83(47), Abstract G22A-13.

Hill, E., and Blewitt, G. (2004a). "Analysis of Vertical Velocities from BARGEN Continuous GPS Data at Yucca Mountain, Southern Nevada." Cahiers du Centre European de Geodynamique et du Seismologie, Proceedings of the workshop: The State of GPS Vertical Positioning Precision, 23.

Hill, E., and Blewitt, G. (2004b). "Spatial Variations in Strain Inferred by GPS Across the Yucca Mountain Region, Southern Nevada." EOS Trans. AGU, 85(47), Fall Meeting Suppl., Abstract G21A-0124.

Houghton, J. G., Sakamoto, C. M., and Gifford, R. O. (1975). "Nevada's Weather and Climate." Special Publication 2, Nevada Bureau of Mines and Geology, Reno.

Jennings, C. W. (1975). "Fault map of California." Geologic Data Map 1, California Division of Mines and Geology, Sacramento.

Johansson, J. M. "Modeling of the Earth Atmosphere in Space Geodetic Applications." Nordic Autumn School of the Nordic Geodetic Commission, Bastad, Sweden, 109-134.

Jones, C. H., Unruh, J. R., and Sonder, L. J. (1996). "The role of gravitational potential energy in active deformation in the southwestern United States." Nature, 381, 37-41.

Kreemer, C., Holt, W., and Haines, A. J. (2003). "An integrated global model of present-

day plate motions and plate boundary deformation." Geophysical Journal International, 154, 8-34.

Langley, R. B. (1998). "Propagation of the GPS signals." GPS for Geodesy, P. J. G. Teunissen and A. Kleusberg, eds., Springer-Verlag, Berlin, 111-149.

Larson, K. M., and Agnew, D. C. (1991). "Application of the Global Positioning System to Crustal Deformation Measurement 1: Precision and Accuracy." Journal of Geophysical Research, 96(B10), 16547-16565.

Lavallee, D. A. (2000). "Tectonic Plate Motions from Global GPS measurements, PhD Thesis," University of Newcastle-upon-Tyne, Newcastle-upon-Tyne.

Lee, J., Spencer, J., and Owen, L. (2001). "Holocene slip rates along the Owens Valley fault, California: Implications for the recent evolution of the Eastern California Shear Zone." Geology, 29(9), 819-822.

Langenheim, V. E., Grow, J. A., Jachens, R. C., Dixon, G. L., and Miller, J. J. (2001). "Geophysical constraints on the location and geometry of the Las Vegas Valley Shear Zone, Nevada." Tectonics, 20(2), 189-209.

Lohman, R. B., Simons, M., and Savage, B. (2002). "Location and mechanism of the Little Skull Mountain earthquake as constrained by satellite radar interferometry and seismic waveform modeling." Journal of Geophysical Research, 107(B6), 10.1029/2001JB000627.

Macilwain, C. (2001). "Out of sight, out of mind?" Nature, 412, 850-852.

McCarthey, D. D. (1996). "International Earth Rotation Service Conventions 1996." IERS Technical Note 21, Paris.

McClusky, S. C., Bjornstad, S. C., Hager, B. H., King, R. W., Meade, B. J., Miller, M. M., Monastero, F. C., and Souter, B. J. (2001). "Present Day Kinematics of the Eastern California Shear Zone from a Geodetically Constrained Block Model." Geophysical Research Letters, 28(17), 3363-3372.

McGill, S. F., and Sieh, K. E. (1993). "Holocene slip rate of the Central Garlock Fault in Southeastern Searles Valley, California." Journal of Geophysical Research, 98, 14217-14231.

Meremonte, M., Gomberg, J., and Cranswick, E. (1995). "Constraints on the 29 June 1992 Little Skull Mountain, Nevada, Earthquake Sequence Provided by Robust Hypocenter Estimates." Bulletin of the Seismological Society of America, 85(4), 1039-1049.

Miller, M. M. (1993). "Regional coseismic deformation from the June 28, 1992, Landers, California, earthquake: Results from the Mojave GPS network." Geology, 21, 868-872.

Miller, M., Johnson, D., Dixon, T. H., and Dokka, R. K. (2001). "Refined kinematics of the Eastern California Shear zone from GPS observations, 1993-1998." Journal of Geophysical Research, 106(B2), 2245-2263.

Niell, A. E. (1996). "Global mapping functions for the atmospheric delay at radio wavelengths." Journal of Geophysical Research, 101(B2), 3227-3246.

Novak, S. W., and Bacon, C. R. (1986). "Pliocene volcanic rocks of the Coso Range, Inyo County, California." USGS Prof Paper, 1383, 43.

Ofoegbu, G. I., and Ferrill, D. A. (1998). "Mechanical analyses of listric normal faulting with emphasis on seismicity assessment." Tectonophysics, 284, 65-77.

Okada, Y. (1985). "Surface deformation due to shear and tensile faults in a half-space." Bulletin of the Seismological Society of America, 75(4), 1135-1154.

Okada, Y. (1992). "Internal deformation due to shear and tensile faults in a half-space." Bulletin of the Seismological Society of America, 82(2), 1018-1040.

O'Leary, D. (2000). "Tectonic Significance of the Rock Valley Fault Zone, Nevada Test Site." Geologic and Geophysical Characterization Studies of Yucca Mountain, Nevada, A Potential High-Level Radioactive-Waste Repository, J. W. Whitney and W. R. Keefer, eds., USGS.

Oswald, J. A., and Wesnousky, S. G. (2002). "Neotectonics and Quaternary geology of the Hunter Mountain fault zone and Saline Valley region, southeastern California." Geomorphology, 42, 255-278.

Parsons, T., Thompson, G. A., and Sleep, N. H. (1994). "Mantle plume influence on the Neogene uplift and extension of the U.S. western Cordillera?" Geology, 22(1), 83-86.

Peltzer, G., Crampe, F., Hensley, S., and Rosen, P. A. (2001). "Transient strain accumulation and fault interaction in the Eastern California Shear Zone." Geology, 29(11), 975-978.

Prescott, W. H., Savage, J. C., and Kinoshita, W. T. (1979). "Strain accumulation rates in the western United States between 1970 and 1978." Journal of Geophysical Research, 84(B10), 5423-5435.

Quittmeyer, R. C. (2000). "Yucca Mountain Site Description." TDR-CRW-GS-000001, Rev 01 ICN 01, United States Department of Energy, Las Vegas.

Reheis, M., and Dixon, T. H. (1996). "Kinematics of the Eastern California shear zone: Evidence for slip transfer from Owens and Saline Valley fault zones to Fish Lake Valley fault zone." Geology, 24(4), 339-342.

Reheis, M., and Sawyer, T. L. (1997). "Late Cenozoic history and slip rates of the Fish Lake Valley, Emigrant Peak, and Deep Springs fault zones, Nevada and California." Geological Society of America Bulletin, 109, 280-299.

Savage, J. C., and Burford, R. O. (1973). "Geodetic determination of relative plate motion in central California." Journal of Geophysical Research, 78(5), 832-845.

Savage, J. C. (1983). "Strain accumulation in Western United States." Annual Reviews of Earth Planetary Science, 11, 11-43.

Savage, J. C., Lisowski, M., and Prescott, W. H. (1990). "An apparent shear zone trending north-northwest across the Mojave Desert into Owen's Valley, Eastern California." Geophysical Research Letters, 17(12), 2113-2116.

Savage, J. C., Lisowski, M., Gross, W. K., King, N. E., and Svarc, J. L. (1994). "Strain accumulation near Yucca Mountain, Nevada, 1983-1993." Journal of Geophysical Research, 99(B9), 18103-18107.

Savage, J. C., and Lisowski, M. (1995). "Strain accumulation in Owens Valley, California, 1974-1988." Bulletin of the Seismological Society of America, 85(1), 151-158.

Savage, J. C. (1998). "Detecting Strain in the Yucca Mountain Area, Nevada." Science, 282, 1007b.

Savage, J. C., Svarc, J. L., and Prescott, W. H. (1999). "Strain accumulation at Yucca Mountain, Nevada." Journal of Geophysical Research, 104(B8), 17627-17631.

Savage, J. C., Gan, W., and Svarc, J. L. (2001). "Strain accumulation and rotation in the Eastern California Shear Zone." Journal of Geophysical Research, 106(B10), 21995-22007.

Schweickert, R. A., and Lahren, M. M. (1997). "Strike-slip fault system in Amargosa Valley and Yucca Mountain, Nevada." Tectonophysics, 272, 25-41.

Scientists from the USGS, S. a. C. (2000). "Preliminary Report on the 16 October 1999 M7.1 Hector Mine, California, Earthquake." Seismological Research Letters, 71(1), 11-23.

Sella, G., Dixon, T. H., and Mao, A. (2002). "REVEL: A model for recent plate velocities from space geodesy." Journal of Geophysical Research, 107(B4), 10.1029/2000JB000033.

Scott, R. B. (1990). "Tectonic setting of Yucca Mountain, southwest Nevada." Basin and Range Extensional Tectonics near the latitude of Las Vegas, Nevada, B. P. Wernicke, ed., The Geological Society of America, Boulder, Colorado, 251-282.

Sieh, K. E., Jones, L., Hauksson, E., Hudnut, K., Eberhart-Phillips, D., Heaton, T., Hough, S., Hutton, K., Kanamori, H., Lilje, A., Lindvall, S., McGill, S. F., Mori, J., Rubin, C. M., Spotila, J. A., Stock, J., Thio, H. K., Treiman, J., Wernicke, B. P., and Zachariasen, J. (1993). "Near-field investigations of the Landers earthquake sequence, April to July 1992." Science, 260, 171-176.

Simonds, F. W., Whitney, J. W., Fox, K. F., Ramelli, A., Yount, J. C., Carr, M. D., Menges, C. M., Dickerson, R. P., and Scott, R. B. (1995). "Map showing fault activity in the Yucca Mountain area, Nye County, Nevada." USGS.

Smith, K. D., Li, L., Brune, J. N., Anooshehpoor, R., and Savage, M. K. (2000). "Preliminary Results from the NPE-Ryan Reversed Refraction Profile." Geological and Geophysical Characterization Studies of Yucca Mountain, Nevada, A Potential High-Level Radioactive-Waste Repository, J. W. Whitney and W. R. Keefer, eds., USGS, Denver, CO, Chapter D, 9 pp.

Smith, K. D., Brune, J. N., de Polo, D. M., Savage, M. K., Anooshehpoor, R., and Sheehan, A. F. (2001). "The 1992 Little Skull Mountain Earthquake Sequence, Southern Nevada Test Site." *Bulletin of the Seismological Society of America*, 91(6), 1595-1606.

Smith, K. D., von Seggern, D., Blewitt, G., Preston, L., Anderson, J. G., Wernicke, B. P., and Davis, J. L. (2004). "Evidence for Deep Magma Injection Beneath Lake Tahoe, Nevada-California." Science, 10.1126, science.1101304.

Smith, R. S. U. (1979). "Holocene offset and seismicity along the Panamint Valley fault zone, western Basin and Range Province, California." Tectonophysics, 52, 411-415.

Stamatakos, J. A., and Ferrill, D. A. (1998). "Strike-slip fault system in Amargosa Valley and Yucca Mountain, Nevada - comment." Tectonophysics, 294, 151-160.

Stewart, J. H. (1967). "Possible large right-lateral displacement along fault and shear zones in the Death Valley-Las Vegas area, California and Nevada." GSA Bulletin, 78, 131-142.

Stewart, J. H. (1988). "Tectonics of the Walker Lane Belt, Western Great Basin:

Mesozoic and Cenozoic Deformation in a Zone of Shear." Metamorphism and crustal evolution of the western United States, W. G. Ernst, ed., Prentice-Hall, 684-713.

Teunissen, P., and Kleusberg, A. (1998a). "GPS observation equations and positioning concepts." GPS for Geodesy, P. Teunissen and A. Kleusberg, eds., Springer-Verlag, Germany, 187-229.

van Dam, T., Wahr, J. M., Milly, P. C. D., Shmakin, A. B., Blewitt, G., Lavallee, D., and Larson, K. M. (2001). "Crustal displacements due to continental water loading." Geophysical Research Letters, 28(4), 651-654.

Wallace, R. E. (1984). "Patterns and timing of late Quaternary faulting in the Great Basin province and relation to some regional tectonic features." Journal of Geophysical Research, 89, 5763-5769.

Wells, S. G., McFadden, L. D., Renault, C. E., and Crowe, B. M. (1990). "Geomorphic assessment of late Quaternary volcanism in the Yucca Mountain area, southern Nevada: Implications for the proposed high-level radioactive waste repository." Geology, 18, 549-553.

Wernicke, B. P., Davis, J. L., Bennett, R. A., Elosegui, P., Abolins, M. J., Brady, R. J., House, M. A., Niemi, N. A., and Snow, J. K. (1998). "Anomalous Strain Accumulation in the Yucca Mountain Area, Nevada." Science, 279, 2096-2100.

Wernicke, B. P., Davis, J. L., and Bennett, R. A. (2002). "Surface Velocity Field in the Yucca Mountain Area, Nevada and California, From BARGEN Continuous GPS Data." Eos. Trans. AGU, 83(47), Abstract U12A-04.

Wernicke, B. P., Davis, J. L., Bennett, R. A., Normandeau, J. E., and Friedrich, A. M. (2004). "Tectonic implications of a dense continuous GPS velocity field at Yucca Mountain, Nevada." Journal of Geophysical Research, 109(12), B12404.

Wesnousky, S. G. (1986). "Earthquakes, Quaternary Faults, and Seismic Hazard in California." Journal of Geophysical Research, 91(B12), 12587-12631.

Wessel, P., and Smith, W. H. F. (1998). "New, improved version of the Generic Mapping Tools released." EOS Transactions, American Geophysical Union, 79, 579.

Wdowinski, S., Bock, Y., Zhang, J., Fang, P., and Genrich, J. (1997). "Southern California Permanent GPS Geodestic Array: Spatial filtering of daily positioning for estimating coseismic and postseismic displacements induced by the 1992 Landers earthquake." Journal of Geophysical Research, 102(B8), 18,057-18,070.

Whitney, J. W., and Keefer, W. R. (2000). "Geologic and Geophysical Characterization

Studies of Yucca Mountain, Nevada, A Potential High-Level Radioactive Waste Repository." Digital Data Series 058, U.S. Geological Survey, Denver, Colorado.

Wicks, C. W., Thatcher, W., Monastero, F. C., and Hasting, M. A. (2001). "Steady-state deformation of the Coso Range, East-Central California, inferred from Satellite Radar Interferometry." Journal of Geophysical Research, 106(B7), 13769-13780.

Williams, S. (2003). "Offsets in Global Positioning System time series." Journal of Geophysical Research, 108(B6), doi:10.1029/2002JB002156.

Zhang, P., Ellis, M., Slemmons, D. B., and Mao, F. (1990). "Right-Lateral displacements and the Holocene slip rate associated with prehistoric earthquakes along the southern Panamint Valley fault zone: Implications for southern Basin and Range tectonics and coastal California deformation." Journal of Geophysical Research, 95(B4), 4857-4872.

Zreda, G., Phillips, F. M., Kubik, P. W., Sharma, P., and Elmore, D. (1993). "Cosmogenic 36C dating of a young basaltic eruption complex, Lathrop Wells, Nevada." Geology, 21(1), 57-60.

Zumberge, J. F., Heflin, M. B., Jefferson, D. C., Watkins, M. M., and Webb, F. H. (1997). "Precise point positioning for the efficient and robust analysis of GPS data from large networks." Journal of Geophysical Research, 102(B3), 5005-5017.

Appendix A

GPS station coordinates

Station	Latitude	Longitude	Height (m)	Distance from LITT (km)
ALAM	-115.158	37.358	1090.225	122.79
APEX	-114.932	36.319	761.256	132.06
ARGU	-117.522	36.050	1791.547	133.51
BEAT	-116.621	37.040	1396.246	42.94
BULL	-116.872	36.918	1344.993	53.77
BUST	-116.451	36.745	992.524	12.75
CHLO	-116.766	36.747	864.429	40.85
CRAT	-116.569	36.808	972.728	24.29
DYER	-118.039	37.743	1512.157	189.32
ECHO	-114.264	37.916	1684.321	222.89
JOHN	-116.099	36.459	871.946	36.95
LIND	-119.058	36.360	144.482	249.87
LITT	-116.308	36.746	1056.717	0.00
MERC	-115.979	36.633	1257.137	32.01
PERL	-116.686	36.902	1351.636	37.92
POIN	-116.120	36.580	916.848	24.98
RAIL	-115.665	38.280	1575.473	179.59
RELA	-116.554	36.715	839.442	22.24
REPO	-116.468	36.840	1479.678	17.73
ROGE	-117.085	36.218	3016.680	91.06
RYAN	-116.650	36.316	1286.391	56.66
SHOS	-116.299	35.971	582.621	85.96
SKUL	-116.211	36.730	1237.528	8.89
SMYC	-115.587	36.320	2562.959	80.06
STRI	-116.338	36.645	1030.066	11.54
TATE	-116.574	36.932	1293.485	31.44
TIVA	-116.230	36.935	2034.434	22.14
TONO	-117.184	38.097	2066.242	168.87

Appendix B

JPL ephemeris data input to the GIPSY processing routines

File type	Information contained
.shad	Shadow events (without this, can get errors in attitude, which affect the phase center of the GPS transmitters)
.eci	Satellite position and velocity
.tdpc	Satellite clock
.tpeo.nml	Time, polar motion, earth rotation information
XFILE	ITRF transformation parameters
de405s_sun4.nio	Planetary ephemeris

Appendix C

GIPSY 'wash template'

```
 $PREP                        !namelist input for preprefilter
  WETZTROP  = .TRUE.
  TROPDRIFT = 5.0d-8    !km/sqrt(sec) = 3.0 mm/sqrt(hr)
 ! CLOCKPSIGMA = 3.0D1,       !white noise clock process noise
 ! YADDSG    = 0.1D0,         !white noise sigma for phase bias
! Parameters for stochastic GPS
  RefClock = 'ALLGPS'
! insert stoch Troposphere gradient stuff
 $END

 $INIT                        !namelist input for filter
  IDIGIT    = 9
  STATE = 1
  YDEL      = 'X*','Y*','Z*','DX*','DY*','DZ*',       !satellite state
params
              'SATACCL*', 'SATDRFT*',                  !satellite clock
params
              'GEOCENTERX','GEOCENTERY','GEOCENTERZ',
              'XPOLEMOTION', 'YPOLEMOTION','UT1-UTC',
              'XPOLERATE', 'YPOLERATE', 'UT1-UTCRATE',
              'HLOVE', 'VLOVE',
              'BIASPSR*',  'DRYZTROP*', 'LMPZTROP*',
              'STAACCL*', 'STADRFT*',                  !station clock
params
              'SATBIAS#*',
      ! insert sta_bias here
        WRTTDP = 'STABIAS*', 'SATBIAS*', 'PHASE*', '*'
        TDPTYP = 'TIMEVARY', 'TIMEVARY', 'CONSTANT', 'TIMEVARY'
        TDPTOL = 1.5D-1,      !500ns
                   9.0D-5,      !0.3ns
                  1.0D10,      !default
                 1.0D10
  TDPSIGMA  = .TRUE.
  SOLPRT    = .TRUE.
  SOLVE     = .TRUE.
  DEBUG     = 1
  OUTNAME   = 'OASIS'
 $END

 $APRIORI                     !namelist input for filter
  APALL     = .TRUE.
  APNAMS(1) =      'UT1-UTC',          APSIGS(1) = 2.156D-8 ! 0.01 mm
  APNAMS(2) =      'XPOLEMOTION',      APSIGS(2) = 7.84D-7  !5 m
  APNAMS(3) =      'YPOLEMOTION',      APSIGS(3) = 7.84D-7  !5 m
  APNAMS(4) =      'WETZTROP*',        APSIGS(4) = 2.0D-4   !20 cm
  APNAMS(5) =      'STABIAS*',         APSIGS(5) = 3.0D5    !1 sec
  APNAMS(6) =      'SATBIAS*',         APSIGS(6) = 3.0D5    !1 sec
  APNAMS(7) =      'PHASE*',           APSIGS(7) = 3.0D5    !1 sec
  APNAMS(8) =      'SOLARSCL*',        APSIGS(8) = 1.0D0    !100 %
  APNAMS(9) =      'Y_BIAS*',          APSIGS(9) = 2.0D0    !2.0D-12
km/sec/sec
  APNAMS(10)=      'X*',               APSIGS(10)= 1.0D0    !1 km
  APNAMS(11)=      'Y*',               APSIGS(11)= 1.0D0    !1 km
```

```
  APNAMS(12)=      'Z*',               APSIGS(12)= 1.0D0    !1 km
  APNAMS(13)=      'DX*',              APSIGS(13)= 1.0D-5   !1 cm/sec
  APNAMS(14)=      'DY*',              APSIGS(14)= 1.0D-5   !1 cm/sec
  APNAMS(15)=      'DZ*',              APSIGS(15)= 1.0D-5   !1 cm/sec
  APNAMS(16)=      'R_OFF   TOP',      APSIGS(16)= 5.0D-3   !5 m
  APNAMS(17)=      'GEOCENTER*',       APSIGS(17)= 5.0D-5   !5 cm
  APNAMS(18)=      'STAX*',            APSIGS(18)= 1.0D-1  !100 m
  APNAMS(19)=      'STAY*',            APSIGS(19)= 1.0D-1  !100 m
  APNAMS(20)=      'STAZ*',            APSIGS(20)= 1.0D-1  !100 m
  APNAMS(21)=      'CONST_H TOP',      APSIGS(21)= 1.0D+6
  APNAMS(22)=      'CONST_C TOP',      APSIGS(22)= 1.0D+6
  APNAMS(23)=      'CONST_L TOP',      APSIGS(23)= 1.0D+6
  APNAMS(24)=      'SIN1_H  TOP',      APSIGS(24)= 1.0D+6
  APNAMS(25)=      'SIN1_C  TOP',      APSIGS(25)= 1.0D+6
  APNAMS(26)=      'SIN1_L  TOP',      APSIGS(26)= 1.0D+6
  APNAMS(27)=      'COS1_H  TOP',      APSIGS(27)= 1.0D+6
  APNAMS(28)=      'COS1_C  TOP',      APSIGS(28)= 1.0D+6
  APNAMS(29)=      'COS1_L  TOP',      APSIGS(29)= 1.0D+6
  APNAMS(30)=      'SIN2_H  TOP',      APSIGS(30)= 1.0D+6
  APNAMS(31)=      'SIN2_C  TOP',      APSIGS(31)= 1.0D+6
  APNAMS(32)=      'SIN2_L  TOP',      APSIGS(32)= 1.0D+6
  APNAMS(33)=      'COS2_H  TOP',      APSIGS(33)= 1.0D+6
  APNAMS(34)=      'COS2_C  TOP',      APSIGS(34)= 1.0D+6
  APNAMS(35)=      'COS2_L  TOP',      APSIGS(35)= 1.0D+6
  APNAMS(36)=      'UT1-UTCRATE',      APSIGS(36)= 1.157D-3  !100 s/day
  APNAMS(37)=      'XPOLERATE',        APSIGS(37)= 1.81D-12  !1 m/day
  APNAMS(38)=      'YPOLERATE',        APSIGS(38)= 1.81D-12  !1 m/day
  APNAMS(39)=      'DX      TOP',      APSIGS(39)= 1.0D-4    !10 cm/sec
  APNAMS(40)=      'DY      TOP',      APSIGS(40)= 1.0D-4    !10 cm/sec
  APNAMS(41)=      'DZ      TOP',      APSIGS(41)= 1.0D-4    !10 cm/sec
  APNAMS(42)=      'CONST_X*',         APSIGS(42)= 5.0       !5.0D-12
km/sec/sec
  APNAMS(43)=      'CONST_Y*',         APSIGS(43)= 0.1       !0.1D-12
km/sec/sec
  APNAMS(44)=      'CONST_Z*',         APSIGS(44)= 5.0       !5.0D-12
km/sec/sec
  APNAMS(45)=      'SOLSCL_X*',        APSIGS(45)= 0.1D0
  APNAMS(46)=      'SOLSCL_Z*',        APSIGS(46)= 0.1D0
  APNAMS(47)=      'TRPAZ*',           APSIGS(47)= 0.0d0
  APNAMS(48)=      'TRPAZCOS*',        APSIGS(48)= 5.0D-4   !half meter
  APNAMS(49)=      'TRPAZSIN*',        APSIGS(49)= 5.0D-4   !half meter
  APNAMS(50)=      'DUMMY',            APSIGS(50)= 1.0d0
  !    insert apnams 51 here
 $END

 $DATAWGHT                !namelist input for filter, edtpnt2, and
postfit
  DATSIG    = 1.0D-3, 1.0D-5, 3.0D-3, 2.0D-5
  DATYPE    =    110,    120,    110,    120
  !insert datrec
  !insert compartials
  !DATREC(1,3) = 'TOP'
  !DATREC(1,4) = 'TOP'
  ELMINSTA  = 15.0d0
  ELMINSAT  =  0.5D0
  !XXMTNM    = 'GPS8'
  !XRECNM    = 'MCMU'
 $END
```

```
$SMINPUT               !namelist input for smapper
 WRTTDP = 'STABIAS*', 'SATBIAS*', 'PHASE*', '*'
 TDPTYP = 'TIMEVARY', 'TIMEVARY', 'CONSTANT', 'TIMEVARY'
 TDPTOL = 1.5D-1,      !500ns
        9.0D-5,  !0.3ns
        1.0D10,  !default
        1.0D10
 SAVESIGMA = .TRUE.
 SAVEUD = 'ALL'
 OUTNAME = 'OASIS'
$END

$APRIORINML              !namelist input for smapper
 APNAMS(1)=      'STAX*',            APSIGS(1)= 1.0D-5   !1 cm
 APNAMS(2)=      'STAY*',            APSIGS(2)= 1.0D-5   !1 cm
 APNAMS(3)=      'STAZ*',            APSIGS(3)= 1.0D-5   !1 cm
 APNAMS(4)= 'TRPAZCOS*',    APVALS(   4)= 0.00D+00,
 APNAMS(5)= 'TRPAZSIN*',    APVALS(   5)= 0.00D+00,
$END

$LIMITS                !namelist input for postfit
 WINDOW =  5.D-3,  2.5D-5, 5.0d-3, 2.5d-5
 DATYPE    =    110,    120,    110,    120
 !insert datrec
 !DATREC(1,3) = 'TOP'
 !DATREC(1,4) = 'TOP'
$END

$EDTINIT               !namelist input for edtpnt2
 DEBUG  = .TRUE.
$END
```

Appendix D

Flow chart showing the GIPSY Precise Point Positioning routine

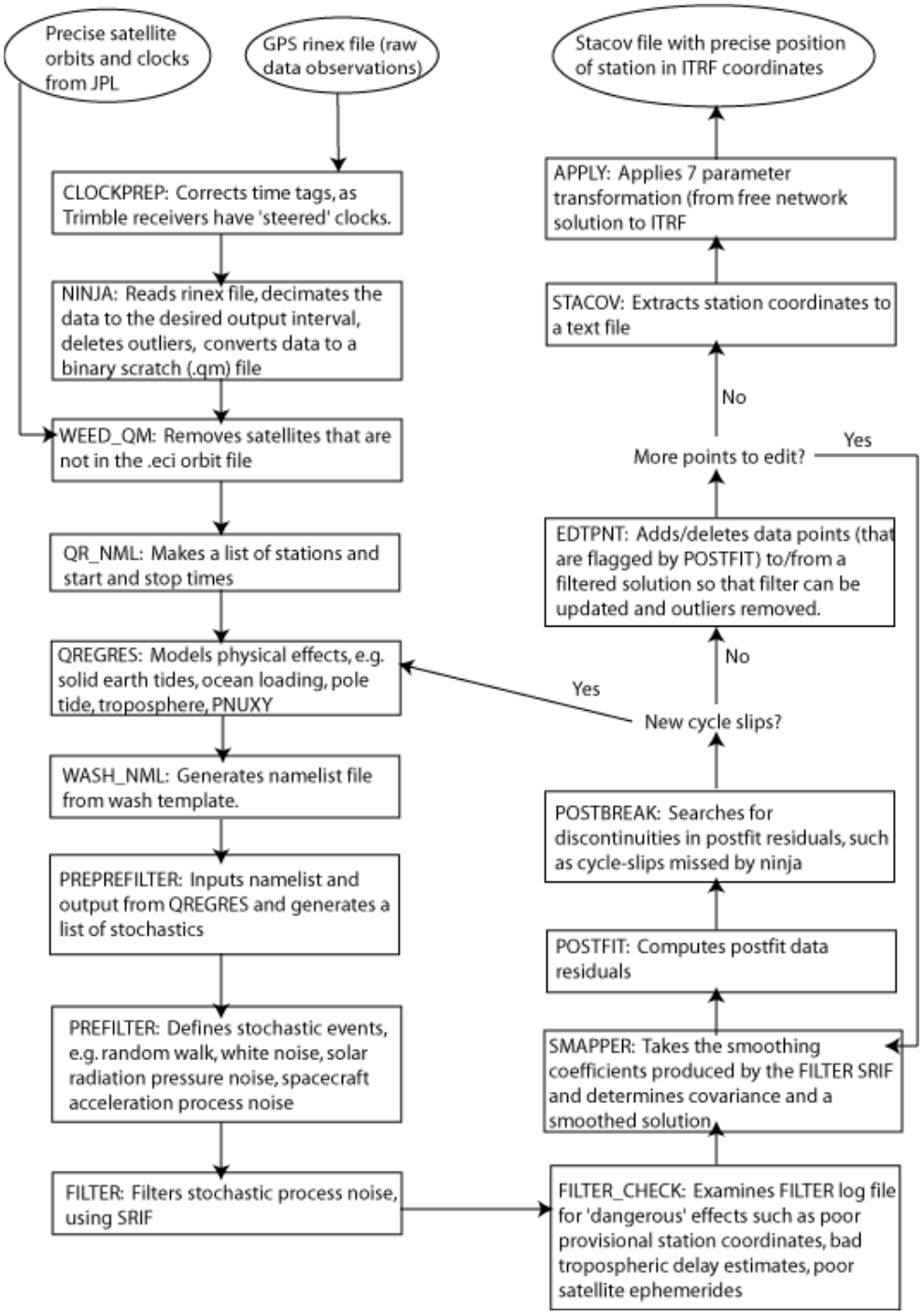

Appendix E

Ambiguity resolution on a line-by-line basis in GIPSY

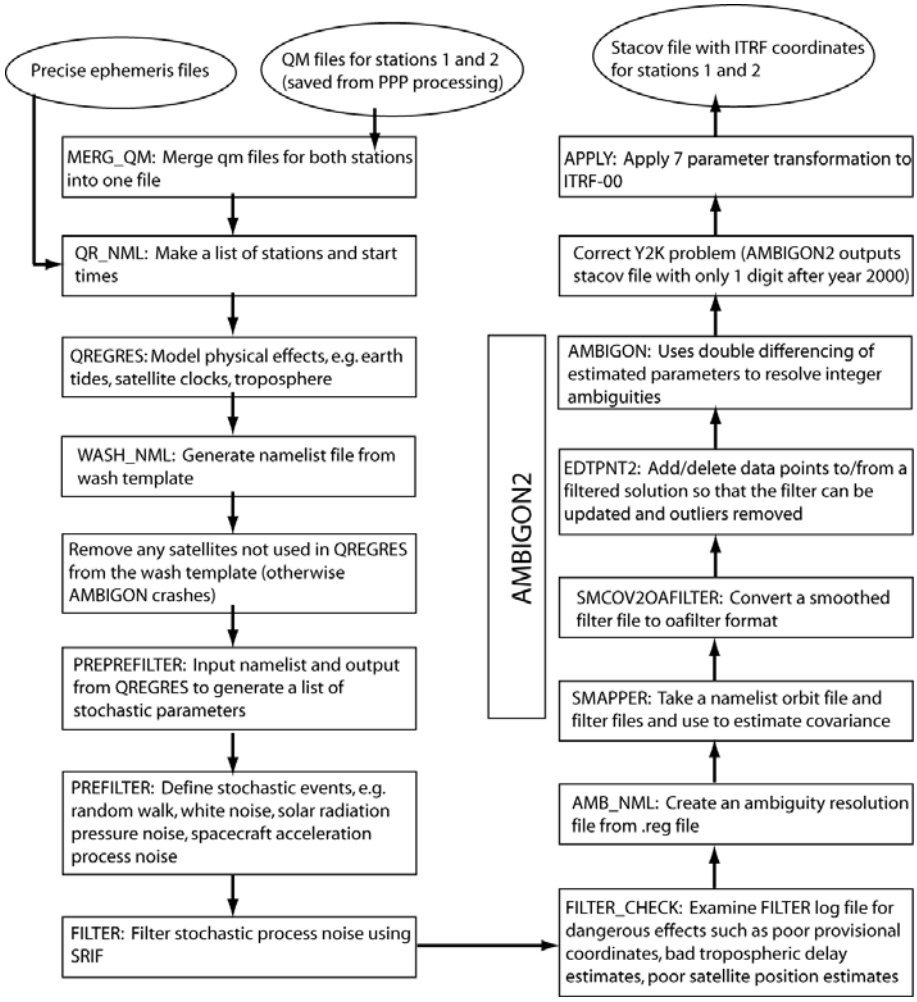

Appendix F

Post processing routine for GIPSY, for data including offsets

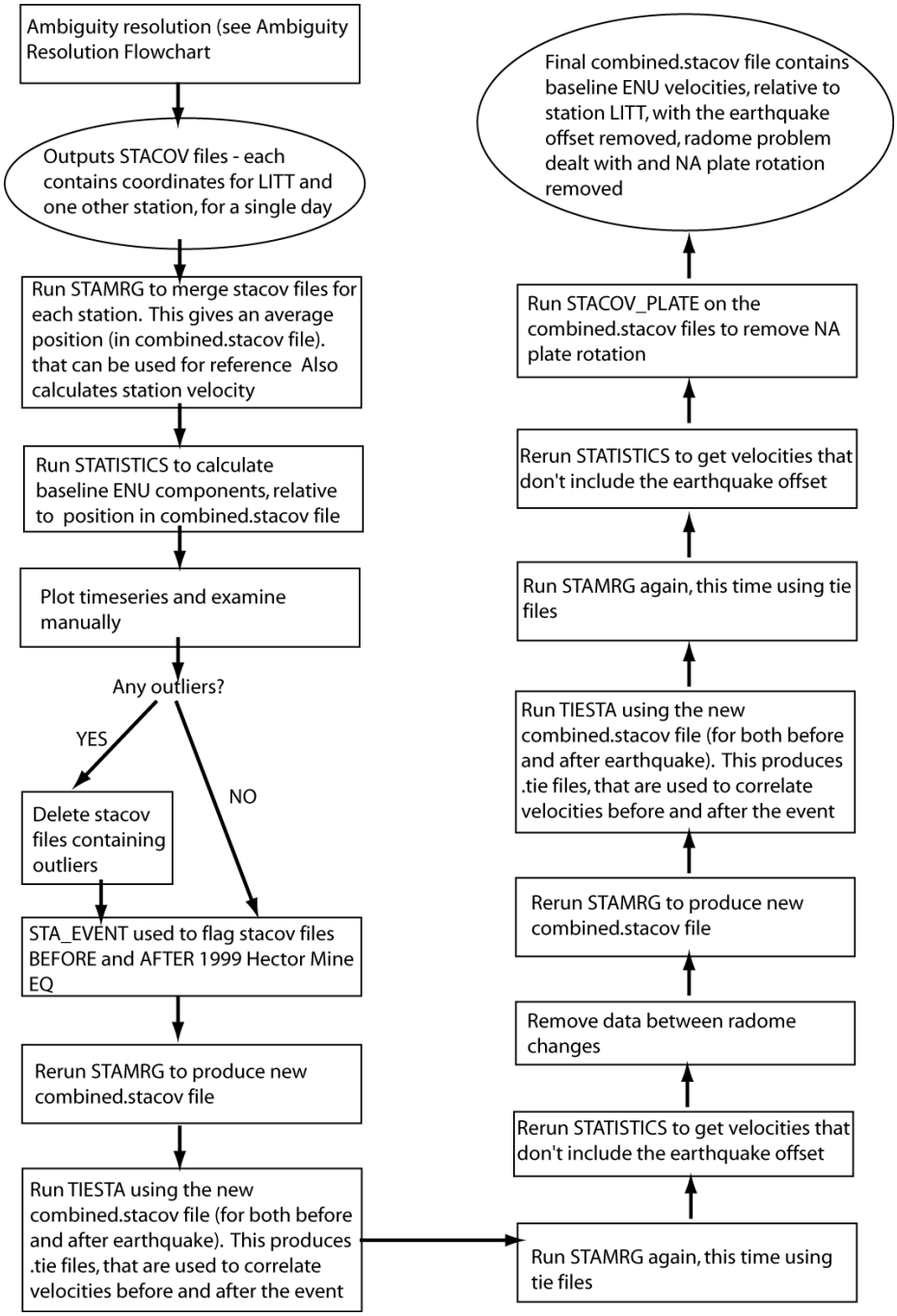

Appendix G

Radome change dates for the Yucca Mountain network and their effect on vertical velocity

Station	Distance from LITT (km)	Date of radome change	Vertical velocity difference (mm/yr)
LITT	0.00	19-Aug-99	-
SKUL	8.89	19-Aug-99	-0.04
STRI	11.54	19-Aug-99	-0.02
BUST	12.75	14-Aug-99	0.08
REPO	17.73	19-Aug-99	0.04
TIVA	22.14	15-Aug-99	0.02
RELA	22.24	13-Aug-99	0.15
CRAT	24.29	13-Aug-99	0.12
POIN	24.98	20-Aug-99	0.04
TATE	31.44	18-Aug-99	0.00
MERC	32.01	21-Aug-99	-0.02
JOHN	36.95	20-Aug-99	0.04
PERL	37.92	17-Aug-99	-0.09
CHLO	40.85	14-Aug-99	0.12
BEAT	42.94	13-Aug-99	0.16
BULL	53.77	13-Aug-99	0.22
RYAN	56.66	16-Aug-99	0.18
SMYC	**80.06**	**3-Sep-99**	**-0.10**
SHOS	85.96	17-Aug-99	0.07
ROGE	91.06	18-Aug-99	0.08
ALAM	**122.79**	**21-Dec-99**	**-1.13**
APEX	**132.06**	**4-Sep-99**	**-0.13**
ARGU	**133.51**	**12-Jan-00**	**-0.91**
TONO	**168.87**	**20-Dec-99**	**-1.04**
RAIL	**179.59**	**20-Dec-99**	**-1.04**
DYER	**189.32**	**16-Dec-99**	**-1.05**
ECHO	**222.89**	**22-Dec-99**	**-1.24**
LIND	**249.87**	**15-Jan-00**	**-1.43**

Vertical velocities were calculated with and without the data between radome changes included, then the difference between them calculated. Velocities were calculated using data from May 1999 to October 2003.

Appendix H

Comparison of velocity estimates from GIPSY and GAMIT.

	GIPSY		GAMIT		GIPSY		GAMIT		Velocity differences	
Station	Ev	Nv	Ev	Nv	E 1σ	N 1σ	E 1σ	N 1σ	Ev	Nv
	(mm/yr)	(mm/yr)	(mm/yr)	(mm/yr)	(mm/yr)	(mm/yr)	(mm/yr)	(mm/yr)	(mm/yr)	(mm/yr)
ALAM	0.22	-0.27	0.19	-0.27	0.04	0.04	0.05	0.05	-0.03	0.00
APEX	-0.05	-0.14	0.09	-0.07	0.04	0.04	0.06	0.05	0.14	0.07
ARGU	-3.93	6.00	-3.92	5.92	0.04	0.04	0.06	0.05	0.01	-0.08
BEAT	-0.12	0.48	-0.15	0.41	0.03	0.04	0.05	0.04	-0.03	-0.07
BULL	-0.39	0.92	-0.29	0.90	0.03	0.04	0.05	0.05	0.10	-0.02
BUST	-0.09	0.34	-0.08	0.37	0.03	0.04	0.05	0.05	0.01	0.03
CHLO	-0.43	0.57	-0.36	0.64	0.03	0.04	0.05	0.05	0.07	0.07
CRAT	-0.05	0.27	-0.07	0.33	0.03	0.04	0.06	0.05	-0.02	0.06
DYER	-1.14	3.13	-1.18	2.93	0.03	0.04	0.05	0.05	-0.04	-0.20
ECHO	0.33	-0.75	0.35	-0.64	0.04	0.04	0.05	0.05	0.02	0.11
JOHN	0.16	-0.05	0.14	-0.01	0.03	0.04	0.06	0.05	-0.02	0.04
LIND	-6.93	9.53	-6.93	9.27	0.04	0.04	0.06	0.05	0.00	-0.26
LITT	-0.01	-0.04	-0.01	-0.06	0.03	0.04	0.05	0.05	0.00	-0.02
MERC	0.13	-0.37	0.19	-0.26	0.03	0.04	0.06	0.05	0.06	0.11
PERL	-0.28	0.55	-0.25	0.49	0.03	0.04	0.05	0.05	0.03	-0.06
POIN	0.15	-0.19	0.07	-0.14	0.03	0.04	0.06	0.05	-0.08	0.05
RAIL	-0.04	-0.32	-0.04	-0.24	0.04	0.04	0.06	0.05	0.00	0.08
RELA	-0.14	0.46	-0.16	0.35	0.03	0.04	0.05	0.05	-0.02	-0.11
REPO	-0.26	0.37	-0.20	0.27	0.03	0.04	0.05	0.05	0.06	-0.10
ROGE	-0.95	3.15	-1.15	2.88	0.04	0.04	0.06	0.05	-0.20	-0.27
RYAN	-0.20	1.17	-0.25	1.04	0.03	0.04	0.05	0.05	-0.05	-0.13
SHOS	-0.42	0.37	-0.39	0.36	0.03	0.04	0.06	0.05	0.03	-0.01
SKUL	-0.12	0.00	-0.11	0.01	0.03	0.04	0.05	0.05	0.01	0.01
SMYC	-0.13	-0.32	-0.02	-0.22	0.03	0.04	0.06	0.05	0.11	0.10
STRI	0.12	0.52	0.19	0.44	0.03	0.04	0.05	0.05	0.07	-0.08
TATE	0.14	0.39	0.14	0.32	0.03	0.04	0.06	0.05	0.00	-0.07
TIVA	0.00	0.00	0.00	0.00	0.00	0.00	0.00	0.00	0.00	0.00
TONO	-0.32	0.64	-0.38	0.65	0.03	0.04	0.05	0.05	-0.06	0.01
Mean of residual velocity differences (east) =				0.006						
Mean of residual velocity differences (north)				-0.026						
RMS of residual velocity differences about the mean (east) =						0.064				
RMS of residual velocity differences about the mean (north) =						0.101				
RMS of residual velocity differences about the zero (east) =						0.065				
RMS of residual velocity differences about zero (north) =						0.105				

Appendix I

Least squares inversion for strain rates

In order to solve for strain rate using multiple observations and linear least squares (in the overdetermined case), I set up the following set of matrices.

$$G = \begin{bmatrix} \Delta E_1 & \Delta N_1 & 0 & 0 \\ 0 & 0 & \Delta E_1 & \Delta N_1 \\ \Delta E_2 & \Delta N_2 & 0 & 0 \\ 0 & 0 & \Delta E_2 & \Delta N_2 \\ \vdots & \vdots & \vdots & \vdots \\ \Delta E_n & \Delta N_n & 0 & 0 \\ 0 & 0 & \Delta E_n & \Delta N_n \end{bmatrix} \qquad m = \begin{bmatrix} \varepsilon_{EE} \\ \varepsilon_{EN} \\ \varepsilon_{NE} \\ \varepsilon_{NN} \end{bmatrix} \qquad d = \begin{bmatrix} \Delta V_{E1} \\ \Delta V_{N1} \\ \Delta V_{E2} \\ \Delta V_{N2} \\ \vdots \\ \Delta V_{En} \\ \Delta V_{Nn} \end{bmatrix}$$

$$W = \begin{bmatrix} 1/\sigma_{E1}^2 & 0 & 0 & 0 & 0 & \cdots & 0 & 0 \\ 0 & 1/\sigma_{N1}^2 & 0 & 0 & 0 & \cdots & 0 & 0 \\ 0 & 0 & 1/\sigma_{E2}^2 & 0 & 0 & \cdots & 0 & 0 \\ 0 & 0 & 0 & 1/\sigma_{N2}^2 & 0 & \cdots & 0 & 0 \\ 0 & 0 & 0 & 0 & \cdots & \cdots & 0 & 0 \\ \vdots & \vdots & \vdots & \vdots & \vdots & \vdots & 0 & 0 \\ 0 & 0 & 0 & 0 & 0 & 0 & 1/\sigma_{En}^2 & 0 \\ 0 & 0 & 0 & 0 & 0 & 0 & 0 & 1/\sigma_{Nn}^2 \end{bmatrix}$$

ΔE_n and ΔN_n are baseline components with respect to the centroid of the local network (in mm), ε_{EE}, ε_{EN}, ε_{NE} and ε_{NN} are unknown cartesian strain components (in yr^{-1}); ΔV_{En} and ΔV_{Nn} are relative velocities (in mm/yr); and σ_{En} and σ_{Nn} are the formal errors for the velocity observations.

The equation

$Gm = d$ (or $WGm = Wd$)

can now be solved using a weighted least squares solution;

$m = \left(G^T G\right)^{-1}\left(G^T d\right)$ (or $m = \left(G^T WG\right)^{-1}\left(G^T Wd\right)$

where m is the matrix of unknowns.

I calculate the least squares covariance matrix using

$$C_x = \left[G^T WG\right]^{-1} = \begin{bmatrix} \sigma^2_{EE} & \sigma_{EENN} & \sigma_{EENE} & \sigma_{EEEN} \\ \sigma_{NNEE} & \sigma^2_{NN} & \sigma_{NNNE} & \sigma_{NNEN} \\ \sigma_{NEEE} & \sigma_{NENN} & \sigma^2_{NE} & \sigma_{NEEN} \\ \sigma_{ENEE} & \sigma_{ENNN} & \sigma_{ENNE} & \sigma^2_{EN} \end{bmatrix}$$

Appendix J

Propagation of errors for engineering strain rates

The least squares calculations output $\sigma\varepsilon_{EE}$, $\sigma\varepsilon_{NN}$, $\sigma\varepsilon_{EN}$ and $\sigma\varepsilon_{NE}$, along with their respective covariances. These errors were propagated through the engineering strain rate calculations to obtain σ_D, σ_Ω, $\sigma_{\gamma 1}$, $\sigma_{\gamma 2}$, $\sigma_{|\gamma|}$ and σ_α, using the general formula for propagation of errors with correlated variables;

For a function $x = f(u,v,\ldots)$, the error will be

$$\sigma_x^2 \approx \sigma_u^2 a^2 + \sigma_v^2 b^2 + 2\sigma_{uv}^2 ab + \ldots$$

where $a = \dfrac{\partial x}{\partial u}$ and $b = \dfrac{\partial x}{\partial v}$

Propagation of errors for dilitation

$$D = \varepsilon_{EE} + \varepsilon_{NN}$$

$$a = \frac{\partial D}{\partial \varepsilon_{EE}} = 1 \qquad b = \frac{\partial D}{\partial \varepsilon_{NN}} = 1$$

$$\sigma_D^2 = \sigma_{EE}^2 + \sigma_{NN}^2 + 2\sigma_{EENN}^2$$

$$\sigma_D^2 = \sigma_{EE}^2 + \sigma_{NN}^2 + 2\sigma_{EENN}^2$$

Propagation of errors for rotation rate

$$\Omega = \frac{1}{2}\left(\varepsilon_{NE} - \varepsilon_{EN}\right)$$

$$a = \frac{\partial\Omega}{\partial\varepsilon_{NE}} = \frac{1}{2} \qquad b = \frac{\partial\Omega}{\partial\varepsilon_{EN}} = -\frac{1}{2}$$

$$\sigma_{\Omega}^2 = \frac{\sigma_{NE}^2}{4} + \frac{\sigma_{EN}^2}{4} - \frac{\sigma_{NEEN}^2}{2}$$

Propagation of errors for shear strain 1

$$\gamma_1 = \varepsilon_{EE} - \varepsilon_{NN}$$

$$a = \frac{\partial\gamma_1}{\partial\varepsilon_{EE}} = 1 \qquad b = \frac{\partial\gamma_1}{\partial\varepsilon_{NN}} = -1$$

$$\sigma_{\gamma 1}^2 = \sigma_{EE}^2 + \sigma_{NN}^2 - 2\sigma_{EENN}^2$$

Propagation of errors for shear strain 2

$$\gamma_2 = \varepsilon_{EN} + \varepsilon_{NE}$$

$$a = \frac{\partial\gamma_2}{\partial\varepsilon_{EN}} = 1 \qquad b = \frac{\partial\gamma_2}{\partial\varepsilon_{NE}} = 1$$

$$\sigma_{\gamma 2}^2 = \sigma_{EN}^2 + \sigma_{NE}^2 + 2\sigma_{ENNE}^2$$

Propagation of errors for shear strain magnitude

$$|\gamma| = \sqrt{\left(\varepsilon_{EE} - \varepsilon_{NN}\right)^2 + \left(\varepsilon_{EN} + \varepsilon_{NE}\right)^2}$$

$$a = \frac{\partial|\gamma|}{\partial\varepsilon_{EN}} = \frac{\varepsilon_{EN} + \varepsilon_{NE}}{\sqrt{\left(\varepsilon_{EN} + \varepsilon_{NE}\right)^2 + \left(\varepsilon_{EE} - \varepsilon_{NN}\right)^2}} \qquad b = \frac{\partial|\gamma|}{\partial\varepsilon_{NE}} = a$$

$$c = \frac{\partial|\gamma|}{\partial\varepsilon_{EE}} = \frac{\varepsilon_{EE} - \varepsilon_{NN}}{\sqrt{\left(\varepsilon_{EN} + \varepsilon_{NE}\right)^2 + \left(\varepsilon_{EE} - \varepsilon_{NN}\right)^2}} \qquad d = \frac{\partial|\gamma|}{\partial\varepsilon_{NN}} = -c$$

$$\sigma_{|\gamma|}^2 = \sigma_{EN}^2 a^2 + \sigma_{NE}^2 b^2 + \sigma_{EE}^2 c^2 + \sigma_{NN}^2 d^2 \ldots$$
$$\ldots + 2\sigma_{ENNE}^2 ab + 2\sigma_{ENEE}^2 ac + 2\sigma_{ENNN}^2 ad + 2\sigma_{NEEE}^2 bc + 2\sigma_{NENN}^2 bd + 2\sigma_{EENN}^2 cd$$

Propagation of errors for orientation of maximum extension

$$\alpha = \frac{1}{2}\arctan\left[\frac{\left(\varepsilon_{EN} + \varepsilon_{NE}\right)}{\left(\varepsilon_{EE} - \varepsilon_{NN}\right)}\right]$$

$$a = \frac{\partial\alpha}{\partial\varepsilon_{EN}} = \frac{1}{2\left(1 + \frac{\left(\varepsilon_{EN} + \varepsilon_{NE}\right)^2}{\left(\varepsilon_{EE} - \varepsilon_{NN}\right)^2}\right)\left(\varepsilon_{EE} - \varepsilon_{NN}\right)} \qquad b = \frac{\partial\alpha}{\partial\varepsilon_{NE}} = a$$

$$c = \frac{\partial\alpha}{\partial\varepsilon_{EE}} = -\frac{\varepsilon_{EN} + \varepsilon_{NE}}{2\left(\varepsilon_{EE}^2 + \varepsilon_{EN}^2 + 2\varepsilon_{EN}\varepsilon_{NE} + \varepsilon_{NE}^2 - 2\varepsilon_{EE}\varepsilon_{NN} + \varepsilon_{NN}^2\right)}$$

$$d = \frac{\partial\alpha}{\partial\varepsilon_{NN}} = -c$$

$$\sigma_\alpha = \sigma_{EN}^2 a^2 + \sigma_{NE}^2 b^2 + \sigma_{EE}^2 c^2 + \sigma_{NN}^2 d^2 + 2\sigma_{ENNE}^2 ab + 2\sigma_{ENEE}^2 ac + 2\sigma_{ENNN}^2 ad + \ldots$$
$$2\sigma_{NEEE}^2 bc + 2\sigma_{NENN}^2 bd$$

Appendix K

GPS constraints on ECSZ slip rate at various orientations

Great circle, with NUVEL 1A pole (orientation ~ N36 °W)				
	Vel para	Vel perp	1s para	1s perp
	(mm/yr)	(mm/yr)	(mm/yr)	(mm/yr)
LIND	0.0	0.0	0.1	0.1
ARGU	-4.4	0.6	0.1	0.1
ROGE	-8.5	0.9	0.1	0.1
RYAN	-10.4	0.3	0.1	0.1
SHOS	-10.8	0.1	0.1	0.1
SMYC	-11.6	-0.3	0.1	0.1
APEX	-11.5	-0.2	0.1	0.1
	RMS perpendicular vel (mm/yr) :			0.3
Great circle, with REVEL pole (orientation ~ N36 °W)				
	Vel para	Vel perp	1s para	1s perp
	(mm/yr)	(mm/yr)	(mm/yr)	(mm/yr)
LIND	0.0	0.0	0.1	0.1
ARGU	-4.4	0.4	0.1	0.1
ROGE	-8.5	0.6	0.1	0.1
RYAN	-10.4	-0.1	0.1	0.1
SHOS	-10.8	-0.3	0.1	0.1
SMYC	-11.6	-0.7	0.1	0.1
APEX	-11.5	-0.7	0.1	0.1
	RMS perpendicular vel (mm/yr) :			0.4
N23°W constant azimuth				
	Vel para	Vel perp	1s para	1s perp
	(mm/yr)	(mm/yr)	(mm/yr)	(mm/yr)
LIND	0.0	0.0	0.1	0.0
ARGU	-4.2	1.4	0.1	0.0
ROGE	-8.1	2.7	0.1	0.0
RYAN	-10.1	2.5	0.1	0.0
SHOS	-10.6	2.4	0.1	0.0
SMYC	-11.5	2.3	0.1	0.0
APEX	-11.3	2.3	0.1	0.0
	RMS perpendicular vel (mm/yr) :			2.5
N31°W constant azimuth				
	Vel para	Vel perp	1s para	1s perp
	(mm/yr)	(mm/yr)	(mm/yr)	(mm/yr)
LIND	0.0	0.0	0.1	0.1
ARGU	-4.4	0.8	0.1	0.1
ROGE	-8.4	1.5	0.1	0.1
RYAN	-10.4	1.1	0.1	0.1
SHOS	-10.8	0.9	0.1	0.1
SMYC	-11.7	0.6	0.1	0.1
APEX	-11.5	0.7	0.1	0.1
	RMS perpendicular vel (mm/yr) :			1.0

Appendix L

Calculation of GPS and fault model rotation rate profiles for a Pacific plate - fixed reference frame

1. Calculate great circle distance from each fault to the Euler pole (r_{fault}).

-given fault and Euler pole latitude and longitude, using Matlab 'distance' function

2. Convert slip rate at each fault to a rotation around the pole.

$$\omega_{fault} = \frac{v_{fault}}{r_{fault}}$$, where v_{fault} is fault slip rate.

3. Calculate Okada model rotation rates at each profile point (Ω_x).

$$\Omega_{fault} = \frac{\omega_{fault}}{\pi} \arctan\left(\frac{r_x - r_{fault}}{D_{fault}} \right)$$

$$\overline{\omega} = \frac{\sum_{fault=1}^{N} \Omega_{fault}}{2}$$

$$\Omega_x = \sum_{fault=1}^{N} \Omega_{fault} - \overline{\omega}$$

r_x is distance to pole of each profile point, D_{fault} is locking depth of each fault and N is the number of faults.

4. Rotate GPS velocities from Cartesian xyz to ENU.

$$\begin{pmatrix} v_N \\ v_E \\ v_U \end{pmatrix} = \begin{pmatrix} -\sin\phi\cos\lambda & -\sin\phi\sin\lambda & \cos\phi \\ -\sin\lambda & \cos\lambda & 0 \\ \cos\phi\cos\lambda & \cos\phi\sin\lambda & \sin\phi \end{pmatrix} \begin{pmatrix} v_x \\ v_y \\ v_z \end{pmatrix}$$

λ is longitude of GPS station and ϕ is GPS latitude.

5. Rotate the ENU GPS velocities into velocities parallel and perpendicular to a great circle around the Euler pole.

$$\begin{pmatrix} v_{Perp} \\ v_{Para} \end{pmatrix} = \begin{pmatrix} \cos\alpha & \sin\alpha \\ -\sin\alpha & \cos\alpha \end{pmatrix} \begin{pmatrix} v_E \\ v_N \end{pmatrix}$$

α is azimuth from GPS station to Euler pole

6. Calculate distance from GPS station to Euler pole (r_{GPS}).

Use Matlab 'distance' function with GPS and Euler pole latitude and longitude as input.

7. Convert GPS 'fault-parallel' velocities to rotation rates.

$$\omega_{GPS} = \frac{v_{Para}}{r_{GPS}}$$

8. Calculate the Okada model value for each r_{GPS} value.

$$\Omega_{fault} = \frac{\omega_{fault}}{\pi} \arctan\left(\frac{r_{GPS} - r_{fault}}{D_{fault}} \right)$$

$$\Omega_{GPS} = \sum_{fault=1}^{N} \Omega_{fault} - \overline{\omega}$$

9. Calculate difference between model and GPS rotation rates.

$$\Omega_{diff} = \omega_{GPS} - \Omega_{GPS}$$

10. Calculate RMS of velocity differences.

$$\Omega_{diff\_mm} = \Omega_{diff} . r_{gps}$$

$$\Omega_{rms} = \sqrt{\frac{1}{M} \sum \Omega^{2}_{diff}}$$

M is number of GPS stations

11. Also calculate RMS in mm/yr.

$$\Omega_{rms\_mm/yr} = \sqrt{\frac{1}{M} \sum \Omega^{2}_{diff\_mm/yr}}$$

12. Finally, plot model profile and GPS 'fault-parallel' velocities relative to distance from Euler pole.

Appendix M

Steps taken to invert the GPS rotation rates for fault location, slip rate and locking depth

1. Convert GPS velocities to velocities parallel to a great circle about the North American Euler pole (v_{GPS}).

2. Calculate distances from GPS stations to Euler pole (r_{GPS}) and faults to the North American Euler pole (r_{fault}).

3. Calculate GPS rotation rates and enter into data matrix.

$$\omega_x = \frac{v_x}{r_x} \qquad d = \begin{bmatrix} \omega_1 \\ \omega_2 \\ \vdots \\ \omega_n \end{bmatrix}$$

4. Create weight matrix of GPS rotation rate errors.

$$W = \begin{bmatrix} 1/\sigma_1^2 & & & \\ & 1/\sigma_2^2 & & \\ & & \ddots & \\ & & & 1/\sigma_n^2 \end{bmatrix}$$

5. Assign a priori values for slip rate, locking depth and distance of fault from the Euler pole, then convert slip rates to rotation rates.

$$\tilde{\omega}_f = \frac{\tilde{s}_f}{\tilde{r}_f}$$

6. Define constraints for slip rate, locking depth and fault location and enter into apriori covariance matrix.

$$C_0^{-1} = \begin{bmatrix} 1/\sigma_{\omega 1}^2 & & & & & & & \\ & \ddots & & & & & & \\ & & 1/\sigma_{\omega m}^2 & & & & & \\ & & & 1/\sigma_{D1}^2 & & & & \\ & & & & \ddots & & & \\ & & & & & 1/\sigma_{Dm}^2 & & \\ & & & & & & 1/\sigma_{rf1}^2 & \\ & & & & & & & \ddots \\ & & & & & & & & 1/\sigma_{rfm}^2 \end{bmatrix}$$

7. Start least squares iteration.

8. Enter provisional values for slip rate and locking depth into the provisional model array.

$$\tilde{m} = \begin{bmatrix} \tilde{\omega}_1 \\ \vdots \\ \tilde{\omega}_m \\ \tilde{D}_1 \\ \vdots \\ \tilde{D}_m \\ \tilde{rf}_1 \\ \vdots \\ \tilde{rf}_m \end{bmatrix}$$

9. Calculate difference between GPS rotation rates and model rotation rates at each station, then enter these into matrix of model adjustments.

$$\Omega_f = \frac{\tilde{\omega}_f}{\pi} \arctan\left(\frac{\tilde{r}_f - r_x}{\tilde{D}_f}\right) - \frac{\tilde{\omega}_f}{2}$$

$$\Omega_x = \Omega_{f1} + \Omega_{f2} \cdots + \Omega_{fm} - \frac{\sum_1^m \omega_f}{2}$$

$$K = \begin{bmatrix} \omega_1 - \Omega_1 \\ \omega_2 - \Omega_2 \\ \vdots \\ \omega_n - \Omega_n \end{bmatrix}$$

10. Calculate the difference between the original and current provisional model values.

$$\Delta m_0 = \tilde{m}_0 - \tilde{m}_n$$

11. Create least squares design matrix using partial differentials of elastic displacement model with respect to slip rate and locking depth.

$$\frac{\partial \Omega_x}{\partial \omega_f} = \frac{1}{\tilde{\omega}_f} \arctan \frac{\tilde{r}_f - r_x}{\tilde{D}_f} - \frac{\tilde{\omega}_f}{2}$$

$$\frac{\partial \Omega_x}{\partial D_f} = \frac{-\tilde{\omega}_f \left(\tilde{r}_f - r_x \right)}{\pi \left(\tilde{D}_f^2 + \left(\tilde{r}_f - r_x \right)^2 \right)}$$

$$\frac{\partial \Omega_x}{\partial r_f} = \frac{\tilde{D}_f \tilde{\omega}_f}{\pi \left(\tilde{D}^2 + \left(\tilde{r}_f - r_x \right)^2 \right)}$$

$$Q = \begin{bmatrix} \frac{\partial \Omega_1}{\partial \omega_{f1}} & \cdots & \frac{\partial \Omega_1}{\partial \omega_{fm}} & \frac{\partial \Omega_1}{\partial D_{f1}} & \cdots & \frac{\partial \Omega_1}{\partial D_{fm}} & \frac{\partial \Omega_1}{\partial r_{f1}} & \cdots & \frac{\partial \Omega_1}{\partial r_{fm}} \\ \vdots & \vdots & \vdots & \vdots & \vdots & \vdots & \vdots & \vdots & \vdots \\ \frac{\partial \Omega_n}{\partial \omega_{f1}} & \cdots & \frac{\partial \Omega_n}{\partial \omega_{fm}} & \frac{\partial \Omega_n}{\partial D_{f1}} & \cdots & \frac{\partial \Omega_n}{\partial D_{fm}} & \frac{\partial \Omega_n}{\partial r_{f1}} & \cdots & \frac{\partial \Omega_n}{\partial r_{fm}} \end{bmatrix}$$

12. Solve constrained least squares problem to get model adjustments.

$$\Delta m = \left[Q^T W Q + C_c^{-1} \right]^{-1} \left[Q^T W K + C_o^{-1} \Delta m_o \right]$$

13. Adjust previous estimates of model values.

$$m_{n+1} = m_n + \Delta m$$

14. If the model adjustments have only changed a small amount, continue. Otherwise, iterate by returning to step 5.

$$e = \begin{bmatrix} (\Delta \omega_{fault}(i-1))E^{-16} \\ \vdots \\ (\Delta D_{fault}(i-1))E^{-8} \\ \vdots \end{bmatrix}$$

If $\Delta m^2 \geq e^2 \Rightarrow$ continue
If $\Delta m^2 \leq e^2 \Rightarrow$ iterate

15. Calculate covariance matrix.

$$C_x = \left[Q^T W Q + C_o^{-1}\right]^{-1}$$

16. Calculate residual rotation rate differences (y) between GPS and model rotation rates at each station, using the estimated fault parameters as input to the elastic displacement model.

17. Convert fault rotation rates, rotation rate errors and residuals back to velocities.

$$s_f = \omega_f r_f$$

$$v_x = y_x r_x$$

18. Calculate RMS of residuals.

$$v_{RMS} = \sqrt{\frac{1}{n}\sum v_x^2}$$

Appendix N

Propagation of errors for estimated model strain

$$\dot{\gamma}_x = \frac{A}{\pi}\left(\frac{D}{x^2 + D^2}\right)$$

$$a = \frac{\partial \gamma_x}{\partial A} = \frac{D}{\pi\left(D^2 + x^2\right)}$$

$$b = \frac{\partial \gamma_x}{\partial D} = \frac{-2AD^2}{\pi\left(D^2 + x^2\right)^2} + \frac{A}{\pi\left(D^2 + x^2\right)}$$

$$c = \frac{\partial \gamma_x}{\partial x} = -\frac{2ADx}{\pi\left(D^2 + x^2\right)^2}$$

$$\sigma_{\dot{\gamma}}{}^2 = a^2\sigma_A^2 + b^2\sigma_D^2 + c^2\sigma_x^2 + 2\sigma_{AD}^2 ab + 2\sigma_{Ax}^2 ac + 2\sigma_{Dx}^2 bc$$